Deep Convection, Magnetism and Solar Supergranulation

by

J.W. Lord

B.A., Whitman College, 2008

M.S., University of Colorado Boulder, 2011

A thesis submitted to the

Faculty of the Graduate School of the

University of Colorado in partial fulfillment

of the requirements for the degree of

Doctor of Philosophy

Department of Astrophysical and Planetary Sciences

2014

This thesis entitled:
Deep Convection, Magnetism and Solar Supergranulation
written by J.W. Lord
has been approved for the Department of Astrophysical and Planetary Sciences

_____

Mark Rast

_____

Matthias Rempel

_____

Phil Armitage

_____

Benjamin Brown

_____

Juri Toomre

Date _____

The final copy of this thesis has been examined by the signatories, and we find that both the content and the form meet acceptable presentation standards of scholarly work in the above mentioned discipline.

Lord, J.W. (Ph.D., Astrophysics)

Deep Convection, Magnetism and Solar Supergranulation

Thesis directed by Prof. Mark Rast

We examine the effect of deep convection and magnetic fields on solar supergranulation. While supergranulation was originally identified as a convective flow from relatively great depth below the solar surface, recent work suggests that supergranules may originate near the surface. We use the MURaM code to simulate solar-like surface convection with a realistic photosphere and domain size up to $197 \times 197 \times 49$ Mm^3. This yields nearly five orders of magnitude of density contrast between the bottom of the domain and the photosphere which is the most stratified solar-like convection simulations that we are aware of.

Magnetic fields were thought to be a passive tracer in the photosphere, but recent work suggests that magnetism could provide a mechanism that enhances the supergranular scale flows at the surface. In particular, the enhanced radiative losses through long lived magnetic network elements may increase the lifetime of photospheric downflows and help organize low wavenumber flows. Since our simulation does not have sufficient resolution to resolve increased cooling by magnetic bright points, we artificially increase the radiative cooling in elements with strong magnetic flux. These simulations increase the cooling by 10% for magnetic field strength greater than 100 G. We find no statistically significant difference in the velocity or magnetic field spectrum by enhancing the radiative cooling. We also find no differences in the time scale of the flows or the length scales of the magnetic energy spectrum. This suggests that the magnetic field is determined by the flows and is largely a passive tracer.

We use these simulations to construct a two-component model of the flows: for scales smaller than the driving (integral) scale (which is four times the local density scale height) the flows follow a Kolmogorov ($k^{-5/3}$) spectrum, while larger scale modes decay with height from their driving depth (i.e. the depth where the wavelength of the mode is equal to the driving (integral) scale).

This model reproduces the MURaM results well and suggests that the low wavenumber power in the photosphere imprints from below. In particular, the amplitude of the driving (integral) scale mode at each depth determines how much power imprints on the surface flows. This is validated by MURaM simulations of varying depth that show that increasing depths contribute power at a particular scale (or range of scales) that is always at lower wavenumbers than shallower flows. The mechanism for this imprinting remains unclear but, given the importance of the balances in the continuity equation to determining the spectrum of the flows, we suggest that pressure perturbations in the convective upflows are the imprinting mechanism.

By comparing the MURaM simulations to SDO/HMI observations (using the coherent structure tracking code to compute the inferred horizontal velocities on both data sets), we find that the simulations have significant excess power for scales larger than supergranulation. The only way to match observations is by using an artificial energy flux to transport the solar luminosity for all depths greater than 10 Mm below the photosphere (down to the bottom of the domain at 49 Mm depth). While magnetic fields from small-scale dynamo simulations help reduce the rms velocity required to transport the solar luminosity below the surface, this provides only a small reduction in low wavenumber power in the photosphere.

The convective energy transport in the Sun is constrained by theoretical models and the solar radiative luminosity. The amplitude or scale of the convective flows that transport the energy, however, are not constrained. The strong low wavenumber flows found in these local simulations are also present in current generation global simulations. While local or global dynamo magnetic fields may help suppress these large-scale flows, the magnetic fields must be substantially stronger throughout the convection domains for these simulations to match observations. The significant decrease in low wavenumber flow amplitude in the artificial energy flux simulation that matches the observed photospheric horizontal velocity spectrum suggests that convection in the Sun transports the solar luminosity with much weaker large-scale flows. This suggests that we do not understand how convective transport works in the Sun for depths greater than 10 Mm below the photosphere.

Contents

Chapter

Tables

Table

Figures

Figure

Chapter 1

Introduction

1.1   Quiet Sun Convection

The outer 30% of the Sun by radius (approximately 200,000 km) is unstable to thermal convection and, consequently, called the solar convection zone (Christensen-Dalsgaard et al., 1996). At the bottom of the convection zone the radiative energy flux (which transports the solar luminosity below the convection zone) continues to transport a significant amount of energy (Miesch, 2005). This radiative flux decays with height up to $\sim 1/3$ of the way into the convection zone where the convection dominates the energy transport. From this point convection transports the energy up to the surface where it is radiated away.

Observations suggest that there are three length scales of convection on the surface of the Sun: granulation, mesogranulation and supergranulation. Granulation has well defined properties: 1000 km diameter, 1 km s^{-1} vertical flow, and a 0.2 hour lifetime (Rieutord & Rincon, 2010). Observations have shown that within granules the vertical velocity is correlated with intensity, a fact that confirms its convection nature (Richardson & Schwarzschild, 1950; Stuart & Rush, 1954; Plaskett, 1954; Canfield & Mehltretter, 1973).

Mesogranulation is an intermediate length scale of convection with a length scale of 5000 km, 60 m s^{-1} vertical flows and a lifetime of 3 hours (Rast, 2003). There is debate about the origin and existence of mesogranulation. It was originally suggested that the mean depth of hydrogen and helium ionization represent length scales of the system and, consequently, ionization enhances the amplitude of convection on these scales (Simon & Leighton, 1964; November et al., 1981).

Thus granular, mesogranular and supergranular scales would reflect the mean depth of hydrogen, helium I, and helium II ionization, respectively. The mechanism underlying this relationship, however, is unclear. Mesogranulation has been observed as a time-averaged feature in Doppler images (November et al., 1981), but there is no enhancement of power at mesogranular scales observed in the velocity spectrum of the photosphere (Hathaway et al., 2000; Rieutord et al., 2010).

The properties of supergranulation are quite different: 32,000 km diameter, 400 m s^{-1} horizontal flow, and a roughly 1.8 day lifetime (Rieutord & Rincon, 2010). While there have been measurements that successfully correlate the vertical velocity with the intensity (finding a 0.1% contrast between cell center and border), the magnetic network makes these measurements difficult (Goldbaum et al., 2009). Supergranules have a scale of motion that does not correspond to any obvious length scale in the convective flow; it is much smaller than the depth of the convection zone and much larger than the scale height at the surface.

Due to the large scale height deep in the convection zone (e.g. density scale height reaches $H_D \sim 100$ Mm Christensen-Dalsgaard et al., 1996) we expect larger scale convection with slower speeds (due to the increased density) typically called giant cells. These giant cell flows are found in global simulations of the solar convection zone with flow amplitudes roughly matched in one-dimensional mixing length models (Miesch, 2005; Christensen-Dalsgaard et al., 1996). The deep convection is difficult to measure in observations as they are dominated by surface convection; observations have only recently found a weak signal of giant cell convection by tracking the motions of supergranules across the solar surface for several days (Hathaway et al., 2013).

The observed solar magnetic field is dominated by the 11 year activity (sunspot) cycle. While the sunspots and other regions with large magnetic flux imbalances are common during times of maximum solar activity, there are ubiquitous magnetic fields present even during times of minimum solar activity with very small flux imbalances (Martínez Pillet, 2013). This suggests two possible origins for the field we observe at the surface: a global dynamo creating buoyant flux ropes that rise from the bottom of the convection zone which produce magnetic features with strong flux

imbalances in the photosphere (Fan, 2009) and a local dynamo near the surface which generates small-scale magnetic field with no net flux imbalance on large-scales (de Wijn et al., 2009). We call the regions of the solar surface with small magnetic flux imbalance (whether during solar maximum or minimum) the quiet Sun which are either a product of the local dynamo or decaying active regions from the global dynamo (Lamb et al., 2010). This quiet Sun magnetic field is advected to the vertices of supergranules where it concentrates into the magnetic network (see §1.1.4.1). While the magnetic network visually dominates observations of quiet Sun magnetic field, there is field observed on smaller scales (these scales are typically called the internetwork) down to the minimum resolution of the current generation of solar telescopes.

1.1.1   Length Scales of Surface Convection

The convection near the surface is both very turbulent and highly stratified. The fluid Reynolds number ($Re = LV/\nu$ where L is the depth of the convective layer in the Sun, V is the typical velocity and ν is the viscous dissipation) of solar convection is between 10^{10} and 10^{13} while laboratory experiments, for a reference point, can achieve root-mean-square (rms) $Re < 10^7$ (Rieutord & Rincon, 2010). The largest direct numerical simulation (DNS) that solves the Navier-Stokes equations with a physical viscosity (that we are aware of) has reached Reynolds number of 5000 (Lee et al., 2013). The convection zone as a whole is extremely stratified with a density ratio between the bottom of the convection zone and photosphere close to 10^6 with half of this change occurring in the uppermost 20 Mm (Nordlund et al., 2009).

The buoyancy driving in the solar convection zone is very strong compared to the thermal and viscous diffusion (Rieutord & Rincon, 2010). The turbulent energy spectrum injection scale is approximately equal to the local scale height (with a pre-factor of order one, Rincon, 2007). Since the scale height increases with depth, this suggests that the length scale of the convection increases with depth within the stratified convection zone. The pressure scale height ranges from $H_p \approx 150$ km at the optical depth unity surface to nearly 60 Mm (where 1 Mm = 1,000 km) at the bottom of the convection zone (Christensen-Dalsgaard et al., 1996). The length scale of granulation is related

to both the local scale height through the energy injection and the width of the thermal boundary layer (i.e. $L_\kappa \sim 1$ Mm the thermal dissipation length scale, Rieutord & Rincon, 2010) through the radiative cooling which generates the downflows. The other dissipation length scales (i.e. viscous and magnetic) are much smaller and do not contribute to the observed scales of convection. The only other length scale in the system is the depth of the convection zone, $L_{SCZ} \approx 200$ Mm, which is much larger than either granular or supergranular scales and does not play a significant role in regulating these surface flows.

The ionization of hydrogen also plays an important role in granulation. The depth of 50% hydrogen ionization is very close to the surface and depends significantly on the local temperature. The upflows are mostly ionized just below the photosphere and hydrogen recombination contributes 2/3 of the convective energy flux near the surface (Rast et al., 1993). The hydrogen is then mostly neutral in the downflows until a few Mm below the surface. While helium is completely neutral near the surface and does not directly affect the granular flows, He I and II play a role in the convection and mean stratification within ~ 30 Mm of the surface. Below this depth both hydrogen and helium are mostly ionized and, since all other elements have such low abundance in the solar atmosphere, the plasma behaves nearly as an ideal gas.

1.1.2   Giant Cell Convection

Theoretical work suggests that the deep convective velocities are much slower than surface flows (Christensen-Dalsgaard et al., 1996) with large-scale, turbulent convective cells aligned with the axis of rotation (Brun et al., 2004). Our understanding of convective energy transport yield expected minimum flow speeds that transport the solar luminosity to the surface based on mixing length models (Christensen-Dalsgaard et al., 1996) and global simulations (Miesch et al., 2000, 2008).

Since these deep convective flows are much slower than at the surface they have timescales comparable to the solar rotation (~ 1 month) which means the the Rossby number is close to one and these flows feel the influence of rotation (Miesch, 2005). Correlations of orthogonal components

of the velocity caused by the interaction of giant cell convection with the Coriolis force transports angular momentum via convection. This angular momentum transport is required to maintain the solar differential rotation and meridional circulation.

The solar differential rotation is one of the most reliable helioseismic measurements (Thompson et al., 2003), and is, consequently, used to compare simulations and observations. The giant cell flows must be rotationally constrained (with the Coriolis force comparable to the inertial force of the flow) to transport angular momentum towards the equator which maintains the observed solar differential rotation with faster rotating equator and slower rotating pole (Miesch et al., 2000, 2008; Hotta, 2014a). The Coriolis force (which is set by the solar rotation rate), consequently, places upper limits on the flow velocities. This upper limit is weaker than the flow amplitudes necessary to transport the solar luminosity in global convection simulations (Hotta, 2014a). This suggests that the solar energy flux is transported with weaker flows or on smaller scales than these simulations capture.

One of the primary issue with global simulations is that they have insufficient resolution to reach the solar Reynolds number (a problem faced by all simulations of solar convection as the largest Reynolds number that DNS can reach is 5000, Lee et al., 2013). As increased computational resources allow for higher resolution and lower diffusivity these simulations enter new parameter regimes. Decreasing the viscosity in global convection simulations requires a reduction of the maximum energy flux transported by the convection (to significantly less than the solar luminosity) for flows to be rotationally constrained (Hotta, 2014a). Since the flows must be rotationally constrained to transport angular momentum equator-ward and maintain the solar differential rotation, this suggests that the properties of the convection are changing as the simulations move closer to the solar parameter regime.

1.1.2.1   Deep Convective Power Spectrum

The high cadence, high resolution observations from the Helioseismic and Magnetic Imager (HMI) on board the Solar Dynamics Observatory (SDO) which launched in 2010, have allowed

time-distance helioseismology to produce new measurements of the large-scale flows below the solar surface. These techniques compare the travel times of waves traveling between a pair of points across the solar surface. The travel times are sensitive to the subsurface flows and thus help measure the convective pattern and flow amplitudes below the surface. These observations have found an upper limit for giant cell flows that are a factor of 100 weaker than predicted by models (Hanasoge et al., 2010, 2012). In Figure 1.1 we compare the spectrum measured by helioseismology (at $0.96R_{sun}$, *solid* black curve) to the global simulations of Miesch et al. (2008, *dotted* blue curve) and local area simulations of Stein & Nordlund (2006, *solid* red curve, both simulation spectra are at $0.98R_{sun}$). Both the global and local area simulations are in good agreement but show excess power several orders of magnitude above this helioseismic upper limit. The global simulations have excess power compared to observations of the low wavenumber convection in the photosphere (results from coherent structure tracking of HMI observations, *long-dashed* green curve, Roudier et al., 2012) which suggests that the convection in the simulations must not imprint on the surface or the amplitude of the convection in the Sun is weaker than in the simulations.

These helioseismic measurements place the strictest limit on giant cell flow velocities to date and challenge the predicted flow speed of theoretical models of solar convection. Deriving the minimum convective velocity required to maintain the Reynolds stress that transports angular momentum provides an estimate of the lower limit on convective flows that is in disagreement with this helioseismic limit (Miesch et al., 2012). It is important to note that these time-distance helioseismic measurements have only been conducted by one group on one data set and have not been reproduced. Preliminary measurements using ring analysis suggests that large-scale flows are closer to the values found in theoretical models (Greer 2014, private communication). While there is some uncertainty about the time-distance helioseismic measurements, this adds to the other evidence (Hotta, 2014a) that deep convective flows in the Sun are weaker than previously thought.
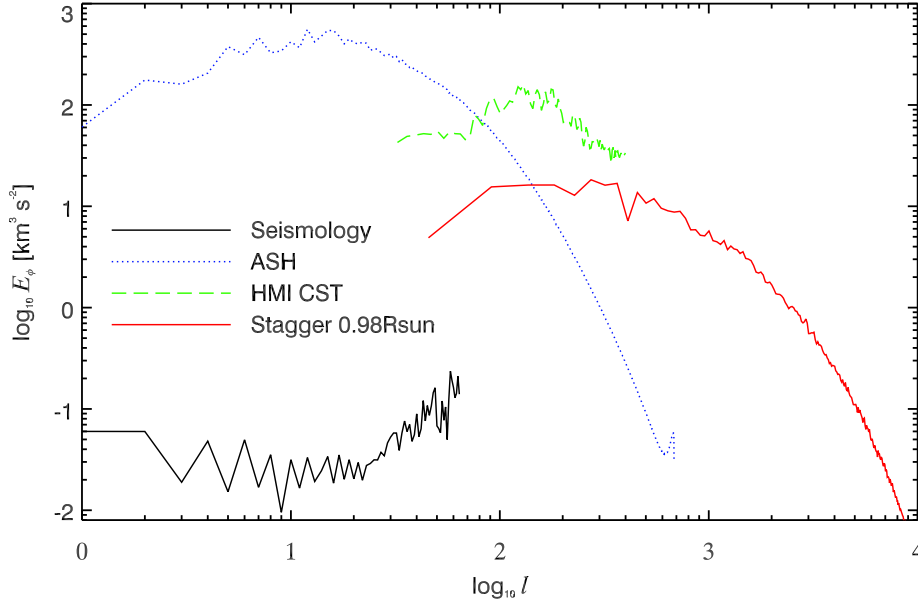
Figure 1.1 The kinetic energy spectrum of longitudinal solar velocities as a function of spherical harmonic wavenumber, l. The *solid* (black) curve shows the observational upper limit measured using time-distance helioseismology on SDO/HMI observations at 0.96 of the solar radius and 1-day averaging from Hanasoge et al. (2012). The *long-dash* (green) curve is computed from applying the granulation tracking (CST) method to SDO/HMI data (Roudier et al., 2012). The *dotted* (blue) curve show results from an ASH global simulation at 0.98 of the solar radius (Miesch et al., 2008) and the *solid* (red) curve show results from a local simulation using the stagger code with domain size $96 \times 96 \times 20\text{Mm}^3$ (Stein & Nordlund, 2006). These results were originally published in Gizon & Birch (2012).

1.1.3   Supergranulation

The origin of supergranulation is the central theme of this thesis. Supergranulation does not correspond to any preferred length scales of the system and understanding the origin of supergranulation will likely provide new insight into turbulent magneto-convection.

1.1.3.1   Early Observations of Supergranulation

The Sun's supergranulation was originally observed as a velocity fluctuation by Hart (1954) who followed up this work with an initial estimate of 26 Mm for the length scale of these fluctuations (Hart, 1956). This was later identified as convection in origin and named "supergranulation" by Leighton et al. (1962), which they suggested as a pattern of convective cells "which come from relatively great depths inside the Sun". In this same work they identified the flow pattern as primarily horizontal and provided initial estimates for the properties of the supergranules. This was shortly followed by new observations which gave more precise measurements of the supergranules that are consistent with the observed properties of supergranulation as found by modern instruments: velocity between $300 - 500$ m s^{-1}, length scale ~ 32 Mm and lifetimes ~ 20 hrs (Simon & Leighton, 1964). Finally, it was also noted in this early stage that there was high spatial correlation between the boundaries of supergranular cells and the photospheric network magnetic field (specifically observations of the Ca II K 393.4nm line which correlates with magnetic field strength, Simon & Leighton, 1964).

The decade between Hart (1954) and Simon & Leighton (1964) was the most productive for the study of supergranulation to date with most of the primary features of supergranules being observationally constrained. While Simon & Leighton (1964) suggested an origin of supergranulation below the surface related to the ionization of helium—due to instabilities caused by changes in the mean molecular weight—theoretical work has been much slower catching up to the observations. There is still no definitive result demonstrating what physical mechanism(s) determine the length scale or lifetime of supergranulation, where supergranules originate (near the surface or deep in the

convection zone), or what governs the relationship between supergranules and the magnetic field. These are the primary questions addressed in this thesis.

1.1.3.2   Suggested Origins of Supergranular Length Scale

As discussed in §1.1.1, supergranulation does not correspond to any of the length scales of the system. It is much smaller than the depth of the convection zone and much larger than the dissipation length scale or the scale height at the surface. There is a depth with scale height equal to 32 Mm but the scale height increases continuously from the surface to the bottom of the convection zone, so there is no a priori expectation that motions at a depth where the scale height is equal to 32 Mm should be selected as a scale of motion represented at the surface.

Given that the mean depth of hydrogen ionization (1 Mm) is similar to the length scale of granulation, it was suggested that a secondary instability related to He II ionization excites supergranular flows (Simon & Leighton, 1964), but this instability has not been found. This hypothesis also suggested an unobserved length scale related to He I ionization which was first discovered by November et al. (1981). The length scales of granulation, mesogranulation and supergranulation suggests a hierarchy of convection which is related the mean depths of ionization of H and He, with the depth of 50% He II ionization (20 Mm below the photosphere) inducing supergranular convection. The identification of mesogranulation was made from time-averaged Doppler images but observations of the photospheric velocity spectrum have not found any mesogranular signal which suggests that it may not be a distinct scale of motion (Hathaway et al., 2000; Rieutord & Rincon, 2010). This calls into question the hierarchy of scales based on the depths of H and He ionization.

Ionization influences four thermodynamic properties of the plasma: the particle number, the specific heat, the specific internal energy, and the opacity. Give that hydrogen is the most abundant element in the Sun, all of these effects are most prominent in regions of partial hydrogen ionization where these changes play a significant role in the energy transport (with the latent heat flux of ionization transporting 2/3 of the enthalpy flux), radiative cooling of the photosphere (with a

significant reduction in opacity due to recombination of hydrogen) and the creation and acceleration of convective downflows (Rast et al., 1993). The ionization also induces instabilities that reduce the thermal damping and enhance the buoyancy driving of the flows, but these instabilities favor small-scale convective motions (Rast, 1991; Rast & Toomre, 1993). In addition, these changes are much less significant at the depths of helium ionization where the thermodynamic perturbations are small and the mean free path of a photon is limited by the increased density of the plasma (due to the stratification) and free electrons from hydrogen. It remains unclear how helium ionization may enhance the amplitude of surface flows at supergranular scales.

Another suggestion is that granular dynamics could organize long-lived downflows separated by a sufficient distance that would then act as the vertices of supergranules. Previous work has demonstrated that this self organization is possible. The mutual advection and interaction of downflow plumes on a horizontal plane (using an n-body simulation with the horizontal velocity profile of downflows) with amplitude and lifetime similar to observed granular downflows can organize into a larger scale convective pattern (Rast, 2003). By using the observed properties of magnetic elements, specifically the advection and flux cancellation (via the collision of opposite polarity elements), to increase the lifetime of the mutually advected particles in the n-body simulation, these elements form a self-organized network of magnetic elements that outline supergranular scale cells with a model that is independent of supergranular flows (Crouch et al., 2007). It has been suggested that the magnetic elements that are organized by the granular flows may play a role in initiating the supergranular flow pattern (Crouch et al., 2007). Such a photospheric self-organization would imply that the surface layers drive supergranular convection and that these scales are then imprinted down into the rest of the convection zone.

1.1.3.3   Radiative MHD Simulations of Supergranulation

Recent radiative hydrodynamic simulations with up to 98×98 Mm^2 horizontal and 20 Mm vertical domain size have found that granulation is the only preferred length scale of convection (Stein et al., 2006). These simulations are deep enough to reach the 50% ionization depth of

He II and find no evidence that helium ionization enhances supergranular scale flows. Similar magnetized simulations have found that magnetic field is advected into a network that is consistent with supergranular cell sizes (Ustyugov, 2010), but limits to the horizontal domain (60×60 Mm^2) leave questions as to whether these simulations capture supergranulation.

While radiative MHD simulations helped improve our understanding of granules, such as the driving from the thermal boundary layer and the generation of downflows (Stein & Nordlund, 1998), no simulations to date have found enhanced power in the photospheric velocity spectrum at the length scales of supergranulation (Ustyugov, 2010; Stein et al., 2009). Similar to the global simulations, these simulations are not able to reach the solar Reynolds number with current computation resources. While the resolution and diffusivity are continuing problems with these simulations, there are other aspects of the physics of solar surface convection that previous simulations did not explore. The most important of these is the depth of the simulation, which (at 20 Mm) captures part of the region of partial He II ionization, but does not include the larger scale deeper flows which may affect the surface (see §1.1.3.5). The relationship of quiet Sun magnetism to supergranulation has also not been confirmed and may prove important to the supergranular length scale.

1.1.3.4   Surface Power Spectrum

Observations of the doppler velocity in the solar photosphere from SOHO/MDI (Hathaway et al., 2000) show the surface velocities (Figure 1.2). Since the supergranular flows are primarily horizontal, we cannot observe the doppler velocities at disk center.

Comparing supergranular scale convection between simulations and observations have focused on comparing the power spectrum of the photospheric horizontal velocities. The velocity spectrum identifies the scale of the energy-containing structures in the photosphere (as compared to structure identification which we discuss in §1.1.4.1). There are, however, limitations to this technique primarily because the Fourier spectrum will identify power in both the size of the convective cell (such as the granular upflows) and the size of the boundary between cells (the downflow lanes). Furthermore, power is spread between modes, especially by any sharp features, which means that
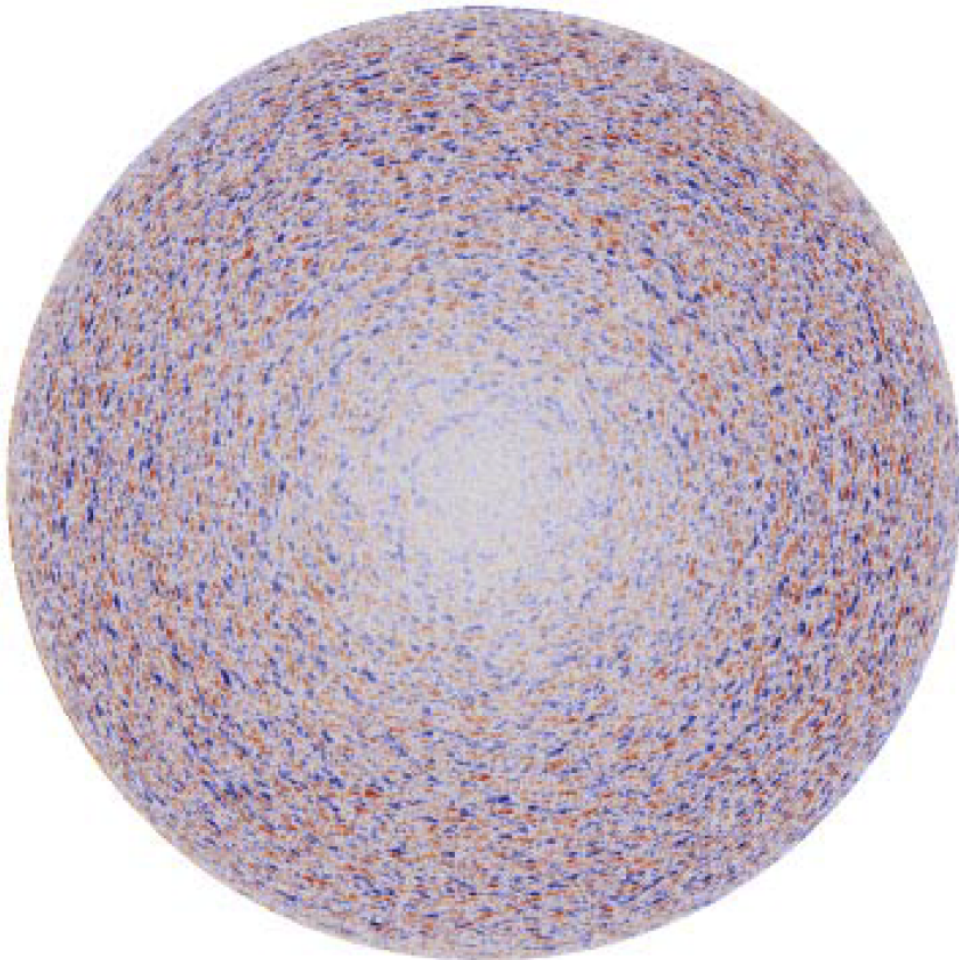
Figure 1.2 The doppler shift velocities using full-disk MDI data from 01:00 UT on 24 May 1996 (image from Hathaway et al. (2000)). Red-shifted plasma is in red and blue-shifted plasma is in blue. The flows are dominated by the $300 - 400$ m s^{-1} horizontal flows of the supergranules.

while we identify the power as coming from a single wavelength mode, there is not a one to one correspondence between structure size and the wavenumber.

Since the early observations of supergranulation (Hart, 1954; Simon & Leighton, 1964), technological improvements have allowed the creation of instruments that provide continuous full-disk observations that resolve motions in the photosphere from granular scales to the largest possible convective scale. The spherical harmonic spectrum of the horizontal velocities computed from the doppler velocities observed by one of these instruments, SOHO/MDI (shown in Figure 1.2), shows a clear peak at both granular and supergranular scales (Hathaway et al., 2000). This peak confirms that supergranulation is a distinct scale of motion on the Sun and provides constraints on the photospheric spectrum of motion that can be compared with the motions in radiative MHD simulations. Other groups use correlation tracking of the continuum intensity to infer large-scale horizontal motions in the photosphere and compute the spectrum of these motions for further comparison (Nordlund et al., 2009).

We show the photospheric velocity spectrum, $V(k) = \sqrt{kP(k)}$, in Figure 1.3 where $P(k)$ is the power spectrum of the horizontal velocity and k is the wavenumber of the spectrum (Nordlund et al., 2009). Converting from a cartesian wavenumber (which are used in the simulations) to spherical harmonic wavenumber uses the relationship $\lambda = \frac{2\pi R_{sun}}{k_{spherical}}$ and $k_{cartesian} = \frac{2\pi}{\lambda}$. The doppler velocity spectrum shows increased power at $k_{spherical} \approx 120$ which corresponds to $\lambda \approx 37$ Mm. The simulations find no enhancement of power at supergranular scales (Stein et al., 2006).

We also refer back to the photospheric power spectrum in Figure 1.1, which shows the spectrum of supergranulation using the coherent structure tracking (CST) method (Roudier et al., 2012). This method infers photospheric horizontal velocities by tracking the motion of granules and computes the spectrum of these motions. This spectrum is the most up to date observations of the solar horizontal velocity spectrum using the full-disk images from HMI (which has increased resolution compared to the telescopes used for observations in Figure 1.3) and we use these results to compare to simulations throughout the thesis. These observed spectra are one of the primary methods for identifying supergranulation (the other, magnetic fields, is discussed in §1.1.4.1) and
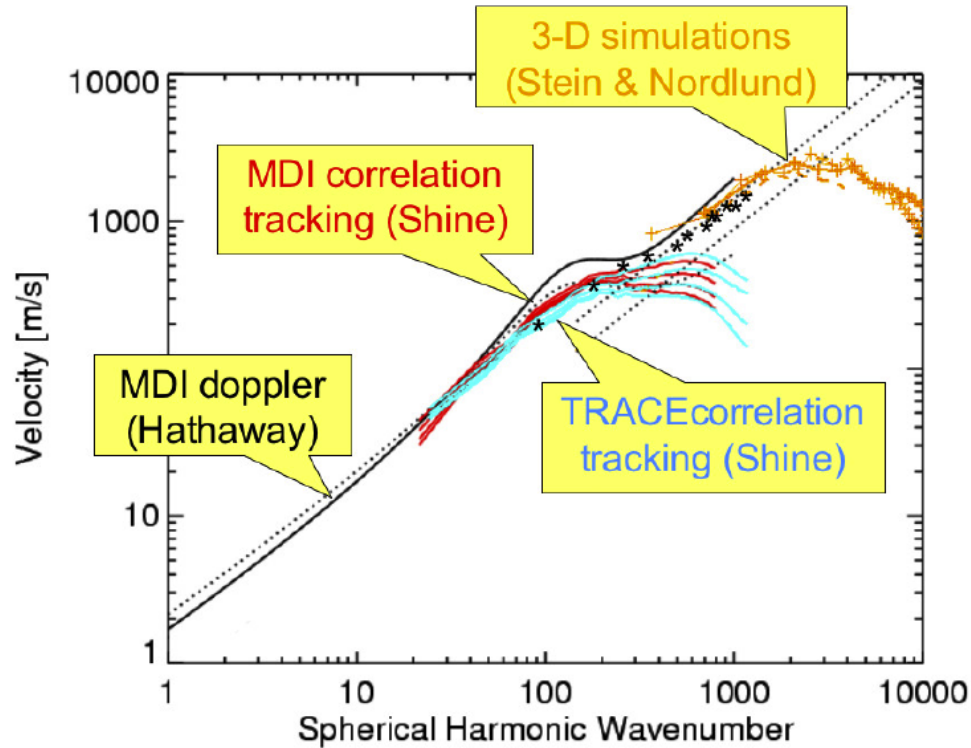
Figure 1.3 The surface horizontal velocity spectrum from observations and simulations as a function of wavenumber from sub-granular scales to global scales. The observations use correlation tracking on TRACE and SOHO/MDI continuum intensity images to compute the velocity spectrum (Shine) or compute the spherical harmonic spectrum directly from MDI doppler images (Hathaway et al., 2000). The simulation results are from two sets of stagger simulations: granulation scale in orange symbols (Stein & Nordlund, 1998) and supergranulation scale in black symbols (Stein et al., 2006; Stein & Nordlund, 2006). This image was originally published in Nordlund et al. (2009).

a key comparison for simulations of supergranulation.

1.1.3.5   Deep or Shallow Supergranulation?

One of the primary unanswered questions about supergranulation is: does supergranular convection originate near the surface or deep in the convection zone? Recent observations of supergranules have been used to probe the properties of the deeper convection zone. By simulating the motion of solar supergranules and comparing to the observed doppler velocities of the solar disk (Figure 1.2), Hathaway et al. (2010) found that the motions of supergranules are consistent with these convective cells being advected by the observed near surface shear of ~ 30 m s^{-1} (a $\sim 3\%$ change in the rotation rate) from the surface to 35 Mm depth (Howe et al., 2007). Based on these results, Hathaway et al. (2010) suggests that supergranules must extend to at least 30 Mm depth. Later work expanded on this idea by tracking supergranules in doppler observations and comparing the wavelength of the supergranule to the rotation profile as a function of depth measured by global helioseismology. This comparison is consistent with the wavelength of the supergranulation (ranging from ~ 10 Mm to ~ 100 Mm) equal to the depth at which the rotation advects the supergranule (Hathaway, 2012a). This suggests that supergranules originate at least ~ 10 Mm below the photosphere and imprint on the surface.

There is no a priori reason to expect the supergranular wavelength to be equal to its depth. While the horizontal length scale of convection increases with depth, this may be related to the increasing scale height which sets the integral scale of the flows (§1.1.1). This may be a consequence of the originating depth of the supergranulation not equaling the depth at which rotation advects the flow or the solar stratification (which determines the scale height with depth) by chance makes the diameter of the convection equal to its depth.

Observers have also used time-distance helioseismology to directly measure supergranular flows as a function of depth. One recent method uses large-separation rays (i.e. pressure waves which travel 10-24 heliospheric degrees horizontally before returning to the photosphere) since they approach the surface primarily in the vertical direction (i.e. with very little horizontal motion).

While measurements using smaller rays cannot separate horizontal and vertical flows, by measuring travel times between pairs of points on the surface with large separation and averaging over many supergranules, this measurement is sensitive to the vertical flows (within a few Mm of the surface). They then use an anelastic approximation to the continuity equation to create a model and find the best fit to the model which gives the horizontal flows. Applying this method, Duvall & Hanasoge (2013); Duvall et al. (2014) finds that supergranular flows peak very close to the surface (1.5-2.5 Mm below the photosphere) with horizontal flows ~ 700 m s^{-1} and vertical flows ~ 240 m s^{-1}. These flows are much faster than supergranular flows at the surface, where the vertical component to supergranulation is estimated to be 30 m s^{-1} (Rieutord & Rincon, 2010). This shallow, high speed supergranulation supports the suggestions that supergranulation originates very close to the surface and does not require deeper flows (as in Rast (2003)).

Validating the methods of time-distance helioseismology by comparing to solar-like convection simulations has encountered difficulty measuring the subsurface flow pattern or amplitude (DeGrave et al., 2014). Using forward-modeling techniques (a separate method from ray theory of Duvall & Hanasoge (2013); Duvall et al. (2014) but commonly used to validate the ray theory approach) in MURaM simulations with domain size $98 \times 98 \times 20$ Mm^3, these methods could not measure the large-scale flows in the simulation. This casts doubt on the measurements of large-scale solar flows using time-distance helioseismology (including the results in Figure 1.1) and, while not nullifying all measurements using these methods, suggests that the techniques must be carefully tested and validated.

1.1.4   Quiet Sun Magnetic Field

The quiet Sun magnetic field is advected by horizontal supergranular motions in the photosphere to the boundaries of the supergranular cells where it forms the magnetic network. We show a full-disk image of the Ca II K line intensity to demonstrate this pattern in Figure 1.4 (with supergranular sizes that compare favorably to Figure 1.2). The connection between magnetic field and solar supergranules was discovered by Simon & Leighton (1964) and many observers use magnetic

field (such as the Ca II K line intensity) to identify supergranular cells (Goldbaum et al., 2009; McIntosh et al., 2011; Berrilli et al., 2013). Unlike the power spectrum, these cell identification techniques can determine the diameter of the supergranules.

These magnetic elements are generally assumed to behave as passive tracers of the convective motions since they are below equipartition field strength. This is because the plasma β, which is the ratio of the gas pressure to the magnetic pressure, is much larger than one and the photosphere is highly conductive which causes the field to be "frozen in", i.e. carried by the motions of the plasma (de Wijn et al., 2009). Recent observations, however, show a change in the length scale of supergranules with solar cycle (McIntosh et al., 2011), suggesting that magnetic fields may play a role in determining the supergranular length scale (Figure 1.5).

The increased diameter of supergranules with increased magnetic activity may indicate that supergranulation is organized by the motions and magnetic element lifetimes in the photosphere (Rast, 2003; Crouch et al., 2007), but this may also be related to changes in subsurface magnetic fields.

1.1.4.1   Local Dynamo and Solar Convection

There is a continuing debate about the generation of quiet Sun magnetic field. The quiet Sun magnetic field has two primary features: network field with flux imbalances on scales larger than supergranulation (Lamb et al., 2010) and internetwork field with very small net flux on supergranular scales (de Wijn et al., 2009). Regions with a large net magnetic flux are associated with active regions (i.e. magnetic flux ropes created at the bottom of the convection zone that buoyantly rise to the surface) generated by the global dynamo (Fan, 2009). As these active regions decay, they contribute a net flux imbalance over large regions of the solar photosphere which suggests that the magnetic network fields are the remnants decaying active regions (Lamb et al., 2010).

Recent observations of internetwork field (i.e. field between the magnetic network) using the Hinode spectropolarimeter (SP) instrument to measure the Zeeman effect (i.e. the splitting of
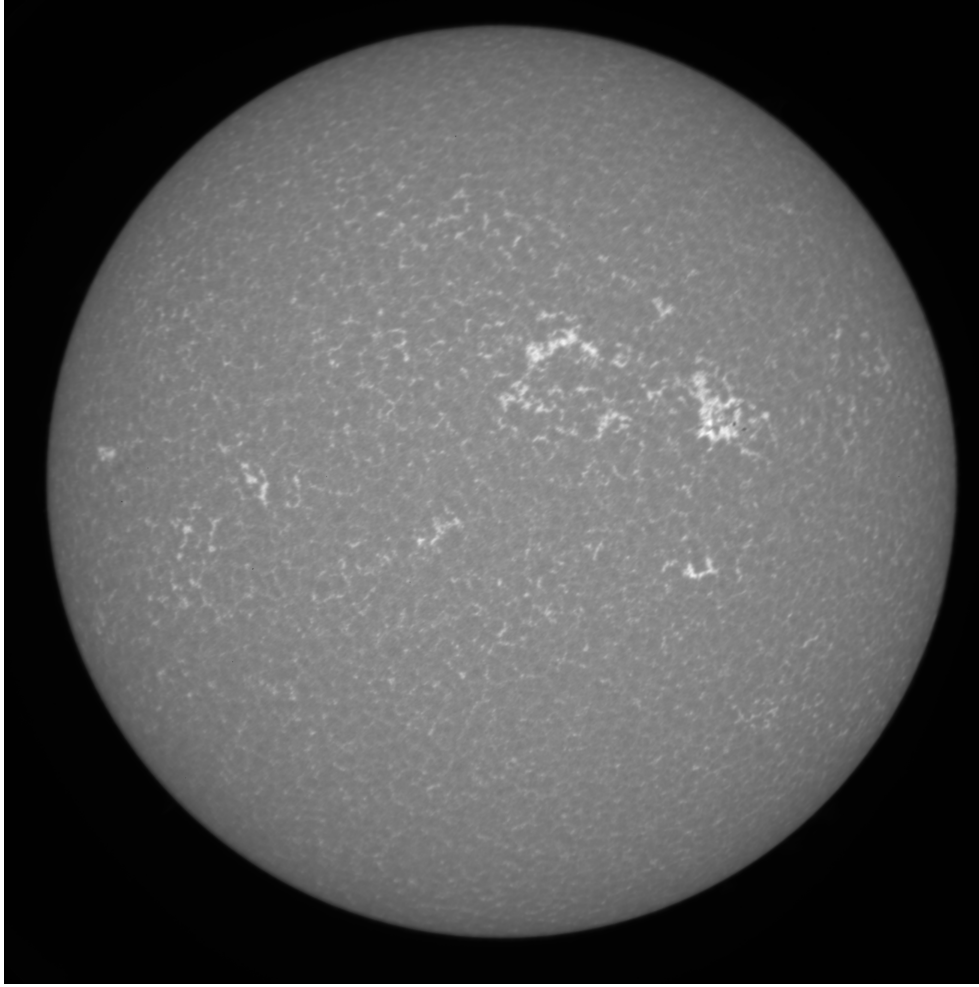
Figure 1.4 The full-disk Ca II K (393.4 nm) intensity, a proxy for chromospheric network magnetic field. Observations from the Precision Solar Photometric Telescope.
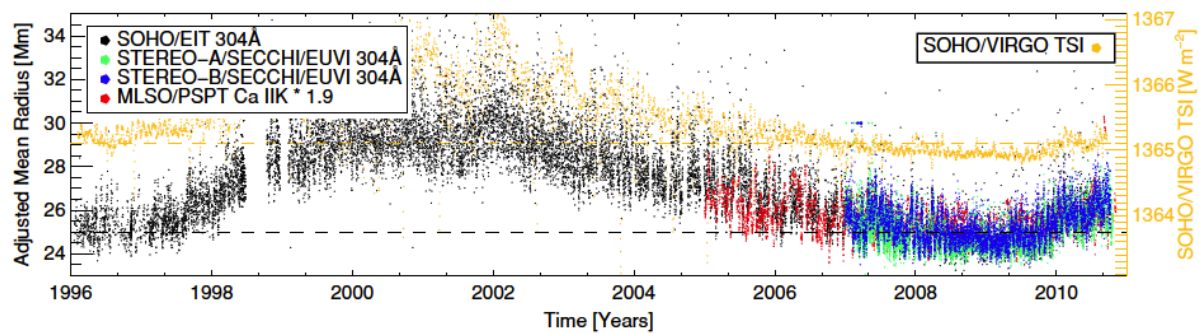
Figure 1.5 The adjusted mean radius of supergranules as a function of time from the year 1996 to 2011. The black (SOHO/EIT), green (STEREO-A/EUVI), and blue (STEREO-B/EUVI) symbols use the watershed segmentation to identify supergranules from the He II 304 Å which is an analog for the chromospheric magnetic field. The red symbols use the medial axis transform method to identify supergranules in the photospheric magnetic network using MLSO/PSPT Ca II K images. The orange symbols are the SOHO/VIRGO TSI measurement which identifies solar maximum and minimum. This figure was originally presented in McIntosh et al. (2011).

atomic energy levels in the presence of magnetic fields) have made significant improvements to our understanding of the quiet Sun magnetism. While internetwork field was traditionally described as primarily vertical (with respect to the surface), Lites et al. (2008) measured transverse field that was noticeably stronger than vertical field. Even with Hinode resolution, much of the magnetic field is missed by these observations due to Zeeman canceling along the line of sight (Danilovic et al., 2010). By computing a spectral synthesis on small-scale dynamo MURaM simulations (with much higher resolution than observations to reduce the Zeeman canceling) and comparing to Hinode observations, the measured unsigned vertical magnetic flux at optical depth unity is $\langle |B_V| \rangle \sim 60$ G G (Danilovic et al., 2010). Observations using inversion codes to infer the filling factor (the fraction of the observed pixel that a real magnetic field component occupies) in Hinode data validate this vertical flux measurement ($\langle |B_V| \rangle \sim 64$ G) and found a total unsigned flux in the photosphere of $\langle |B| \rangle \sim 220$ G with transverse flux $\langle |B_T| \rangle \sim 198$ G much stronger than vertical field (Orozco Suárez & Bellot Rubio, 2012). This method is unable to determine a field strength in all pixels (with nearly 75% of pixels ignored because the inversion could not determine the filling factor) but, as this value does not depend on filling factor, this provides an additional estimate that we can compare with simulations which suggests that the unsigned vertical flux is ~ 60 G.

Much debate has centered on whether the quiet Sun magnetic field is generated from a local small-scale dynamo or if this field comes from another source. The global dynamo generates active regions that are primarily vertical magnetic field in the photosphere. It is difficult to explain how the transverse field could be stronger than the vertical field without being generated by a local dynamo, which suggests that a small-scale dynamo is active in (or near) the solar surface (Martínez Pillet, 2013).

A small-scale dynamo is expected to operate in very high magnetic Reynolds number regimes where the magnetic field is generated from the stretching and twisting of the field by the plasma flows. Several recent radiative MHD simulations with a realistic photosphere have an operational small-scale dynamo (Martínez Pillet, 2013). In particular, recent MURaM simulations with resolution up to 2 km computed small-scale dynamos that reached $\langle |B_V| \rangle \sim 60$ G (similar to the

measurements from Hinode using Zeeman splitting (Danilovic et al., 2010; Orozco Suárez & Bellot Rubio, 2012)) and suggested that the local dynamo produces strong field, with magnetic energy density comparable to the kinetic energy density below the photosphere (Rempel, 2014). Another important aspect of these simulations is that more than half of the magnetic energy exists on scales smaller than 100 km (Rempel, 2014) which is below the resolution limit of Hinode (but can be explored by the upcoming DKIST).

The problem with all of these simulations, however, is that they operate in a regime where the magnetic Prandtl number (the ratio of viscous to magnetic diffusion) is ~ 1 while the Sun has a magnetic Prandtl number ranging 10^{-3} to 10^{-7} (i.e. magnetic diffusivity is much stronger than viscosity) (Martínez Pillet, 2013). At small magnetic Prandtl number the ohmic dissipation occurs on much larger scales than viscous dissipation. Thus, during the kinematic growth phase of the dynamo, the motions on scales larger than the resistive length scale will stretch and bend the magnetic field lines which causes the magnetic energy to grow, but the turbulent motions on scales smaller than the resistive length scale will act as a turbulent diffusion and destroy magnetic energy. Previous simulations have found that for magnetic Prandtl number $<< 1$ the critical (i.e. minimum) magnetic Reynolds number required for dynamo action increases and the asymptotic limit for the critical magnetic Reynolds number may be infinite, meaning that a small-scale dynamo is not possible in the Sun (Martínez Pillet, 2013). Recent simulations, however, have found a small-scale dynamo acting in a low magnetic Prandtl number regime with a compressible code (Brandenburg, 2011).

The ratio of kinetic to magnetic energy primarily depends on the magnetic Reynolds number ($Re_M = LV/\eta$ where L is a typical convective length scale, V is the rms velocity and η is the magnetic diffusivity). Thus large magnetic Reynolds number dynamos can have magnetic fields that reach super-equiparitition when compared to the kinetic energy (Brandenburg, 2014). Dynamo simulations have the same limitations on magnetic Reynolds number as in the fluid Reynolds number (with the maximum fluids Reynolds number reaching 5000 in the largest DNS simulation to date, see §1.1.1). Furthermore, small-scale dynamo simulations suggest that low magnetic Prandtl

number dynamos remove nearly all kinetic energy on scales smaller than the resistive length scale and dissipate this energy via ohmic dissipation (Brandenburg, 2009, 2014). Therefore, if a small-scale dynamo in the Sun reaches the saturated phase (as it would have in the Sun if a small-scale dynamo is active) then the magnetic field in the solar convection zone, with magnetic Reynolds number $\sim 10^5 - 10^9$ (Martínez Pillet, 2013), may have super-equipartition field strength (i.e. magnetic energy density that exceeds kinetic energy density) and diffuse most energy on the magnetic diffusion length scale, increasing the effective length scale of kinetic energy diffusion.

If a small-scale dynamo operates on the Sun and generates the network magnetic field, it is unclear how this may interact with the global dynamo or how the small-scale dynamo field below the photosphere may change with solar cycle. Since supergranulation is associated with network magnetic field, the creation of surface magnetic field and its interaction with the flows may play an important role in supergranular convection.

Chapter 2

The MURaM Code

As we stated in §1.1.3 this thesis is focused on three primary questions: what physical mechanism(s) determine the length scale or lifetime of supergranulation, where do supergranules originate (near the surface or deep in the convection zone), and what governs the relationship between supergranules and the magnetic field?

To explore these questions in solar-like numerical convection simulations we require a code that: provides wide enough domains to examine the supergranular length scale (32 Mm); allows large enough domain depth to determine if supergranules originate from the deep flows; is optimized to examine multiple supergranular lifetimes (1.8 days) to find a statistically significant result; computes the radiative transfer to create a realistic photosphere; and uses the equations of magnetohydrodynamics (MHD).

Based on the length scale of supergranulation (32 Mm) we expect the required domain width to be at least the same size as previous simulations 98×98 Mm^2. This domain size allows ~ 12 supergranules equal to the mean diameter which provides a marginal reduction in statistical noise. The domain depth must be greater than 20 Mm depth to explore the assumption that width of supergranules is equal to the depth at which they originate (Hathaway, 2012a). We need a realistic photosphere to explore the suggestions that supergranules are generated in the surface by organization of granular downflows or magnetic elements (Rast, 2003; Crouch et al., 2007).

Based on those criteria we chose to explore solar surface convection with the MURaM code. The development of this code is detailed in Vögler et al. (2005); Rempel et al. (2009); Rempel

(2014). While we primarily use the existing code, we added an artificial energy flux, a computation of the Fourier transform power spectrum at any depth and iteration, a potential flow bottom boundary condition (which was unstable and is not discussed further), and improved the data output options. The MURaM code: computes radiative transfer with opacities that include the elements important to photospheric radiative transfer; uses an equation of state with all elements that have ionization states that influence the properties of the solar convection zone (especially H and He ionization); and low enough diffusivity to induce a small-scale dynamo to explore quiet Sun magnetic fields. These features allow us to compute simulations that are larger than any previous solar-like simulations with a realistic photosphere with domain size up to $197 \times 197 \times 49$ Mm^3 with 5.5 days of relaxed data. We call the hydrodynamic simulation with the largest domain size the reference simulation. These simulations are also the most stratified solar convection simulations that we are aware of.

The primary limitation of the MURaM code is the open bottom boundary. Open boundaries in convection simulations are universally problematic since they require assumptions about the nature of the convection outside of the domain. We explore the smoothing of inflows and test the boundary conditions by comparing simulations with varying domain depth to understand the influence of the open boundary on the simulations.

The main solar physics that we do not include in these simulations are rotation and the near surface shear layer (a ~ 30 m s^{-1} shear from the photosphere down to 35 Mm depth (Howe et al., 2007)). We also do not include the change in gravity or energy flux with radius. The mean density is increased by $\sim 15\%$ compared to a hydrostatic stratification with gravitational acceleration ($\frac{Gm(r)}{r^2}$ with G the gravitational constant, $m(r)$ the mass interior to the current radius r) that accounts for the change in mass and radius. The energy flux is weaker by $\sim 15\%$ than we would expect from approximating the solar energy flux as $\frac{L_{sun}}{4\pi R^2}$ at the bottom of our 49 Mm deep reference simulation (where $R = 0.93R_{sun}$).

2.1 The Code

The MURaM code solves the MHD equations using a conservative 4th order spatial finite difference scheme and short characteristics to compute the radiative transfer. The code uses cartesian coordinates with the positive z-direction as vertically outward (the direction of radiative flux out of the simulation domain) and a tabulated $OPAL$ equation of state (Rogers & Iglesias, 1996). The horizontal boundaries are periodic, the top boundary is closed, and the bottom boundary is open to mimic the influence of the deeper convection zone (for details see 2.1.4).

2.1.1 Modified MHD Equations

We adopt the notation of Rempel (2014) to show the equations that the code solves (a modification of the MHD equations):

$$\frac{\partial \rho}{\partial t} = -\nabla \cdot (\rho \mathbf{v}) \tag{2.1}$$

$$\frac{\partial \rho v}{\partial t} = -\nabla \cdot (\rho \mathbf{v}\mathbf{v}) + \frac{f_{v_A}}{4\pi}\nabla \cdot (\mathbf{B}\mathbf{B} - \frac{1}{2}\mathbf{I}B^2) - \nabla P + \rho \mathbf{g} \tag{2.2}$$

$$\frac{\partial E_{HD}}{\partial t} = -\nabla \cdot [\mathbf{v}(E_{HD} + P)] + \rho \mathbf{v} \cdot \mathbf{g} + \frac{\eta}{4\pi}(\nabla \times \mathbf{B})^2 + \tag{2.3}$$
$$\mathbf{v} \cdot \frac{f_{v_A}}{4\pi}\nabla \cdot (\mathbf{B}\mathbf{B} - \frac{1}{2}\mathbf{I}B^2) + Q_{rad} + \nabla \cdot \mathbf{F}_{artificial}$$

$$\frac{\partial \mathbf{B}}{\partial t} = \nabla \times (\mathbf{v} \times \mathbf{B} - \eta\nabla \times \mathbf{B}) \tag{2.4}$$

$$\frac{\partial^2 \phi}{\partial t^2} + \beta\frac{\partial \phi}{\partial t} - \alpha\nabla^2\phi = 0 \tag{2.5}$$

where ρ is the density, $\mathbf{v}$ is the fluid velocity, P is the gas pressure, and $\mathbf{B}$ is the magnetic field. The viscous terms are not solved within these equations with the diffusive fluxes added to

the values in the grid cells in between timesteps in the integration scheme which is described in §2.1.3.

Defining the other terms in the momentum equation (2.2): we use $\mathbf{I}$ to denote the identity matrix, $\mathbf{g}$ to be the gravitational acceleration which is a constant in the z-direction equal to -2.74×10^4 cm s^{-2}, and f_{v_A} is a term that does not appear in the true MHD momentum equation that we describe below.

In the energy equation (2.3) we use E_{HD}, which is the internal (E_{int}) plus kinetic energy ($\frac{1}{2}\rho\mathbf{v}^2$). We separate out the hydrodynamic and magnetic energy sources to decrease numerical instability in regions with very strong magnetic energy (small plasma $\beta = 8\pi P/B^2$). These regions only occur above the photosphere where most of the internal energy of the plasma is radiated away and the flows are not driven by convective instability. We include the magnetic diffusivity η for completeness but it is set to zero and replaced by a numerical diffusivity (see §2.1.3) in all simulations presented in this thesis. The term Q_{rad} represents the radiative cooling and is computed in the code as the divergence of the radiative flux in the radiative transfer scheme (see §2.1.5). Finally, we include another term in some simulations which is not in the MHD equations, $\nabla \cdot \mathbf{F}_{artificial}$, which is an optional artificial energy flux that can transport energy without affecting any other part of the code (§2.1.6). Finally, we include the induction equation (2.4) is solved with $\eta = 0$ in all simulations.

The f_{v_A} term in the momentum and energy equations is used to limit the Alfvén velocity ($v_A = B/\sqrt{4\pi\rho}$):

$$f_{v_A} = \frac{1}{\sqrt{1 + (\frac{v_A}{v_{max}})^4}}, \tag{2.6}$$

where $v_{max} = 31.6$ km s^{-1} is the maximum Alfvén velocity that we allow. This limit was originally created for simulations of sunspots with much stronger magnetic field than our quiet-Sun field strength simulations. The term helps prevent regions with very low density (which only occur above the photosphere and do not influence the surface dynamics) from reducing the timestep. In

the simulations presented here, this term affects less than $3 \times 10^{-3}\%$ of grid cells. This limiting of the Alfvén velocity increases the timestep of the magnetized simulations by a factor of ~ 16.

We correct errors in the computation of $\nabla \cdot \mathbf{B}$ by iteratively solving a hyperbolic differential equation (Dedner et al., 2002) to reduce the amplitude of any regions with non-zero magnetic divergence. Equation 2.5 is derived from the relationships $\frac{\partial \phi}{\partial t} = \alpha \nabla \cdot \mathbf{B} - \beta \phi$ and $\frac{\partial \mathbf{B}}{\partial t} = \nabla \phi$. This is related to a damped wave equation with the maximum possible wave speed $\alpha = \Delta x^2 / \Delta t^2$ and damping term $\beta = 0.65 \Delta x / \Delta t$ which has been determined empirically.

2.1.2   Numerical Methods

We use a 4th order centered finite difference derivatives and an explicit 4th order accurate time integration scheme.

2.1.2.1   Finite Difference Derivatives

Taking u_i to be the value of a solution variable in the ith grid cell, the first spatial derivative is given by

$$(\frac{\partial u}{\partial x})_i = \frac{1}{12\Delta x}(-u_{i+2} + 8u_{i+1} - 8u_{i-1} + u_{i-2}) \tag{2.7}$$

and the second derivative is

$$(\frac{\partial^2 u}{\partial x^2})_i = \frac{1}{12\Delta x^2}(-u_{i+2} + 16u_{i+1} - 30u_i + 16u_{i-1} - u_{i-2}), \tag{2.8}$$

where Δx is the grid spacing in the direction that the derivative is applied. Horizontal boundaries are periodic. The vertical derivatives require two ghost cells to compute the five grid cell stencil for these derivatives (see §2.1.4). To compute mixed derivatives we apply equation 2.7 successively in the directions of the derivatives.

2.1.2.2   Time Integration

Using a vector representation for the solution we have $\mathbf{U}_0 = (\rho, \rho\mathbf{v}, E_{HD}, \mathbf{B})(x, y, z, t_0)$ at time t_0 and spatial position (x, y, z). Then the system of partial differential equations is

$$\frac{\partial \mathbf{U}}{\partial t} = \mathbf{R}(\mathbf{U}), \tag{2.9}$$

where $\mathbf{R}(\mathbf{U})$ is the vector containing the spatial derivatives and source terms in the system of equations. The timesteps of the 4th order integration scheme are then:

$$\mathbf{U}_{\frac{1}{4}} = \mathbf{U}_0 + \frac{\Delta t}{4}\mathbf{R}(\mathbf{U}_0),$$

$$\mathbf{U}_{\frac{1}{3}} = \mathbf{U}_0 + \frac{\Delta t}{3}\mathbf{R}(\mathbf{U}_{\frac{1}{4}}),$$

$$\mathbf{U}_{\frac{1}{2}} = \mathbf{U}_0 + \frac{\Delta t}{2}\mathbf{R}(\mathbf{U}_{\frac{1}{3}}),$$

and finally the solution at the new timestep is

$$\mathbf{U}_1 = \mathbf{U}_0 + \Delta t\mathbf{R}(\mathbf{U}_{\frac{1}{2}}). \tag{2.10}$$

2.1.3   Numerical Diffusion

Solar convection is highly turbulent with $Re \geq 10^{10}$ (Rieutord & Rincon, 2010), so simulations of solar convection attempt to limit the viscosity as much as possible to reach the maximum possible Reynolds number. There is a minimum viscosity, however, that is required to dissipate kinetic energy so that this energy does not pile up on small scales and cause spurious oscillations on the grid scale. To reach a minimum viscosity that is similar to the Sun (estimated as $\nu \sim 10^{-3}$ m^2 s^{-1} (Rieutord & Rincon, 2010)) requires that the simulation resolve the diffusive length scale (estimated as $l_\nu \sim 0.1$ cm (Rieutord & Rincon, 2010)) which is prohibitively expensive for

current supercomputers. Thus, even the highest resolution simulations currently available that use an explicit viscosity are much more diffusive than the solar photosphere.

Thus, in order to maintain the numerical stability but reduce the diffusivity on well resolved features, we use a slope-limited diffusion scheme based on shock capturing diffusion schemes. This scheme was designed by Rempel et al. (2009) and Rempel (2014) to diffuse energy only on small scales while being minimally diffusive on large scales. Since the numerical instability caused by insufficient viscosity manifests as a zig-zag pattern on the grid scale, our diffusion scheme uses a piecewise linear reconstruction designed to diffuse small-scale features with monotonicity changes.

To compute the diffusion, we determine the slope between grid cells using the monotonized central difference limiter. This limiter tests the slope computed from solution values in adjacent grid cells and then comparing each adjacent grid cell both from the left and right to the central grid cell. The limiter then selects the minimum of all tested slopes (and returns zero slope if the tested slopes are both positive and negative). We then use the slope given by our limiter to extrapolate the value at both the left and right interface between the cells. The goal of the slope limiter is to prevent mismatches between the extrapolated interface values based on extreme slopes, but still create maximum diffusion for any monotonicity changes where the reconstruction is disabled. We compute the diffusive flux between cells by comparing the difference between the two extrapolated interface values (extrapolated from the left side and right side of the interface).

The equation for the monotonized central difference limiter based on the discrete solution u_i (where the subscript denotes the value in the ith grid cell) is:

$$\Delta u_i = \text{minmod}[(u_{i+1} - u_{i-1})/2, 2(u_{i+1} - u_i), 2(u_i - u_{i-1})] \tag{2.11}$$

where the minmod function returns the smallest absolute value of the inputs unless there are both positive and negative inputs, in which case it returns zero. We call this quantity (Δu_i) the reconstruction slope. Using this slope we can extrapolate the value at the cell interfaces:

$$u_l \;=\; u_i + 0.5\Delta u_i \qquad\qquad (2.12)$$

$$u_r \;=\; u_{i+1} - 0.5\Delta u_{i+1}. \qquad\qquad (2.13)$$

These equations solve for the cell interface values, u_l and u_r, based on the reconstruction slopes and cell-centered values of the solution on the left (for u_l) and right (for u_r) side of the interface. Using the extrapolated interface values, we compute the diffusive fluxes of the numerical scheme at the cell interface:

$$f_{i+\frac{1}{2}} = -\frac{1}{2}c_{i+\frac{1}{2}}\Phi_h(u_r - u_l, u_{i+1} - u_i) \cdot (u_r - u_l), \qquad\qquad (2.14)$$

where $c_{i+\frac{1}{2}}$ is a characteristic velocity computed from the fluid velocity and Aflvén at the cell interface. Since $c_{i+\frac{1}{2}}$ does not include the sound speed, the scheme is less diffusive for low Mach number flows than a scheme that includes the sound speed. The function Φ_h is

$$\Phi_h = \max[0, 1 + h(\frac{u_r - u_l}{u_{i+1} - u_i} - 1)]. \qquad\qquad (2.15)$$

We set $\Phi_h = 0$ for all regions where $(u_r - u_l) \cdot (u_{i+1} - u_i) \leq 0$ to prevent anti-diffusion, i.e. where quantities diffuse from cells with smaller values to larger values. This function was devised by Rempel et al. (2009) and Rempel (2014) to decrease the diffusivity on well resolved features. We use the parameter $h = 2$ in our simulations which sets the diffusive fluxes to zero for all regions with $|(u_r - u_l)/(u_{i+1} - u_i)| < 1 - 1/h = 1/2$. This choice of $h = 2$ prevents any diffusion for well-resolved, smooth features (with small values of $|(u_r - u_l)/(u_{i+1} - u_i)|$) but keeps the same diffusion specified by the slope limiter for small-scale features with monotonicity changes. Testing this diffusive scheme using a one-dimensional advection simulations we find that the diffusion is zero for a sine wave that is resolved by more than six grid cells. Thus, though this scheme is not physical, the diffusion is negligible for large-scale features, similar to the solar viscosity. This scheme is not comparable to an effective diffusivity or Reynolds number because it is highly intermittent, inhomogeneous and depends on scale.

We apply the diffusion to the primitive variables $\log(\rho)$, v_x, v_y, v_z, $\epsilon = E_{int}/\rho$, B_x, B_y and B_z and we implement this scheme in each dimension separately to maximize numerical stability. We apply the diffusive fluxes to the solution after a full time-step update of the 4th order time integration and add the artificial viscous and ohmic heating to the internal energy.

We apply our diffusion scheme to the mass density to prevent numerical instability. Since there is no diffusion of mass in the MHD equations this numerical mass diffusion requires careful accounting. We assume that the diffusive mass flux ($\mathbf{f}_\rho$) transports both momentum and energy. Thus our momentum flux has an additional $\mathbf{f}_\rho \mathbf{v}$ term and our energy flux has the additional term $\mathbf{f}_\rho \epsilon$. Additionally, in regions of where the density contrast between adjacent grid cells exceeds a factor of 10 we use the maximum velocity allowed by the CFL condition (see §2.1.3.1 for details on the CFL condition) in place of $c_{i+1/2}$ to maximize the diffusive flux.

We use a constant pressure at the bottom boundary (see §2.1.4) which causes spurious oscillations on the grid scale in the vertical direction that are too weak (compared to the stratification) to cause monotonicity changes and, consequently, are not sufficiently diffused by the scheme outlined above. In particular, these oscillations are caused by the different pressure in upflows and downflows which is forced to be equal at the boundary. We use an additional 4th order hyper-diffusion term that scales with the vertical velocity to damp these oscillations. This additional diffusion is applied to the $\log(\rho)$, v_z and ϵ in the vertical direction.

2.1.3.1   CFL Condition

The Courant-Friedrichs-Lewy (CFL) condition limits the maximum timestep of the solution to $\Delta t_{max} = f_{CFL} \frac{\Delta x_{min}}{v_{max,all}}$ where the pre-factor f_{CFL} is an empirically derived parameter, Δx_{min} is the minimum grid spacing in any direction and $v_{max,all}$ is the maximum of all velocities (fluid, sound and Alfvén velocity). This CFL condition depends on the numerical methods of the code and typically uses a pre-factor value of $f_{CFL} < 1$ (often 0.4 to 0.8) to ensure numerical stability. Heuristically, the CFL condition prevents the maximum velocity from transporting a quantity (e.g. mass, pressure waves, or Alfvén waves) to a grid cell that is greater than Δx_{min} away. For our

code the maximum velocity is the speed of sound at the bottom boundary and minimum grid spacing is in the vertical direction. If we used the maximum advective velocity we could achieve approximately a factor of 7.5 improvement in the timestep.

It is a curious empirical result that the MURaM code with the specific time integration and finite-difference derivative scheme outlined in §2.1.2 can operate with $f_{CFL} = 1.95$ and maintain numerical stability. The curiosity arrises from the fact that this violates the heuristic example above, allowing a quantity to travel nearly two (vertical) grid cell lengths in one timestep. The specific value of f_{CFL} also depends on the ratio of the grid spacing in the horizontal and vertical direction. All of our simulations use a horizontal grid that is three times larger than the vertical grid spacing. Keeping this ratio greater than two prevents the maximum velocity from transporting quantities past both a vertical and horizontal grid cell in one timestep which requires a reduction in f_{CFL}. To prevent problems with the numerical diffusion with $f_{CFL} = 1.95$ we limit the maximum velocity used in the diffusion scheme ($c_{i+\frac{1}{2}}$) to $0.975\frac{\Delta x_{min}}{\Delta t}$, where 0.975 is a numerical safety factor and Δt is the timestep of the simulation. This prevents the maximum velocity in the diffusive scheme from being capable of transporting quantities in the solution through one grid cell.

2.1.4   Upper and Lower Boundary Conditions

For both the upper and lower boundaries we use two ghost cells outside the simulation domain (to compute derivatives with our fourth order finite difference scheme, §2.1.2.1) with the boundary positioned between the first ghost cell and the outermost grid cell. We apply symmetric or anti-symmetric behavior to most variable values in the ghost cells for simplicity of implementation. Symmetric boundary conditions ensure that all odd derivatives are equal to zero whereas anti-symmetric boundary conditions specify that the solution value is zero at the boundary. For symmetric boundaries we take the values of the first, u_1, and second, u_2, grid cells and set the values of the corresponding ghost cells to $u_1^* = u_1$ and $u_2^* = u_2$ (where u_1^* is the ghost cell nearest to the boundary). For anti-symmetric behavior we set $u_1^* = -u_1$ and $u_2^* = -u_2$.

For both the upper and lower boundaries we enhance the viscosity in the outermost 8 grid

cells by changing the computation of the reconstruction slope so that the diffusion operates on large-scales, i.e. for regions where $|(u_r - u_l)/(u_{i+1} - u_i)| < 1/2$ and the diffusion scheme in the rest of the domain is turned off. This increases the effective diffusion in these regions significantly. This results in inflows at the bottom boundary that are broad and slow. Without this enhanced viscosity the resulting inflows have a very small-scale pattern (similar to the downflows) which destroys the standard convection pattern at the bottom (see Figure 2.1 for comparison of the normal and enhanced viscosity boundary condition). This smaller scale convection persists with the large-scale pattern seen in the enhanced viscosity boundary simulations reforming near the middle of the domain (though there are still smaller scale motions evident in the reduced viscosity boundary simulation). The convection in the middle of the domain of a deeper simulation is more consistent with the broad, slow upflows of the enhanced viscosity boundary condition. Additionally, simulations with magnetic fields generated from a small-scale dynamo produces a similar smoothing without any enhancement to the viscosity. For these reasons we use the enhanced viscosity boundary conditions for all hydrodynamic simulations (and do not use the enhanced viscosity in magnetized simulations).

2.1.4.1   Bottom Boundary

The bottom boundary conditions on the hydrodynamic variables are open to mimic the presence of the deep convection zone beneath the domain. All three components of the mass flux are set to be symmetric (resulting in all odd derivatives equal to zero on the boundary). The pressure on the boundary (between the first domain cell and first ghost cell) $P_{BND} = P_{gas} + B_z^2/(8\pi)$ is uniform and fixed at the boundary. For the values of the pressure in the first and second domain grid cell P_1 and P_2 we extrapolate the ghost cell pressure values using the existing stratification:

$$P_1^* = 1.5P_{gas} - 0.5\sqrt{P_1 P_2} \tag{2.16}$$

$$P_2^* = 2.5P_{gas} - 1.5\sqrt{P_1 P_2}. \tag{2.17}$$
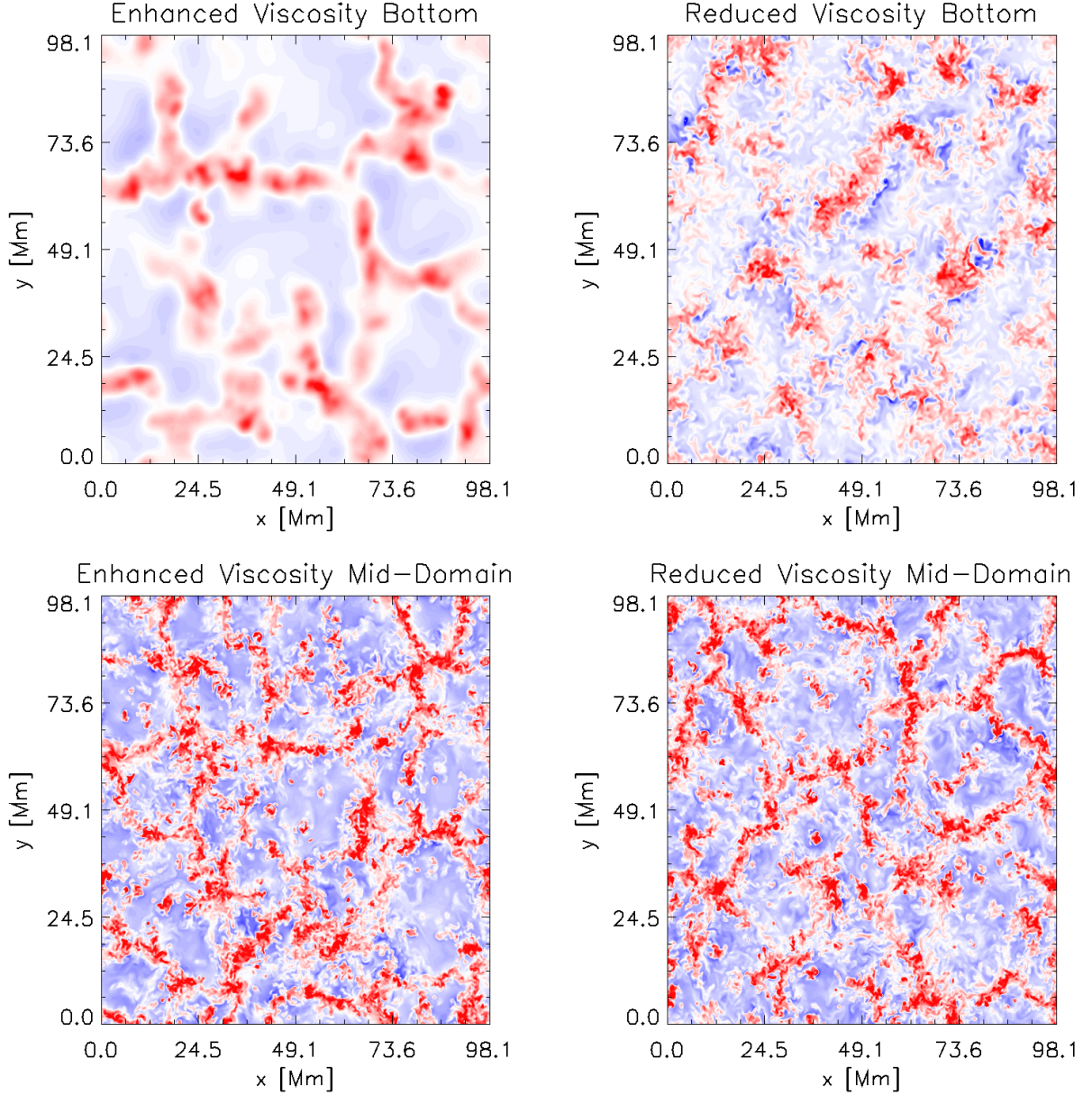
Figure 2.1 The vertical velocity at the bottom boundary (19.9 Mm below the $\tau = 1$ surface) and in the middle of the domain from the simulation with enhanced viscosity (used in all hydrodynamic simulations) and reduced viscosity (where the viscosity is the same at the boundary as in the rest of the domain). All figures use the same color table saturated at ± 1 km s^{-1} with blue representing upflows (towards the surface) and red representing downflows (away from the surface). Enhancing the viscosity smooths the inflows at the bottom boundary which suppresses the high wavenumber flows. If we do not enhance the viscosity then the high wavenumber flows at the bottom boundary inflows propagate into the domain and reduce the amplitude of the low wavenumber flows. Simulations with small-scale dynamo magnetic field smooth the inflows through the Lorentz force and do not require enhanced viscosity.

The entropy is symmetric in outflows and the inflows are given a uniform entropy value that is empirically determined such that the simulation has photospheric radiative losses equal to the solar luminosity to within a few percent (this entropy value is also used to initiate the simulation, see §2.2). The density and internal energy are then determined by the equation of state.

Since the pressure is fixed across the boundary this does not allow for a different pressure in upflows and downflows which we find dynamically throughout the rest of the simulation domain. Thus, this boundary underestimates the horizontal divergence in inflows than we would expect from the upflows at this depth in a deeper simulation (caused by the positive pressure perturbation in the upflows). By keeping a constant pressure, however, we maintain the mass of the box and the stability of the simulation. The pressure at the bottom boundary is a measure of the total mass in the simulation (gravitational force per area). Thus, if mass is leaving the domain without being replaced the pressure in the bottom grid cells will be lower than a hydrostatic stratification. This creates a stronger than hydrostatic pressure gradient that increases the mass flux of inflows and slows the outflows. Thus the pressure that we choose for the bottom boundary determines the total amount of mass in the simulation domain (aside from variations over short timescales).

The properties of these inflows are based on several assumptions. While some of these assumptions are based on the expected physical properties of the convection (e.g. the constant entropy in inflows is a good approximation for the entropy in upflows throughout the simulation domain), other choices are used primarily for numerical stability or mass conservation. Currently, there is no method to create an open boundary with realistic physics. All open boundaries include implicit and explicit assumptions about the properties of the inflows. One of the best ways to test the effect of the boundary is to compare the properties of the solution in simulations with different domain depths. Thus, we compute simulations at several depths (see §2.2) to validate our results.

2.1.4.2   Magnetic Bottom Boundary

Using an open boundary with the magnetic field requires additional consideration. While recent global simulations have found evidence of a small-scale dynamo operating throughout the

convection zone (Hotta et al., 2014; Hotta, 2014b), we do not have an a priori expectation for the amount (or scale) of field is advected into the near-surface layers. The most conservative magnetic boundary would not allow any horizontal field to be advected into the simulation domain to replace what is lost via the outflows (Pietarila Graham et al., 2010). This boundary, however, underestimates the magnetic field strength produced by a saturated dynamo throughout the convection zone (Rempel, 2014). To experiment with increased field strength Rempel (2014, see this work for further details) developed a boundary condition to allow horizontal magnetic field to be advected into the domain by using a symmetric boundary condition for all three components of the magnetic field. We employ this boundary condition in all magnetized simulations.

This introduces the possibility that we are increasing the root-mean-square (rms) field strength throughout the simulation through the boundary condition and not via dynamo action. Therefore, we set an upper limit to the root-mean-square (rms) field strength in inflow regions which changes based on domain depth and limit the maximum local horizontal magnetic field strength to three times the maximum rms value. This upper limit increases roughly as the equipartition field strength $B_{eq} = \sqrt{4\pi\rho}v_{rms}$ (for the 49 Mm deep $\langle B_z \rangle = 0$ G simulation this value was $B_{max} = 3400$ G). The net horizontal magnetic flux is set to zero in inflow regions and we rescale the vertical magnetic field such that the horizontal and vertical rms field strength are identical in inflow regions. Based on small-scale dynamo simulations we expect the magnetic field in the deep convection zone to be nearly isotropic (Hotta et al., 2014; Hotta, 2014b), but our simulations underestimate the horizontal divergence of inflows which leads to a vertical field that is too strong in inflows without this constraint.

The small-scale dynamo magnetic field also suppresses small-scale motions in the bottom of the domain. Thus any simulation with magnetic field does not use enhanced viscosity at the bottom boundary, instead using the Lorentz force to smooth the flows.

2.1.4.3   Upper Boundary

The upper boundary is placed at 700 km above the $\tau = 1$ surface. This boundary is closed with antisymmetric vertical velocity condition which sets $v_z = 0$ on the boundary. The horizontal magnetic field condition is also anti-symmetric to ensure that $B_x = B_y = 0$. All other variables have symmetric boundary conditions which ensures that all odd derivatives of the density, internal energy, horizontal velocity, and vertical magnetic field are set to zero at the boundary.

2.1.5   Radiative Transfer

We use the same radiative transfer scheme that solves the equation of radiative transfer along rays (with short characteristics) described in Vögler et al. (2005, for further details on this method see this text). The equation of radiative transfer is $\frac{dI_\nu}{d\tau_\nu} = S_\nu - I_\nu$ where ν denotes the frequency, I denotes the radiative intensity, τ is the optical depth and S_ν is the source function. In all of our simulations we use a grey atmosphere (no frequency dependence of the radiation) but still label the quantities as frequency dependent in this text since the code possesses the capability of computing non-grey atmospheres. The solution to the radiative transfer equation gives the intensity $I_\nu(\boldsymbol{\mu})$ in the ray direction described by the unit vector $\boldsymbol{\mu}(\omega)$ as a function of solid angle ω. From the intensity the radiative flux is given by

$$\mathbf{F}_\nu = \int_{4\pi} I_\nu(\boldsymbol{\mu})\boldsymbol{\mu}d\omega \tag{2.18}$$

and the average intensity is

$$J_\nu = \frac{1}{4\pi} \int_{4\pi} I_\nu(\boldsymbol{\mu})d\omega, \tag{2.19}$$

where ω is the unit of solid angle. By assuming that we are in local thermodynamic equilibrium we can set the source function equal to the Planck Function, i.e. $S_\nu = B_\nu$, and solve for

$$Q_{rad} = -\int_\nu (\nabla \cdot \mathbf{F}_\nu) d\nu = 4\pi\rho \int_\nu \kappa_\nu (J_\nu - B_\nu) d\nu \qquad (2.20)$$

where κ is the opacity of the plasma given by the ATLAS9 stellar atmosphere package (Kurucz, 1993). We use both of these equations to solve for Q_{rad} with the first equation used for optical depth $\tau_\nu > 0.1$ and the second equation used above the photosphere in optically thin regions.

2.1.6 Artificial Energy Flux

We add an optional artificial energy flux term, $\mathbf{F}_{artificial}$, to equation 2.3 in order to test the properties of the convection with reduced energy flux (without changing the stratification). The artificial flux influences the energy equation when the divergence of the flux is non-zero and we only examine artificial fluxes with purely vertical profiles so that there is no horizontal variation in the divergence of the flux. Thus, in regions of non-zero divergence, $\mathbf{F}_{artificial}$ heats upflows and downflows equally (see §4.2.3 for details).

2.2 Simulations

To initiate simulations we compute an isentropic (adiabatic), hydrostatic stratification with zero velocity. The entropy value is determined empirically to be the entropy required in inflows at the bottom boundary to maintain the solar radiative energy flux escaping from the simulation top boundary. Since the mean entropy of the upflows is nearly independent of depth, we use the same entropy value for all simulations (unless there is an equation of state change). Before the simulation begins, we add a random noise component to the internal energy equal to less than 1% of the mean value for the layers above the mean optical depth one surface. As the simulation relaxes from its initial state this mean optical depth one surface will shift. Thus we can only determine the geometric depth of the optical one surface after the simulation is running.

We then start the simulation and the radiative transfer begins cooling the surface plasma which begins to form overdense, low entropy downflows that descend deeper into the domain.

These downflows then start convection as they penetrate the adiabatic stratification. The simulation is considered relaxed when the flows reach a statistically steady state which is determined by examining time series of the Fourier power spectra of the velocity. If we are computing a magnetic simulation we add the field after the flows have reached a statistically steady state to save computational resources.

An additional consideration for relaxation is that the energy flux is balanced but this happens in our simulations before the flows are dynamically relaxed. The traditional thermal relaxation time (i.e. taking the full energy content of the simulation divided by the radiative energy flux out of the domain) is much longer than the entire simulation time, but this overestimates the time it takes for the energy flux to be balanced. Since the superadiabatic gradient is very close to the initial adiabatic gradient, the relaxation time of the energy flux is the time it takes for the stratification to reach the final superadiabaticity. Empirically we find this time to be shorter than the dynamical relaxation time.

2.2.1 Resolution

To explore solar supergranulation in our simulations and address how deep flows play a role in supergranular scale motions of at the surface we want to compute simulations with domain size $197 \times 197 \times 49$ Mm^3 and at least three supergranular lifetimes (i.e. 3×1.8 days=5.4 days). To relax the simulations (both relaxing the flows and reaching the saturated phase of a small-scale dynamo) requires additional time, approximately 5 days of computational time (i.e. physical time of the solution). For the simulations presented in this work, we needed to determine how to best use the 18 million cpu hours that we had been awarded to compute simulations with this increase domain size.

Our early simulations use a grid spacing of 128 km in the horizontal direction and 32 km in the vertical direction. This resolution already under-resolves the narrowest photospheric downflows at ~ 200 km and marginally resolves the solar photosphere which has a pressure scale height of approximately 100 km in the vertical direction. Given that the current version of the MURaM code

runs at 200,000 grid cell updates per cpu second on Sandy Bridge processors, these new wider and deeper simulations would use more than 8 million cpu hours to compute a single hydrodynamic case at this resolution. We thus tested several coarser resolutions to determine how much we could lower the resolution with acceptable changes to the simulation properties. We tested the resolution in a series of $49.152 \times 49.152 \times 4.096$ Mm^3 hydrodynamic simulations. We compare horizontal resolutions of 128 km, 192 km, and 256 km. While each decrease in resolution changes the amplitude of the high wavenumber power (and removes some high wavenumber modes) in the photospheric velocity spectrum, the 192 km (unlike 256 km) resolution only changes the very high wavenumber modes whose amplitude in the highest resolution simulation is at least one order of magnitude below the peak (granulation) power. Thus, we consider the changes due to the 192 km resolution as acceptable in the photospheric velocity spectrum.

We also compare the vertical resolution of 32 km and 64 km. Due to the small-scale height of the photosphere, this primarily affects the radiation in the simulation. We found that reducing the resolution decreases the radiative luminosity of the simulation for the same entropy at the bottom boundary. Comparing the resolutions from 128 km $\times$ 128 km $\times$ 32 km to 192 km $\times$ 192 km $\times$ 64 km we find that the decreased resolution changes the radiative energy flux from 6.3 to 6.1×10^{10} erg cm^{-2} s^{-1}. This decreased radiative energy flux induces flows with similarly weaker convective energy flux. Since typical variations of the convective energy flux are $\sim 10\%$ below a few Mm depth (the energy flux has much smaller fluctuations near the photosphere), we consider this to also be an acceptable change to the energy flux of the simulation.

By decreasing the resolution from 128 km $\times$ 128 km $\times$ 32 km to 192 km $\times$ 192 km $\times$ 64 km we decrease the number of grid cells that we compute by a factor of 4.5. Furthermore, by decreasing the vertical resolution we also increase the timestep by a factor of two since $\Delta t_{max} = f_{CFL} \frac{\Delta z}{c_{sound}}$ where c_{sound} is the speed of sound at the bottom boundary. This change decreased the computational time of each simulation from 8 million cpu hours to approximately 1 million cpu hours.
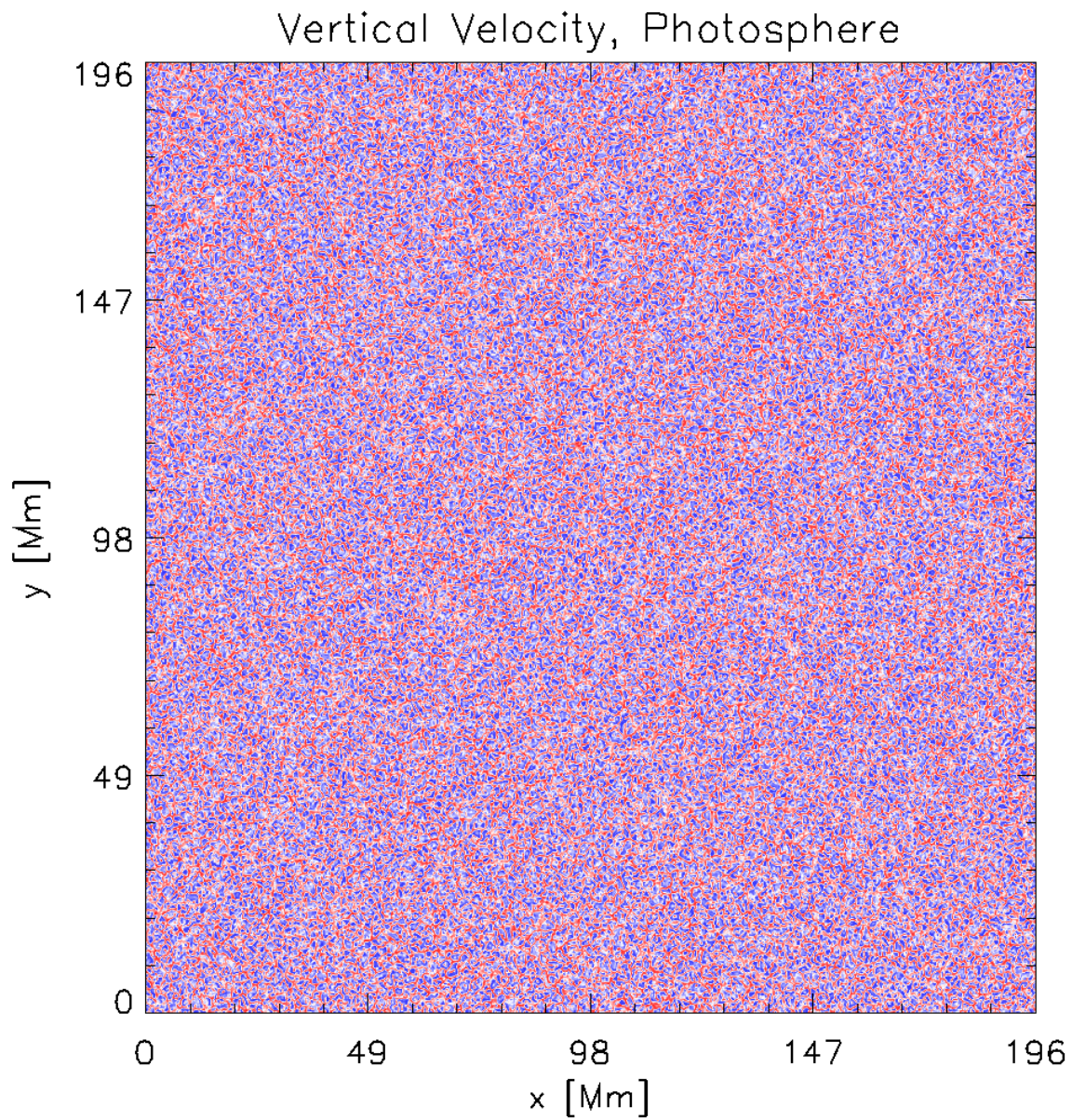
Figure 2.2 Snapshot of the vertical velocity from the reference simulation at the photosphere. The color table is saturated at ± 5 km s^{-1} with blue representing upflows (towards the surface) and red representing downflows (away from the surface).
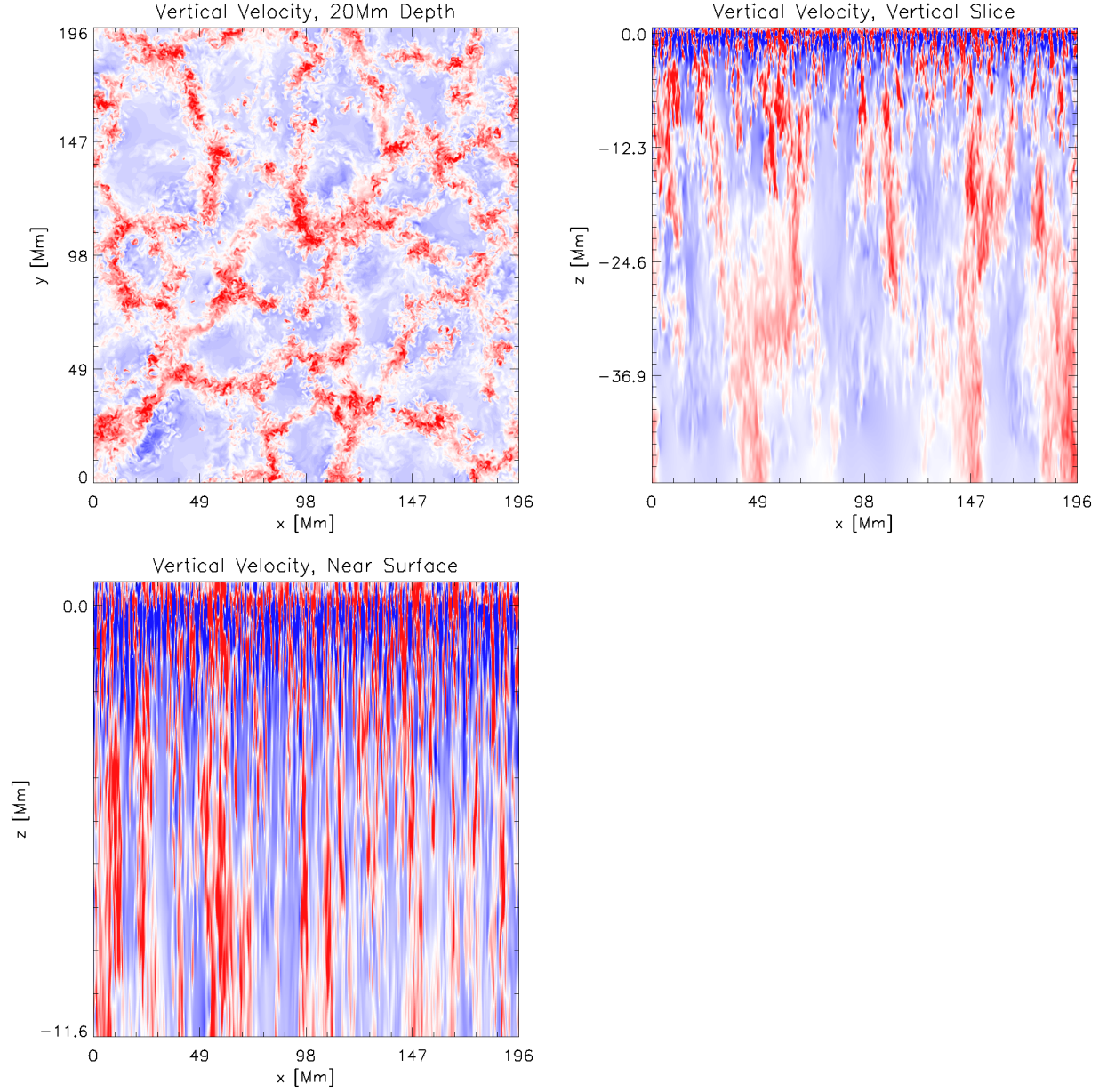
Figure 2.3 Snapshots of the vertical velocity from the reference simulation at 20Mm depth, a vertical slice and only the near surface layers of the vertical slice. All figures use the same color table (saturated at ± 1 km s^{-1}) with blue representing upflows (towards the surface) and red representing downflows (away from the surface).

2.2.2   Mean Properties of Simulations

To familiarize the reader with these simulations we show some snapshots (of velocity and entropy) and mean profiles of the hydrodynamic reference simulation ($197 \times 197 \times 49$ Mm^3 with 192 km $\times$ 192 km $\times$ 64 km resolution). The snapshots of vertical velocity (Figure 2.3) show the granulation in the photosphere where the local scale height and thermal boundary layer determine the dominant length scale of convection. While supergranular scale motions are present (as we show in §4), they are not evident due to the dominance of the much stronger granular flows. The flows at 20 Mm depth have increased length scale due to the increased scale height at this depth. These flows have length scales consistent with supergranulation, but we do not have an a priori expectation for how these flows relate to surface supergranular flows. The vertical slice of the vertical velocity also shows the transition from smaller scale convection at the surface ($z = 0$ Mm) to increasingly large-scale flows (due to increasing scale height) below the photosphere.

We also show the entropy perturbation ($S_{pert} = \frac{S - \langle S \rangle}{\langle S \rangle}$ in Figure 2.4) for the same heights and at the same simulation time as above. We see the same convective pattern at each depth as in the vertical velocity. Upflows throughout the simulation have the same entropy since we set the entropy in inflows at the bottom boundary and there is very little recirculation of cooler fluid into the upflows. At the photosphere the plasma cools (via the radiative transfer) to become downflows with an entropy deficit. This entropy contrast between upflows and downflows drives the convective energy transport. At 20 Mm depth the downflows maintain an entropy deficit but it is significantly smaller than in the photosphere. This is because the overturning mass from the upflows entrains into the downflows and heats the plasma which increases the entropy. While the maximum entropy perturbation in the photosphere is $\sim 10\%$, at 20 Mm depth this is reduced to 0.01%. We also show the vertical slice of the entropy perturbation with the photospheric saturation of 10% and the 0.01% saturation of the color table to show the entropy perturbations in the deeper layers.

Finally, we show the mean profiles of density, temperature, pressure and entropy in Figure 2.5. These thermodynamic quantities follow a nearly adiabatic stratification since the superadiabaticity
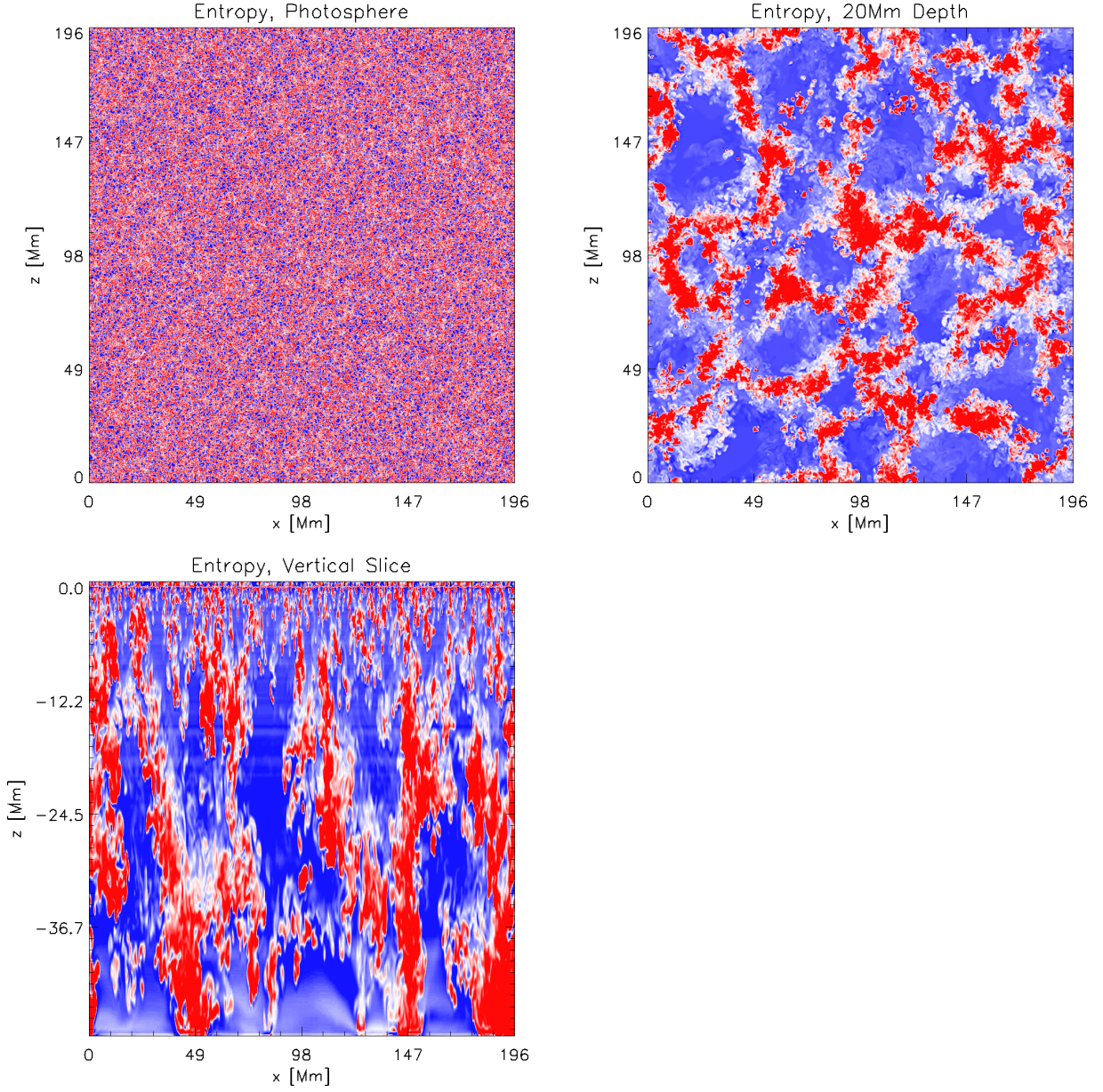
Figure 2.4 Snapshots of the normalized entropy perturbation from the reference simulation at the photosphere, 20 Mm depth, and a vertical slice. We show the normalized perturbation of the entropy (S_{pert}) at each height, where $S_{pert} = \frac{S - \langle S \rangle}{\sigma(S)}$ and $\langle S \rangle$ is the mean and $\sigma(S)$ at each height. The blue is positive entropy perturbation and red is negative (with white being zero entropy perturbation). The color table at each height saturates at one standard deviation.
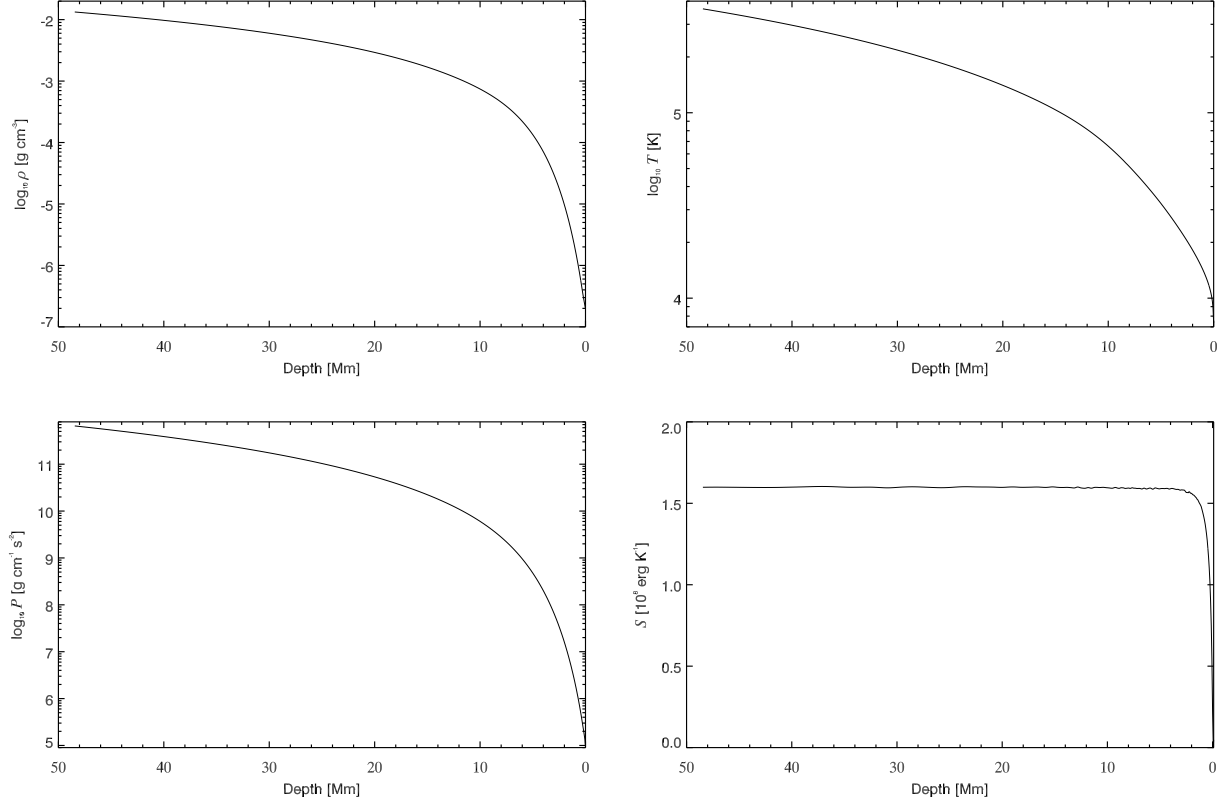
Figure 2.5 The mean stratification of the thermodynamic variables in the $197 \times 197 \times 49$ Mm^3 hydrodynamic reference simulation. The nearly five orders of magnitude change in density from the photosphere to the bottom of the simulation makes this the most stratified solar-like simulation to date.

of the convection zone is very small. Our deepest simulation (49 Mm domain depth) has a density contrast of nearly five orders of magnitude, which makes it the most stratified solar-like simulation that we know of. The change in the entropy between photosphere (which is determined by the radiative cooling) and the bottom (which we set in the inflows) of the domain determines the total convective driving in the simulation. We normalize the entropy profile so that it is zero in the photosphere (which is the entropy minimum). As stated above, the mean entropy (especially in upflows) is nearly uniform in the bottom part of the simulation because there is very little recirculation of plasma into the upflows.

2.2.3   List of Simulations

Finally, we list here all of the simulations presented in this work in Table 2.1. The shallow simulations are only described by the depth while the deeper simulations have specific names used in the captions of figures in later chapters. We also differentiate the simulations with no magnetic field as "hydrodynamic" from the simulations with a small-scale dynamo generated field but $\langle B_z \rangle = 0$ as "zero net flux".

Table 2.1.   List of Simulations

Name	N_x and N_y	N_z	Δx and Δy	Δy	**B**
2Mm	768	64	128km	32km	hydrodynamic
4Mm	768	128	128km	32km	hydrodynamic
8Mm	768	256	128km	32km	hydrodynamic
12Mm	768	384	128km	32km	hydrodynamic
16Mm	768	512	128km	32km	hydrodynamic
20Mm	768	640	128km	32km	hydrodynamic
20Mm, reduced viscosity	768	640	128km	32km	hydrodynamic
20Mm	1024	320	192km	64km	hydrodynamic
Reference	1024	768	192km	64km	hydrodynamic
80Mm	1024	1280	192km	64km	hydrodynamic
H, He I, He II	1024	768	192km	64km	hydrodynamic
H, He I	1024	768	192km	64km	hydrodynamic
H	1024	768	192km	64km	hydrodynamic
Art. Flux 10Mm	1024	768	192km	64km	hydrodynamic
Art. Flux 2.56Mm	1024	768	192km	64km	hydrodynamic
Art. Flux 10Mm, 15G	1024	768	192km	64km	$\langle B_z \rangle = 15$G
Art. Flux 2.56Mm, 15G	1024	768	192km	64km	$\langle B_z \rangle = 15$G
Art. Flux 10Mm, Enh. Rad.	1024	768	192km	64km	$\langle B_z \rangle = 15$G
Art. Flux 2.56Mm, Enh. Rad.	1024	768	192km	64km	$\langle B_z \rangle = 15$G
Zero Net Flux	1024	768	192km	64km	$\langle B_z \rangle = 0$G
10G Mean Field	1024	768	192km	64km	$\langle B_z \rangle = 10$G
Enhanced Radiative Cooling	1024	768	192km	64km	$\langle B_z \rangle = 0$G

Note. — The list of simulations presented in this work. While there are two shallow simulations labeled as 20Mm (since they have the same depth) it is clear from the text and figure captions when we introduce the wider simulation. The three simulations labeled with H and He use a Saha equilibrium equation of state with hydrogen and helium (different from the OPAL equation of state of all other simulations, see §4). The artificial flux simulations are labeled based on the depth of the center of the hyperbolic tangent artificial flux profile. The enhanced radiative cooling simulations (also labeled "Enh. Rad.") increase the rate of cooling in regions of strong magnetic field (see §5.1.1.

Chapter 3

The Role of the Deep Convection in Surface Flows

While there are consistent observational constraints on the length scale and lifetime of super-granulation, the depth dependence is a matter of continuing debate. Recent observations (Hathaway et al., 2010; Hathaway, 2012a) link the size of the supergranules at the surface to the mean flows below the surface (i.e. the differential rotation and meridional circulation). This work assumes that supergranules are anchored at a depth that is equal to their horizontal width at the surface, ranging from 10 Mm to 100 Mm deep. While there is no a priori physical expectation that the width should directly correspond to the depth of the supergranule, we know that the increasing scale height with depth increases the length scale of the convective cells. Thus we would expect the width of supergranules to depend on the local scale height which may appear to be a direct width to depth relationship.

Using ray theory techniques and large-separation rays (i.e. pressure waves which travel 10-24 heliospheric degrees horizontally before returning to the photosphere) with time-distance helioseismology, Duvall & Hanasoge (2013); Duvall et al. (2014) found that the maximum subsurface solar supergranular horizontal and vertical flow speeds occur within 3 Mm of the photosphere. While there are questions about the effectiveness of time-distance helioseismology at measuring these large-scale flows (DeGrave et al., 2014), these observations support a surface model of supergranulation and suggest that the surface flows may organize into large-scale motions (Rast, 2003; Crouch et al., 2007). The depth of supergranulation is a fundamental unanswered question that we address in this chapter: do supergranular flows originate in or near the photosphere (top-down) or do they

imprint from below (bottom-up)?

To investigate the dependence of supergranular scale motions on simulation depth we compare the photospheric velocity power spectrum for simulations with domain depths between 2 Mm and 49 Mm in §3.1. We find that shallower simulations have weaker horizontal flows for modes larger than granulation while granular scale flows remain unchanged. This suggests that granulation is driven locally and depends only on the physics of the photosphere, and that supergranular scale flows are primarily driven at depth and imprint from below. Increasing the depth of the simulations yields increased power in lower wavenumber modes but leaves high wavenumber modes unchanged which suggests that each depth contributes power to a specific mode (or range of modes) in the photosphere.

While the photospheric horizontal velocities show significant dependence on depth, there is no dependence of low wavenumber vertical velocity power in the photosphere on simulation depth (§3.1.3). This is true even after removing the influence of the p-modes. The vertical power spectrum 1.3 Mm below the photosphere, however, shows increased low wavenumber power for increasing simulation depth. The dominant continuity balance changes between 1.3 Mm depth and the photosphere. In the photosphere the horizontal density gradient becomes important and the low wavenumber vertical flows are much stronger which dominates any imprinted velocity there.

Based on the relationship between large-scale deep flows and the low wavenumber power in the photosphere, this suggests that the supergranular motions are bottom-up. Computing the correlations of the supergranular scale horizontal divergence in §3.2, however, finds that the flow pattern originates in the photosphere and propagates down on the timescale of the downflows. This result is confirmed by correlating the fluctuations of the low wavenumber horizontal velocity power which also propagates down on an advective timescale. This suggests that the downflows generated in the photosphere dominate the pattern of the large-scale convection at all depths. Thus, if the supergranulation imprints from below, then these flows must adjust to fit between the faster, denser downflows.

3.1   Domain Depth

To determine how deep solar convection affects the low wavenumber photospheric flows we compute a series of hydrodynamic simulations with constant domain width of 98×98 Mm^2 (with 96×96 km^2 resolution) and domain depths ranging from 20 Mm to 2 Mm (with 32 km resolution). Shallow simulations of 2 Mm depth still have realistic granular dynamics (as has been found previously (Stein & Nordlund, 1998; Vögler et al., 2005)) but there is significant influence on the subsurface flows from the bottom boundary. Comparing simulations of different domain depths helps examine the effect of the bottom boundary on the simulation. We revisit the bottom boundary effect on the convection in §4 by using an artificial energy flux to transport the solar luminosity which creates a stably stratified layer and limits the effect of the boundary condition.

Our primary tool for comparing the supergranular scale convection is the horizontal velocity spectrum. As described in §1, the horizontal velocity spectrum is one of the main methods used to identify solar supergranulation (other identification techniques are discussed in Appendix A) and, consequently, a tool that we consistently apply to our simulations.

3.1.1   Power Spectrum

We compute the power spectrum by taking the two-dimensional fast Fourier transform (FFT) of horizontal slices on the MURaM Cartesian grid (where x and y are the horizontal axis) of a variable, typically the velocity, which we denote FFT(u) = ũ. Applying the horizontal FFT is simplified since the FFT assumes periodic boundaries and the simulations are horizontally periodic. The FFT can be applied in the vertical direction but, since the stratification dominates all quantities, the FFT only measures the periodic features on the scale of the domain depth and the sharp contrast between the bottom and top of the domain will cause ringing in Fourier space.

After taking the FFT we multiply the Fourier transformed velocity by its complex conjugate to get the velocity power (denoted ũ^2). Since all of our simulations are equal size in x and y with equal grid spacing, we have $N_x = N_y$ (i.e. the number of grid cells) and $\Delta_x = \Delta_y = l/N_x$

where Δ_x is the grid spacing and l is the horizontal domain size. We then shift the data so that the zero-frequency mode (DC) is in the center of the horizontal slice and define the spatial frequency of the modes (the wavenumber divided by 2π) by distance from the DC: $f_{x,y}(j_x, j_y) = \sqrt{(j_x - j_{x,DC})^2 + (j_y - j_{y,DC})^2}/(N_x\Delta_x)$ where j_x is the x-index from 0 to $N_x - 1$, j_y is the y-index from 0 to $N_y - 1$, $j_{x,DC}$ and $j_{y,DC}$ are the x and y index of the DC mode. We define the one-dimensional frequency of the modes as $f(j) = j \times \delta f$ where $\delta f = \frac{1}{N_x\Delta_x}$ which extends from the DC ($j = 0$) to the Nyquist ($j = N_x/2$). Finally, to get the power spectrum we compute the mean of all modes in an annulus from $f(j) - \delta f/2$ to $f(j) + \delta f/2$ multiplied by a geometric factor $\frac{j}{\delta f}$. Thus the power spectrum is $P(j) = \frac{j}{\delta f}\langle \tilde{u}^2 \rangle_{f(j)-\delta f/2}^{f(j)+\delta f/2}$. We plot the power spectrum as a function of frequency but we label it, as is the convention, as a function of wavenumber: $k_h/2\pi = f_h = 1/\lambda_h$.

The horizontal velocity spectrum is the sum of the power spectra from the two horizontal components of the velocity: $P_h = P_x + P_y$. We can compute this spectrum at any height at the vertical resolution of the simulation. The power spectrum from the photosphere (unless otherwise stated) is taken to be the geometric slice with the minimum mean optical depth that is still greater than one.

When we require separation of the spectrum into two components (i.e. different horizontal scales of motion) we use a general division of scales into granulation and supergranulation. The observed size scale of granules is ~ 1 Mm with supergranules typically observed as ~ 30 Mm (Rieutord & Rincon, 2010). We do not explicitly examine mesogranular scales (with length scale ~ 10 Mm) in our simulations and include these modes in our definition of granular scale motions. Observations find that 20 Mm is the minimum length scale associated with the supergranular peak in the solar photospheric power spectrum (Roudier et al., 2012). Thus, we use this scale to separate granular scale flows for wavelengths $\lambda_h < 20$ Mm and $k_h/2\pi > 0.05$ Mm^{-1} from supergranular scale flows for $\lambda_h \geq 20$ Mm and $k_h/2\pi \leq 0.05$ Mm^{-1}.

3.1.2   The Horizontal Surface Motions Dependence on Domain Depth

We show the horizontal velocity spectrum at the photosphere for six simulations with varying domain depths in Figure 3.1. The horizontal velocity spectrum from the 20 Mm deep simulation was computed from 3 days of solar time (that we consider to be relaxed) and this simulation was used as the basis for the other simulations in Figure 3.1. Each shallow simulation was started from the same snapshot of the 20 Mm deep simulation with some portion of the lower domain removed. These shallower simulations were all run for 24 hours of time (in the simulations physical units) with the power spectrum computed from the last 12 hours of the simulation.

The most prominent feature in Figure 3.1 is that increasing the simulation depth increases the low wavenumber power. There is an order of magnitude decrease in the power of the largest scale mode ($\lambda_h = 98$ Mm) when comparing the 20 Mm simulation (black curve) and 2 Mm deep simulation (red curve). While all of these simulations match at high wavenumbers, decreasing the depth of the simulation decreases the largest scale at which one of the shallower simulations match the 20 Mm deep simulation. Thus the low wavenumber power in the photosphere depends on the existence of deeper convection, with increasing domain depth increasing power in the large-scale photospheric flows.

3.1.2.1   Scales with Equal Power

By showing these power spectra as a fractional difference with the deepest simulation (P_h / $P_{h,\text{20Mm deep}} - 1$ in Figure 3.2) we can more easily visualize the scale where the shallower simulations have power equal to the 20 Mm deep simulation. The negative values are the wavenumbers for which the shallow simulations have less power than the 20 Mm deep simulation (with the positive portion representing the reverse). Though there are some differences in power at smaller scales, we take the division between the weaker scales due to domain depth and scales with sufficient power (compared to the deeper simulations) as the largest mode where the power in the shallower simulation is equal to the power in the 20 Mm deep simulation (where curves cross zero in Figure 3.2). The largest
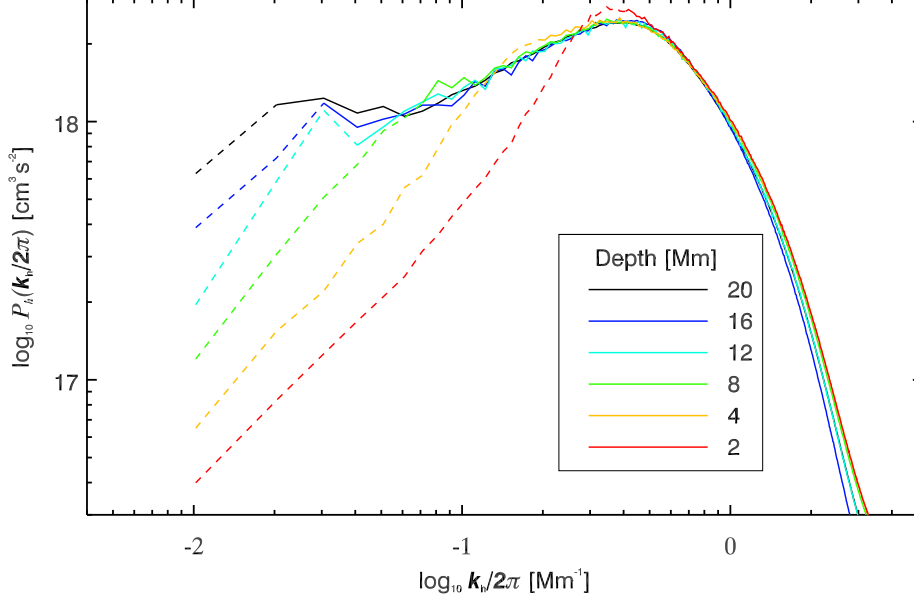
Figure 3.1 The photospheric horizontal velocity spectrum for hydrodynamic MURaM simulations of different depths. The domain of these simulations is 98×98 Mm^2 and the domain depth ranges from 20 Mm to 2 Mm for the six simulations corresponding to the different line colors (see figure legend). The change to *dashed* linestyles shows the range of Fourier wavenumbers that have driving depth outside the simulation domain (see §4). Shallower simulations have statistically significantly less low wavenumber power. The increased power in shallower simulations compared to the 20 Mm deep simulation (e.g. the 2 Mm simulation at granular scales) is due to a box mode artificial enhancement (see §3.1.2.2). Since the simulation timestep is based on the speed of sound at the bottom boundary, we have different timesteps in each of these simulations. This changes the effective viscosity which is why there is slight differences between the power at very high wavenumbers.

horizontal scale with equal power ranges from the depth of the simulation up to 1.85 times the depth of the simulation (see Table 3.1). The horizontal scales larger than the depth of the simulation (or somewhat larger than the depth depending on the simulation) do not match the power in a deeper simulation at those scales. This suggests that we require a domain depth of ~ 50 Mm to run a simulation with sufficient depth to have full power in the largest scale mode (56 Mm) in the peak of the solar photospheric velocity spectrum (Roudier et al., 2012).

We expect deeper flows to have larger scale motions based on the increasing scale height with depth. We do not, however, have an a priori expectation that the low wavenumber power in the photosphere depends on these deeper flows. The evidence from Figures 3.1 and 3.2 suggest that only granular scale motions are driven in the photosphere and that the presence (or absence) of the subsurface convection determines the large-scale flows at the surface. Furthermore, the flows in deeper simulation domains, which have increased horizontal length scale due to the increasing scale height, contribute power to larger scale modes in the photosphere but do not add power at smaller scales. This suggests that each depth contributes a specific scale (or range of scales) of motion to the photospheric spectrum.

The change in linestyle in both Figures 3.1 and 3.2 identifies the separation between modes that we expect to be fully driven inside the domain (*solid*) and modes that are only partially driven inside the domain (*dashed*). This separation is based on a driving (integral) scale for the convection $(4H_\rho)$ at each depth which is derived from the model that we present in §4. Since no modes with *solid* linestyle have an amplitude that is influenced by the domain depth while the *dashed* modes increase with increasing domain depth, this validates $\lambda_h = 4H_\rho$ as the driving (integral) scale of the convection at each depth.

3.1.2.2   Box Mode in Shallow Simulations

There are, however, issues with comparing simulations with smaller domain depth. We begin examining these problems by investigating the box mode of the simulation. The box mode is a feature of the horizontal velocity spectrum that shows excess power compared to deeper simulations.

Table 3.1.　Photospheric Horizontal Velocity Spectrum

Depth [Mm]	Largest Equal Power Scale [Mm]	Ratio of Equal Power Scale and Depth	Peak of Box Mode [Mm]	Ratio of Box Mode and Depth
16.384	16.384	1.0	32.678	2.0
12.288	16.384	1.33	32.678	2.66
8.192	14.043	1.70	12.288	1.50
4.096	7.562	1.85	6.144	1.50
2.048	3.781	1.85	2.891	1.41

Note. — The largest scale of the photospheric horizontal velocity spectrum with equal power is determined by finding the lowest wavenumber mode in Figure 3.1 that has greater power in the shallower simulation than the 20.48 Mm deep simulation. The peak box mode is determined by identifying the lowest wavenumber local minimum in the fraction difference in power between the shallow simulation and the 20.48 Mm deep simulation (Figure 3.2). In both measurements the deeper simulations (16 Mm and 12 Mm) are less reliable since they are closer in depth to the reference simulation and the spectral resolution limits the number of modes that can discern between the largest scales.
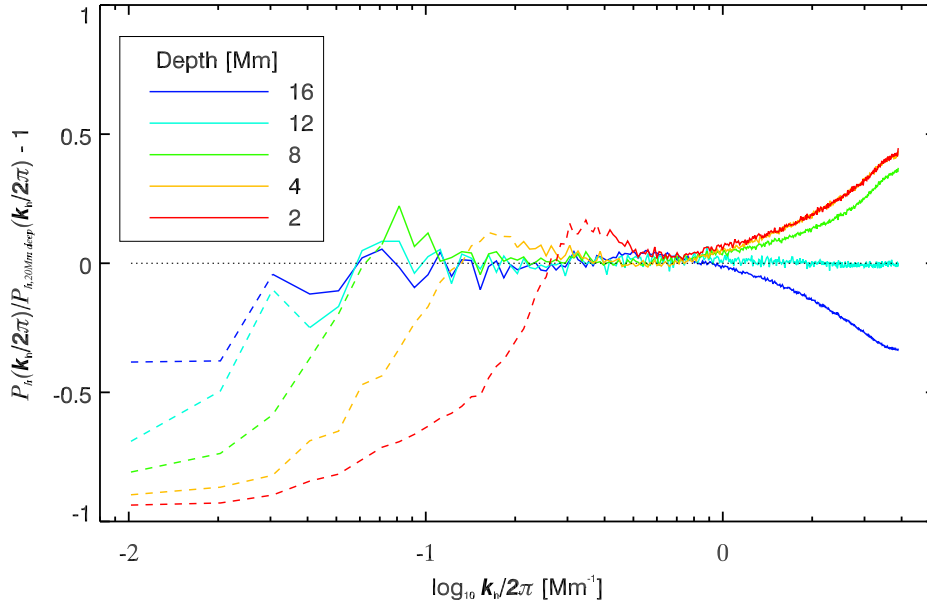
Figure 3.2 The ratio of the horizontal velocity spectrum of the 20 Mm deep simulation with the shallower simulations. This illustrates the wavenumber where the shallower simulation first has the same power as the 20 Mm deep simulation (where the lines crosses from negative to positive values) and the box mode enhancement (the local maximum at wavenumbers just above the previously mentioned crossover). The differences at high wavenumber are due to the different diffusivity based on the change in timestep (which is set by the sound speed at the bottom boundary). These differences are not statistically significant and have very low amplitude in all simulations (see Figure 3.1).

Precisely, we measure this as the local maximum in Figure 3.2 near the largest scale with power equal to the 20 Mm deep simulation. This box mode is evident in each of the shallower simulations when compared to the deepest simulation. The excess power in these modes is an artifact of the MURaM computation (and other types of simulations) that we call the box mode and is related to the bottom boundary condition and the domain size. The approximate range of scales for the box mode is 1.5 times simulation depth to 2.5 times simulation depth (See Table 3.1).

We measure the maximum increase in power due to the box mode to be between 10% and 20% in the 8 Mm, 4 Mm, and 2 Mm deep simulations compared to the power spectrum from the 20 Mm deep simulation. The width of the peak around the box mode is ±30% of the central wavenumber of the box mode itself, which suggests that while we are identifying this as a single mode the elevated power affects a range of scales of motion.

While the box mode influences our identification of the mode with equal power to the 20 Mm deep simulation, since we consistently see statistically significantly weaker low wavenumer power with shallower simulations, the box mode does not invalidate the decreased low wavenumber power that we observe in the photosphere of these simualtions. The primary concern with the box mode is for analysis of the power spectrum from the deepest simulation available (see §3.1.6 for more analysis of this mode).

3.1.2.3 The Effect of the Bottom Boundary

The other primary concern with comparing simulations with different domain depth is the influence of the bottom boundary condition, which is moved closer to the photosphere as the domains become shallower. Our standard boundary condition uses enhanced viscosity in the bottom eight grid cells that results in broader, slower inflows than outflows. Thus, the bottom boundary smooths inflowing plasma.

To test the effect of this boundary we compare a 20 Mm deep simulation with reduced viscosity (the same viscosity that is used in the rest of the domain) that results in narrow, fast inflows which are qualitatively similar to the outflows. These fast and narrow inflows create small
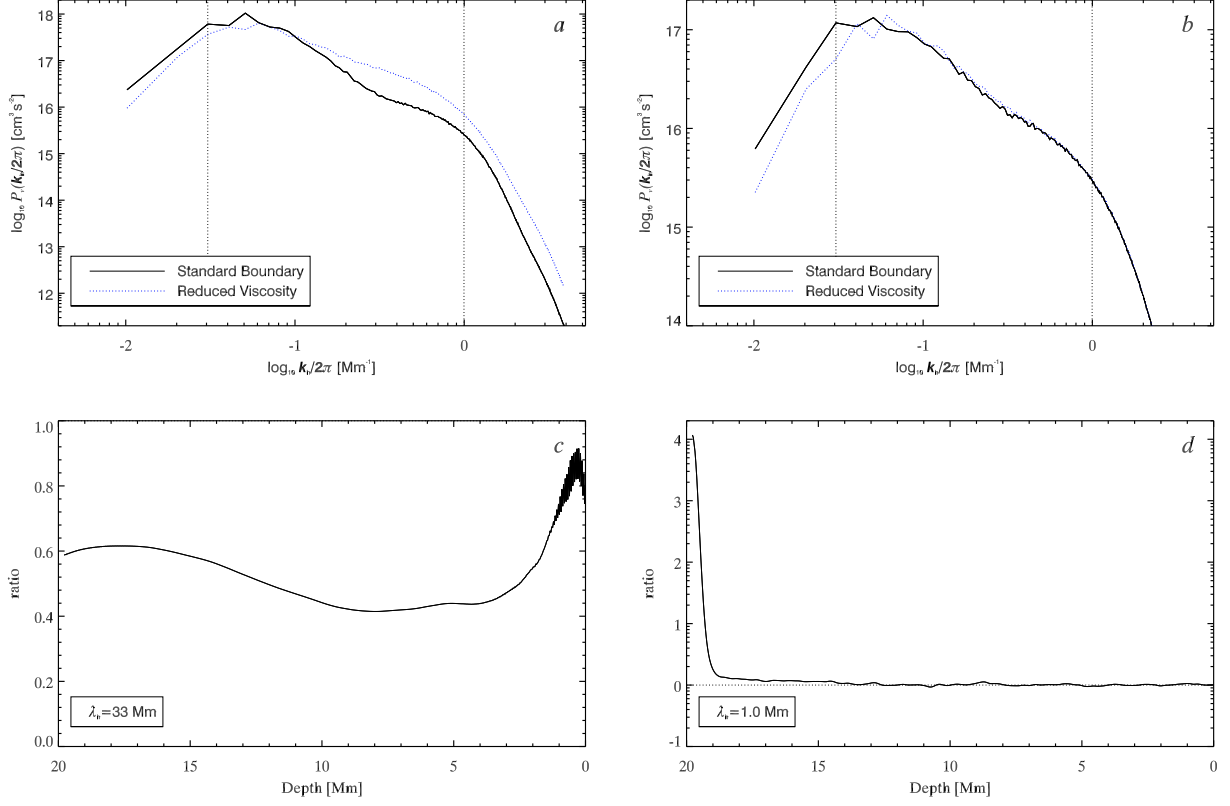
Figure 3.3 Comparison of the reduced viscosity boundary condition to the standard (enhanced) viscosity boundary. We show the vertical velocity spectrum at 640 km above the bottom boundary (*a*, which is outside of the depths with enhanced viscosity) and in the middle of the 20 Mm deep domain (*b*). Overplotted are two vertical lines at $k/2\pi = 0.03$ Mm^{-1}, $\lambda_h = 33$ Mm and $k/2\pi = 1.0$ Mm^{-1}, $\lambda_h = 1$ Mm for modes that we examine in more detail. We show the ratio of the power (reduced viscosity boundary simulation divided by standard boundary simulation) for the $\lambda_h = 33$ Mm (*c*) and $\lambda_h = 1$ Mm (*d*) modes. The low wavenumber modes have reduced power at the boundary and throughout the simulation domain whereas the high wavenumber modes have increased power in the reduced viscosity boundary simulation but this power is equal in both simulations within a few Mm of the boundary (with the fiducial horizontal line in *d* showing where these simulations are equal).

scale turbulence at the bottom of the domain that disrupts the large-scale convective pattern which reforms in the middle of the domain (which we show in §2.1.4 and Figure 2.1 for details).

To determine the effect of the boundary on the deep flows we show the velocity spectrum at 640 km above the bottom boundary (a) and in the middle of the 20 Mm deep domain (b) from both the reduced viscosity boundary and standard boundary simulations in Figure 3.3 (note that 640 km above the bottom boundary is outside the depths with enhanced viscosity in the standard boundary simulation). The flows in the simulation with the reduced viscosity boundary have reduced low wavenumber power and increased high wavenumber power near the boundary which persists in flows well above the boundary (albeit with smaller amplitude difference in high wavenumber modes). Without enhancing the viscosity, the flows also have increased rms velocity (which determines the total integrated power in the spectrum) within ~ 2 Mm of the bottom boundary but this rms velocity is equal to the standard boundary simulation in the rest of the domain. Thus, the velocity spectrum of the simulation with reduced viscosity have increased integrated power near the bottom of the domain (a). On the other hand, the spectrum from both simulations in the middle of the domain (b) have equal integrated power where the decreased low wavnenumber flows are balanced by a slight increase in higher wavenumber power (in the wavenumber range $0.06 < k/2\pi < 0.5\mathrm{Mm}^{-1}$).

To investigate how the low and high wavenumber modes behave in these two simulations we compute the ratio of power (i.e. power in the reduced viscosity simulation divided by the standard boundary simulation) as a function of depth for the modes shown by the fiducial vertical lines from the spectra plotted in Figure 3.3 a and b. The low wavenumber mode ($k/2\pi = 0.03$ Mm^{-1}, $\lambda_h = 33$ Mm) has decreased power at the bottom of the domain of the reduced viscosity simulation which persists throughout the simulation domain. This suggests that the boundary condition can influence the amplitude of the low wavenumber flows throughout the simulation. The high wavenumber mode ($k/2\pi = 1.0$ Mm^{-1}, $\lambda_h = 1$ Mm), however, has much larger amplitude without enhancing the viscosity near the boundary, but this amplitude drops until the ratio is equal for all depths greater than ~ 1 Mm above the bottom boundary. This suggests that the reduced viscosity boundary creates high wavenumber flows with excess amplitude that is self-corrected inside the

simulation domain.

The best way to determine which boundary condition is more physically realistic is to compare to simulations with varying domain depth. We find that the convection in the middle of a simulation with a deeper domain is consistent with the broad, slow inflows of the enhanced viscosity boundary. The enhanced high wavenumber flows of the reduced viscosity boundary that corrects itself within ~ 1 Mm of the boundary also suggests that the reduced viscosity boundary is not consistent with the flows in the rest of the simulation domain. Attempting to compare with observations of subsurface solar convection to determine if vertical flows at this depth in the Sun are broad and slow or narrow and fast is not possible with current techniques. While time-distance helioseismology is commonly used to measure subsurface convection, recent attempts to measure the subsurface vertical flow patterns in MURaM have raised serious concerns about applying these methods to measure solar flows (DeGrave et al., 2014). Thus, based on the evidence from these simulations without any assistance from solar observations, we use the enhanced viscosity boundary because the flows are more consistent with the flows in the middle of a deeper domain.

Finally, we compare the photospheric horizontal velocity spectrum of these two simulations in Figure 3.4 (we also show the spectrum for horizontal velocities averaged over 30 minutes to remove p-modes, see §3.1.4). The *solid* (black) curve, from the simulation with normal boundary simulation, is the same spectrum used to compare against shallower simulations above (see Figure 3.1). The *dotted* (blue) curve, from the simulation with reduced boundary viscosity, has decreased low wavenumber power in the photosphere. Thus the decreased power of the low wavenumber flows deep in the domain decreases the imprinted horizontal velocity power in the photosphere. This suggests that the amplitude of the deeper, large-scale flows (and not just the presence of deeper flows) determine the low wavenumber power in the photosphere.

3.1.3   Surface Vertical Velocity

Solar supergranules are dominated by horizontal flows (400 m s^{-1}) in the photosphere with vertical flows approximately one order of magnitude weaker (~ 30 m s^{-1}, Rieutord & Rincon, 2010).
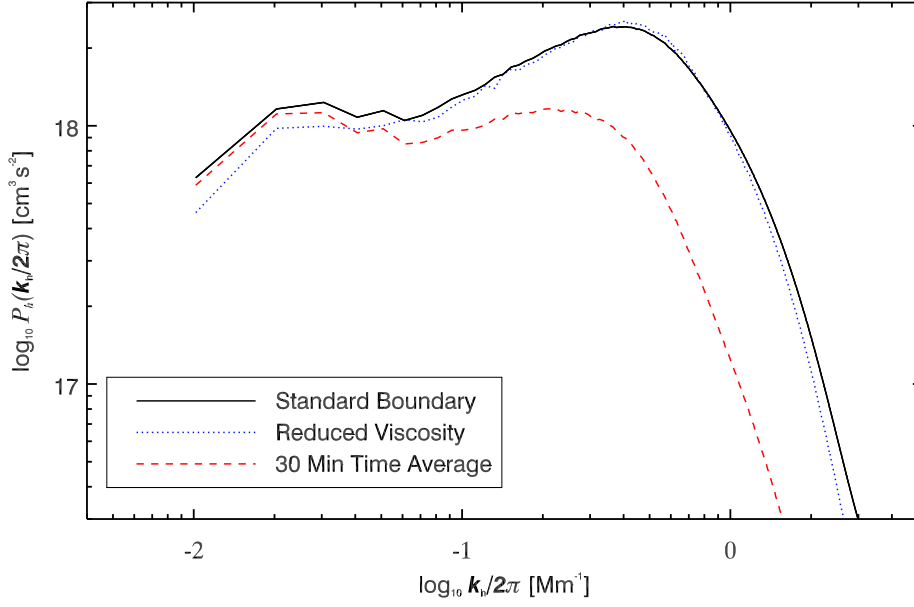
Figure 3.4 The photospheric horizontal velocity spectrum of the 20 Mm deep simulation (*solid* black curve, the same as in Figure 3.1), this same simulation with photospheric velocities averaged over 30 minutes (*dashed* red curve) and another 20 Mm deep simulation with reduced viscosity on the bottom boundary (*dotted* blue curve). Reducing the viscosity on the bottom boundary decreases the power of low wavenumber flows near the bottom of the simulation which results in decreased low wavenumber power in the photosphere. Time averaging removes p-modes (see §3.1.4) but also significantly reduces the power in high wavenumber flows.

While we expect the supergranular scale vertical flows to be weaker in our simulations than the horizontal flows, we also examine the vertical velocity spectrum to determine if there is a similar trend of decreasing supergranular scale vertical velocity with decreasing simulation domain depth as we saw with the horizontal flows.

The vertical velocity spectrum (Figure 3.5) at the photosphere is dominated by granulation. The drop in vertical velocity power from the granulation peak ($k/2\pi = 0.8$ Mm^{-1}) to the smallest supergranular scale ($k/2\pi = 0.05$ Mm^{-1}) is a decrease of more than one order of magnitude. The drop in horizontal velocity power from the granular peak to supergranular scales, on the other hand, is only $\sim 20\%$ for the 20 Mm deep simulation. Just as in the observations, the vertical velocity power in the supergranular modes ($\lambda_h > 20$ Mm) in our simulations is much weaker than the horizontal power in the photosphere.

Furthermore, we do not see the same dependence of low wavenumber vertical velocity power on the simulation domain depth as we saw in the horizontal flows. None of the differences in the vertical velocity power of these simulations are statistically significant (see one standard deviation error bars in Figure 3.5 measured from the time series of the power in this mode in the 20 Mm deep simualtion) and there is no qualitative order to the low wavenumber power based on simulation depth. We explore potential problems with this measure in §3.1.4 and revisit this issue in §3.1.4.2.

3.1.4   P-modes in the Simulations

While the low wavenumber vertical velocity power does not have any dependence on simulation depth, these modes have significant contamination from power in the acoustic waves (p-modes). We know that p-modes are a significant source of low wavenumber power in the solar photosphere, but we do not know how significant these p-modes are in the simulations.

We plot the $k - \omega$ diagram for the 20 Mm deep simulation (Figure 3.6) which shows the contours of the vertical velocity power (with darker colors representing increasing power) as a function of wavenumber ($k_h/2\pi$ [Mm^{-1}]) and timescale (ω [s^{-1}]). The convective power (concentrated in the bottom right of the figure) is separated from the p-mode power (upper left) by the theo-
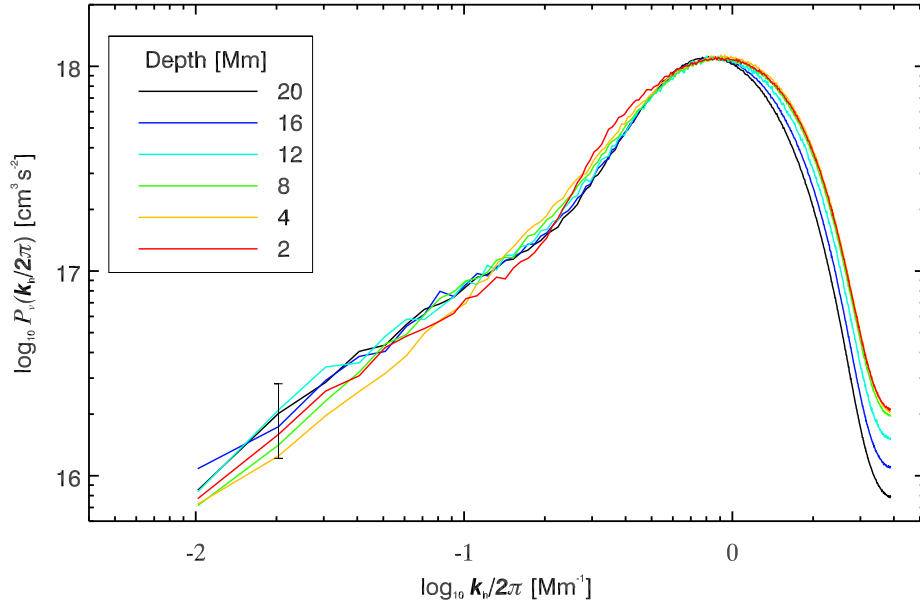
Figure 3.5 The photospheric vertical velocity spectrum for hydrodynamic MURaM simulations of different depths. These are the same simulations as in Figure 3.1 with domain depths ranging from 20 Mm to 2 Mm for the six simulations corresponding to the different line colors (see figure legend). We plot the one standard deviation error bars for the 20 Mm deep simulation which shows that none of the differences in power are statistically significant.
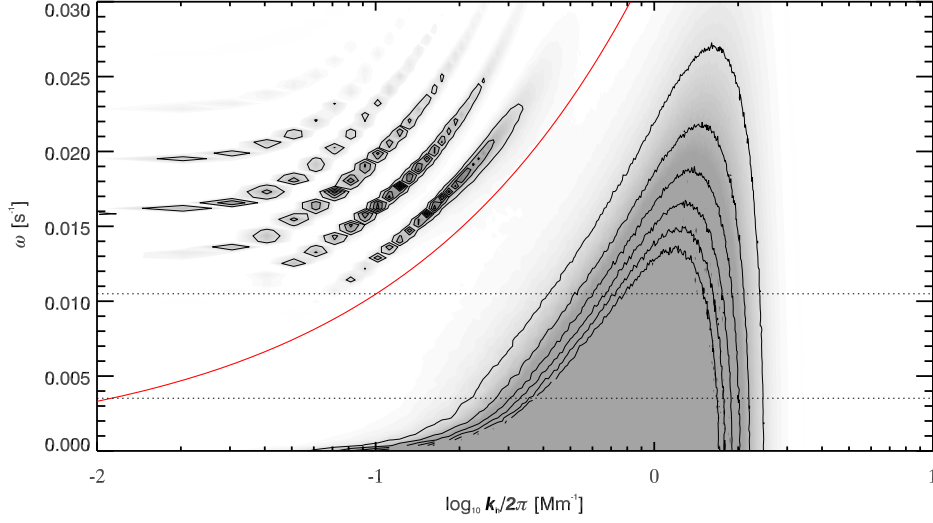
Figure 3.6 The photospheric k-ω diagram for the 20 Mm deep simulation vertical velocity where darker colors correspond to increased velocity power. This diagram shows the timescale ($\omega = 2\pi/t$ where t is the time in seconds) and length scales of the vertical velocity power. The convective power is concentrated at the bottom-right portion of the plot, while the p-mode power is the ridges in the upper left portion of the plot. We plot the logarithm of k_h to compare to the other velocity power spectrum while most plots of the observed solar k-ω diagram plot the linear k. We show the theoretical f-mode $k_h g = \omega^2$ where g is the gravitational acceleration (2.74×10^4 cm s^{-1}) as the *solid* red curve. We also show the fiducial horizontal lines that correspond to the time scale of 10 minutes ($\omega = 0.0105$ s^{-1}) which shows that the p-mode power is concetrated on shorter timescales and the 30 minutes ($\omega = 0.0035$ s^{-1}) that corresponds to our time averaging of the velocity to remove p-modes.

retical f-mode that follows the curve $k_h g = \omega^2$ where g is the gravitational acceleration equal to 2.74×10^4 cm s^{-1} (*solid* red curve).

3.1.4.1   Time Averaging to Remove P-modes

Most of the p-mode power is on a timescale shorter than 10 minutes ($\omega > 0.0105$ s^{-1}, upper fiducial horizontal line in Figure 3.6), while most of the convective power is on a timescale longer than 10 minutes. Thus we can remove the p-mode power by time averaging the velocities. We choose to average the photospheric velocities for 30 minutes before computing the power spectra to remove more than 99% of the p-mode power. This averaging also reduces the power in the convective motions for $\omega < 0.0035$ s^{-1} (lower fiducial horizontal line in Figure 3.6), primarily at granular scales ($k_h/2\pi > 0.1$ Mm^{-1}, $\lambda_h > 10$ Mm). While we could use a k-ω filter to remove these p-modes, this time averaging is sufficient to remove the p-mode power and only influences convective power of vertical motions at the scales of granulation.

The power in the p-modes is similar in both the horizontal and vertical velocity power, approximately 1.0×10^{18} cm^3 s^{-2} total p-mode power, i.e. power above the f-mode, in the x, y, and z components of the velocity. The horizontal convective power, however, is much greater than the vertical convective power at supergranular scales ($\lambda_h > 20$ Mm). Specifically, at supergranular scales there is ~ 10 times more p-mode power than convective power in the photospheric vertical velocity and ~ 5 times less p-mode power than convective power in both the x or y components of the velocity.

We find that using the 30 minute time averaging on the horizontal velocity spectrum (Figure 3.4 *dashed*, red curve) reduces the power across all modes at supergranular scales ($k/2\pi < 0.05$ Mm^{-1}) but maintains the same spectral shape, albeit with a smaller reduction at the lowest wavenumbers. This averaging also reduces the power in the granular scale motions significantly. Since the p-mode power is a weak influence on low wavenumber horizontal convection and does not change the shape of the spectrum at supergranulation scales, we plot the un-averaged horizontal velocity spectrum unless explicitly stated otherwise.
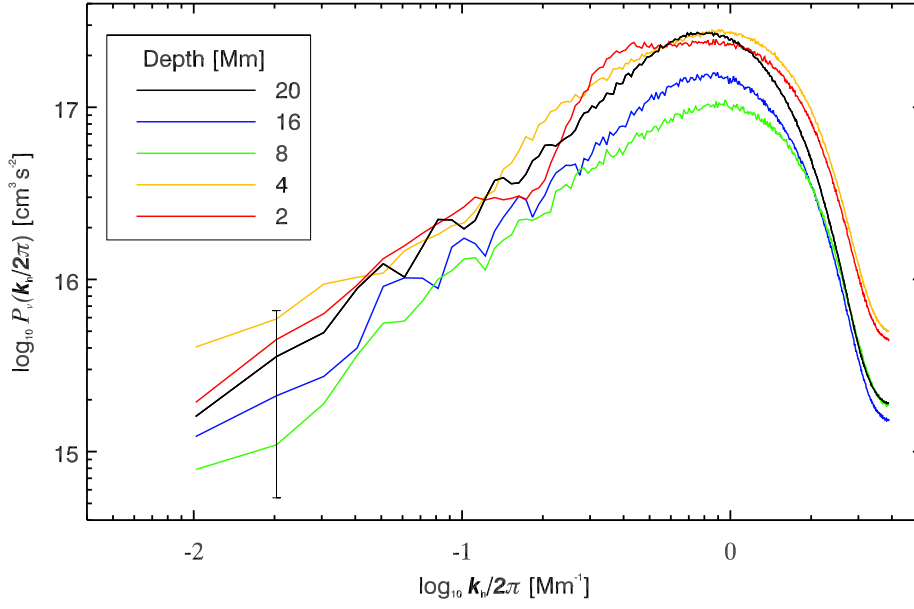
Figure 3.7 The photospheric vertical velocity spectrum that have been averaged over 30 minutes from simulations with varying depths. We show the one standard deviation error bars for the 20 Mm deep simulation which shows that none of the differences in power are statistically significant. Unlike the horizontal velocity spectrum (Figure 3.1) there is also no clear order to the photospheric power based on the depth of the simulation. Note that we do not have the data to compute the time-averaged velocity for the 12 Mm deep simulation.

As shown in Figure 3.5, there is no statistically significant differences when comparing the photospheric vertical velocity power at supergranular scales from simulations with different domain depths. Since the power in these modes is dominated by the p-modes (with ~ 10 times more p-mode power than convective power), we compare the time averaged vertical velocity power in Figure 3.7 to determine if the convective power depends on simulation domain depth. This time averaging requires careful consideration since the timestep of each simulation is different (which is based on the speed of sound at the bottom boundary and the sound speed is slower closer to the photosphere). The time averaging decreases the velocity power but the decrease in power primarily depends on how many snapshots are averaged. Thus, we use the same number of snapshots (that span 30 minutes) for the averaging of each simulation.

Despite removing the p-mode power, there is still no consistent order of the photospheric vertical velocity power. There is no a priori expectation that the observed low wavenumber flows in the solar photosphere are generated at the surface or imprint from below. While the surface is dominated by convection at the scales of granulation and supergranular scale convection occurs in deeper layers with increased scale height, it has been suggested that supergranulation could result purely from self-organization of motions in the photosphere (Rast, 2003; Crouch et al., 2007). Since low wavenumber power in the horizontal velocity spectrum increases with increasing domain depth (Figure 3.1) this suggests that the low wavenumber horizontal flows imprint from below. The low wavenumber vertical velocity spectrum (Figure 3.7), however, has no dependence on the domain depth of the simulation which suggests that the low wavenumber vertical flows are generated in the surface. This leaves us with the following question: how do the large-scale motions below the surface imprint on the surface horizontal flows (and not the vertical flows)?

3.1.4.2   Deeper Horizontal and Vertical Spectrum

To address this question we show the horizontal and vertical power spectrum at a depth of 1.3 Mm below the photosphere (Figure 3.8). Both the vertical and horizontal velocity spectra at this depth shows the same trend that we see in the horizontal velocity spectrum at the photosphere:

low wavenumber modes have less power in shallower simulations. Furthermore, these results are statistically significant as shown by the one standard deviation error bars for the deepest and shallowest simulations. While the vertical velocity spectrum in the photosphere is not influenced by simulation domain depth, the low wavenumber vertical power at 1.3 Mm depth increases with increasing domain depth. This suggests that the large-scale subsurface motions do imprint on the vertical velocity, but we can only measure this imprinting power below the photosphere.
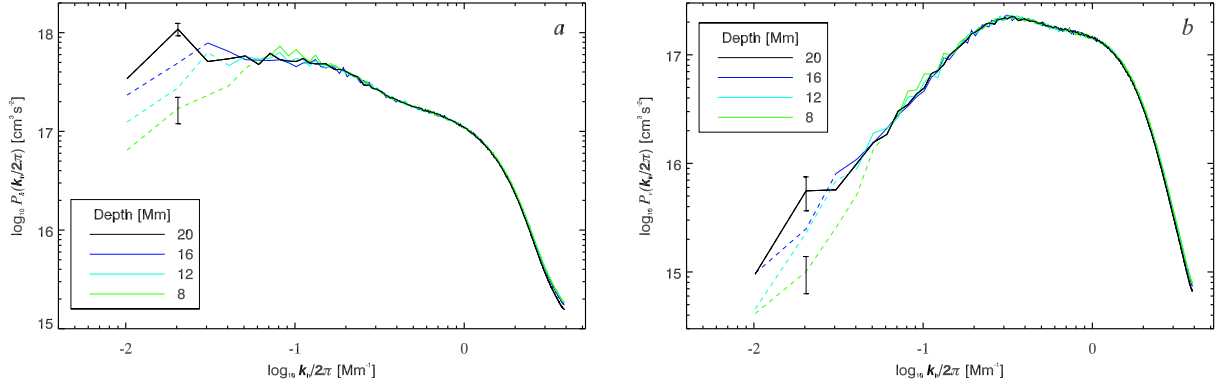
Figure 3.8 The horizontal (a) and vertical (b) velocity spectrum at 1.3 Mm below the photosphere from simulations of varying depth. This shows that both the vertical and horizontal power at this depth depends on the depth of the simulation. Thus, while the vertical power in the photosphere does not increase with increasing simulation depth, the vertical flows below the surface follow this trend. We change the linestyle (from *solid* to *dashed*) for modes with wavelengths greater than four times the maximum density scale height in the simulation domain ($4 \max(H_\rho)$). We show the one standard deviation error bars for the deepest (20 Mm) and shallowest (8 Mm) simulations. We do not include the 4 Mm and 2 Mm deep simulation since this depth is too close to the bottom boundary of both simulations and they are qualitatively different at every scale.

By examining four of the low wavenumber modes of the vertical velocity power spectrum (normalized by the maximum power of each mode) as a function of depth (Figure 3.9) we find that these modes decay with height until approximately 200 km below the photosphere. This suggests that while the large-scale convection imprints on the upper layers, the power decays to very small values at the surface and the low wavenumber vertical velocity power observed in the photosphere is generated locally.
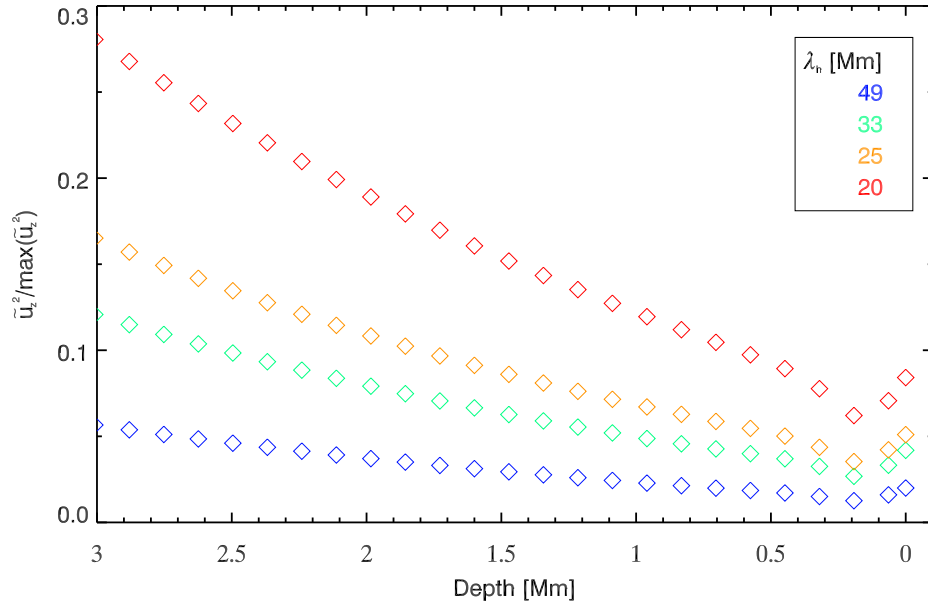
Figure 3.9 Four of the low wavenumber modes of the vertical velocity spectrum from the hydro-dynamic reference simulation (see §3.1.5) as a function of depth. These modes decay with height until right below the photosphere where they begin to increase again. The modes are indicated by the color (see legend).

3.1.4.3   Continuity Equation in the Photosphere

We introduce a model derived from a simplified continuity equation (using an anelastic approximation) in §4. This model provides a relationship between the low wavenumber power in the horizontal and vertical velocity using the approximation $\nabla_h \cdot u_h \approx \frac{u_z}{H_\rho}$ (i.e. we ignore horizontal derivatives of density and $\frac{\partial u_z}{\partial z}$). We use this equation to compute the inferred vertical velocity based on the horizontal velocity (*dashed* red curve) and compare to the actual vertical velocity power (*solid* blue curve) in the photosphere (Figure 3.10). This shows that the amplitude of the low wavenumber vertical power required to drive horizontal modes is much weaker than the amplitude of vertical motions there. This is because the density scale height is so small in the photosphere that even small vertical velocities are amplified in the $\frac{u_z}{H_\rho}$ term that relate to horizontal flows. This suggests something is driving low wavenumber vertical flows at the surface.
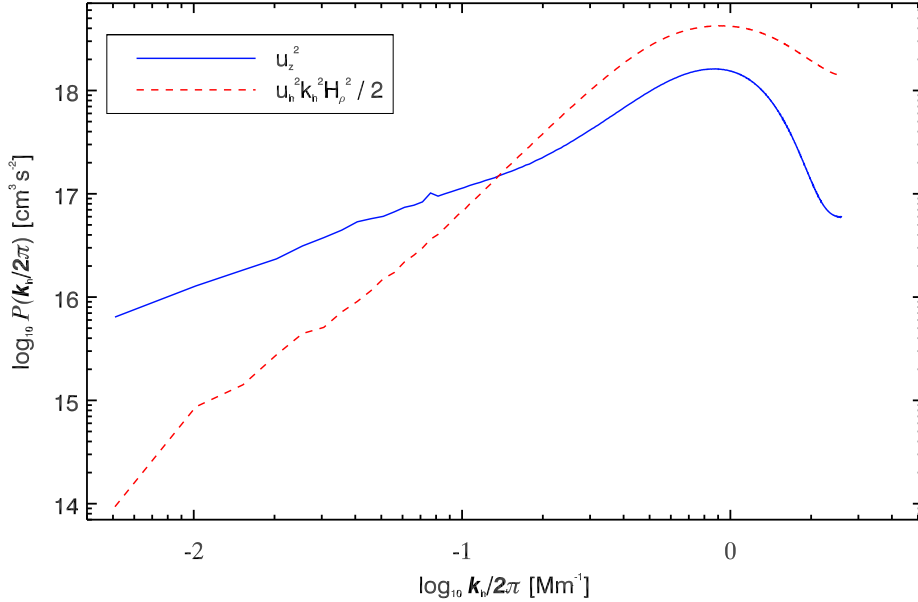
Figure 3.10 The vertical velocity spectrum and inferred vertical velocity spectrum using the two component model in the photosphere of the reference simulation. The amplitude of the vertical velocities is much stronger than required to match horizontal flows.

In Figure 3.11 we compare the spectrum of terms from the continuity equation ($\frac{\partial \rho}{\partial t} = \nabla \cdot (\rho \mathbf{u})$) in the photosphere (*a*) and 1.3 Mm below the surface (*b*). We examine balances in a statistically

steady state which ignores the term $\frac{\partial \rho}{\partial t}$. At 1.3 Mm depth $\rho(\frac{\partial u_x}{\partial x} + \frac{\partial u_y}{\partial y})$ (*dashed* red curve) is balanced by $\mathbf{u} \cdot \nabla \rho$ (*dot-dash* green curve) at low wavenumbers and by $\rho \frac{\partial u_z}{\partial z}$ (*solid* blue curve) at high wavenumbers. Note that the horizontal derivatives of density are negligible at this depth which means that $\mathbf{u} \cdot \nabla \rho \approx u_z \frac{\partial \rho}{\partial z}$ (this is one of the assumptions inherent to the model). At 1.3 Mm depth our model assumptions are valid and at low wavenumber we can use $\nabla_h \cdot u_h \approx \frac{u_z}{H_\rho}$ to derive the horizontal velocity spectrum from the vertical velocity spectrum (or the opposite).
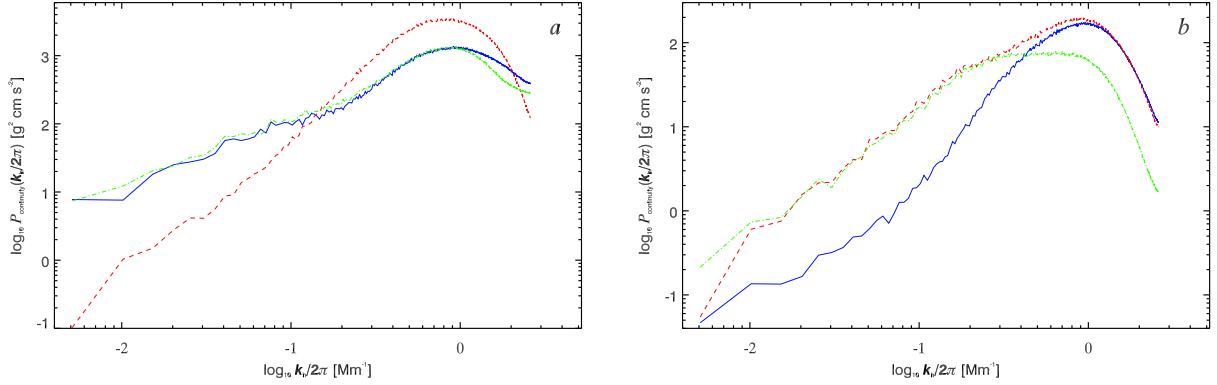
Figure 3.11 The power spectrum of the terms in the continuity equation from the reference simulation (see §3.1.5) at the photosphere (*a*) and 1.3 Mm below the surface (*b*). The dominant balance for low wavenumber modes in the photosphere is $\mathbf{u} \cdot \nabla \rho$ (*dot-dash* green curve) and $\rho \frac{\partial u_z}{\partial z}$ (*solid* blue curve) while $\rho(\frac{\partial u_x}{\partial x} + \frac{\partial u_y}{\partial y})$ (*dashed* red curve) is much weaker. At 1.3 Mm depth the low wavenumber balance is between $\rho(\frac{\partial u_x}{\partial x} + \frac{\partial u_y}{\partial y})$ and $\mathbf{u} \cdot \nabla \rho$. The wavelength that marks the crossing between $\mathbf{u} \cdot \nabla \rho$ and $\rho \frac{\partial u_z}{\partial z}$ at 1.3 Mm depth is $\lambda_h = 4H_\rho$ at this depth which is consistent with the model in §4.

In the photosphere (*a*) the continuity equation spectrum shows a balance at low wavenumbers between $\mathbf{u} \cdot \nabla \rho$ (*dot-dash* green curve) and $\rho \frac{\partial u_z}{\partial z}$ (*solid* blue curve) while $\rho(\frac{\partial u_x}{\partial x} + \frac{\partial u_y}{\partial y})$ (*dashed* red curve) is much weaker. At high wavenumbers these terms balance such that $\mathbf{u} \cdot \nabla \rho + \rho \frac{\partial u_z}{\partial z} \approx \rho(\frac{\partial u_x}{\partial x} + \frac{\partial u_y}{\partial y})$. In addition, the horizontal derivatives of the density have significant power (i.e. the flows are highly compressible) which violates the assumptions of the model. Thus, the continuity balance in the photosphere is different from deeper layers with significant contribution from the horizontal derivatives to the density gradient ($\mathbf{u} \cdot \nabla \rho$) which balances the increased large-scale vertical motions in the photosphere.

All of this evidence suggests a complicated picture of the low wavenumber vertical velocity

power in the photosphere. For depths greater than 1.3 Mm (as we show in §4) the amplitude of the large-scale flows (both vertical and horizontal) is determined by the imprinting of deep convection (Figure 3.8).

As the scale height decreases towards the photosphere, the large-scale modes of the vertical velocity spectrum decay with height (Figure 3.9). Since the scale height is so small at the surface, these vertical motions are sufficient to match the higher amplitude horizontal flows at the surface (Figure 3.10). In the photosphere, the imprinted power on the vertical flows is much weaker than the power in low wavenumbers of the vertical velocity spectrum. Near the surface, the balance in the continuity equation changes with the increased vertical velocity power approximately equal to the density gradient in the continuity equation (which has significant contributions of the horizontal derivatives of the density, unlike the continuity balance below the photosphere, Figure 3.11).

While the large-scale vertical flows near the surface are balanced by the density gradient, the continuity equation by itself does not determine the flows. The rapid radiative cooling at the surface drives vigorous downflow plumes. The granular upflows do not depend on the deeper convection (which is evident from the independence of the granular flows to the depth of the simulation) and only respond to the pressure gradient and buoyancy forces induced by the downflows (Rast, 1995). Thus, the vertical motions in the photosphere are dominated by the processes in the radiative boundary layer. These processes drive vertical velocities on the scales of supergranulation in the photosphere with much larger amplitude than any imprinted power there.

3.1.5   Wider and Deeper Simulations

While the set of simulations described above provide a valuable examination of supergranular scale convection in the uppermost 20 Mm, the photospheric horizontal velocity spectrum of these simulations (Figure 3.1) suggests that deeper simulations should imprint larger scale motions on the surface. Since the modes of the horizontal velocity spectrum with wavelengths smaller than ~ 1.5 times the depth of the simulation have equal power when comparing shallower simulations to deeper simulations (Table 3.1) and observations of the solar photosphere show that the maximum

wavelength in the supergranular peak is approximately $56 - 75$ Mm (Roudier et al., 2012), we compute a simulation with domain depth increased to 49 Mm to capture these horizontal scales of motion. Based on the length scale (32 Mm) and lifetime (1.8 days, Rieutord & Rincon (2010)) of supergranulation we increase the domain width (197×197 Mm^2) and the amount of relaxed data (5.5 solar days, three times the lifetime of supergranulation) to increase the number of potential supergranules and reduce the noise in our investigations. Assuming that supergranules are approximately 50 Mm in diameter (the maximum of the peak in observations of the photospheric horizontal velocity spectrum Roudier et al., 2012), the width of these simulation domains could include up to ~ 20 supergranules in any snapshot. Assuming a typical supergranular lifetime of 1.8 days (Rieutord & Rincon, 2010), these simulations are approximately 3 times this lifetime, giving a total of ~ 60 potential supergranules. The increased width is especially important when increasing the depth since the scale height of the simulation increases down to 49 Mm depth which increases the diameter of convection and the narrower simulations could have only one downflow at the bottom boundary of such a simulation (see Figure 2.3). These wider simulations also include a larger number of Fourier modes to discriminate between the large-scale motions.

We use the $197 \times 197 \times 49$ Mm^3 hydrodynamic simulation with the resolution reduced to $192 \times 192 \times 64$ km^3 (see §2.2.1 for discussion of the resolution) as the base case or reference simulation for the rest of this thesis. We have done the most extensive testing and comparison with this simulation and it is the widest and deepest simulation that we consider well relaxed (we discuss a 80 Mm deep simulation in §3.1.6.2). We compare the horizontal velocity spectrum from this simulation to the previously presented, narrower 20 Mm deep simulation and a 20 Mm deep simulation with the new reduced resolution and wider domain size. In Figure 3.12 we see that the two 20 Mm deep simulations (blue curve for wider simulation and green *dotted* curve for narrower simulation) have significantly less low wavenumber power than the 49 Mm deep simulation (black curve) but nearly identical high wavenumber power. This adds to the evidence that each depth imprints a specific scale (or range of scales) of motion to the photospheric spectrum, with the convective flows in deeper simulation domains contributing power only to larger scale modes at the surface.

The decreased power in the narrower 20 Mm deep simulation compared to the wider simualtions is due the fact that the geometric depth that we select as the photosphere (the height with the minimum mean optical depth greater than one) is not the depth with the maximum rms velocity (whereas the photosphere in the 197×197 Mm^2 simulations is also the depth with the maximum rms velocity). This is caused by the change in resolution between the two simulations but does not affect the shape of the spectrum.

3.1.6   The Box Mode in the Reference Simulation

While the shallower simulations have enhanced photospheric power that we call a box mode at scales between 1.5 and 2.5 times the domain depth (see §3.1.2), the enhanced power is particularly strong in the $197 \times 197 \times 49$ Mm^3 simulation. The $k/2\pi = 0.01$ Mm^{-1} ($\lambda_h = 98$ Mm, twice the depth of the simulation) mode is consistently the strongest large-scale mode and there is a significant amount of time during the simulation that this mode exceeds the granular peak (see Figure 3.13 compared to typical granulation peak at $\sim 2 \times 10^{18}$). Note that the total power (integrated over all wavenumbers) is dominated by the granulation at all times. The power in the box mode (which may include multiple scales in the Fourier spectrum) is in disagreement with observations of the supergranulation spectrum showing a decline in power for scales larger than 75 Mm (Roudier et al., 2012).

This mode requires careful consideration before including in our analysis and may contribute significant power to neighboring modes which makes them unreliable as well. Thus we examine this mode in detail to determine whether it is different in character from the other modes of the power spectrum, what causes the excess power in box mode and identify which low wavenumber modes are contaminated by this excess power.

3.1.6.1   Time Scale of Box Mode

The box mode in the reference simulation varies over a time scale of several days (Figure 3.13) unlike the smaller scale modes. We use the full width at half maximum (FWHM) of the tempo-
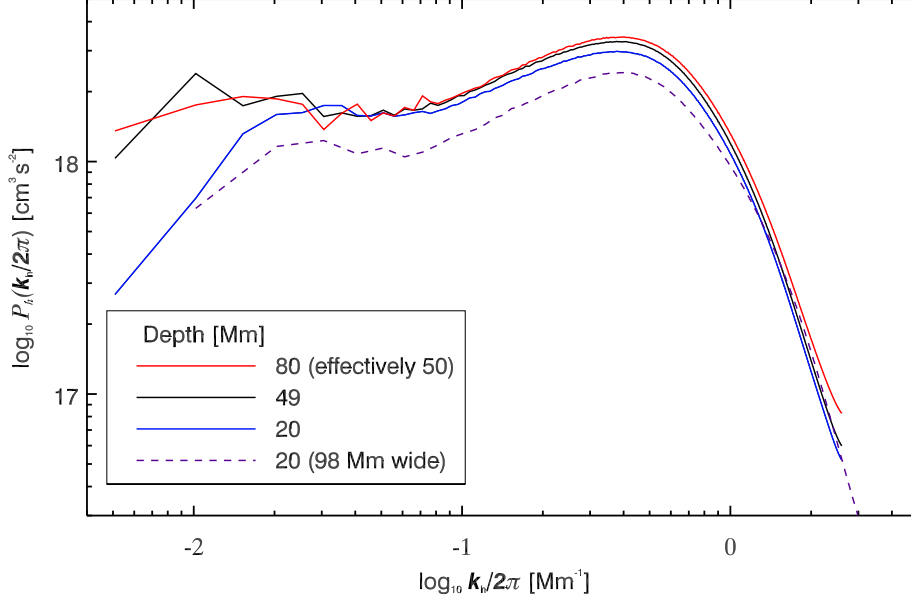
Figure 3.12 The photospheric horizontal velocity spectrum of simulations of different depths. We introduce the reference simulation (*solid* black curve, domain width of 197×197 Mm^2 and 49 Mm depth) and compare it to the previous 20 Mm deep simulation, a new wider 20 Mm deep simulation and an 80 Mm deep simulation that uses an artificial energy flux in the bottom 30 Mm to mimic the radiative energy flux in the bottom of the convection zone. This deeper simulation is effectively a 50 Mm deep convection simulation with 30 Mm devoted to the bottom boundary condition. We find that the shallow simulation has significantly less power in the photosphere and using the artificial flux to improve the boundary reduces the influence of the box mode when compared to the reference simulation. The difference between the narrower and wider 20 Mm deep simulations is due the fact that the geometric depth that we select as the photosphere (the height with the minimum mean optical depth greater than one) is not the depth with the maximum rms velocity (whereas the photosphere in the 197×197 Mm^2 simulations is the depth with maximum rms velocity). This is caused by the change in resolution between the two simulations but does not affect the shape of the spectrum.
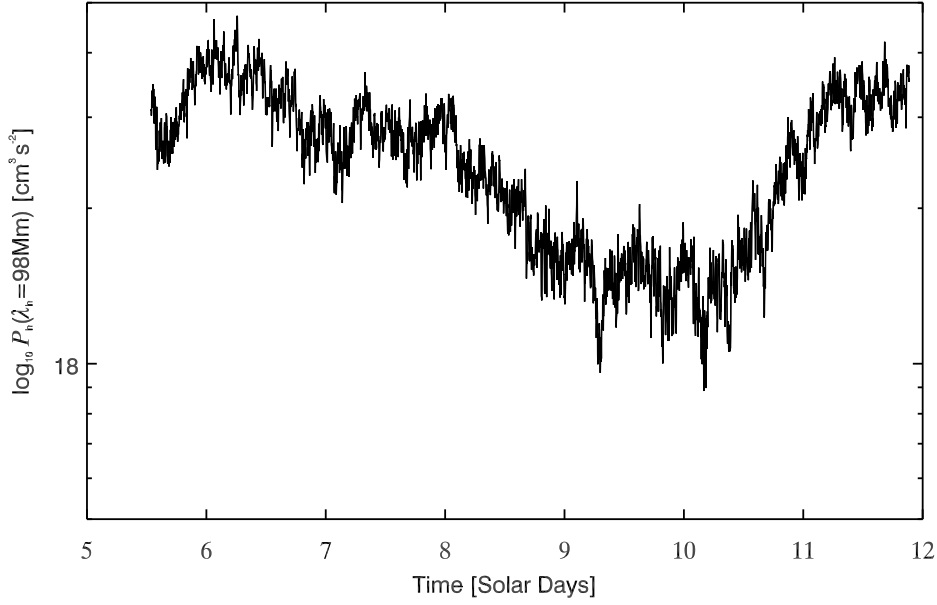
Figure 3.13 The photospheric horizontal velocity power of the $\lambda_h = 98$ Mm box mode of the reference simulation over the 6 days of relaxed time during the simulation. The box mode has very long timescales variations. While we have very limited data, this time series appears to be undergoing the first period of a periodic variation (~ 6 days). It is unclear, however, if continuing this computation would yield different results.

Table 3.2.   The full-width at half max of the temporal autocorrelation of the seven largest modes in the photospheric horizontal velocity power spectrum from the reference simulation.

λ_h [Mm]	FWHM [hrs]
197	22
98	34
66	9.1
49	18
39	19
33	13
28	2.9

Note. — All modes with scales smaller than 30 Mm have a FWHM less than 4 hours.

ral autocorrelation of the large scale modes from the photospheric horizontal velocity spectrum to compare the time scales of different supergranular scale modes in Table 3.2. The temporal autocorrelation of the horizontal velocity power (P_h) correlates a shifted and unshifted time series of P_h (see Figure 3.13 for the time series of the box mode, $\lambda_h = 98$ Mm). The autocorrelation is equal to one with no shift and drops with increasing (positive and negative) time shifts (see Figure 3.15 for an illustration of temporal correlation). For increasing time shifts we remove the edges of the time series from the correlation measurement since the data set is not periodic. The FWHM is defined as the time between negative and positive shifts where the correlation coefficient drops to one half. This is a method that measures the time it takes for the power to become de-correlated.

The FWHM of the box mode (34 hours) is significantly longer than any other supergranular scale mode. Since the time series (Figure 3.13) shows a significant peak at the beginning and end of the available data, this suggests that there may be a periodic signal that has a period of $\sim$ 6 days (though our limited data only observes one period and cannot predict if this would continue). This potential periodic behavior would not be included in the measurement of the de-correlation time since we cut off the edges of the data for increasing time shifts. The largest wavelength $\lambda_h = 197$ Mm mode has longer FWHM correlation time, similar to the $\lambda_h = 98$ Mm mode (especially considering the decreased power in this mode and, as we will discuss in §4, the fact

that the driving scale $4H_\rho = 197$ Mm is outside the simulation domain). The decreased FWHM for modes with wavelength $\lambda_h \leq 66$ Mm, however, suggests that the contamination from the box mode to these smaller modes is minimal.

3.1.6.2   80 Mm Deep Simulation

Finally, we compute an 80 Mm deep simulation using artificial energy flux (see §2.1.6) in the bottom 30 Mm to try to reduce the influence of the bottom boundary condition, which may be directly responsible for the enhanced power in the box mode in these simulations. We use this artificial energy flux to reduce the convective energy flux in this region which reduces the flow amplitudes there. This is similar to the bottom of the convection zone where the divergence of the radiative energy flux heats the flows and reduces the convective energy flux. In the bottom 3 Mm the artificial energy flux is equal to the solar energy flux. Thus we would expect this region to transport zero energy flux via convection (we see this in other simulations in §4.2.3). This simulation is effectively a 50 Mm deep region of solar-like convection with a 30 Mm bottom boundary condition.

Preliminary results from this deeper simulation show 37% less power in the $k/2\pi = 0.01$ Mm^{-1}, $\lambda_h = 98$ Mm mode (Figure 3.12) than the reference simulation which suggests that the increased power in the reference simulation is an artifact of the boundary condition or domain depth. The power in the smaller scale modes, on the other hand, does not show any significant difference from the reference simulation. This provides additional evidence (along with the de-correlation time of each mode) that the box mode power is concentrated for modes with $k/2\pi \leq 0.01$ Mm^{-1} and does not significantly contaminate the smaller scale motions. We thus remove the two largest scale modes from any further analysis but continue to include them in all spectra for completeness.

There are significant limitations of the 80 Mm deep simulation that make further examination unreliable and, consequently, we only use it to test the box mode. The deeper stratification never reached a balanced energy flux since the timescales are longer and would require significant additional computational resources to reach a relaxed state.

3.2   Where do the Supergranular Flows Originate?

We have found that increasing the depth of these simulations increases the low wavenumber horizontal power in the photosphere. This suggests that the low wavenumber horizontal power imprints on the photosphere. We also found that increasing the domain depth of the simulation increases low wavenumber power but does not influence the smaller-scale flows. This suggests that each depth contributes a specific scale (or range of scales) to the power in the photosphere. We still do not know, however, precisely where the supergranular scale ($\sim 20-50$ Mm) flows originate. We try to answer this question by comparing the time and depth variations in the supergranular scale flow pattern and the power in the low wavenumber modes.

3.2.1   Correlating the Flow Pattern

To measure the precise depth where the supergranular scale flows originate we correlate the convective flows at different depths and different times. This can help measure if changes in the flow pattern travels up or down and if they originate at a particular depth. There is significant small scale structure in the full resolution images that causes the flows to de-correlate quickly both in time and with depth so we use a Fourier filter to isolate the supergranular scale flows.

3.2.1.1   The Fourier Filter

To apply the Fourier filter we first compute the two-dimensional FFT of a horizontal slice of the chosen quantity. Since the simulation is horizontally periodic there are no issues with the boundaries. We then select the scales that we want to remove. To exclude the influence of the box mode we remove the two lowest wavenumber modes (see §3.1.6) and then to isolate the supergranular scale flows we remove all scales with $\lambda_h < 20$ Mm. The rest of the scales remain and we refer to them as the unfiltered modes.

To determine the scale of the modes we use the two dimensional horizontal wavenumber $k_h(k_x, k_y) = \sqrt{k_x^2 + k_y^2}$. This is in contrast to the wavenumber we use while plotting the power

spectrum which is a one-dimensional function described in §3.1.1. To prevent ringing we apply a cosine to the fourth power at the high and low wavenumber edges of the unfiltered modes. Finally, the data is inverse Fourier transformed and we take the real part of this new data set as our Fourier filtered data. This process is very similar to smoothing but isolates particular modes which is necessary to exclude the two largest scale modes.
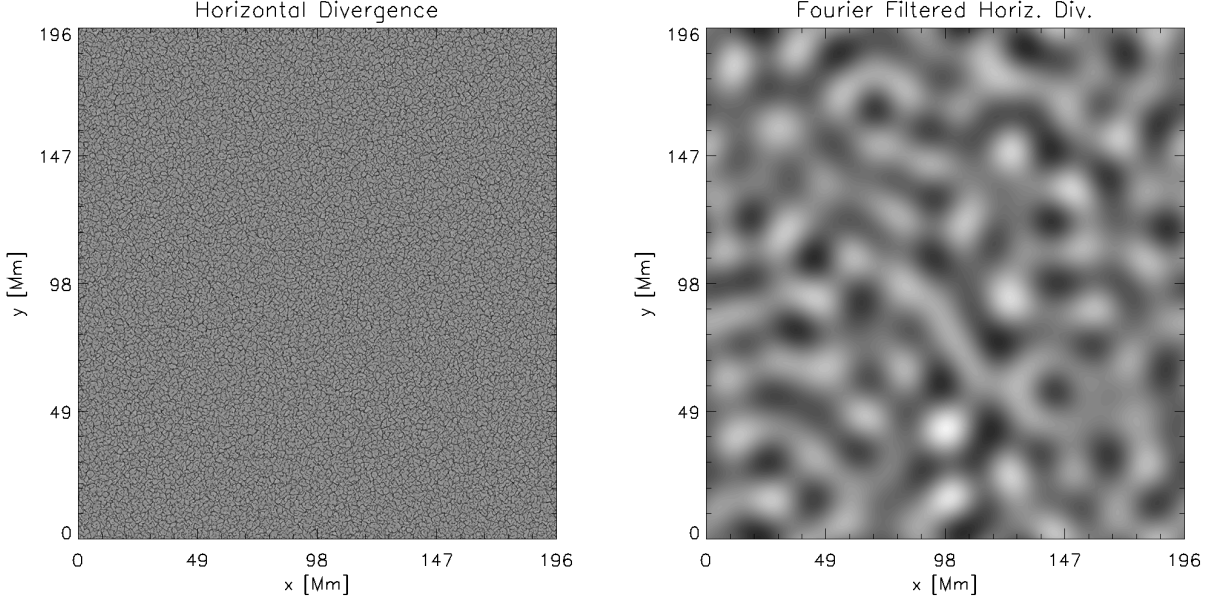
Figure 3.14 The photospheric horizontal divergence (*a*) and Fourier filtered horizontal divergence (*b*) to include all modes with length scales between 20 Mm and 50 Mm. These snapshots are from the reference simulation.

3.2.1.2   The Flow Pattern is Top-Down

Supergranulation is primarily a horizontal feature in the photosphere. To incorporate both components of the horizontal flow we use the horizontal divergence $\nabla_h \cdot \mathbf{u} = \frac{\partial u_x}{\partial x} + \frac{\partial u_y}{\partial y}$ which is the best measure of the flow that advects the magnetic vertices that help outline and identify solar supergranules. Near the surface the horizontal divergence is strongly correlated with the vertical velocity (i.e. horizontal flows converge at downflows and diverge at upflows with correlation coefficient ~ 0.9) making it appear to be a similarly suitable variable to represent the supergranular flows. As we have seen, however, the vertical flows in the photosphere are dominated by granular

convection and contain very little information about the supergranular scale flows (§3.1.4.2). Thus the horizontal divergence of the horizontal flows (which, in spectral space, is horizontal velocity spectrum multiplied by k_h^2 and, consequently, includes the supergranular scale flows and their depth dependence as discussed in §3.1.2.1) is the best choice for measuring supergranular scale convection.

To measure the originating depth of the supergranular flow pattern, we correlate a single shallower slice with slices from deeper flows that span several hours. The minimum time separation between slices is approximately 130 seconds, so this determines the minimum temporal variations that we can resolve. Since the deep flows have increased lifetime, we increase the total time spanned by our shift for increasing depth. For each depth we repeat this process for 25 separate instances of this correlation measurement across the full 5.5 days of relaxed data. We have made the same measurement with reversed roles for the two depths, i.e. using a single deeper slice and correlating with shallower slices at different times, and find that the two methods give the same results.

We show the correlation of the Fourier filtered horizontal divergence as a function of time between the photosphere and 3.392 Mm depth in Figure 3.15. Since the lower slice is being shifted the negative time means that it is an earlier time at 3.392 Mm depth compared to the photosphere and positive means that it is later. The *solid* (black) curve shows the average of 25 measurements. The maximum correlation (with a correlation coefficient of approximately 0.87) occurs roughly 40 minutes later than the photosphere. In other words the supergranular scale flows at 3.392 Mm are most strongly correlated with the photosphere after waiting approximately 40 minutes.

The *dot* (blue), *dash* (green), and *dot-dash* (red) curves show a sample of extreme individual measurements (including the earliest and latest maximum correlation time) of the correlation between these two depths. Even for the earliest maximum correlation time (*dot-dash* (red) curve), it is clearly at a later time than the photosphere. This pattern is consistent: the maximum correlation time is always later for deeper flows. This suggests that the horizontal divergence below the surface is always reacting to changes in the flow pattern up above. This is an apparent contradiction with the results from §3.1, which we revisit at the end of this section.
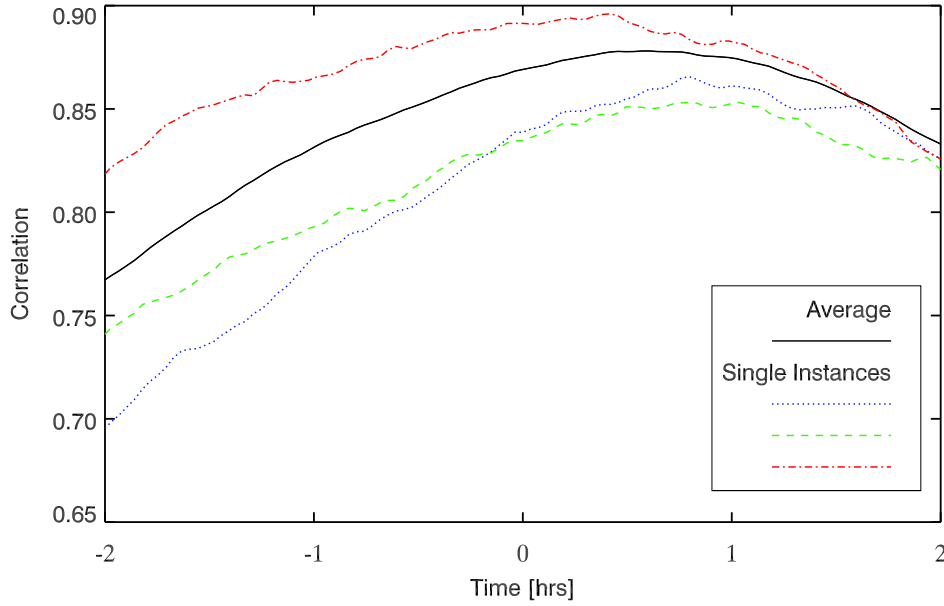
Figure 3.15 The correlation of the Fourier filtered horizontal divergence as a function of time between the photosphere and 3.392 Mm depth. The Fourier filtering removes all modes smaller than $\lambda_h = 20$ Mm and the two lowest wavenumber modes (which includes the box mode). This shows an average maximum correlation time that is at later times below the photosphere which suggests that the supergranular scale photospheric horizontal divergence pattern travels down and influences the deeper layers.

3.2.1.3 Time Scale of Pattern Changes

Beyond using this temporal correlation to measure an originating depth of the supergranular flow pattern, we can determine the speed at which these changes are occurring by using the maximum correlation between each depth. Correlating the horizontal divergence from horizontal slices for all available depths gives us nine measures of this time scale between depths. Since the local maximum in any correlation is very noisy (see Figure 3.15), we fit a second degree polynomial to the correlation time series and find the maximum of this polynomial. We use this maximum correlation across all 25 independent measurements of the maximum correlation time. This means that the shallower data is well separated in time but the deeper flow time scales are so long that there is some overlap in the data used for the correlation. We correlate the photospheric flow with the horizontal slice that is closest to the photosphere and shift in time to determine the maximum correlation time between these two depths (3.392 Mm, see Figure 3.15). We then repeat this process by correlating each new depth with the nearest depth below and continue this process down to correlating the two lowest depths (where the number of depths is limited by the simulation data output). This allows us to measure the maximum correlation time between each depth from the photosphere down to 40 Mm near the bottom boundary (at 49 Mm).

In Figure 3.16 we plot the mean of the measured maximum correlation times from the photosphere down to each depth (*diamonds*) with one standard deviation error bars. These error bars estimate the error between each slice but the successive errors from the photosphere down would be additive (which we do not show here). We over-plot an advective timescale computed by integrating the mean and root-mean-square (rms) downflow velocity from the photosphere down to the bottom, i.e. $t_z = t_{z+dz} + dt_z$ where $dt_z = dz/|\langle u_{downflow} \rangle_z|$ for the mean downflow velocity or $dt_z = dz/\sqrt{\langle u^2_{downflow} \rangle_z}$ for the rms downflow velocity and $u_{downflow}$ includes all $u_z < 0$ at each height. These two estimates of the advective timescale agree quite well with the correlation time of the large-scale horizontal divergence. This suggests that the convective pattern is dominated by the downflows and responds to changes higher in the atmosphere on a timescale that is consistent
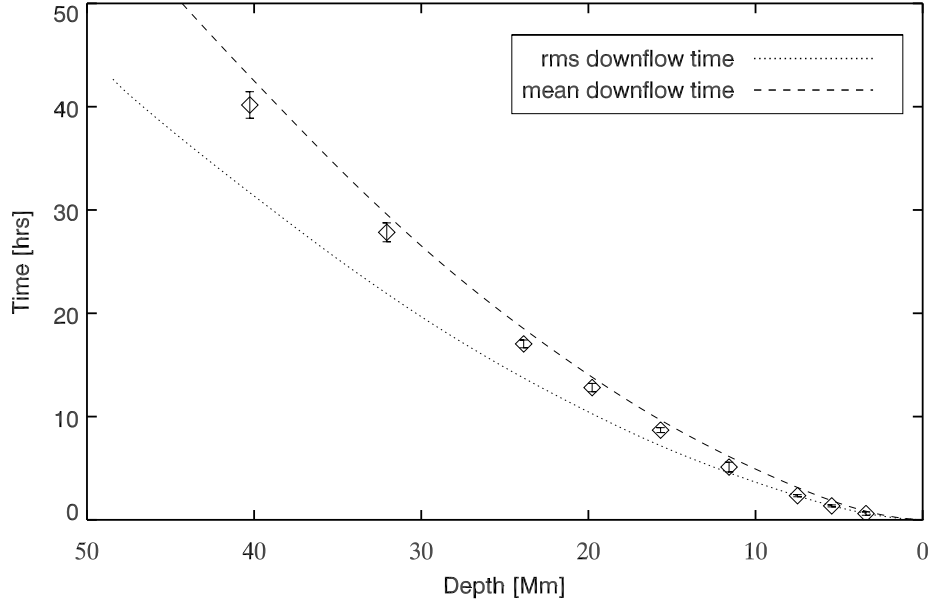
Figure 3.16 The maximum correlation time between select depths (which is limited to the data output of the reference simulation) of the Fourier filtered horizontal divergence compared to the photosphere (i.e. the time it takes for the pattern to travel down from the photosphere). Error bars show one standard deviation from the mean of the maximum correlation time. The *dashed* and *dotted* curve show the mean and rms downflow time (respectively) integrated from the photosphere down. The travel time of the supergranular scale horizontal divergence pattern is consistent with the travel time of downflows.

with the downflows traveling between those depths.

3.2.2 Correlating The Horizontal Velocity Power

Examining the correlations of the horizontal divergence finds a top-down supergranular scale pattern, but our primary method for identifying supergranulation is the horizontal velocity spectrum. By computing similar correlations between depths of the horizontal velocity spectrum we can determine if temporal variations in the spectrum of supergranulation imprint from below (as we saw in §3.1) or the travels down as we saw in the correlations of the horizontal divergence. We show the time series of one of the supergranular scale modes ($\lambda_h = 33$ Mm) at different depths in Figure 3.17.
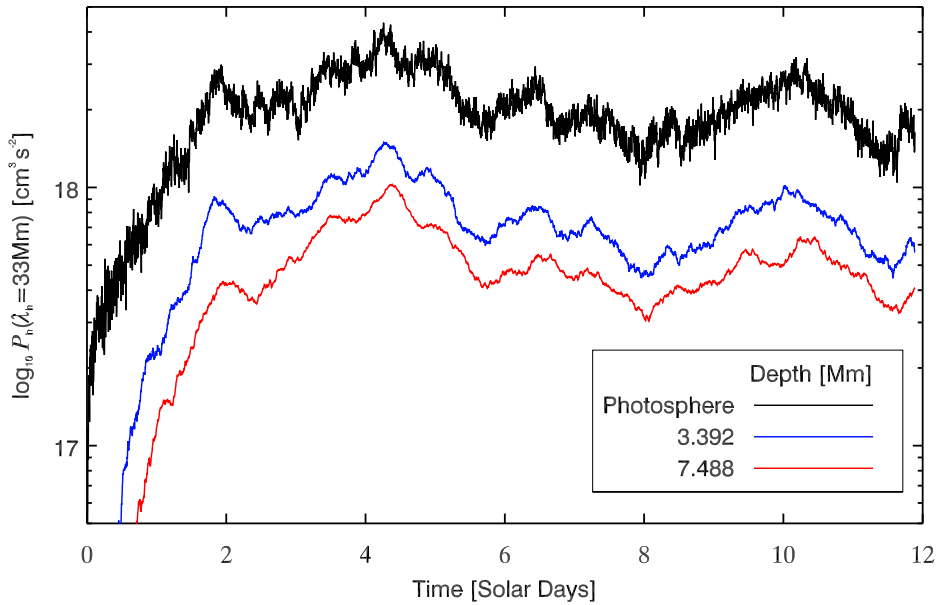
Figure 3.17 The time series of the power in the $\lambda_h = 33$ Mm mode at three depths: photosphere (black), 3.392 Mm (red), and 7.488 Mm (blue). At early times the power grows slowly in the supergranular scale first in the photosphere and deeper down at later times. The variation of the power of this mode is also visibly (very slightly) later for the deeper flows.

The simulation begins with zero velocity (see §2.2) which allows us to examine the initial growth in the power of this mode. The power in the photosphere (black curve) grows more quickly than the power in the deeper layers. This is consistent for all supergranular scale modes at all

depths: the initial power grows in upper layers before deeper layers of the atmosphere. This suggests that the initial increase in power is top-down. This is an apparent contradiction with the evidence in §3.1 that the presence (and amplitude) of the deep flows determines the power in the photosphere.

The variations in the power after the simulation has relaxed (the relaxed data is the last 5.5 days of simulation time) are also very similar for each of the depths shown. We examine the variations in the power in the supergranular modes (20 Mm $< \lambda_h <$ 50 Mm, to match the Fourier filter of the horizontal divergence in §3.2.1) by correlating the power across depths. Similar to the correlations of the flow pattern, we correlate the power between depths while varying the temporal shift. These correlations also show that the temporal fluctuations in horizontal power travel down, with deeper power following variations of the power in upper layers after some period of travel time (similar to Figure 3.16).

We added a computation of the velocity spectrum within the MURaM code which allows us to compute and output the power for every other depth with high time cadence. With this increased data (as compared to the flow pattern correlations above), we determine the most accurate maximum correlation time between depths by correlating each depth with the 10 depths above and below and then average those 30 maximum correlation times. This method provides an improved measure of the maximum correlation time with a standard deviation that is too small to plot (typically < 0.01 hrs).

We show the maximum correlation time of the fluctuations in supergranular scale power in the horizontal velocity spectrum from the photosphere to each depth (*solid* curve) in Figure 3.2.2. This compares quite well to the rms downflow time (same as in Figure 3.16) until depths greater than 25 Mm at which point the horizontal power variation travels somewhat faster than the rms downflow speed (though slower than the fastest downflow velocities). This confirms that both the flow pattern and the supergranular scale velocity power are determined from the top-down on an advective timescale.
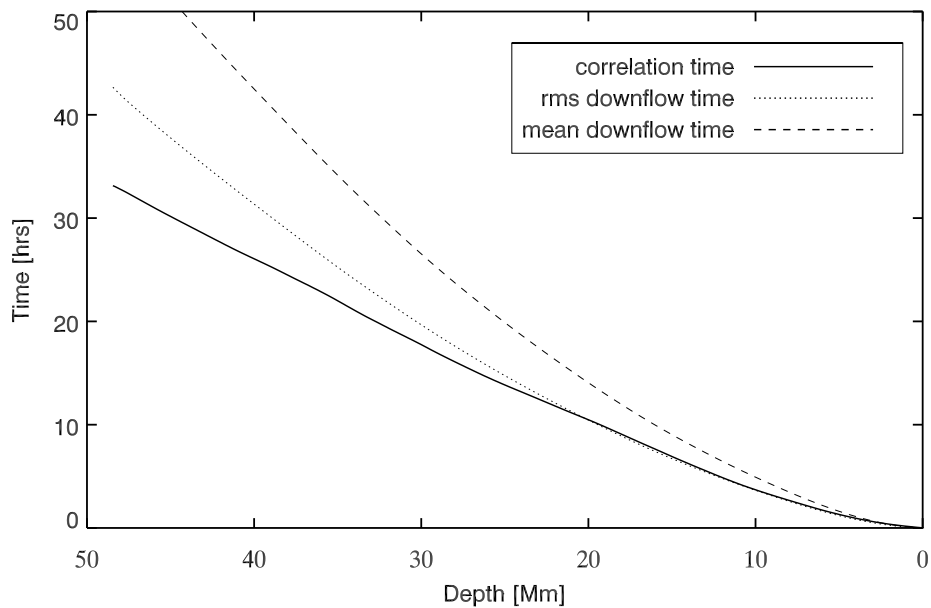
Figure 3.18 The maximum correlation time of the power in the supergranular scale modes of the horizontal velocity spectrum. To compute the maximum correlation time at each depth, we compute the maximum correlation time between the supergranular scale modes for the nearest 10 spectra above and below each depth and take the mean correlation time from all these nearest depths. The standard deviation of this method is too small to show in error bars. The *dashed* and *dotted* curve show the mean and rms downflow time (respectively) integrated from the photosphere down. The supergranular scale horizontal velocity spectrum power has shorter correlation time and thus travels slightly faster than either of these measures.

3.3   Conclusion

In this chapter we have examined the fundamental question: do supergranular flows originate in or near the photosphere (top-down) or do they imprint from below (bottom-up)?

We know that the length scale of flows increase with depth due to the increasing scale height and recent observations have linked the length scale of the supergranules to the depth at which they originate (Hathaway et al., 2010; Hathaway, 2012a). Comparing simulations with domain depths ranging from 49 Mm to 2 Mm, we find that the low wavenumber horizontal velocity power in the photosphere depends both on the presence and amplitude of the larger scale flows deep in the domain. Furthermore, we find that each successively deeper simulation adds photospheric power on larger scales (and is consistent with the shallower simulations for all smaller scale modes). This suggests that each depth contributes power to horizontal motions in the photosphere at a specific length scale (or range of scales) with the contributed scales increasing with depth. This helps motivate the model that we introduce in §4.

Curiously, while the low wavenumber vertical velocity power below the surface (measured at a depth of 1.3 Mm) also depend on the simulation domain depth, the low wavenumber vertical power in the photosphere does not. Based on a relationship taken from our model in §4, the amplitude of the low wavenumber vertical flows required to drive the horizontal motions in the photosphere are much weaker than the power in the photospheric vertical velocity spectrum. We also find that the dominant balances of the continuity equation change between the photosphere and 1.3 Mm depth with the density gradient (including horizontal derivatives of the density which are weak below the photosphere) balancing the increased power in the low wavenumber vertical flows in the photosphere. While the large-scale vertical flows in the photosphere are balanced by the density gradient, the continuity equation by itself does not determine the flows. The vertical motions in the photosphere are dominated by the processes in the radiative boundary layer. These processes drive vertical velocities on the scales of supergranulation in the photosphere with much larger amplitude than any imprinted power there.

Table 3.3.   Evidence for supergranulation that originates near the surface (Top Down) or at depth (Bottom Up).

Bottom Up	Top Down
Low wavenumber horizontal flow amplitudes in the photosphere depend on the simulation domain depth.	Convective pattern is dominated by photospheric downflows.
Deeper flows increase the power in larger scale motions in the photosphere.	Fluctuations in the horizontal velocity spectrum are dominated by photospheric downflows.
The balance of the continuity equation determines the spectrum of flows at each depth.	

In order to pinpoint the specific depth at which the supergranular scale in the photosphere originates we correlate both the horizontal divergence pattern and temporal fluctuations of the horizontal velocity spectrum between depths. Both of these measures find that any temporal variations originate in the photosphere and travel down on the time scale of advection via downflows. This suggests that the downflows (with greater momentum than the upflows) dominate both the convective pattern and the variations in the low wavenumber horizontal power.

This leaves us with an apparent contradiction. We have evidence that supports a surface origin for supergranulation (top down) and that the deep flows that imprint on the surface (bottom up) which we outline in Table 3.3. To reconcile this conflicting evidence, we consider the role of the continuity equation in generating these flows. The balance of terms in the continuity equation determines the flow spectrum at depth. Thus, the large-scale flows deep in the convection zone have non-zero $\nabla \cdot (\rho \mathbf{u})$ which creates pressure perturbations on these scales. These pressure perturbations travel at the sound speed and reach the photosphere on timescales much shorter than we examine in our correlations (the mean sound crossing time from the bottom of the 49 Mm deep reference simulation is ~ 21 minutes). Thus, the imprinting may be caused by positive pressure perturbations of the upflows at all depths which drive large-scale divergence in the photosphere. Additional work, however, must be done to confirm this hypothesis by examining the relationship between deep flows

and the pressure in the photosphere.

Chapter 4

The Role of Subsurface Convection: Modeling the Spectrum of Supergranular and Larger Scale Flows

4.1   Lord et al. (2014)

Here we present Lord et al. (2014) in its entirety. This paper introduces a model which tries to address the question of where the large-scale photospheric flows originate. This model also identifies which features of the simulation are most important to the spectrum of the surface flows.

The contributions of the different authors are detailed here. I collaborated with Robert Cameron on creating the initial model, the conversion between horizontal and vertical flows, and the driving scale which separates flows that are locally driven and flows that are decaying from below. I then examined the continuity equation in detail to determine the final functional form of these equations with help from Mark Rast and validated our assumptions in both the stratified and homogeneous simulations. I conducted the experiments to determine the validity of the spectrum produced by the two-component model. I computed new equations of state with help from Matthias Rempel, a mixing length model that was validated by comparing with the model S atmosphere, and new three dimensional simulations to examine the effect of helium ionization. Finally, I ran the simulation with the artificial energy flux and, using the coherent structure tracking (CST) algorithm from Thierry Roudier, I compared the power spectra by applying the CST algorithm to both HMI observations and the MURaM simulations with help from Robert Cameron. Matthias Rempel gave advice throughout and helped set up the simulations. Mark Rast also gave advice throughout, suggesting several tests of the model, helping significantly with the editing, and helping

to work through the mathematics.

4.1.1 Introduction

Solar supergranulation is observed as horizontal divergent flow within magnetic network boundaries (Leighton et al., 1962; Simon & Leighton, 1964), either by Doppler imaging away from disk center (Hathaway et al., 2000) or by correlation (November & Simon, 1988; DeRosa & Toomre, 2004; Meunier et al., 2007) or structure tracking near disk center (Rouder et al., 1999; Roudier et al., 2012). The power spectrum of the horizontal motions shows a characteristic peak at horizontal scales ranging from approximately 20 Mm to 50 Mm, and the motions at these scales are identified as supergranulation. There is a dramatic drop in spectral power for scales larger than supergranulation with very weak giant cell flows only recently confirmed by observations (Hathaway et al., 2013).

The physical origin of the supergranular length scale remains a mystery. Suggestions range from possible dynamical effects of the second ionization of Helium (Leighton et al., 1962; Simon & Leighton, 1964; November et al., 1981) to spatial correlation or self organization of granular flows (Rieutord et al., 2000; Rast, 2003; Crouch et al., 2007). Radiative hydrodynamic simulations of solar surface convection fail to yield clear evidence for supergranulation, even in very large domains spanning up to 96 Mm by 96 Mm in width and 20 Mm in depth (Stein et al., 2009; Ustyugov, 2010). Recent simulations in even larger domains of up to $196 \times 196 \times 49$ Mm^3 suggest that the domain depth, and the consequent stratification captured by the simulation, may be as critical as domain width (Lord, 2014). Based on these broad and deep simulations of solar surface convection we have developed a model of the convective velocity spectrum which reproduces the simulation spectrum and provides insight into how the deep convective flows help build the observed photospheric spectrum.

The model assumes that, at each depth, vertical motions are driven at scales four times the local density scale height. The amplitudes of smaller scale motions is taken to be consistent with the spectrum of unstratified and incompressible turbulence. Larger scale vertical motions imprint from below with reduced amplitude and are observed as primarily horizontal flows at the

surface (Sprout et al., 1990). In other words, modes with wavelengths smaller than the integral (driving) scale are assumed to have amplitudes that follow the spectrum of isotropic homogeneous turbulence given by Kolmogorov (1941), while vertical motions of scales larger than the integral scale are assumed to decay with height from their driving depth. The integrated power of the vertical velocity is determined using a mixing length model of energy transport, and the spectrum of horizontal velocity follows from the vertical velocity spectrum at each depth by mass continuity.

Key scalings in the model are verified using the radiative hydrodynamic simulations of Lord (2014), and the simplified model spectra agree with those of the simulations over a wide range of wavenumbers. They also match observations at supergranular scales. However, power at lower wavenumbers, in both the model and radiative hydrodynamic simulation spectra, significantly exceeds that observed. This suggests either that large scale flows deep in the solar convection zone are weaker than predicted by convection simulations or that rotation and the consequent near surface shear layer, not captured in our studies, plays a decisive role in masking large scale motions. We note however, that recent helioseismic observations (Hanasoge et al., 2010, 2012) and global scale numerical simulations, with and without a near surface shear layer (Hotta, 2014a), also suggest that large scale convection in the Sun is weaker than numerical models predict. It is possible that magnetic fields play a role, that convection in the Sun is fundamentally magnetized. Preliminary studies of radiative magnetohydrodynamic simulations (Lord, 2014) in very large domains show some suppression of low wavenumber power in highly magnetized solutions, though the mechanism is still under investigation and the effect so far appears insufficient to explain solar observations. In this paper we focus on strictly hydrodynamic effects to elucidate the important role of stratification and the secondary influence of ionization in shaping the photospheric horizontal velocity power spectrum at supergranular and larger scales.

In §4.1.2 we describe the simplified two-component continuity balance on which our model is based, and transform the balance equations into relationships between the vertical and horizontal velocity spectra. We use these relationships to identify the driving scale of the modes and demonstrate that these relationships hold in fully compressible hydrodynamic simulations. In §4.1.3 we

describe the construction of the mixing length atmosphere which sets the amplitude of the model spectrum, identify two possible decay rates for the large scale modes, and explicitly outline the model steps employed in the construction of the surface horizontal velocity spectrum. In §4.1.4 we test the components of the model spectrum against the full radiative hydrodynamic solutions and verify that the model can reproduce the shape of the spectrum produced by those simulations. In §4.1.5 we discuss the results of the model spectrum, focusing on the spectrum at supergranular scales and larger. We show, using feature tracking, that for scales larger than supergranulation the radiative hydrodynamic spectra can only match the observations when the convective forcing is removed entirely below 10 Mm. We conclude, in §4.1.6 with a discussion of the broader implications of the weak low wavenumber amplitudes to our understanding of deep solar convection.

4.1.2   Mass continuity and the effects of stratification

We use the equation of mass continuity to examine how stratification affects flow velocity. Explicitly,

$$\frac{\partial \rho}{\partial t} + \nabla \cdot (\rho \mathbf{u}) = \frac{\partial \rho}{\partial t} + \rho(\frac{\partial \mathrm{u}_x}{\partial x} + \frac{\partial \mathrm{u}_y}{\partial y} + \frac{\partial \mathrm{u}_z}{\partial z}) + \mathrm{u}_x \frac{\partial \rho}{\partial x} + \mathrm{u}_y \frac{\partial \rho}{\partial y} + \mathrm{u}_z \frac{\partial \rho}{\partial z} = 0 \qquad (4.1)$$

where ρ is the mass density, $\mathbf{u}$ is the fluid velocity, and subscripts x and y and z indicate components in Cartesian coordinates. We ignore curvature, and take gravity, and thus increasing density in the stratified domain, to be in the positive z direction.

In the solar convection zone we can make a number of further simplifying assumptions. Since we are looking for the statistically steady velocity amplitudes over time periods much longer than the convective turnover time, we take $\frac{\partial \rho}{\partial t} \to 0$. Moreover, we know from hydrodynamic simulations that the horizontal gradients of the density are small compared to the vertical stratification below the first few hundred kilometers beneath the solar photosphere, so $\mathrm{u}_x \frac{\partial \rho}{\partial x}$ and $\mathrm{u}_y \frac{\partial \rho}{\partial y}$ are ignored. Together these assumptions yield an anelastic-like continuity equation (Gough, 1969) that maintains the steady state stratification by balancing the vertical advection of mass with the divergence of

the flow,

$$\nabla_h \cdot \mathbf{u}_h = -\frac{\partial \mathbf{u}_z}{\partial z} - \frac{\mathbf{u}_z}{H_\rho} \ , \tag{4.2}$$

where $\mathbf{u}_h = \mathbf{u}_x \hat{i} + \mathbf{u}_y \hat{j}$, $\nabla_h = \hat{i}\frac{\partial}{\partial x} + \hat{j}\frac{\partial}{\partial y}$, and $H_\rho = \left(\frac{1}{\rho}\frac{d\rho}{dz}\right)^{-1}$ is the density scale height.

This form of the continuity equation suggests two possible flow regimes: for $\frac{\partial \mathbf{u}_z}{\partial z} \gg \frac{\mathbf{u}_z}{H_\rho}$ the motions may be considered nearly divergenceless and isotropic whereas for $\frac{\partial \mathbf{u}_z}{\partial z} \ll \frac{\mathbf{u}_z}{H_\rho}$ the stratification is most important in determining the flow component speeds. Heuristically, small scale overturning eddies would fall in the first regime, while eddies larger than the local scale height would fall in the second, with the largest isotropic eddies increasing in size with depth as the density scale height increases. Thus we expect the dominant balance in Equation 4.2 to depend on the length scale of the flow and depth within the convection zone.

Maintaining the mean stratification in a statistically-steady stratified convective flow requires that most of the mass must overturn as the fluid rises through one scale height; over each scale height the density of rising fluid must decrease by a factor of $1/e$, implying that $1 - 1/e$ of the mass must overturn. Similarly, downwelling fluid must entrain mass at this rate. If the flow geometry is approximated by vertical cylinders of radius r and height H_ρ, then for all of the mass to overturn within one scale height, $2\pi r H_\rho \rho \mathbf{u}_h = \pi r^2 \rho \mathbf{u}_z$. This yields a characteristic horizontal scale for the motions (Nordlund et al., 2009)

$$r = 2\alpha H_\rho \frac{\mathbf{u}_h}{|\mathbf{u}_z|} \ , \tag{4.3}$$

where α is a factor of order 1 and includes a weak dependence on geometry and the $1/e$ fraction of the mass that does not overturn. We take this length scale to be the crossover between those motions that feel the stratification and those that do not. We demonstrate in the next section that such a crossover is seen in the spectra of three-dimensional simulations. This length scale is also the integral scale of the velocity spectrum in solar-like hydrodynamic simulations (Stein et al., 2009), and henceforth we refer to it as the driving or integral scale of the convection.

4.1.2.1 The spectra of horizontal and vertical motions

Equation 4.2 can be written as

$$i\mathbf{k}_h \cdot \tilde{\mathbf{u}}_h = -\frac{\partial \tilde{\mathrm{u}}_z}{\partial z} - \frac{\tilde{\mathrm{u}}_z}{H_\rho} \ , \tag{4.4}$$

where the overlying tildes indicate the complex Fourier amplitudes resulting from a two-dimensional horizontal Fourier transform at each depth z and $\mathbf{k}_h$ is the horizontal mode wavevector. By squaring both sides and taking two limits of Equation 4.4 we can define a relationship between the power in horizontal and vertical motions without directly solving for the phases of the modes. For modes smaller than the integral scale we take the limit $\frac{\partial \tilde{\mathrm{u}}_z}{\partial z} \gg \frac{\tilde{\mathrm{u}}_z}{H_\rho}$, while for larger scale modes we take $\frac{\partial \tilde{\mathrm{u}}_z}{\partial z} \ll \frac{\tilde{\mathrm{u}}_z}{H_\rho}$. Even in these limits, defining the relationship between vertical and horizontal power is difficult for two reasons: when squaring Equation 4.4, the cross terms between horizontal modes $\tilde{\mathrm{u}}_x$ and $\tilde{\mathrm{u}}_y$ on the left side do not have an a priori known form, and the vertical derivative on the right hand side cannot be simply related to the wavenumber of the horizontal Fourier modes.

To proceed we make simplifying assumptions which we have empirically verified to hold in stratified (Lord, 2014) and incompressible turbulence simulations (Mininni et al., 2006) as appropriate. At small scales the flow is nearly isotropic and homogeneous, with unstratified homogeneous and isotropic turbulence simulations showing that $k_x^2 \tilde{\mathrm{u}}_x \tilde{\mathrm{u}}_x^* \approx k_y^2 \tilde{\mathrm{u}}_y \tilde{\mathrm{u}}_y^* \approx \frac{\partial \tilde{\mathrm{u}}_z}{\partial z} \frac{\partial \tilde{\mathrm{u}}_z^*}{\partial z}$, which together with incompressibility yields $\frac{\partial \tilde{\mathrm{u}}_z}{\partial z} \frac{\partial \tilde{\mathrm{u}}_z^*}{\partial z} \approx \frac{1}{4} k_h^2 \tilde{\mathbf{u}}_h \cdot \tilde{\mathbf{u}}_h^*$. The simulations also suggest a relationship between the vertical and horizontal gradients, $\frac{\partial \tilde{\mathrm{u}}_z}{\partial z} \frac{\partial \tilde{\mathrm{u}}_z^*}{\partial z} \approx \frac{1}{4} k_h^2 \tilde{\mathrm{u}}_z \tilde{\mathrm{u}}_z^*$, and together these yield a relationship between horizontal and vertical power:

$$\tilde{\mathbf{u}}_h \cdot \tilde{\mathbf{u}}_h^* = \tilde{\mathrm{u}}_z \tilde{\mathrm{u}}_z^* \ , \tag{4.5}$$

where $\tilde{\mathbf{u}}_h \cdot \tilde{\mathbf{u}}_h^* = \tilde{\mathrm{u}}_x \tilde{\mathrm{u}}_x^* + \tilde{\mathrm{u}}_y \tilde{\mathrm{u}}_y^*$. At large scales, the cross terms, which result from squaring the left hand side of Equation 4.4, are measured in stratified simulations to be small and are set to zero. This implies that $k_x^2 \tilde{\mathrm{u}}_x \tilde{\mathrm{u}}_x^* + k_y^2 \tilde{\mathrm{u}}_y \tilde{\mathrm{u}}_y^* \approx \tilde{\mathrm{u}}_z \tilde{\mathrm{u}}_z^* / H_\rho^2$, and the horizontal and vertical power in the modes are related as

$$\tilde{\mathbf{u}}_h \cdot \tilde{\mathbf{u}}_h^* = \frac{2}{\mathrm{k}_h^2 H_\rho^2} \tilde{\mathrm{u}}_z \tilde{\mathrm{u}}_z^* \ , \tag{4.6}$$

where $k_h^2 = k_x^2 + k_y^2$.

Finally, without approximation, the driving scale that separates these two behaviors (Equation 4.3) can be rewritten as

$$\lambda_h = 4\alpha H_\rho \frac{u_h}{|u_z|} \ , \tag{4.7}$$

where $\lambda_h = 2\pi/k_h$ is the wavelength of the Fourier mode corresponding to a convective cell diameter of $d = 2r$. By taking α and $u_h/u_z \approx 1$ we approximate the driving scale as $\lambda_h \approx 4H_\rho$. It is on the basis of these relationships (Equation 4.5 at small scales and Equation 4.6 at large scales with the crossover between them given by the driving scale $\lambda_h = 4H_\rho$ at each depth) that we calculate the horizontal velocity power spectrum from the vertical.

Analysis of large scale radiative hydrodynamic simulations of solar convection (for details, see §4.1.5.1 and Lord (2014)) helps validate these relationships. Below 1.3 Mm beneath the photosphere, the mass continuity in the simulations matches the anelastic balance (Equations 4.2 and 4.4) to within a few percent. Near the photosphere this balance breaks down because of fluid compressibility, particularly at high wavenumber. We thus restrict our model analysis to depths below 1.3 Mm. At low wavenumbers, p-mode contributions can still be important at the shallowest depths. We remove these when comparing the numerical simulations to the model by averaging the simulation velocities over 30 minutes. This averaging also reduces the amplitude of the high wavenumber convective motions, but preserves the relationships between horizontal and vertical flows of Equations 4.5 and 4.6. This is illustrated by Figure 4.1, in which the horizontal velocity spectra measured at several depths in a solar-like radiative hydrodynamic simulation are plotted. Overplotted are the horizontal velocity spectrum deduced from the vertical velocity spectra of the simulation at the same depths using Equations 4.5 and 4.6 (*dotted* and *dashed* line-styles respectively). The two component reconstruction of the horizontal velocity spectrum from the vertical reproduces the shape and amplitude of the actual spectrum quite well. Moreover, the driving scale estimate of $4H_\rho$ is in good agreement with the crossover between the two behaviors. Plotted in Figure 4.2 is the crossover wavenumber as a function of depth (defined as smallest wavenumber in
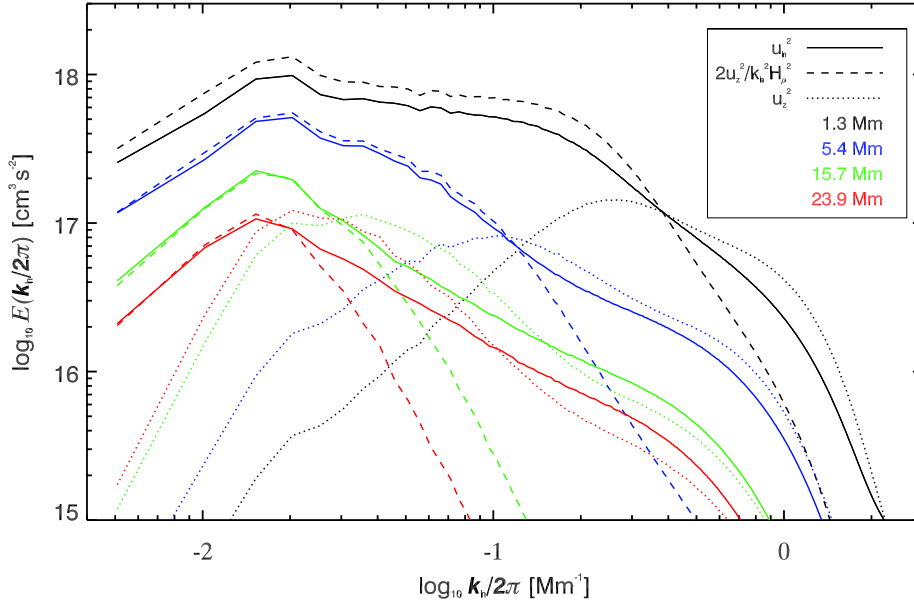
Figure 4.1 The horizontal velocity power spectra (*solid* curves) from hydrodynamic simulations using a Saha equation of state (see §4.1.3.1 and §4.1.5.2 for details) at four depths: black 1.3 Mm, blue 5.4 Mm, green 15.7 Mm, and red 23.9 Mm below the photosphere. The *dashed* and *dotted* curves show the horizontal velocity spectra deduced from the vertical velocity based on Equations 4.5 and 4.6 respectively. The velocity is averaged over 30 minutes before computing these spectra to remove p-modes. This averaging also reduces power in high wavenumber convective motions.

the simulations for which the balance in Equation 4.6 begins to fail, meaning that the difference between the two terms at neighboring larger horizontal wavenumbers is increasingly large). For comparison, $4H_\rho$ is overplotted in *red*. They are in good agreement. Note that the discontinuities in the measured values are due to the finite spectral resolution of the simulation; many depths in the simulation appear to have the same crossover scale because there are no modes that can discriminate between them.

4.1.3   Model components

Having verified the two component continuity balance, we construct the horizontal spectrum of horizontal motions from the horizontal spectrum of the vertical velocity using the relationships derived. To do this we must model the vertical velocity spectrum at each depth. This depends on the driving (integral) scale at that depth, the spectrum of the small scale motions, and the decay rate of the large scale modes that are driven below the height of consideration. We have already defined the driving scale as $4H_\rho$, and we choose the spectrum of the higher wavenumber motions to follow a turbulent cascade with a $k^{-5/3}$ Kolmogorov slope. The Kolmogorov spectrum does not match the spectrum of motions in the hydrodynamic simulations exactly, but we use it in the model for simplicity and in place of an ad hoc fit to the simulations, which themselves may not match the spectrum of solar motions (see §4.1.4). The integrated spectral power is determined using the rms velocity of a mixing length model of solar convection (§4.1.3.1). Thus the amplitudes of modes with scales larger than the driving scale are determined by their decay with height from the depth at which they were last driven (§4.1.3.2), and the remaining power (the rms velocity squared minus the power in large scale modes) is distributed among all modes at the driving scale or smaller according to a Kolmogorov distribution.

4.1.3.1   Mixing length transport by small scale modes

We employ a simplified hydrostatic mixing length atmosphere of pure hydrogen and helium in Saha equilibrium, integrating the mixing length equations (Prandtl, 1925; Böhm-Vitense, 1958)
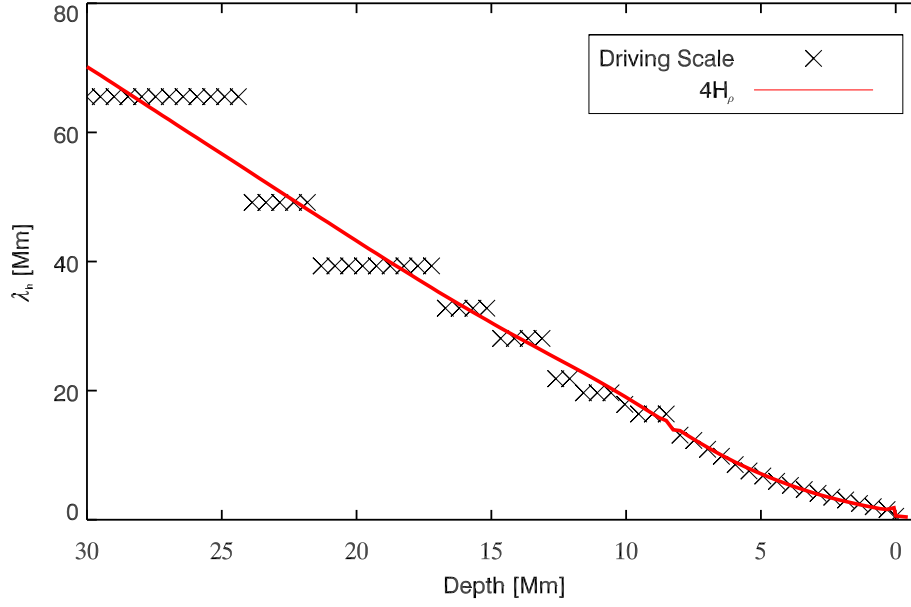
Figure 4.2 The *crosses* show the driving scale in the hydrodynamic simulation. This scale separates the small scale divergenceless motions that follow Equation 4.5 and the large scale motions that feel the stratification and follow Equation 4.6. The driving scale is taken to be the smallest wavenumber where the horizontal velocity spectrum begins to systematically diverge from Equation 4.6. The *solid* (red) curve shows $4H_\rho$ from the hydrodynamic simulation.

using the observed density and temperature of the solar photosphere as boundary conditions. We take the convective flux to be equal to the photospheric radiative output (6.3×10^{10} erg cm^{-2} s^{-1}) as appropriate for efficient convection, and note that this introduces an error in the lower portions of the model where, in the Sun, radiation transports a significant fraction of the energy flux. This error makes a small contribution to the excess model power at the largest scales (§4.1.4).

Explicitly, we solve the equation for the convective energy flux $F_c = \frac{1}{2}\rho v C_p T \frac{l}{H_p}(\nabla - \nabla')$ along with that of hydrostatic balance $\frac{dP}{dz} = -\rho g$. Here ρ is the fluid density, v is the velocity, C_p is the specific heat at constant pressure, T is the temperature, ∇ is the mean temperature gradient, ∇' is the temperature gradient within the convective cell, P is the pressure, and $g = Gm(z)/r(z)^2$ is the gravitational acceleration with $r(z)$ the distance from the Sun's center, $m(z)$ the mass within that radius and G the gravitational constant. We employ the equation of state $P = \rho k T/\mu$, where k is the Boltzmann constant and μ is the mean molecular weight of the plasma, and assume that the convective motions are adiabatic, so that $\nabla' = \nabla_{\mathrm{ad}} = \left.\frac{\partial lnT}{\partial lnP}\right|_{\mathrm{ad}}$, the adiabatic temperature gradient. Finally, the rms convective velocity is given by $v^2 = \frac{1}{8}gQ\frac{l^2}{H_p}(\nabla - \nabla')$, where l is the mixing length measured in units of the pressure scale height H_P. Note that $Q = 1 - \left.\frac{\partial ln\mu}{\partial lnT}\right|_P$, C_p, ∇_{ad}, and μ account for the non-ideal effects of hydrogen and helium ionization (where the number density of each ionization state is determined in collisional equilibrium as a Saha balance).

The equations are integrated numerically from the photosphere downward, yielding the convective rms velocity and the local density scale height at each depth.

4.1.3.2   Decay of large scale modes with height

In all simulations of solar convection the amplitude of the vertical velocity at low wavenumbers decreases towards the surface where granular scale convection is dominant. The rate of this decrease for the largest scale convective modes is a fundamental uncertainty in our understanding of solar convection. While global simulations predict giant cell convection throughout much of the convection zone (e.g., Miesch et al., 2008), surface observations have only very recently found evidence for weak flows at these scales (Hathaway et al., 2013). Numerical simulations have difficulty

directly addressing the photospheric amplitude of large scale motions. They are either of limited extent in depth (Stein et al., 2009; Ustyugov, 2010; Lord, 2014) or do not capture the non-ideal and highly compressible nature of the uppermost layers (Miesch et al., 2008).

Because of these uncertainties, we examine two possible vertical velocity amplitude decay profiles. Starting from the depth at which the wavelength of the mode exceeds the integral scale, we decay the modes either by approximating the flow as potential (van Ballegooijen, 1986) or by using a cubic polynomial fit to the observed decay of modes with wavelengths between 20 Mm to 50 Mm in the hydrodynamic simulations (shown as *diamonds* in Figure 4.3). The potential flow approximation takes the flow to be irrotational, allowing a direct solution to the large-scale continuity balance, written as

$$\frac{\partial \tilde{\phi}}{\partial z} = -\mathrm{k}_h H_\rho \tilde{\phi} \;, \tag{4.8}$$

where the ϕ is the velocity potential with $\tilde{\mathrm{u}}_z = \frac{\partial \tilde{\phi}}{\partial z}$. This yields a profile for the velocity amplitude with height

$$\tilde{\mathrm{u}}_z(z) = \tilde{\mathrm{u}}_z(z_d) \frac{H_\rho(z)}{H_\rho(z_d)} \exp\left[k_h^2 \int_{z_d}^{z} H_\rho(z') dz' \right] \;, \tag{4.9}$$

where z_d is the driving depth. This velocity profile can be integrated numerically for any wavenumber k_h, the results of which are shown with *triangles* in Figure 4.3. The polynomial fit, on the other hand, approximates the decay of the modes by a single function determined from the hydrodynamic simulations (solid line in Figure 4.3). The fit groups the behavior of all modes between 20 and 50 Mm together and is thus inadequate to reproduce the hydrodynamic simulation in detail (see §4.1.4). It is employed in the model because of its simplicity. The two schemes are quite different in form, and together provide a test of the sensitivity of the model to this key unknown function.

4.1.3.3   Construction of the model spectrum

In summary, we construct the model surface horizontal velocity spectrum as follows. To calculate the spectrum of the vertical velocity we:
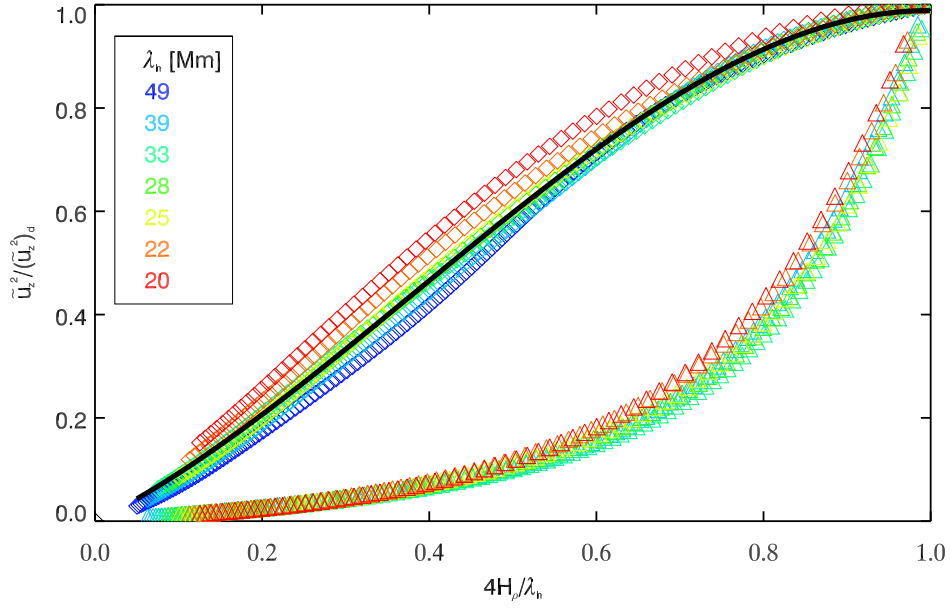
Figure 4.3 The *diamonds* show vertical velocity power from the driving depth, $\lambda_h = 4H_\rho$, up to 1.3 Mm below the photosphere in the hydrodynamic simulation. The different colors show different modes from 20 Mm (red) to 50 Mm (purple). The *black* curve is the cubic polynomial fit to the observed decay rate. The *triangles* show the decay rate for a potential flow (Equation 4.9) for the same range of modes.

(1) Construct a mixing length model of the solar convection zone integrating from the photo-sphere downward to 200 Mm, the approximate depth of the solar convection zone.

(2) Determine the wavelength of the largest scale mode allowed at the bottom of the model atmosphere, $\lambda_h = 4H_\rho$, and use this as the integral (driving) scale (i.e. the lowest wavenum-ber mode) in a $k^{-5/3}$ turbulent cascade. The highest wavenumber in the spectrum is taken to be the Nyquist frequency of the hydrodynamic simulations on which the model is based ($2\pi/384$km, see §4.1.5.1), and the spectrum is normalized so that the integrated power is equal to the mixing length velocity squared at the bottom of the model atmosphere.

(3) Move one step up in the atmosphere (a grid spacing of 64km is used to again match the hydrodynamic simulations). Decay modes with wavelengths longer than the local integral scale ($4H_\rho$) using one of the two decay functions discussed in §4.1.3.2. Compute the inte-grated power in the decaying modes and normalize the remaining $k^{-5/3}$ spectrum by the squared mixing length velocity minus the power in the decaying modes.

(4) Repeat Step 3 until the top of the model atmosphere is reached.

From the vertical velocity spectrum, the horizontal velocity spectrum at any height is computed using Equations 4.5 and 4.6.

4.1.4   Testing the Model

We used the model outlined above to compute the horizontal velocity spectrum at a depth of 1.3 Mm below the solar photosphere (as previously discussed model assumptions break down above this height and results from hydrodynamic simulations validate this spectra as a close approximation to the surface spectrum for supergranular and larger scale motions). The resulting spectrum is shown as a *solid* (red) curve in Figure 4.4*a*. For clarity we show the spectrum obtained when employing the large scale mode decay rate as measured in the hydrodynamic simulation only (we discuss the potential decay below). The spectrum has two notable low-wavenumber features: monotonically increasing power at scales larger than supergranulation and a small plateau of power

at supergranular scales. The monotonic increase of power to lower wavenumbers is not observed on the Sun. The horizontal velocity spectrum of solar motions shows decreasing power at scales larger than supergranulation (see §4.1.5.1). The small supergranular plateau extends from $\lambda_h \sim 20 - 30$ Mm (corresponding to $k/2\pi \sim 0.03 - 0.05$ Mm^{-1} in Figure 4.4a), matching supergranular scales in solar observations. The high wavenumber features of the spectrum, in particular the discontinuity at the 1.3 Mm depth integral scale, occur at scales for which the model is ill suited.

To test the sensitivity of the model to the mixing length atmosphere employed we compared the spectrum shown in Figure 4.4a to one computed using a more sophisticated non-local mixing length formulation (Christensen-Dalsgaard et al., 1996). The non-local formulation employs the OPAL (Rogers & Iglesias, 1992) equation of state and opacities, more carefully accounting for the chemical composition of the convection zone. Importantly, it also accounts for the transport of energy by radiation in the lower portion of the convection zone, which reduces the convective flux and consequent driving amplitudes there. The resulting horizontal velocity spectrum has nearly identical shape as that computed using our simplified Saha balance. Only the largest scale mode shows any notable difference, with the amplitude of that mode somewhat reduced as it is the only mode driven in lower third of the convection zone where the Christensen-Dalsgaard et al. (1996) convective velocities are weaker as a result of the more careful accounting of the radiative energy flux.

As there is no a priori expectation for the decay rate of the large scale modes, this aspect of the model is more difficult to assess. We chose to compare the spectrum shown in Figure 4.4a (obtained using the large scale mode decay rate measured in the hydrodynamic simulations) to one employing an analytic potential flow assumption (van Ballegooijen, 1986) because the later yields an exponential decay of the mode amplitudes (Equation 4.9) and may thus represent a somewhat limiting case. The surface horizontal velocity spectrum computed with the exponential decay shows significant reduction in overall power, particularly at small scales, but quite similar shape at supergranular scales. It exhibits a nearly identical monotonic increase of power at scales larger than supergranulation to that seen in Figure 4.4a. The relative amplitudes of low wavenumber modes
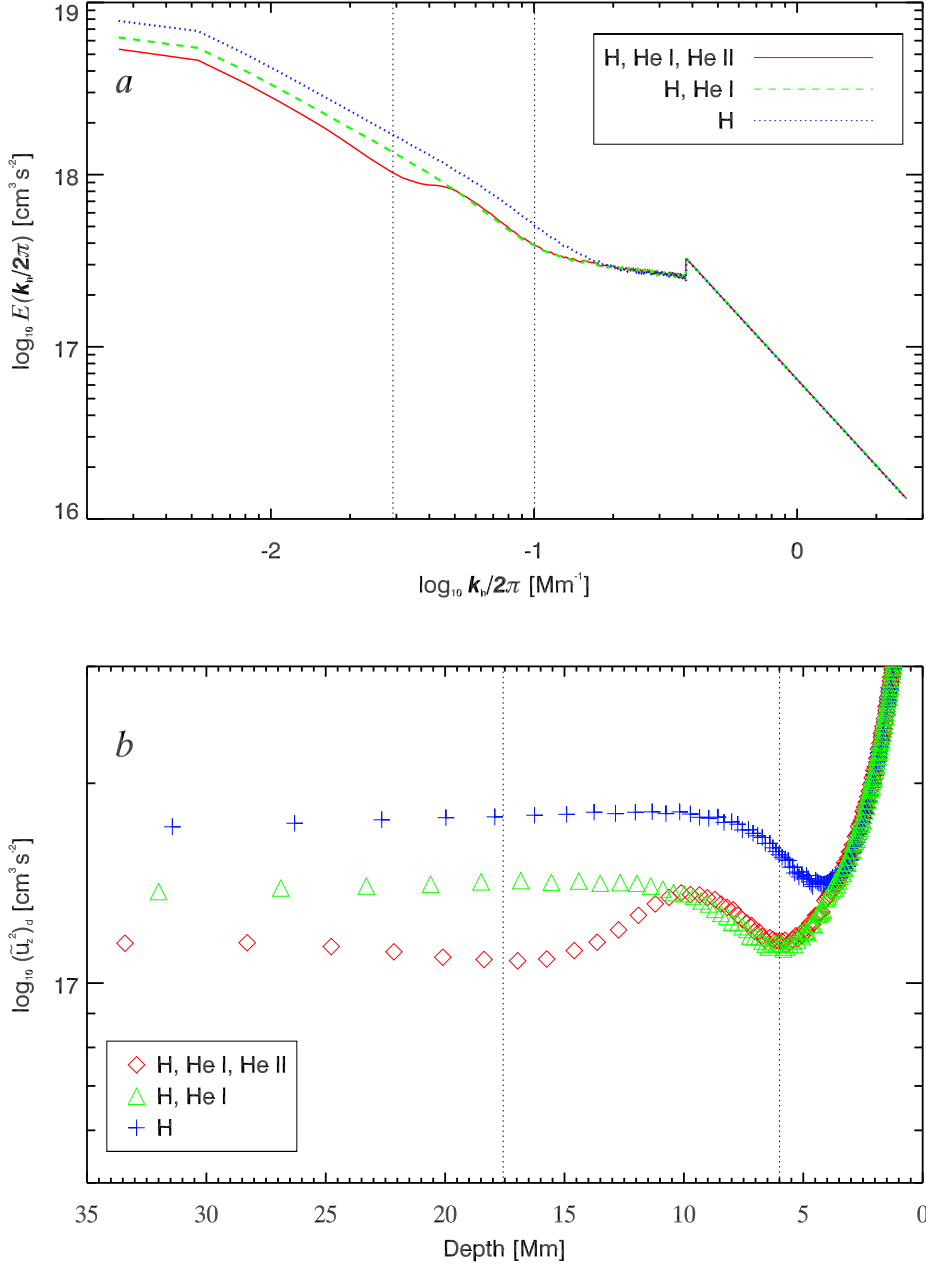
Figure 4.4 The spectra computed from the two component model using the decay rate fit to the hydrodynamic simulations. We show the horizontal velocity spectrum at a depth of 1.3 Mm in part a and the vertical velocity power at the driving depth in part b. The *solid* (red) curve in part a and *diamonds* in part b (red) shows the spectrum computed from a mixing length atmosphere with a Saha equation of state that includes H, He I, and He II ionization; the *dashed* in a and *triangles* in b (green) is computed from an atmosphere with no He II ionization; and the *dotted* in a and *crosses* in b (blue) is computed from an atmosphere with no He I or II ionization. The vertical *dotted* lines show the depths of 50% He I (6 Mm and $k/2\pi = 0.1$ Mm^{-1}) and He II (17.5 Mm and $k/2\pi = 0.03$ Mm^{-1}) ionization in part b and driving scale, where $\lambda_h = 4H_\rho$, at those depths in part a.

is quite insensitive to the imposed mode decay function. The low wavenumber power distribution is primarily determined by the mode amplitudes at depth, with those amplitudes constrained by convective flux requirements of the model atmosphere.

Finally, we looked to validate the model using the three-dimensional hydrodynamic simulations directly. When taking the driving scale $(4H_\rho)$ and rms velocity amplitude directly from the simulation itself, rather than from a mixing length atmosphere, the model matches the horizontal velocity spectrum of simulation to within 10% over the wavenumber band $k/2\pi = 0.02-0.15$ Mm^{-1} $(\lambda_h \sim 7-50$ Mm) at all depths below 1.3 Mm. This is achieved, however, only by fitting the decay rate of each mode individually and reducing the overall amplitude of the spectrum by a constant offset factor of two. The increased power in the model spectrum results because the power at the driving depth in the model is overestimated by the assumed Kolmogorov power distribution of the isotropic modes. The factor of two can be removed by using a non-Kolmogorov spectrum at depth, but this introduces additional free parameters that can not be constrained by solar observations. This highlights an important result: the shape of the horizontal velocity spectrum in the upper layers of the model is largely determined by the vertical velocity amplitude of the modes at depth. The relative amplitudes of large scale modes in the solar photosphere depends critically on the vertical velocities at the depth. This is further supported by the models inability to reproduce the simulation results for scales $\lambda_h > 50$ Mm $(k/2\pi < 0.02$ Mm$^{-1})$. For these very large scale motions the driving depth lies near the bottom of the simulation domain and the mode amplitudes, as well as the measured decay rates, are influenced by the simulation lower boundary condition.

4.1.5   Surface Convection Dependence on Motions at Depth

The model tests discussed above confirm that the monotonically increasing low wavenumber power and much less prominent supergranular plateau are robust features of the horizontal velocity spectrum. That the model can reproduce the shape of the hydrodynamic simulation spectrum validates the underlying assumption that there are two components to the flow separated by the integral (driving) scale which reflects the local scale height at each depth. Larger scale motions are

driven deep in the convection zone and decay from below with height. Smaller scale motions behave as isotropic homogenous turbulence. Mismatches between the model and hydrodynamic simulation spectra and observations however raise broader questions. What is the spectrum of solar convective motions at depth and what governs the decay of these motions with height?

4.1.5.1 The Problem of Excess Low Wavenumber Power

Both the simplified model and the full three dimensional radiative hydrodynamic spectra show more power than the Sun at scales larger than supergranulation, with that power increasing monotonically toward lower wavenumbers because large scale flows are convectively driven in the deep layers of the domains. It is worth noting that if the solar spectrum matched either the simplified model or the radiative hydrodynamic simulation spectrum, giant cell convection would be relatively easy to observe as the power in these large scale modes would exceed that in supergranulation.

To make a more direct comparison between our numerical simulations and observations, we employed a Coherent Structure Tracking (CST, Roudier et al., 2012) algorithm to infer the horizontal velocities on large scales from measurements of the motions of granules. In Figure 4.5 we compare the CST horizontal velocity spectra of a large scale radiative hydrodynamic simulation (*solid* red curve) using the OPAL equation of state (Rogers & Iglesias, 1992) with that of solar observations (*dash* black curve) from the Helioseismic and Magnetic Imager aboard the Solar Dynamics Observatory (HMI/SDO). The measurements in both cases employ a 22 hour sequence of continuum intensity images with each HMI image separated by 45 seconds and each simulation image separated by ~ 40 seconds. We break this sequence into 11 two-hour subsets and use the CST method to compute the velocity for each two hour window. The spectrum shown is the average spectrum of those 11 velocity computations. The HMI observations are of 192x192 Mm^2 region at disk center with a low magnetic activity on 19 June 2010. The simulation solution was computed using the MURaM code (Vögler et al., 2005) in a 196x196x49 Mm^3 domain with 192x192x64km^3 grid spacing (Lord, 2014).

We note that the spectra in Figure 4.5 are truncated at high wavenumber because the CST method is not reliable for scales smaller than 2.5 Mm. Moreover, low wavenumber modes, those with wavenumbers below $k < 0.013$ Mm^{-1} (indicated by the vertical fiducial line and *dot-dash* linestyle in Figure 4.5) have length scales larger than the integral (driving) scale at the bottom of the simulation domain and consequently have lower photospheric amplitudes than they would likely have in a deeper simulation. Between these extremes are two notable mismatches between the simulation and observation spectra: the simulation shows an excess of power at low wavenumbers and a deficit of power at high wavenumbers when compared to observations. Our very wide and deep simulations resolve supergranular scale motions well but under-resolve granular motions. This leads to an inferred CST velocity with reduced power at high k, a result that is inconsistent with the actual simulation velocities and HMI observations. The excess of low wavenumber power is, on the other hand, a fundamental difference between the resolved motions in the simulation and those in observations and is robust, as the CST constrains large scale motions better than small scale motions (Roudier et al., 2012). Thus understanding the observed solar supergranulation spectrum requires understanding the origin of this low wavenumber reduction in power along with any mechanism that may enhancement power at supergranular scales.

Our simplified mixing length model suggests that the low wavenumber vertical motions are driven deep in the convection zone and decrease in amplitude towards the surface. The radiative hydrodynamic simulations behave similarly (§4.1.4), and reducing the vertical flow velocities at depth reduces the low wavenumber horizontal velocity power in the simulated photosphere and improves the match between simulations and observations. We demonstrate this conclusively via simulations in which convective velocities in the deep layers are reduced without changing the mean stratification of the atmosphere (which is also fundamental to the surface spectrum). This was done using an artificial energy transport term. Specifically, we added an artificial flux function to the energy equation that depends only on depth. The artificial flux carries the full solar flux below a specified depth and none of the flux at heights above this. The hyperbolic tangent flux profile employed is 5.12 Mm wide centered at 10 Mm (where $4H_\rho \sim 20$ Mm), effectively supporting

radiative losses from the photosphere by depositing the heat where the divergence of the function is nonzero. In Figure 4.5 (*dotted* blue curve) we plot the resulting photospheric horizontal velocity spectrum using the same CST method described above. There is substantially reduced power in the photosphere of the artificial flux simulation in those modes that are driven at depths below ~ 10 Mm (scales larger than ~ 20 Mm). This is the region of the domain for which the artificial energy flux is important and consequently convective (rms) velocities are reduced by a factor of ~ 2.5.

The artificial energy flux experiment confirms the hypothesis that low wavenumber modes are driven deep in the simulated convection zone and imprint as horizontal flows in the surface layers. The photospheric power spectrum reflects a hierarchy of driving scales with depth even in fully nonlinear radiative hydrodynamic simulations. It also suggests that neither the radiative hydrodynamic solutions nor the simplified model spectrum capture the true dynamics of the solar convection below ~ 10 Mm. In other words, in the Sun, low wavenumber flows carry much less of the convective energy flux or transport the energy at substantially lower velocities than expected based on the simulations or the model. Flow/enthalpy correlations, essential to convective transport, may thus not be correctly captured by hydrodynamic simulations. This may be due to their limited resolution or result from the boundary conditions applied. For example, the open boundary condition commonly employed in radiative hydrodynamic simulations of photospheric convection may smooth perturbations in the inflowing plasma. Alternatively, magnetic fields, not included in the simulations we have discussed in this paper, may maintain flow correlations and allow convective transport on smaller scales or at lower velocities than predicted by purely hydrodynamic models. Preliminary results from magnetized simulations favor this hypothesis, though the underlying mechanisms are still under investigation and the effect so far appears insufficient to explain solar observations (Lord, 2014).
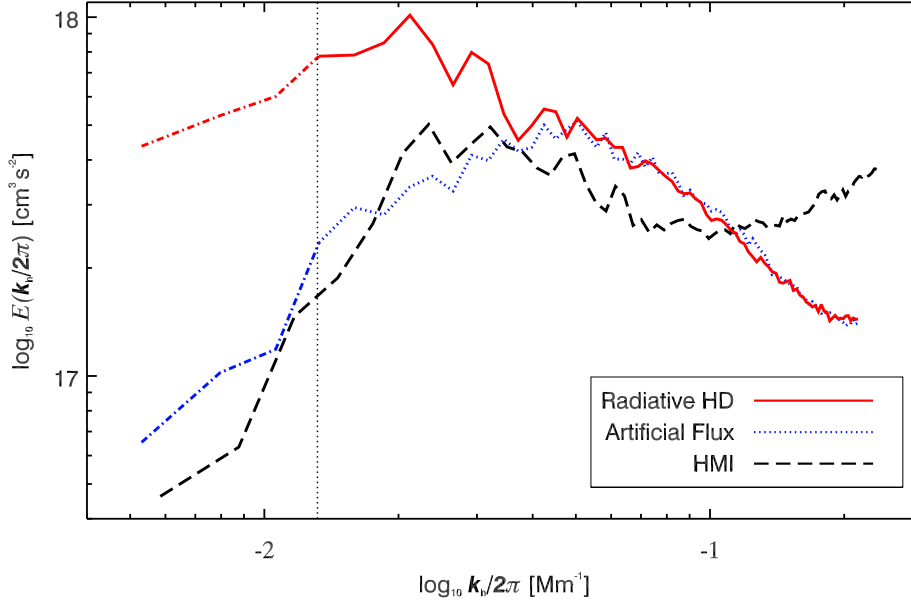
Figure 4.5 The photospheric power computed from the Coherent Structure Tracking (CST) algorithm of Roudier et al. (2012). The *dashed* curve is the HMI observations, the *solid* (red) curve is the spectrum computed from continuum intensity from the radiative hydrodynamic simulation with domain size 196x196 Mm^2 wide and 50 Mm deep using the OPAL equation of state. The *dotted* (blue) curve is the spectrum computed in the same way from a simulation with an artificial energy flux that carries the solar energy flux below 10 Mm. Modes with wavenumbers below $k < 0.013$ Mm^{-1} (indicated by the vertical *dotted* fiducial line and change to *dot-dash* linestyle) have length scales larger than the integral (driving) scale at the bottom of the simulation domain and consequently have lower photospheric amplitudes than we would expect from a deeper simulation. We use 192x192 Mm^2 HMI images to match the simulation domain size and degrade the resolution of the simulations to match the observations (~ 370 km). To compute the spectrum of the CST velocities we cut off the two outermost cells and zero-pad by adding twice the number of grid cells in each direction (and multiply the amplitudes by a factor of 4 to maintain the integrated spectral power before zero-padding) to remove the influence of the non-periodic boundary.

4.1.5.2   Helium Ionization Plays a Minor Role

The small plateau of power at supergranular scales (*solid* red curve in Figure 4.4a at $k_h \sim$ 0.04 Mm^{-1}) reflects the role of helium ionization in determining the convective velocities at depth. Superimposed on the horizontal velocity spectrum in Figure 4.4a we have plotted fiducial vertical lines to highlight the integral (driving) scale at the depths of 50% He I ($k/2\pi = 0.1$ Mm^{-1}, 6 Mm depth) and He II ($k/2\pi = 0.03$ Mm^{-1}, 17.5 Mm depth) ionization. The plateau of supergranular power falls between these two fiducial lines. We have also computed the horizontal velocity spectrum for mixing length background atmospheres with an equation of state which does not allow He II or both He I and He II ionization (Figure 4.4, *dashed* (green) and *dotted* (blue) curves respectively). These test atmospheres show a continuous power law increase toward low wavenumbers with no feature at supergranular scales. More precisely these spectra do not show the suppression of power at scales corresponding to the integral scale at the depths of 50% He I or He II when the ionization processes are disallowed. The differences between the ionizing and non-ionizing spectra at yet lower wavenumbers result because the stratification in the deep layers lies along a different adiabat. The velocity differences at depths below helium ionization, reflected in the low wavenumber horizontal velocity spectra in the near surface, are due to differences in the mean stratification as the medium is nearly fully ionized. In the region of partial ionization, convective velocities are also influenced by the availability of ionization energy in heat transport via perturbations about the mean ionization state.

Helium ionization is thus responsible for the small supergranular plateau in the model spectrum, albeit in a curious fashion. The ionization of helium yields a slight reduction in the driving scale mode amplitudes in the partially ionized regions (where the driving scale $\lambda_h \sim 10$ Mm for He I and $\lambda_h \sim 35$ Mm for He II), producing a small apparent enhancement of power in the upper layers at wavenumbers that lie between them (where $\lambda_h \sim 20$ Mm). The reduction in mode amplitudes results because ionization energy contributes to the heat transport. In a partially ionized fluid the heat can be transported by ionization state perturbations as well as thermal perturbations (Rast

et al., 1993; Rast & Toomre, 1993), and convective velocities in the mixing length model are thus reduced in partially ionized regions. We note that the mixing length model is a local transport model and does not take into account other effects of ionization such as the increased linear (Rast, 1991) and nonlinear (Rast, 2001) instability of the fluid, though these may play a role in solar convective flows or in our more complete three dimensional simulations. The vertical velocity amplitudes of modes that begin their decay at the depths of helium ionization (the integral or driving scale modes at those depths) are thus suppressed, resulting in a reduction in their horizontal velocity power near the surface. Since ionization energy transport depends on ionization state perturbations, with transport in a fully neutral or fully ionized plasma behaving as an ideal gas, modes with peak amplitudes (those with integral scales equal to $4H_\rho$) at depths that lie between the partially ionized regions (10 Mm for example where $\lambda_h \sim 20$ Mm and $k/2\pi = 0.04$ Mm^{-1}) have more power than neighboring modes.

This is illustrated by Figure 4.4b, which shows the vertical velocity power at the driving depth (i.e. the depth where the wavelength of the mode is equal to the integral (driving) scale) for mixing length model atmospheres which do or do not allow He I or He II ionization. The driving scale modes in the regions of partial ionization have lower amplitudes than those outside of it, with minima in the mode amplitudes occurring at the depths of 50% ionization when it is allowed. The role of hydrogen ionization is difficult to illustrate as its effect is dominant in the surface layers where hydrogen recombination supports radiative losses. The region of H partial ionization is broad in depth and integral to the structure of the radiative boundary layer, and experiments preventing H ionization dramatically alter the mean state of the atmosphere and result in dramatic changes in the velocity spectrum across a wide range of wavenumbers. Thus we do not explicitly consider an atmosphere that disallows hydrogen ionization, but it is clear from Figure 4.4b that the effect of hydrogen ionization on mode amplitudes overlaps that of He I (compare *crosses* (blue) and *triangles* (green)).

The simple model we have presented thus suggests that there is an apparent enhancement of photospheric power at ~ 20 Mm scales that occurs because helium ionization reduces the flow

speeds in the regions of partial ionization which suppresses power at larger ($\sim$ 35 Mm from He II) and smaller ($\sim$ 10 Mm from He I) scales, not because He II ionization enhances the driving of flows at this depth as has been previously suggested. This apparent enhancement, however, is much smaller than the increased power in observations of solar supergranulation. To investigate the suppression of photospheric power by helium ionization in the context of solar-like convection we use the same Saha equations of state described above in three dimensional radiative hydrodynamic simulations. We use the MURaM (Vögler et al., 2005) code to run simulations that use 192x192km^2 horizontal resolution and 64km vertical resolution with 1024x1024x768 grid cells (giving a domain size of 196x196x49 Mm^3). The results presented here are from more than 5 days of solar time after the simulation has reached a relaxed equilibrium (Lord, 2014).

Figure 4.6a shows a comparison of the photospheric horizontal velocity spectrum from three such simulations, one which allows H, He I, and He II ionization (*solid* red curve), one in which only H and He I ionization are permitted (*dashed* green curve), and one with only H ionization (*dot* blue curve). The resulting horizontal velocity spectra show similar suppression of photospheric power as that seen the simplified model (Figure 4.4) when ionization is allowed. The two lowest wavenumber modes (*dot-dash* linestyle) have driving depths outside of the simulation domain and are consequently unreliable and weaker that what would be expected in a deeper simulation. The modes with integral (driving) scales equal to $4H_\rho$ in the regions of partial helium ionization again have reduced amplitudes. This is particularly apparent at the wavenumbers corresponding to modes that peak in the He II partial ionization region ($k/2\pi$ near 0.013 Mm^{-1} in Figure 4.6a) which is well separated from the effects of hydrogen ionization. Not allowing He II ionization (*dash* green and *dot* blue curves) causes a small but significant elevation of photospheric power at those wavenumbers. Disallowing He I ionization (*dot* blue curve) induces smaller differences due to the dominant role of hydrogen in the surface layers.

The same reduction in the mode amplitude of the vertical velocity spectrum at the driving depths corresponding to partial helium ionization seen in the simplified model is apparent in these hydrodynamic simulations (Figure 4.6b). Modes with scales equal to $4H_\rho$ at the depths of partial

He I and He II ionization have reduced amplitudes, though this reduction is noisier in the simulation than in the mixing length atmosphere (we note that the rms velocity amplitudes, not shown here, also very clearly increase at the nominal ionization depths when ionization is disallowed). This is due to three primary factors: the spectral resolution of the simulation is limited by the domain width, the three dimensional simulation is non-local which makes using a single depth a poor representation of the vertical velocity power that reaches the surface, and the intrinsic temporal variation in the power of the modes below ~ 10 Mm is long compared to the 5 days of simulation time. Moreover, other nonlinear effects of ionization may play some role, as discussed above. These experiments do however confirm, in the context of fully nonlinear three-dimensional radiative hydrodynamic simulations, two important results of the simplified model: the horizontal velocity spectrum in the photosphere reflects the amplitude of the vertical velocity at depth and the reduced amplitude of vertical velocity in the regions of partial helium ionization plays a minor role in shaping the spectrum of supergranular flows at the surface.

4.1.6   Conclusion

We have constructed a model that computes the horizontal velocity spectrum near the solar surface based on the amplitudes of modes deep in the solar convection zone. The model has three primary features: it is able to match the shape of the photospheric spectrum in three dimensional radiative hydrodynamic simulations, shows a small supergranular scale enhancement of power at 20-30 Mm, and an excess of power at lower wavenumbers not seen in observations.

We used the model to examine the role that helium ionization plays in shaping the solar photospheric velocity spectrum. We showed that near the depths of 50% He I and He II ionization the amplitudes of the vertical motions are reduced because the solar energy flux can be transported at lower velocities due to contribution of ionization energy. This manifests itself as a suppression of horizontal velocity power in the surface layers at scales neighboring supergranulation (~ 35 Mm scales for He II and ~ 10 Mm scales for He I). We confirmed this effect in three dimensional radiative hydrodynamic simulations that examined convection with and without helium ionization.
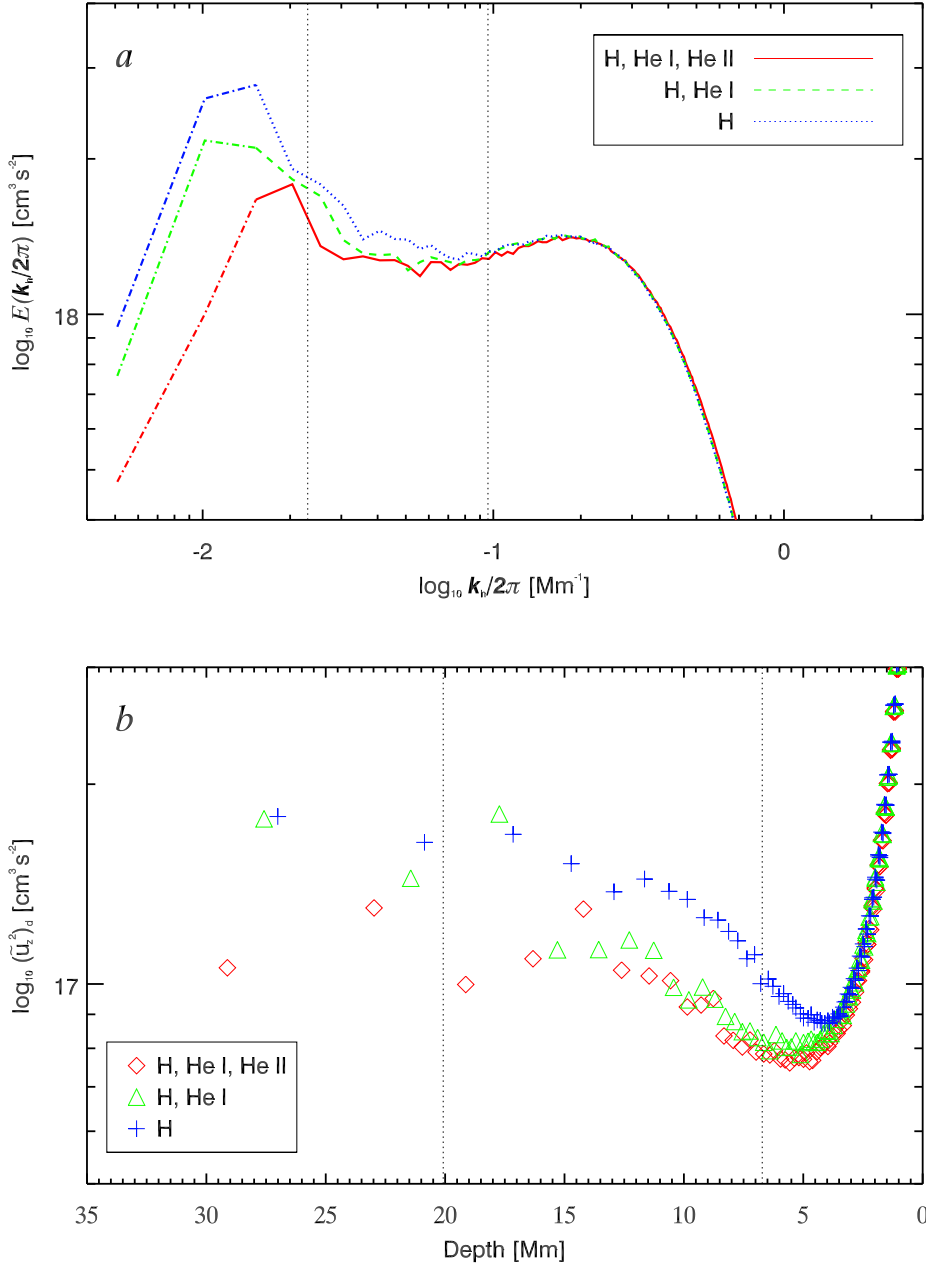
Figure 4.6 The spectra computed from hydrodynamic simulations with three different equations of state. We show the horizontal velocity spectrum at the photosphere in part *a* and the vertical velocity power at the driving depth in part *b*. The *solid* curve in part *a* and *diamonds* in part *b* (red) show the spectrum computed with a Saha equation of state that includes H, He I, and He II ionization; the *dashed* in *a* and *triangles* in *b* (green) is computed with an equation of state with no He II ionization; and the *dotted* in *a* and *crosses* in *b* (blue) is computed with an equation of state with no He I or II ionization. The vertical *dotted* lines show the depths of 50% He I (7 Mm and $k/2\pi = 0.1$ Mm^{-1}) and He II (20 Mm and $k/2\pi = 0.025$ Mm^{-1}) ionization in part *b* and driving scale, where $\lambda_h = 4H_\rho$, at those depths in part *a*. Note that the two largest scale modes are shown in the *dot-dash* linestyle here because the have length scales larger than the integral (driving) scale at the bottom of the simulation domain and consequently have lower photospheric amplitudes would be expected in a deeper simulation.

We conclude that, instead of enhancing a particular flow scale, He I and He II ionization act to highlight supergranular scales by reducing the power in the adjacent modes. This enhancement is, however, smaller in the models than the observed enhancement of solar photospheric power at supergranular scales.

A robust feature of both the model spectrum and the hydrodynamic simulations is an excess of power at low wavenumber when compared to solar observations. This highlights two uncertainties that require further study. First, we do not know the convective flux spectrum in the deep layers of the Sun. While we took the flow spectrum to be Kolmogorov for all scales below the integral scale, this assumption only approximates the spectrum observed in hydrodynamic simulations, and it may significantly underestimate the role small scale motions play in transporting heat through the solar convection zone. Moreover, the large scale hydrodynamics simulations also show excess power at large scales compare to the Sun. Preliminary results from similarly large scale magnetohydrodynamic simulations suggest that magnetic fields may play a role in reducing convective flow speeds or maintaining the correlations required for the energy flux to be carried by smaller scale motions (Lord, 2014), but as yet these effects are too small to explain observations. Second, we do not know how the amplitude of the vertical motions decreases with height in the solar convection zone. The decay rates (with height) of low wavenumber modes may be influenced by solar rotation and the near surface shear layer which are not included in our analysis. It is likely that the supergranular excess in the solar power spectrum is largely defined by the observed decrease in power to lower wavenumbers, and has thus been elusive in simulations which show a monotonic increase in power to lower k.

The excess low wavenumber power we find in both our simplified model and realistic simulations adds to other recent evidence that large scale flows deep in the solar convection zone are weaker than previously thought. It supports suggestions that numerical simulations more generally may have difficulty matching solar observations if they are required to carry all of the solar energy flux in the resolved modes (N. Featherstone 2014, private communication). Helioseismic observations (Hanasoge et al., 2010, 2012) yield estimates of flow velocities that are an order of

magnitude or two below those found in either global (e.g. Miesch et al., 2008) or local area (Lord, 2014) simulations. Moreover, as global simulations become more turbulent, with lower diffusivities, flow speeds increase and differential rotation profiles flip to an anti-solar configuration, with a slow equator and fast poles, because rotational constraints are too weak. This transition to anti-solar behavior can be avoided by decreasing the heat flux through the convection zone or increasing the rotation rate (J. Toomre et al. 2013, private communication; P. Charbonneau 2014, private communication; Hotta, 2014a). We found that reducing the convective transport role of large scale modes (by employing an artificial energy flux at all depths below 10 Mm which reduces the deep rms velocities by a factor of ~ 2.5) can significantly improved the match between the CST spectra of the simulations and observations. These separate lines of evidence all suggest that the Sun transports energy through the convection zone while maintaining very low amplitude large scale motions. Something is missing from our current theoretical understanding of solar convection below ~ 10 Mm.

4.2 Addendum to the Paper

We add to the discussion of Lord et al. (2014) to examine some aspects of the effects of helium ionization and the artificial energy flux in more depth.

We start by examining the effect of the latent heat flux of helium ionization in §4.2.1. In particular we compare the change in stratification (which are caused by the differences in particle number) when preventing He ionization to the change to the latent heat flux. This helps clarify the how much of the change in the photospheric horizontal velocity spectrum is due to the latent heat flux.

We then examine the artificial energy flux in more detail. Using the artificial energy flux helps examine how the deep convection affects the surface flows without the problems of changing the domain depth of the simulation (§3.1). We compare the reference simulation to the simulation with the artificial energy flux to explore precisely how this artificial flux changes the flows §4.2.3.

4.2.1 Mixing Length Atmospheres and Helium Ionization

We introduce three mixing length model atmospheres with differing equations of state in Lord et al. (2014). Two of these equations of state include H I ionization but disallow He I or II ionization to compare to an equation of state with H I, He I and II ionization and explore the effects of He ionization. While we discussed the effects of the latent heat flux of helium ionization and the change in the mean molecular weight of the plasma, we did not show exactly how these different equations of state change the atmosphere.

4.2.1.1 Helium Ionization

Since the two-component model uses the velocity and density scale height to determine the amplitude of the spectrum and the driving (integral) scale at each depth, we begin by showing the velocity perturbation and scale height perturbation in Figure 4.7 (*a* and *b*, respectively) comparing the velocity in the mixing length atmosphere with H, He I, and He II ionization to the velocity

in an atmosphere with no He II ionization (*dotted* green curve) and no He I or He II ionization (*dashed* blue curve) in the uppermost 50 Mm. Since each of these model atmospheres have the same properties in the photosphere (matching the observed density and temperature of the Sun), and helium is fully neutral near the photosphere, each model atmosphere has the same values in the uppermost few Mm.
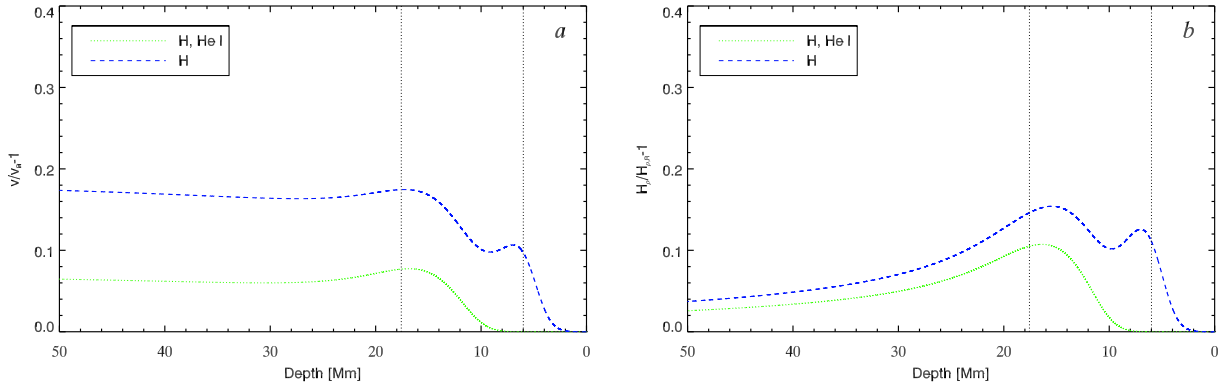
Figure 4.7 The perturbation of the mixing length velocity (*a*) and density scale height (*b*) between the three mixing length atmospheres. We use the atmosphere with the Saha equation of state that includes H, He I, and He II ionization as the reference (labeled with subscript R) and compare to the atmospheres with no He II ionization (*dashed* green curve) and no He I or He II ionization (*dotted* blue curve). The fiducial vertical *dotted* lines show the mean 50% ionization depth for He I (6 Mm) and He II (17.5 Mm).

The differences below the photosphere are caused by the changes in the particle number and latent heat flux due to helium ionization. We plot fiducial vertical lines to show the mean depth of 50% ionization for He II (17.5 Mm depth) and He I (6 Mm depth) in both. In the atmospheres that disallow He ionization the mixing length model establishes a stronger superadiabatic gradient to transport the energy flux. Since the velocity is primarily determined by the mixing length (which is a function of the pressure scale height which is less sensitive to He ionization) and the difference between the mean and adiabatic temperature gradients, this new superadiabatic gradient increases the velocity. The increased velocity compared to the mixing length model atmosphere with full H and He ionization at the bottom of Figure 4.7*a* is consistent to the bottom of the convection zone. Since the velocity determines the integrated power of the velocity spectrum at each depth, this

explains why we see increased power in the driving scale mode and at the surface in Figure 4.4.

4.2.1.2 What Happens Below The Region of Partial Ionization?

Helium is nearly fully ($> 95\%$) ionized for depths greater than 40 Mm below the photosphere. Below this depth the flows behave as a (nearly) fully ionized ideal gas in all three atmospheres but differences persist in the velocity (and driving scale power). As stated above, the ionization of helium affects both the energy transport and the mean molecular weight of the plasma. Preventing helium ionization both reduces the non-thermal energy flux and changes the mean stratification of the atmosphere. By plotting the mixing length velocity as a function of depth (a) and density (b) in Figure 4.8, we can compare the changes to the velocity from the new stratification to the changes due to the latent heat flux. We chose the density range in b that correspondes to the depths shown in a for the model atmosphere that allows H I, He I and II ionization.
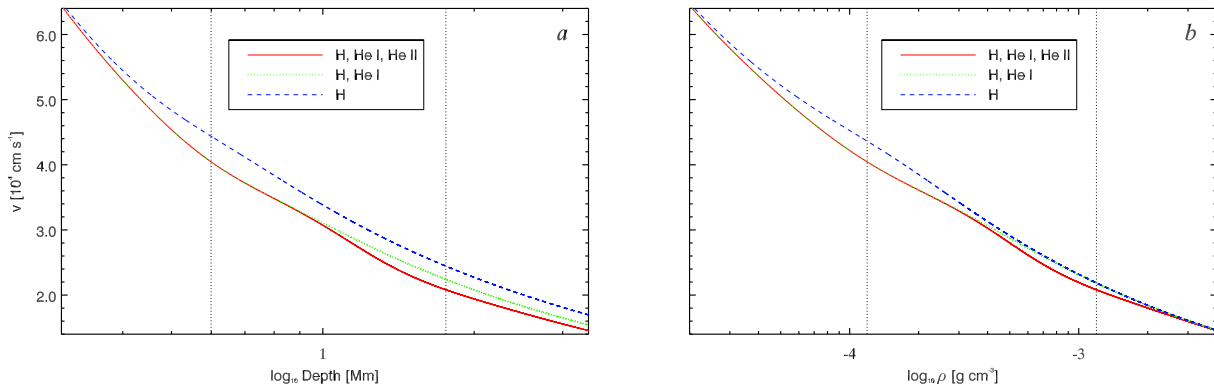
Figure 4.8 The rms vertical velocity from the mixing length atmospheres using the three Saha equations of state as a function of $\log_{10}$ depth (a) and $\log_{10}$ density (b). The *solid* (red) curve shows the spectrum computed from a mixing length atmosphere with a Saha equation of state that includes H I, He I, and He II ionization; the *dotted* (green) curve is computed from an atmosphere with no He II ionization; and *dashed* (blue) curve is computed from an atmosphere with no He I or II ionization. The vertical *dotted* lines show the depths of 50% He I (depth= 6 Mm, $\rho = 1.19 \times 10^{-4}$) and He II (depth= 17.5 Mm, $\rho = 1.19 \times 10^{-3}$) ionization.

Using the constant density surfaces (b) removes the effects of the change in stratification. Since the majority of the velocity reduction in the region of partial ionization remains if we compare the plot as a function of depth (a) or density (b), this confirms that the latent heat flux of ionization

is the dominant effect. In particular, there is a $\sim 10\%$ and $\sim 5\%$ reduction in the velocity amplitude in the respective regions of He I and II partial ionization due to the energy transport by helium ionization. Below ~ 30 Mm, however, the latent heat flux of ionization is very weak and the difference in velocity is due to the change in stratification (i.e. how $\rho(z)$ differs between each model atmosphere).

4.2.2   MURaM Simulations and Helium Ionization

We extend the examination of helium ionization from the mixing length model to the MURaM simulations. These simulations allow us to explore non-local effects of helium ionization in three dimensions. We start by computing the latent heat flux.

As the ions recombine they release a photon which increases the temperature of the surrounding plasma. The opposite is true for ionizing atoms. While advecting through the stratified atmosphere this effect increases (decreases) the thermal energy as the ionization fraction is decreasing (increasing). By transporting hot, ionized plasma from deep in the convection zone that recombines as it reaches the cooler upper layers, convective upflows transport this non-thermal energy source.

From Figure 4.9 we can see the convective energy flux (*solid* red curve) and latent heat flux of ionization (*dashed* blue curve). There are typical variations in the convective energy flux that keep it within $\sim 10\%$ of the solar energy flux (these variations only occur at depths greater than a few Mm below the photosphere). The ionization energy flux, however, has significant depth dependence. Hydrogen ionization and recombination occurs very close to the surface with significant differences between upflows and downflows. This manifests itself as a peak in the latent heat flux at $\sim 2/3$ of the solar energy flux with much of this energy is converted directly to radiation (Rast et al., 1993). The contribution of He I ionization is not obvious (since it is dominated by H I ionization) but adds significant ionization energy flux near the 50% He I ionization depth (7 Mm). Since He II ionization requires significantly more energy than H I or He I ionizatoin, it is well separated from the other ionization states and produces a peak in the ionization energy flux near 17 Mm depth. The
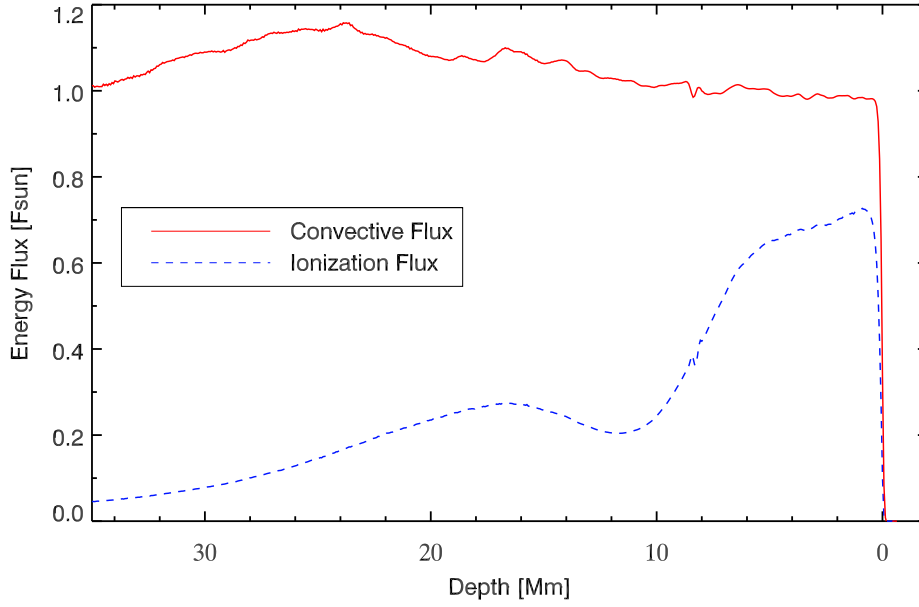
Figure 4.9 The convective energy flux (*solid* red curve) and latent heat flux of ionization (*dashed* blue curve) for the MURaM simulation using the Saha equation of state with H I, He I and II ionization. The convective energy flux is within 10% of the solar energy flux $(6.3 \times 10^{10} \text{erg cm}^{-2} \text{ s}^{-1})$ and is not a flat curve because we have not sampled one full energy flux oscillation period for this figure. The ionization latent heat flux depends on depth with local maxima in the regions of partial ionization.

ionization energy flux then significantly decays below the depth of He II ionization since heavier atoms have very low number density and, consequently, contribute very little ionization energy. The energy flux is non-zero in deeper layers due to the very slow transition from $\sim 90\%$ to 100% He II ionization.

4.2.2.1   Comparing Latent Heat Flux to Stratification in MURaM

By examining the vertical rms velocity in the MURaM simulations as a function of depth (a) and density (b), we can determine whether the latent heat flux or change in stratification dominates the increased rms velocity, similar to the mixing length model (§4.2.1.2). Each of these simulations use the same three equations of state as above with H, He I, and He II ionization (*solid* red curve), no He II ionization (*dotted* green curve) and no He I or He II ionization (*dashed* blue curve). Just as in the mixing length model atmospheres, we find that the majority of the decreased rms velocity in the region of partial ionization (fiducial vertical lines) remains after correcting for the stratification (in part b). Thus the velocity differences in the depths of partial ionzation are caused by the latent heat flux. The velocity differences below the regions of partial helium ionization (seen in the deep layers of part a), however, are due to the changes in the stratification (which is caused by the different particle numbers without He ionization) and disappears after we correct for the stratification (in part b). We also note that the drop in the rms velocity in the deepest layers (and the largest values of density) is due to the enhanced viscosity at the bottom boundary.

This confirms, in both the mixing length model and the MURaM simulations, that the changes in the surface spectrum computed by the two-component model (Figures 4.4 and 4.6) have two well separated effects. At supergranular scales, near the two fiducial vertical lines, the latent heat flux is the primary difference between the two simulations, while at lower wavenumbers the new density stratification causes the changes in the spectrum.
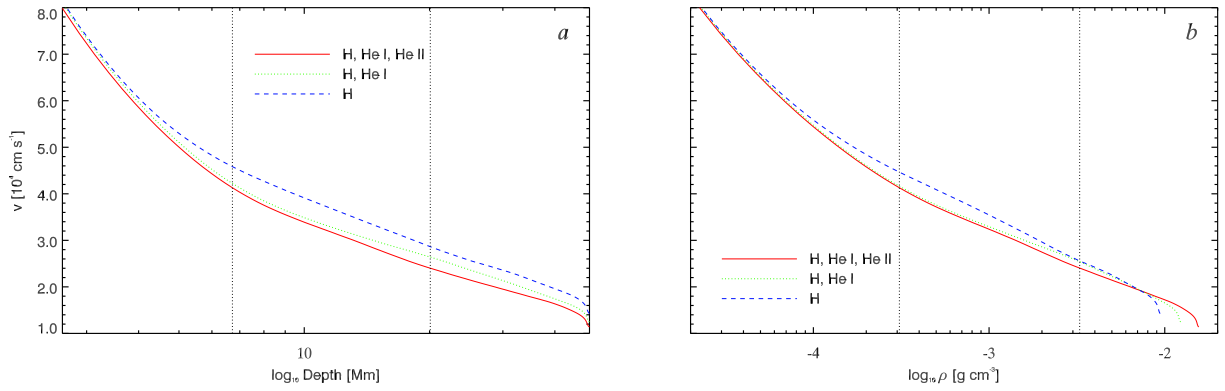
Figure 4.10 The rms vertical velocity from the MURaM atmospheres using the three Saha equations of state as a function of $\log_{10}$ depth (*a*) and $\log_{10}$ density (*b*). The *solid* (red) curve shows the spectrum computed from a mixing length atmosphere with a Saha equation of state that includes H I, He I, and He II ionization; the *dotted* (green) curve is computed from an atmosphere with no He II ionization; and *dashed* (blue) curve is computed from an atmosphere with no He I or II ionization. The vertical *dotted* lines show the depths of 50% He I (depth= 6.5 Mm, $\rho = 3.08 \times 10^{-4}$) and He II (depth= 20 Mm, $\rho = 3.28 \times 10^{-3}$) ionization.

4.2.3   Non-thermal Energy Transport

Experiments that change the ionization properties of the equation of state influence several properties of the plasma. Preventing helium ionization changes the the mean molecular weight, the latent heat flux, and instabilities of the flows. The first two of these factors affect both of the main inputs in the two-component model: the flow speed and the mean stratification. To isolate the effect of the rms velocity on the surface velocity spectrum in three-dimensional radiative hydrodynamic simulations, we employ an artificial energy flux (see §2.1.6) which mimics the effect of the latent heat flux without changing the mean stratification.

4.2.3.1   What is the Artificial Flux?

The artificial energy flux is an artificial term in the energy equation that behaves as a volume heating computed from the divergence of the flux (see §2.1.6 for details). We use a purely vertical flux with a hyperbolic tangent profile that raises the artificial flux from zero at the surface to 6.3×10^{10} erg cm^{-2} s^{-1} (the solar radiative energy flux at the photosphere) throughout the deep part of the simulation (Figure 4.11). Since our simulations are cartesian this value is the full energy flux required at depth for the radiative losses at the surface to equal the solar luminosity. We examine a simulation that has the same dimension and resolution as the reference simulation ($1024 \times 1024 \times 768$ and 192 km $\times$ 192 km $\times$ 64 km) but uses a hyperbolic tangent artificial flux that is 5.12 Mm wide centered at a depth of 10 Mm (this simulation is henceforth referred to as "artificial flux 10 Mm"). Wherever the artificial flux is non-zero it reduces the convective energy flux proportionally, which we see in Figure 4.11. The non-zero convective energy flux below 15 Mm is decaying from the initiation of convection at the start of the simulation (see §2.2 for description of initial condition of these simulations). We do not have sufficient computational resources to relax this simulation further but the data presented here has been ran for at least 11 days after the initiation of convection. While it is unclear where the fully relaxed convective flux would settle, the temporal behavior of the convective energy flux up to this point suggests that it would be

approximately zero.

It is clear from Figure 4.11 that the convective flux is only affected at the depths where the artificial flux is non-zero. By comparing the artificial flux 10 Mm and the reference simulation we find that there is less than 0.1% difference in the mean density and mean density scale height for all depths. Thus the artificial flux only causes negligible change to the mean stratification of the simulation, which, along with the rms velocity, is one of the key inputs to the two-component model. The question remains though: since the convective energy flux is reduced to nearly zero, what properties of the plasma are different between the artificial flux and reference simulations?

In Figure 4.12 we show the ratio of the entropy (in a), density and temperature (in b) in upflows and downflows from both the reference and artificial flux 10 Mm simulations. Above the influence of the artificial energy flux these two simulations exhibit the same convective properties. Since each simulation has the same radiative energy flux at the surface, they have the same entropy contrast in upflows and downflows which drives the convective energy flux. In the region where the artificial energy flux is carrying the full solar energy flux, the entropy is nearly equal in upflows and downflows which is why these flows do not transport any energy. Thus, this is similar to convective overshooting into an adiabatic layer.

The artificial flux acts as a volume heating on the flows in regions where the $\nabla \cdot \mathbf{F}_{artificial} \neq 0$. All of the thermodynamic properties of the upflows and downflows are nearly equal below this volume heating due to the artificial flux. This heating raises the temperature of both the downflows and the upflows. Consequently there is no contrast between the thermodynamic properties of the upflows and downflows in the deep domain while the upflows match the reference simulation above the heating.

As we move above the region of artificial energy flux the upflows have the same properties (and contrast with downflows) in both simulations. Since the upflows reach the surface with the same thermodynamic properties, the downflows, which are created by the radiative cooling in the photosphere, have the same entropy deficit and same entrainment from the diverging upflows in both simulations. While the artificial energy flux dramatically reduces the contrast between
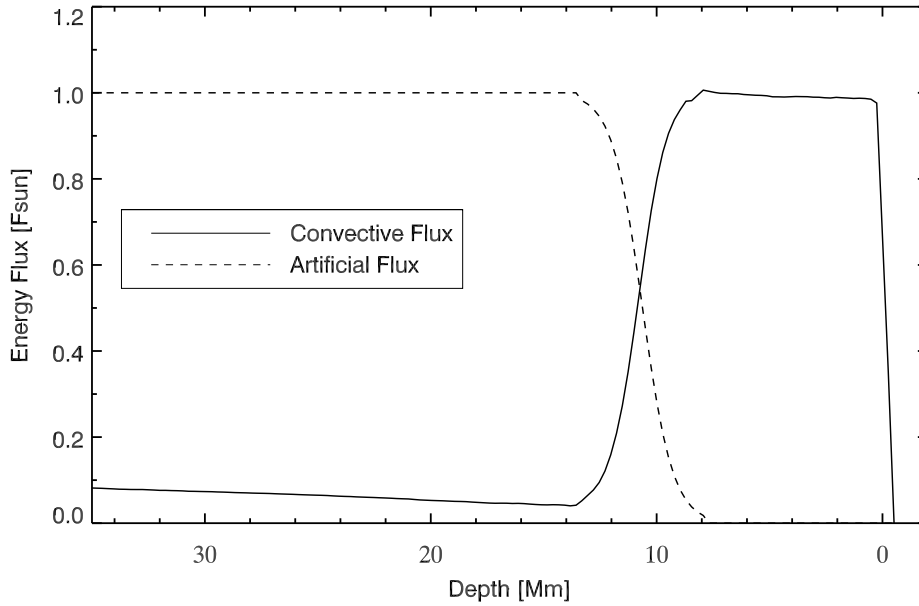
Figure 4.11 The convective flux (*solid*) and artificial energy flux (*dashed*) in units of the solar energy flux (Fsun=6.3×10^{10} erg cm^{-2} s^{-1}) in the artificial flux 10 Mm simulation. The flux is equal to the solar energy flux in the deep layers and then a hyperbolic tangent that is 5.12 Mm wide and centered at a depth of 10 Mm reduces the artificial flux to zero near the surface. The convective flux is proportionally reduced in regions of non-zero artificial flux.
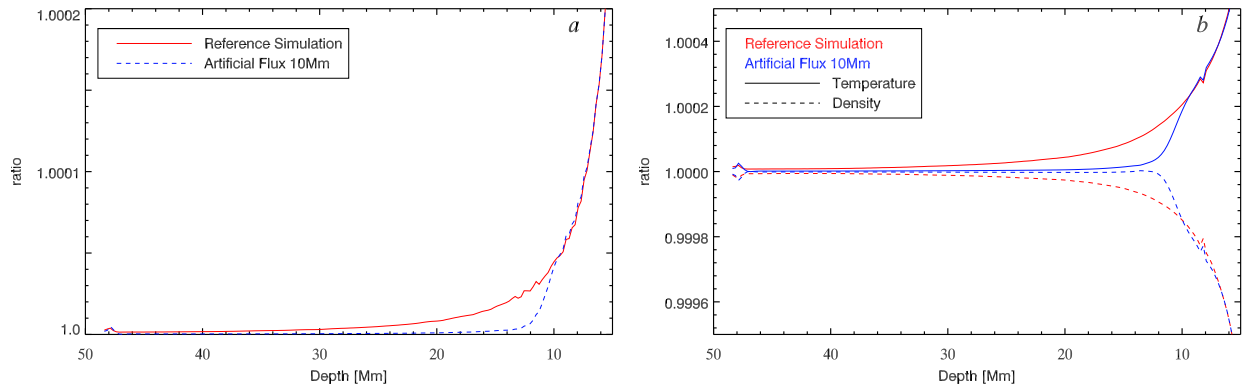
Figure 4.12 The ratio of the entropy (*a*), temperature (*b*, *solid* curve) and density (*b*, *dashed* curve) in the upflows and downflows comparing the reference simulation (red) and artificial flux 10 Mm (blue). The differences between the thermodynamic quantities in upflows and downflows is significantly reduced by the artificial energy flux and thus these flows carry nearly zero convective energy flux. The feature at 8 Mm depth is a problem with the equation of state table that likely does not have too much influence over the simulations and the jump near 50 Mm is due to the bottom boundary condition.

upflows and downflows, it has a minimal effect on the properties of the convection above the region with non-zero divergence of the artificial flux. Since the stratification remains unchanged, this helps isolate the convection in the uppermost 10 Mm without introducing any of the problems of reducing the domain depth (see §3.1).

4.2.3.2   How Does the Artificial Flux Affect the Convection Below This Heating?

By comparing the unsigned vertical mass flux between the artificial flux 10 Mm and reference simulations in Figure 4.13b, we find that there is decreased mass flux in the part of the domain where the artificial energy flux transports the energy (i.e. below 10 Mm). The motions in the region with an artificial energy flux must maintain the mean stratification but these motions transport very little energy or mass in the vertical direction.
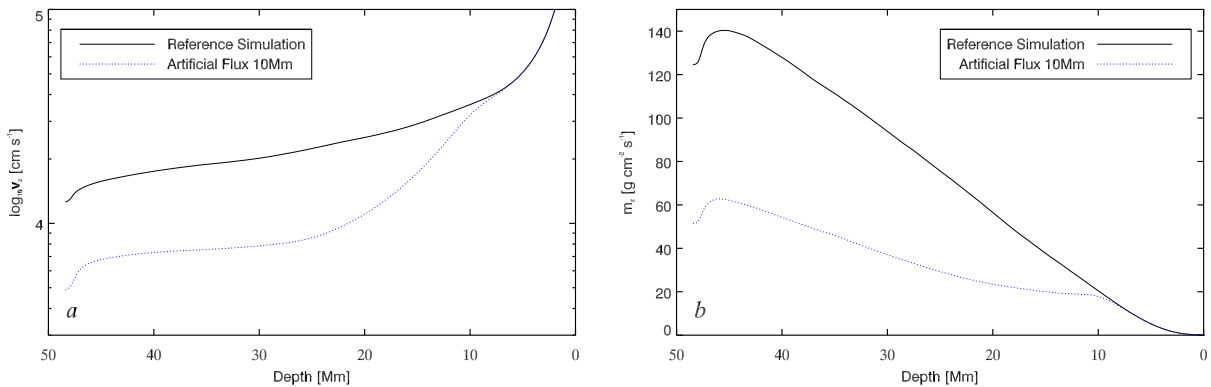
Figure 4.13 The rms vertical velocity as a function of depth (a) and vertical mass flux (b) comparing the reference (*solid* black curve) and artificial flux 10 Mm simulation (*dotted* blue curve). The vertical velocities below 25 Mm depth are reduced by a factor of 2.5 due to the artificial energy flux. The vertical mass flux is also significantly reduced by the artificial energy flux which suggests that there is increased mixing of the plasma below 10 Mm.

Based on the two-component model we expect the vertical rms velocity deep in the domain to produce the low wavenumber power in the photosphere. The decreased horizontal velocity power in the photosphere of the artificial flux 10 Mm simulation (Figure 4.5) suggests that the rms velocity deep in the domain is suppressed. By comparing the velocity in the reference simulation and the artificial flux 10 Mm simulation (Figure 4.13 a) we find that the artificial energy flux simulation has

reduced the rms velocity (which is equal to the total integrated power of the spectrum) by a factor of ~ 2.5 at depths greater than 25 Mm below the photosphere. Since this simulation matches the low wavenumber power in the observations, this provides an estimate for the excess velocity in the deep flows of the reference simulation. In particular, we would expect any simulation that matched observations to be able to transport the solar energy flux (through physical terms in the energy as opposed to our artificial energy flux) with rms velocity a factor of ~ 2.5 slower than our reference simulation.

We know that the amplitude of the low wavenumber flows (and not just the rms velocity) determine the imprinting on the photosphere from comparing the reduced viscosity boundary condition to our standard boundary condition (see §3.1.2.3). This is also true for the two-component model which assumes that modes with scales smaller than the driving (integral) scale follow a Kolmogorov spectrum. Any changes to the shape of the spectrum would change the driving (integral) scale power at depth and, consequently, the imprinted power at the surface. By taking the ratio of the vertical velocity spectrum from the artificial flux 10 Mm and reference simulation we can determine if the artificial energy flux primarily reduces the amplitude at the flows at all wavenumbers or changes the shape of the spectrum. Starting at the depth 5.44 Mm (above the influence of the artificial flux) we see from Figure 4.14 that the artificial flux simulation has nearly identical power for $k/2\pi > 0.06$ Mm^{-1} (i.e. modes with scales smaller than the driving (integral) scale at 10 Mm depth) but significantly reduced power at lower wavenumbers. This is consistent with the assumptions of the two-component model: the modes with wavelengths smaller than the driving (integral) scale ($4H_\rho = 19$ Mm at 10 Mm depth) are driven locally while the low wavenumber power imprints from below.

By a depth of 11.5 Mm the artificial flux is transporting nearly the full solar energy flux (since it is a hyperbolic tangent profile with width 5.12 Mm) and both the low and high wavenumber power is reduced. This trend continues with more high wavenumber power than low wavenumber power until very deep in the domain. By 32 Mm below the photosphere we have a nearly flat ratio between the vertical velocity spectrum in the artificial flux simulation and the reference simulation.
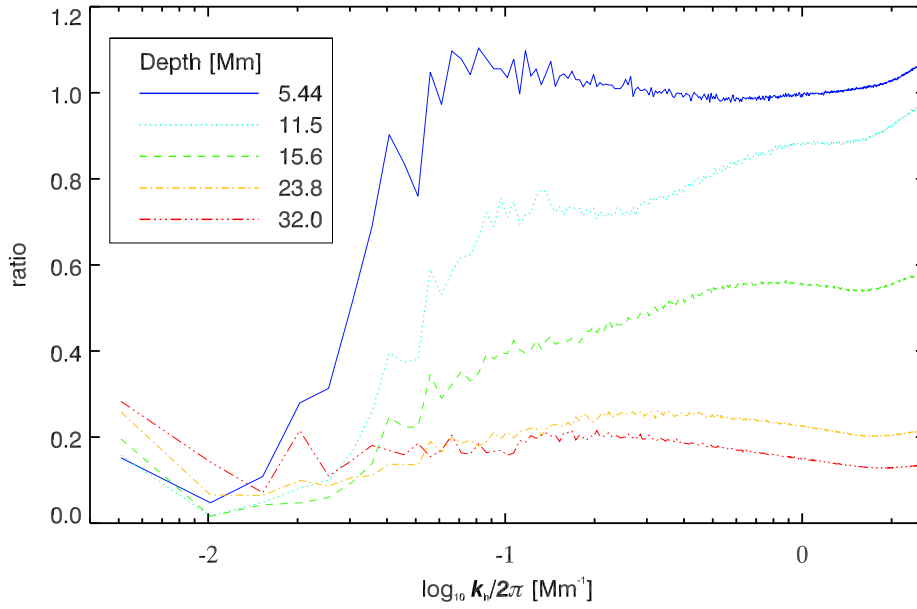
Figure 4.14 The ratio of the vertical velocity spectrum in the reference and artificial flux 10 Mm simulation at five depths: 5.44 Mm, 11.5 Mm, 15.6 Mm, 23.8 Mm, and 32.0 Mm. Above the influence of that artificial energy flux (5.44 Mm, *solid* blue curve) the low wavenumber flows are reduced due to the influence of the artificial energy flux but both simulations have the same power in all modes with scales smaller than $4H_\rho$ at 10 Mm depth. The spectra deep in the domain (32.0 Mm *dash-dot-dot-dot* red curve) has reduced power equally among all modes in the simulation with the artificial flux. We also note that the ratio of the horizontal velocity spectrum between these two simulations (not shown here) is nearly identical to the ratio of the vertical velocity spectrum.

Thus, in the deepest layers of the domain, the reduction in vertical rms velocity (Figure 4.13a) due to the artificial energy flux can be approximated as a uniform decrease in the vertical velocity spectrum. Since the shape of the spectra is qualitatively similar between the artificial flux 10 Mm and reference simulations, we see a similar reduction in the rms velocity (Figure 4.13 a) and the power in the driving (integral) scale mode (Figure 4.14). Thus, the imprinted power on the photosphere is decreased (as we see in Figure 4.5). We revisit this issue in §5.2.

4.2.3.3 Photospheric Motions

Finally, we compare the photospheric horizontal velocity spectrum between the artificial flux 10 Mm (*dotted* blue curve) and reference (*solid* black curve) simulations in Figure 4.15. We also compare to the spectrum computed from the CST method applied to full-disk HMI observations (*long-dash* green curve) (Roudier et al., 2012). While the comparison between the simulations and observations is not as robust as Figure 4.5 (since it does not use the CST method to compute the velocities in both cases), both figures are in qualitative agreement except at high wavenumber where the CST method is less reliable.

In order to compare to the series of shallower simulations in §3.1, we compute an additional artificial flux simulation (red *dash* curve) in Figure 4.15 which has an artificial flux with a hyperbolic tangent profile that is 5.12 Mm wide centered at 2.56 Mm depth with the same domain size and resolution as the reference simulation and artificial flux 10 Mm simulation. The volume heating due to the divergence of the artificial flux in this new simulation begins directly below the photosphere. This simulation helps explore the effects of the near-surface convection without any influence of deeper convection and provides a spectrum of photospheric motions that are purely driven at the surface without the influence of the bottom boundary in very shallow domains (see §3.1). For both artificial energy flux simulations we include the wavenumber corresponding $4H_\rho$ at 10 Mm depth ($k/2\pi = 0.053$ Mm^{-1}, blue circle) and 2.56 Mm depth ($k/2\pi = 0.28$ Mm^{-1}, red circle) which divides the locally driven flows above the region with the artificial flux and the flows that have driving (integral) scale deeper in the domain. This new simulation (which we denote "artificial
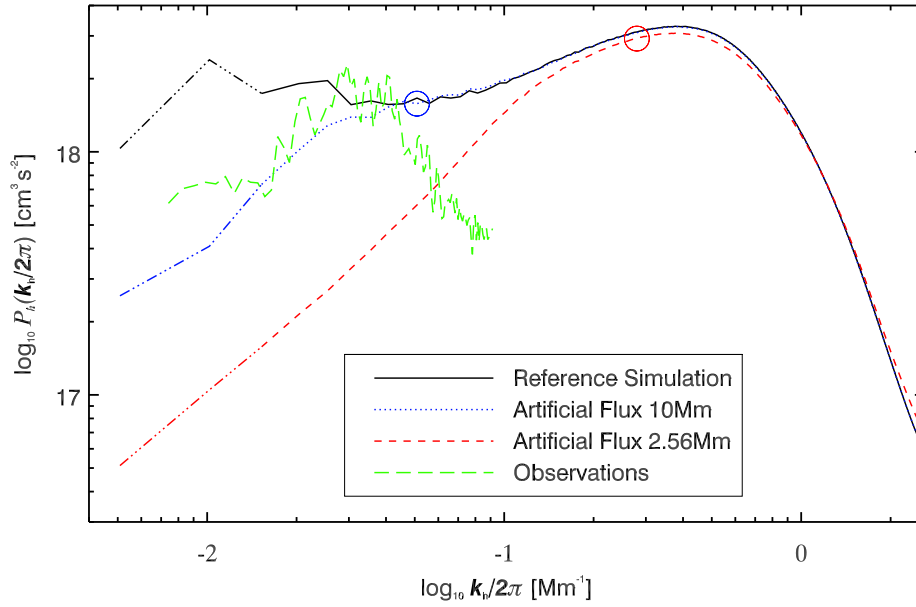
Figure 4.15 The photospheric horizontal velocity spectrum comparing MURaM and HMI observations. The spectra compares the reference simulation (*solid* black curve), artificial flux 10 Mm (*dotted* blue curve), artificial flux 2.56 Mm (*dashed* red curve), and HMI observations computed using CST velocity from Roudier et al. (2012). The blue and red circles show the wavenumber corresponding to $4H_\rho$ at 10 Mm ($4H_\rho = 19$ Mm, $k/2\pi = 0.053$ Mm^{-1}) and 2.56 Mm ($4H_\rho = 3.6$ Mm, $k/2\pi = 0.28$ Mm^{-1}) respectively. For all simulations we change the linestyle to *dash-dot-dot-dot* for the two largest scale modes which have driving depths that are outside the simulation domain and have consequently lower power than we would expect from a deeper simulation.

flux 2.56 Mm") further confirms that the low wavenumber power in the photosphere imprints from below the surface.

For all three simulations we change the linestyle to *dot-dot-dot-dash* for the two lowest wavenumber modes. These simulations have domain depth of 49 Mm where $4H_\rho$ is less than the wavelength of these two modes. Thus, based on our two-component model and previous experiments with shallow simulations (see Figure 3.1), we expect these simulations to underestimate the power that would be present in a deeper simulations. Furthermore, the box mode (see §3.1.6) strongly influences these modes in the reference simulation making them unreliable.

Chapter 5

The Role of Magnetic Fields

Our work with hydrodynamic simulations in the previous chapters suggests that deeper simulations have excess power in modes with wavelengths larger than supergranulation. There are two physical mechanisms in the Sun that we have not examined that may explain our mismatch with observations: rotation (along with the near surface shear layer) and magnetism. In this chapter we focus on the effects of quiet Sun magnetic fields on the flows.

The observed quiet Sun magnetic field occurs on many scales but is visually dominated by the magnetic network which have the strongest field strengths of any quiet Sun magnetic elements. This network field is primarily found in downflows at the vertices of supergranules and is thought to be a passive tracer due to the low plasma β and high conductivity in the photosphere. Recent observations, however, find increased length scale of the supergranules (in quiet Sun regions) at solar maximum in both the photosphere and chromosphere (McIntosh et al., 2011). This suggests that magnetic fields may influence the length scale of supergranulation. Previous theoretical work has suggested that the magnetic field provides a physical mechanism that determines the length scale of the supergranules (Crouch et al., 2007). Magnetic elements that are advected to downflows (with lifetime increased by strong magnetic flux elements) may organize convection on larger scales based on purely photospheric motions (Rast, 2003). This is inconsistent with our previous results suggesting that low wavenumber power imprints from deeper flows.

While quiet Sun magnetism is associated with weak net magnetic flux at the surface, the magnetic network in the solar photosphere exhibits net magnetic flux on scales larger than super-

granulation which suggests that it is field from decaying active regions generated by the global dynamo (Lamb et al., 2010). Thus, to explore quiet Sun magnetism we compute small-scale dynamo simulations with a range of small net magnetic flux (where 0 G $\leq \langle B_z \rangle \leq 15$ G does not change from the initial value in the simulation) that represent a range of influences from the global dynamo. We use magnetic Prandtl number (i.e. the ratio of viscous to magnetic diffusion) approximately one (similar to Rempel, 2014). While the magnetic network field visually dominates quiet Sun magnetism, recent observations have improved our understanding of the internetwork field. These observations show stronger transverse field than vertical field in the photosphere which is evidence of a small-scale dynamo active at the solar surface. There is significant debate about how well small-scale dynamo simulations represent the solar convection zone where the magnetic Prandtl number is $\sim 10^{-5}$ in the solar photosphere (with significant variation in this value near the surface, Martínez Pillet, 2013). Thus all of these simulations assume that magnetic Prandtl one is a reasonable approximation to the solar small-scale dynamo (we continue this discussion in §5.3).

The small-scale dynamo magnetic fields in our simulations do not enhance the flow power at any scale. We also add magnetic fields to the artificial energy flux simulations that we introduced in §4. This artificial energy flux is a term, $\mathbf{F}_{artificial}$, in the energy equation (see §2.1.6) that artificially transports energy at specified depths. Since this could be confused with magnetic flux (measured in G cm^{-2}) in the following chapter, we call specific attention to the difference here. We refer to the two artificial energy flux simulations as artificial flux 10 Mm and 2.56 Mm based on the depth at which the hyperbolic tangent profile of $F_{artificial}$ is centered. These simulations always allow the full energy flux at the photosphere and then we increase $F_{artificial}$ from zero (in the top of the simulation) to be equal to the solar radiative energy flux (in the bottom of the simulation). These artificial energy flux simulations allow us to test the suggestion that magnetic fields organize larger scale flows in simulations where the low wavenumber convection is weak.

Our simulations find that, unlike the suggestions of Crouch et al. (2007), the quiet Sun magnetic fields qualitatively decrease low wavenumber horizontal velocity power in the photosphere. Thus magnetic fields may be a mechanism that helps decrease the excess low wavenumber power

in the hydrodynamic simulations (Figure 4.5). This decreased low wavenumber power, however, is insufficient to match solar observations. We find that the decreased low wavenumber power at the surface is due to suppressed rms velocities deep in the domain; the Lorentz force decreases the kinetic energy carried by downflows which allows the convection to maintain the solar energy flux with reduced upward enthalpy flux.

5.1   The Effect of Magnetic Fields on Photospheric Motions

While solar active regions have super-equipartition magnetic fields that inhibit flows in the form of sunspots and pores, the magnetic fields in the quiet Sun are weaker on average than equipartition and thought to be passive tracers of surface flows. We explore the influence of the magnetic field by adding either a zero net flux (i.e. $\langle B_z \rangle = 0$ with $B_{rms} \approx 0.5$ G) or a 10 G mean magnetic field to our reference simulation. This field then grows through small-scale dynamo action (see §1.1.4). All of these these simulations were run for 5.5 days of relaxed time after the kinematic growth phase of the dynamo. The resulting photospheric field strength for the zero net flux simulation (unsigned vertical flux of 37G) is weaker than the best estimates of solar magnetic field from Hinode Zeeman data (unsigned vertical flux of $\sim$ 60G, Danilovic et al. (2010); Orozco Suárez & Bellot Rubio (2012)) while the 10 G mean field simulation is similar to quiet Sun field strength (unsigned vertical flux 68G, see Table 5.1). This is in part because of the relatively low resolution of these simulations (192 km horizontally) which restricts the twisting of magnetic fields in the photosphere where flow scales are the smallest. This low resolution also increases the magnetic diffusivity of the simulation which limits dynamo action.

The resolution of our simulations does not allow magnetic field on scales smaller than 192 km. This artificially increases the low wavenumber power in the magnetic field spectrum compared to well resolved small-scale dynamo simulations of the solar photosphere (Rempel, 2014). Simulations with horizontal resolution ranging from 32 km to 2 km find that half of magnetic energy is on scales smaller than 100 km (Rempel, 2014). Despite the issues with resolution near the photosphere, these simulations are well resolved for dynamo action deep in the domain and, as far as we are aware,

are the most stratified solar-like small-scale dynamo simulations with a realistic photosphere to date. Thus, these simulations provide insight into the effects of the small-scale dynamo on the deep convection and how that impacts the imprinting on the surface.

We compare the photospheric horizontal velocity spectrum from these magnetized simulations and the reference simulations in Figure 5.1. Adding magnetic field to the reference simulation does not enhance the flows at any scale. There is a qualitative reduction in photospheric power from both the zero net flux and 10 G mean field, but the wavenumber with largest difference in power between magnetized and hydrodynamic simulations is not statistically significant (shown using one standard deviation error bars computed from the time series of power at $k/2\pi = 0.025$ Mm^{-1}). As we know from §4, the reference simulation has excess low wavenumber power compared to observations. Thus, while these results are not statistically significant, this suggests that magnetic fields are a possible mechanism to reduce low wavenumber flows in the photosphere. We revisit this in §5.2.

5.1.1   Enhancing the Radiative Losses

The magnetic field concentrations in the supergranular vertices help sustain increased radiative losses. The magnetic pressure reduces the density, and consequently, the opacity of the plasma which allows the photons to escape from deeper in the photosphere where the temperature is higher. Previous work has linked increased downflow lifetime with larger scale flows (Rast, 2003). It has been suggested that the lifetime of magnetic elements in the photosphere is longer than hydrodynamic flow timescales (Crouch et al., 2007). These longer lived network magnetic elements are collocated with downflows and increase the rate of cooling. Thus magnetized downflows may have increased lifetime (compared to hydrodynamic downflows) since they are sustained by increased cooling and stabilized by the longer lived magnetic elements. Increasing the lifetime of downflows *may* organize the flows larger scales (Rast, 2003).

We test this hypothesis by taking the zero net flux small-scale dynamo simulation and enhancing the radiative cooling term in the energy equation (the divergence of the radiative flux)
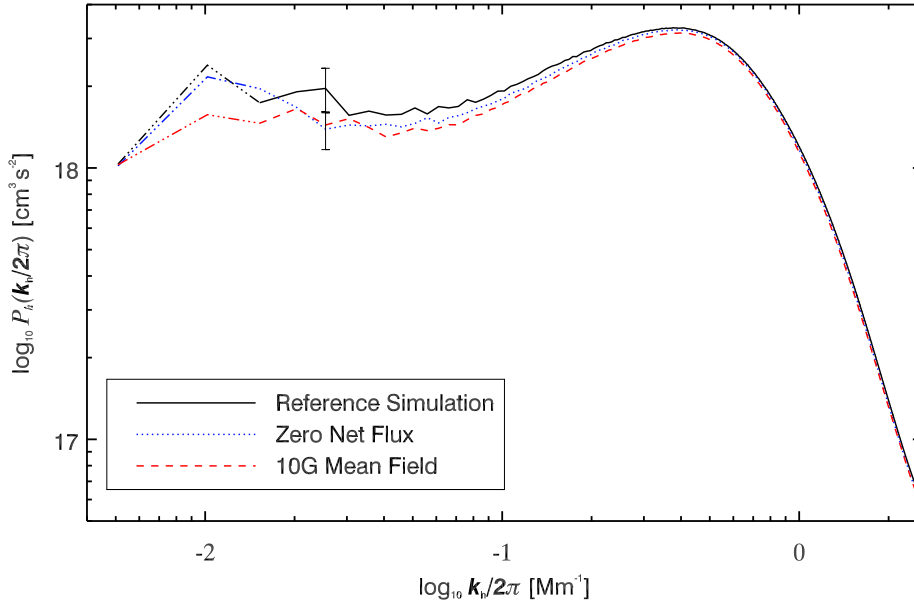
Figure 5.1 The photospheric horizontal velocity spectrum from the reference (*solid* black curve), zero net flux (*dotted* blue curve), and 10 G mean field (*dashed* red curve) small-scale dynamo simulations. While the magnetic simulations have qualitatively less power at low wavenumbers, we show that the one standard deviation error bars overlap for the mode with the biggest different between the reference and 10 G mean field simulations. We change the linestyle to *dash-dot-dot-dot* for the modes that have driving depths outside the simulation domain and consequently lower power than we would expect from a deeper simulation.

as a function of vertical magnetic field, specifically $(1 + \alpha_{cooling}(\frac{B_z}{1000\text{G}})^2)$ for $|B_z| < 1000$G and $(1 + \alpha_{cooling})$ for $|B_z| \geq 1000$G. By using $\alpha_{cooling} = 3$, a maximum enhancement of a factor of 4 for all $|B_z| \geq 1000$G (this choice was made to ensure a significant change in the cooling rate), we find that our simulation has 10% increased radiative cooling for photospheric regions with field strength $|B| > 100$G and overall this increases the radiative energy flux by approximately 1.8%. Comparing the zero net flux simulation to the simulation with enhanced radiative losses (Figure 5.2) we find that the horizontal velocity spectrum is qualitatively identical with no difference in power at any scale. This suggests that the enhanced radiative cooling through the magnetic network does not have a significant effect on the surface flows.

5.1.2   Spectrum of Magnetic Fields

We found that enhancing the radiative energy flux in regions of strong magnetic field does not enhance the flows but this may still influence the magnetic field distribution. We compare the magnetic energy spectrum to determine if it induces different scale magnetic fields (Figure 5.3). This spectrum is computed in the same way as the velocity power spectrum, see §3.1.1, by substituting the magnitude of the magnetic field for velocity. This spectrum shows that enhancing the radiative losses through the magnetic network does not influence the distribution of the magnetic field. This simulation has the same rms field strength (which is proportional to the square root of the integral of the magnetic field spectrum) and qualitatively identical magnetic field spectrum to the zero net flux simulation, which suggests that enhancing the cooling has minimal effect on the photospheric flows and magnetic field distribution. This is evidence that the low wavenumber flows in the photosphere are primarily determined by the deeper convection and the contribution of the magnetic field to the properties of photospheric radiation do not influence the flows there.

Adding a 10 G mean field, however, increases the rms field strength in the photosphere by nearly a factor of two (see Table 5.1) and concentrates the field on larger scales. These larger scale features are visible as magnetic pores which are concentrations of magnetic fields with $|B| > 1000$ G that inhibit convective motions, similar to sunspots (see Figure 5.6). These magnetic pores are only
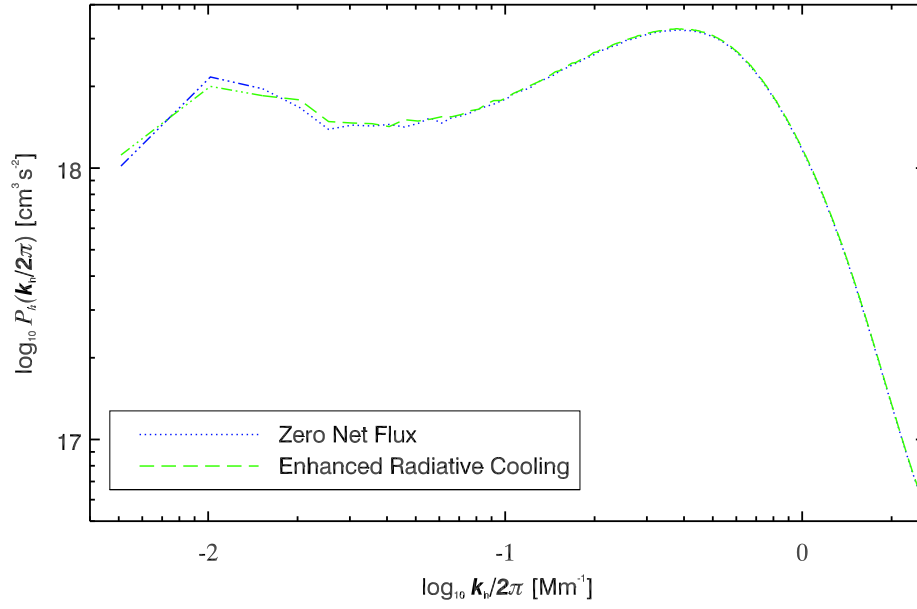
Figure 5.2 The photospheric horizontal velocity spectrum from zero net flux small-scale dynamo (*dotted* blue curve) and a simulation with same magnetic field strength that enhances the radiative losses through the magnetic field (*long-dash* green curve). We change the linestyle to *dash-dot-dot-dot* for the modes that have driving depths outside the simulation domain and consequently lower power than we would expect from a deeper simulation.
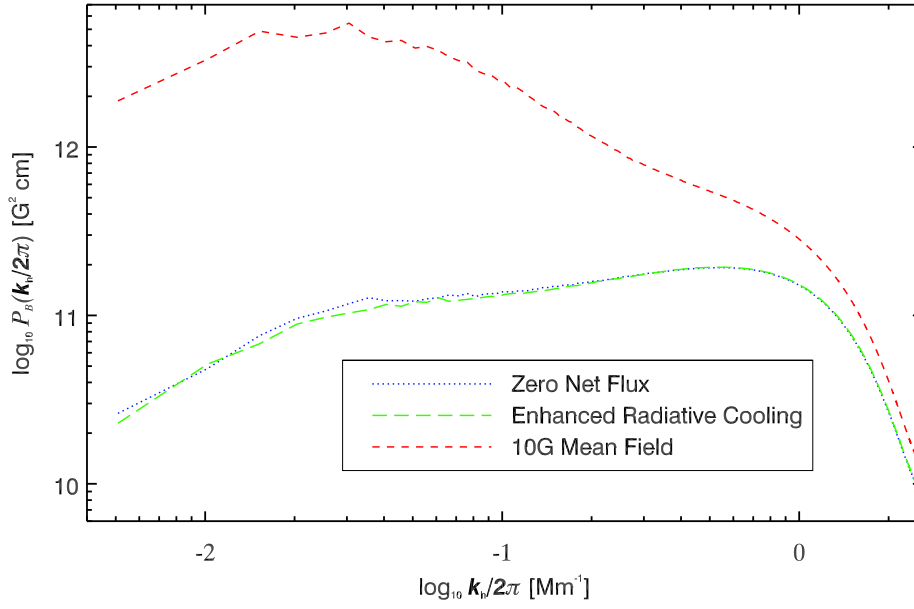
Figure 5.3 The photospheric magnetic field spectrum for the 10 G mean field (*dashed* red curve), zero net flux (*dotted* blue curve), and enhanced radiative cooling (*long-dash* green curve) simulations. The 10 G mean field simulation has significantly more rms field strength in the photosphere and, consequently, increased power in the magnetic spectrum. The enhanced radiative cooling simulation shows no qualitative differences from the zero net flux simulation.

Table 5.1.   Photospheric Magnetic Field Strength

	Zero Net Flux	10 G Mean Field	Artificial Flux 10 Mm, 15 G	Artificial Flux 2.56 Mm, 15 G
$\sqrt{<B^2>}$	140G	269G	202G	159G
$<|B_z|>$	37.2G	68.5G	53.2G	45.3G

Note. — The rms field strength (first row) and mean unsigned vertical magnetic flux (second row) for the four primary magnetic field simulations that we analyze in §sec:magsurface. Observations of the quiet Sun measure the unsigned vertical magnetic flux as ~ 64G (Orozco Suárez & Bellot Rubio, 2012).

found in the solar photosphere in magnetically active regions with net magnetic flux larger than 10 G that we associate with the global dynamo. Quiet Sun magnetic field is concentrated on smaller scales than found in the 10 G mean field simulation. Recent small-scale dynamo simulations have found that more than half of quiet Sun magnetic energy is on scales smaller than 100 km (Rempel, 2014). Furthermore, reducing the simulation resolution artificially enhances the magnetic power at low wavenumbers because lower resolution restricts the modes in the spectrum (Rempel, 2014). Thus, the magnetic power on large-scales is artificially enhanced in our simulations since we use such a low resolution (192 km horizontally).

5.1.3   Magnetic Fields with Artificial Flux

Based on our comparison with observations in §4, we know that the magnetized and hydrodynamic reference simulations have excess photospheric power at low wavenumbers. Using an artificial energy flux that transports the solar energy flux below 10 Mm (see §4.2.3), we reduce the amplitude of the deep convective flows and match solar observations of the horizontal velocity spectrum. Since most of the low wavenumber photospheric power originates from deeper flows, any enhancement of low wavenumber flows by the enhanced radiative cooling may be dominated by the contribution from the large-scale deep convection. To determine the effect of the magnetic fields to the photospheric motions without excess low wavenumber power, we add a 15 G mean magnetic field (which grows due to small-scale dynamo action) to the artificial flux 10 Mm and artificial flux 2.56 Mm simulations. To save computing time we reduce the domain depth of these artificial flux

with magnetic field simulations such that the bottom 50% of the domain transports the full energy flux using the artificial energy flux: 24.576 Mm (for the artificial flux 10 Mm simulation) and 10.24 Mm (for the artificial flux 2.56 Mm simulation). The decreased depth of these simulations does not have any noticeable impact on the photospheric properties.

We also test the influence of the radiative losses through the magnetic network by re-computing these magnetized artificial energy flux simulations with an artificially enhanced radiative cooling with $\alpha_{cooling} = 1$ which doubles the cooling for field strength greater than 1000 G (see §5.1.1 for details on the artificially enhanced radiative cooling).
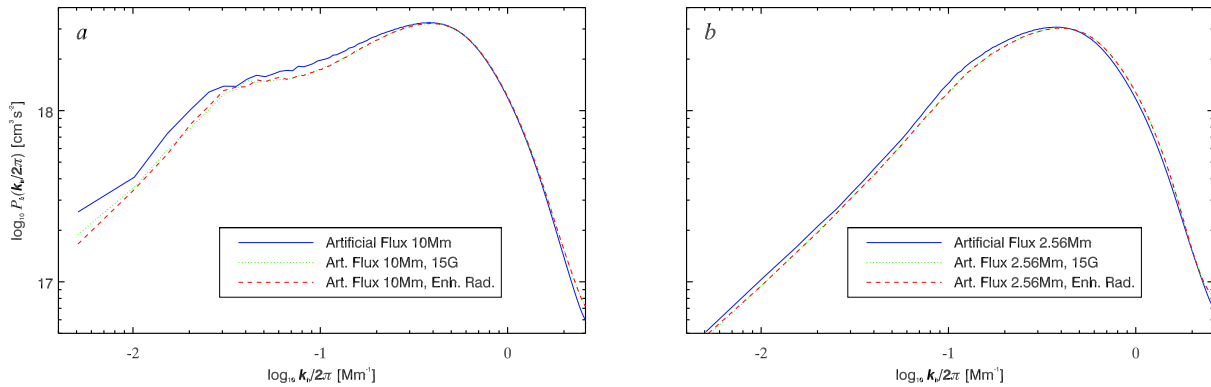
Figure 5.4 Photospheric horizontal velocity spectrum for three simulations with artificial energy flux: hydrodynamic (*solid* blue curve), 15 G mean field (*dotted* green curve), and enhanced radiative cooling (*dashed* red curve). We use artificial flux 10 Mm in part *a* and artificial flux 2.56 Mm in part *b*. Similar to Figure 5.1, the magnetic field qualitatively decreases the power for modes with scales larger than granulation.

Similar to Figure 5.1, adding magnetic fields to the artificial energy flux simulations qualitatively reduces the low wavenumber horizontal velocity power in the photosphere (Figure 5.4*a* and *b*). These results, however, are not statistically significant. This confirms the previous result that the quiet Sun magnetic fields do not enhance the flows at any scale and instead decreases the power in the large-scale motions in the photosphere.

Just as in Figure 5.2, artificially enhancing the radiative cooling in strong magnetic field regions is qualitatively identical to the simulation with normal cooling. This adds more evidence that the effects of the magnetic fields on the radiative properties of the photosphere does not alter

the flows.

5.1.3.1   Scales of Surface Magnetic Field with Artificial Energy Flux

Adding magnetic fields to the artificial energy flux simulations verifies that the magnetic field does not enhance the flows at any scale. These simulations can also help us understand the relationship between the low wavenumber photospheric flows and the spectrum of photospheric magnetic fields. In Figure 5.5 we compare the magnetic field spectrum for the 10 G mean field, zero net flux and the two 15 G mean field simulations with artificial energy flux near the surface (at 10 Mm and 2.56 Mm depth). The artificial energy flux has two effects on the surface magnetic field. These simulations have reduced rms field strength which we explore in §5.1.3.2. In addition to this reduced field strength, we find that the increased low wavenumber flows of the simulations without an artificial energy flux organizes the magnetic field on larger scales. While the artificial energy flux also reduces the magnetic field strength, we can compare the two weakest field simulations (artificial flux 2.56 Mm with 15 G mean field as *long-dashed* yellow curve and zero net magnetic flux *dotted* blue curve) and two strongest field simulations (artificial flux 10 Mm with 15 G mean field *dashed* green curve and 10 G mean field *solid* red curve) to help isolate the effects of the low wavenumber flows. Both comparisons have similar photospheric magnetic field strength (see Table 5.1). This suggests that the large-scale deep flows have a strong effect on the magnetic energy spectrum; large amplitude low wavenumber flows organize the magnetic energy on larger scales in the photosphere.

This difference in the separation of the strongest magnetic elements is also visible in the snapshots of the vertical magnetic field from all four simulations (Figure 5.6). The 10 G mean field simulation has the strongest magnetic fields concentrations (including magnetic pores) at very large scales. On the other hand, the artificial energy flux 10 Mm simulation with 15 G mean field, which has similar photospheric rms field strength, shows a field separation much more similar to quiet Sun magnetic network with typical separation on the scale of supergranules. Comparing the zero net flux simulation and the artificial flux 2.56 Mm simulation with 15 G mean field (which also have similar rms field strength, see Table 5.1), the scales for the artificial energy flux simulation are
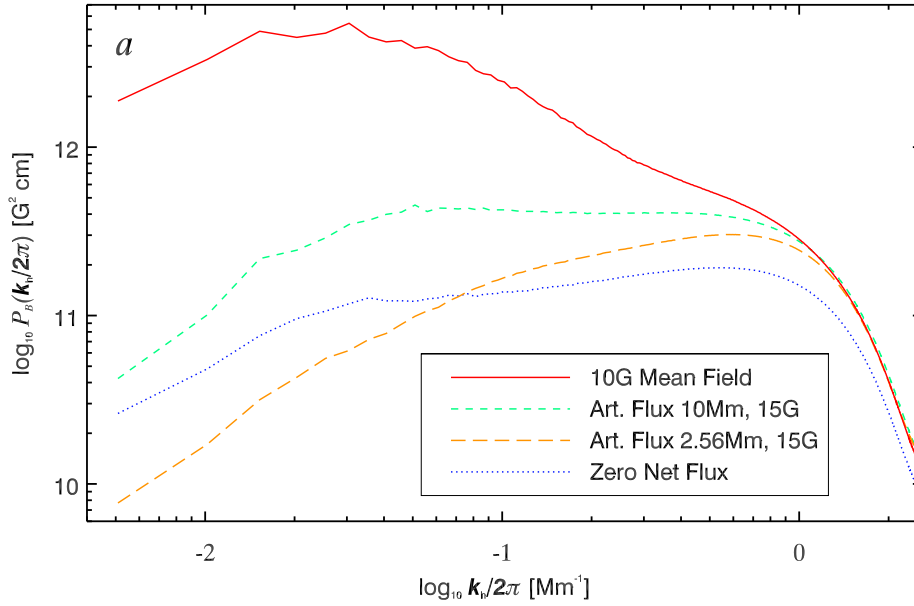
Figure 5.5 The photospheric magnetic field spectrum for the zero net flux (*dotted* blue curve), 10 G mean field (*solid* red curve), artificial flux 10 Mm, 15 G (*dashed* green curve) and artificial flux 2.56 Mm, 15 G (*long-dashed* yellow curve) simulations. The 10 G mean field simulation has statistically significantly increased low wavenumber power. Higher resolution small-scale dynamo simulations (with zero net flux) find that more than 50% of the magnetic energy is on scales smaller than our resolution allows (Rempel, 2014).
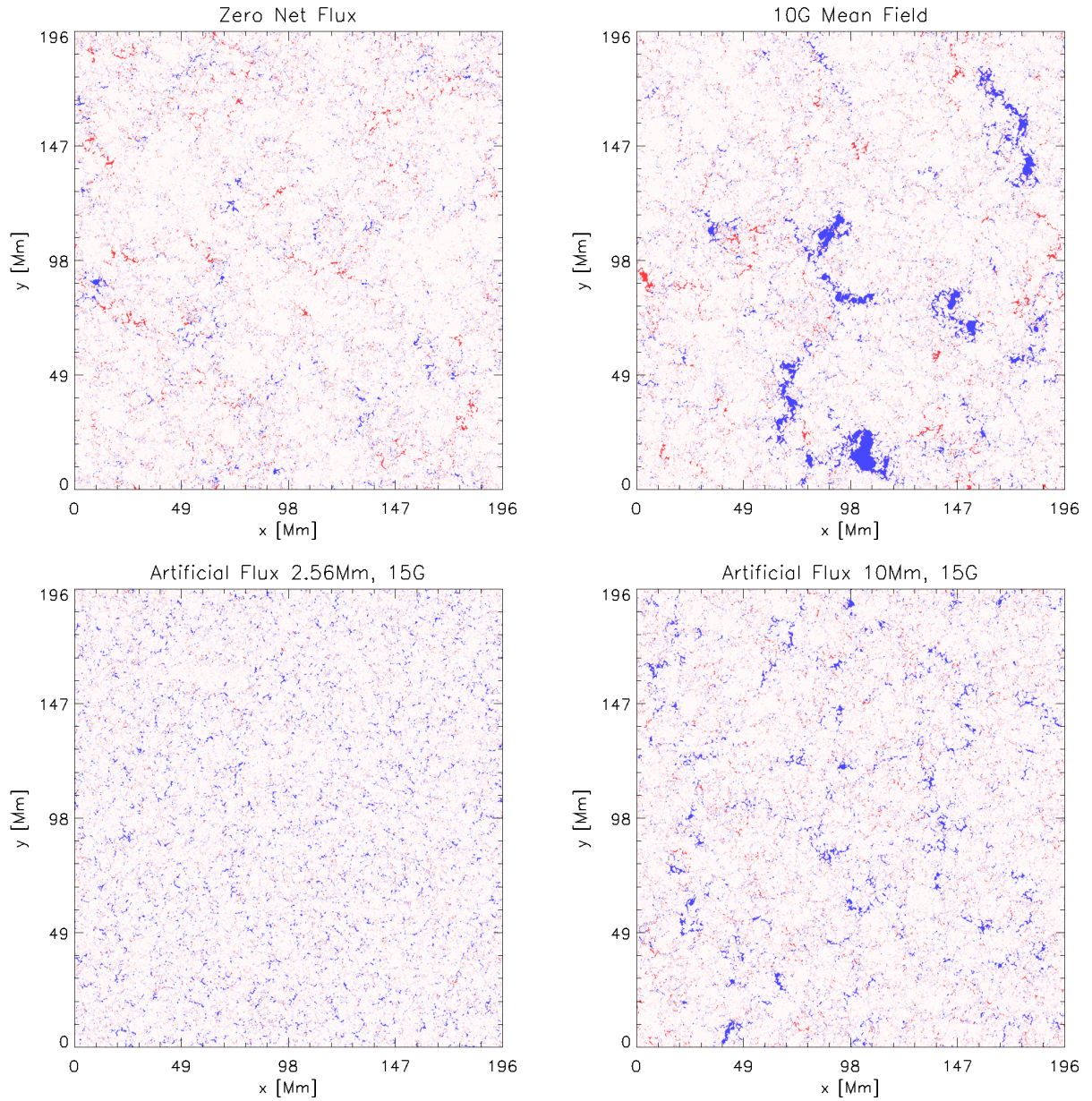
Figure 5.6 The photospheric vertical magnetic field for the zero net flux, 10 G mean field, artificial flux 10 Mm, 15 G and artificial flux 2.56 Mm, 15 G simulations. The color table for all four magnetograms are normalized so that blue displays magnetic field that is saturated at +500G and red shows magnetic field that is saturated at -500G (with white being zero magnetic field).

significantly smaller. This suggests that the magnetic fields in the photosphere are largely passive tracers as has been previously assumed and that the flows dominate the pattern of the photospheric magnetic field.

We also note that the zero net flux simulation also has significant magnetic flux imbalances on scales larger than supergranulation. Magnetic flux imbalances observed in the network field has been suggested as evidence that the magnetic network are remnants from decaying active regions generated by the global dynamo (Lamb et al., 2010). Examining the mean vertical magnetic field in a box that is 49×49 Mm^2 in size, we find that the zero net flux simulation has a maximum magnetic flux imbalance of $\langle B_z \rangle_{box} = 13$ G in the photospheric magnetic field snapshot shown in Figure 5.6. This averaging is done by shifting the box (which is one quarter of the horizontal length of the domain) across the full domain. Since a small-scale dynamo in the solar photosphere must maintain zero net magnetic flux across the full photosphere (which has an area more than 150 times larger than our simulation domain width), this suggests that large-scale magnetic flux imbalances in the solar photosphere can be generated by a local dynamo even if the local dynamo produces zero net magnetic flux when averaging over the full solar surface.

5.1.3.2   Why is the Photospheric Magnetic Field Weaker with the Artificial Energy Flux?

Since the bottom boundary condition of our magnetized simulations advects horizontal field into the domain (see §2.1.4.2), based on previous small-scale dynamo simulations we expect the strength of the photosphere to primarily depend on the resolution and net flux in the simulation and not the depth of the simulation (Rempel, 2014). Additionally, since the dynamo efficiency largely depends on the rate of plasma recirculation and the simulations with artificial energy flux have increased plasma recirculation, as we found in Figure 4.13b, we might expect the simulations with the artificial energy flux to have a higher dynamo efficiency. The field strength in the photosphere of the artificial energy flux simulations, however, is weaker than the standard simulations despite having stronger net flux.
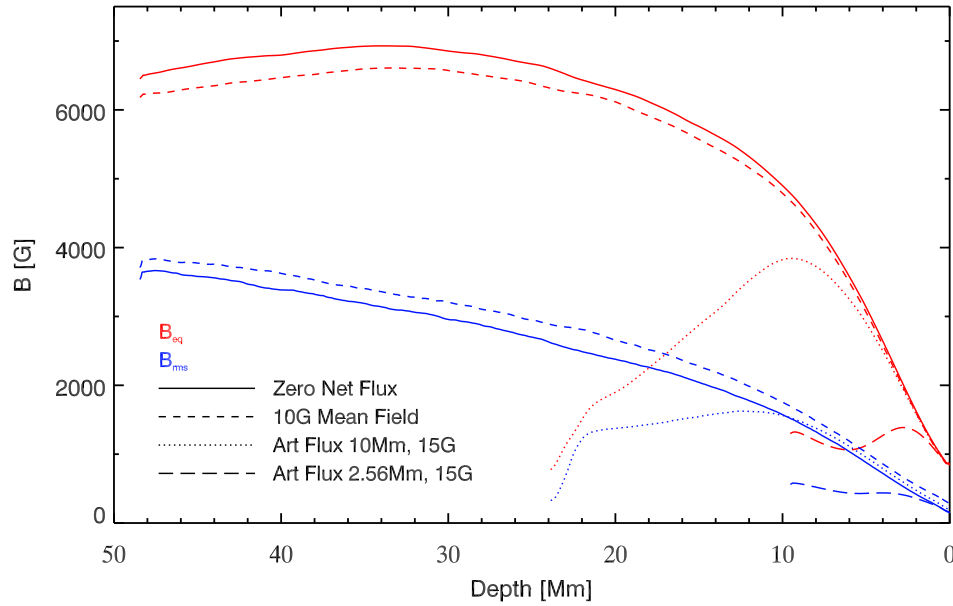
Figure 5.7 The rms (blue) and equipartition (red) field strength for the zero net flux (*solid* curve), 10 G mean field (*dashed* curve), artificial flux 10 Mm, 15 G (*dotted* curve) and artificial flux 2.56 Mm, 15 G (*long-dashed* curve) simulations. The reduction in rms field strength in the artificial flux simulation is largely due to the decreased equipartition field strength, which may be an upper limit for the small-scale dynamo field. The 10 G mean field simulation has increased rms field strength compared to the zero net flux simulation but this reduces the flow speeds which feeds back into the equipartition field strength. Thus these equipartition field strengths are upper limits estimates.

Since, as we discussed in §4.2.3, we know that the photospheric dynamics of the artificial energy flux and standard energy flux simulations is similar, we examine the subsurface magnetic field to determine why the photospheric field is weaker. In Figure 5.7, we find that the artificial energy flux simulations have significantly weaker rms field strength (blue curves) at depths where the artificial energy flux is active (right below the photosphere in the case of the artificial flux 2.56 Mm simulation and below 7.44 Mm in the artificial flux 10 Mm simulation). This occurs because the artificial energy flux decreases the rms velocity at depth, which reduces the equipartition field strength defined as $B_{eq} = \sqrt{4\pi\rho}\ v_{rms}$ (red curves in Figure 5.7). We use the ratio of the rms magnetic field strength, B_{rms}, to the equipartition field strength as a measure of the dynamo efficiency. While the dynamo is just as efficient in the artificial energy flux simulations (or, at some depths, more efficient), the reduced subsurface flow speeds also reduces the kinetic energy available to be converted to magnetic energy. Since the magnetic field is advected to the surface, the simulations with higher rms field strength at depth have increased photospheric magnetic field.

We also note that the 10 G mean field simulation has increased rms field strength throughout the domain compared to the zero net flux simulation but this increased field strength reduces the flow speeds (see Figure 5.10) which feeds back into the equipartition field strength. Thus the plotted equipartition field strengths are actually upper limits estimates for the equipartition field strength, since a simulation that reached equipartition between the kinetic energy and magnetic energy would have reduced kinetic energy compared the simulations presented here. This suggests that having rms field strength equal to the equipartition field strength would not be sufficient to reduce the rms velocity of the deep flows (below ~ 10 Mm) by a factor of 2.5, the estimate for the velocity reduction required to match the low wavenumber power in observations of the photospheric horizontal velocity spectrum (§4).

5.1.4 Photospheric Time Scales

While the evidence from our small-scale dynamo simulations is that magnetic fields do not enhance photospheric flows on any scale, the scale enhancement stemmed from the suggestion that

magnetic fields could increase the timescale of the flows. The original suggestions were that the downflows associated with network magnetic field may live longer than weak-field downflows either because the radiative cooling is enhanced by strong magnetic fields or strong magnetic flux elements require an opposite signed magnetic flux element to cancel the field which is longer than the flow lifetimes with weak magnetic field (Crouch et al., 2007).

5.1.4.1 Lifetime of Supergranular Scale Horizontal Divergence

To compare the dominant horizontal supergranular motions in the photosphere between simulations, we compute the temporal autocorrelation of the Fourier filtered horizontal divergence (similar to the correlations in §3.2). We correlate these horizontal divergence maps across 12 hours before and after the central snapshot and then recompute these correlations for a total of 25 realizations spread across the full 5.5 days of simulated solar time. Since the granular scale motions dominate the photospheric timescales, we apply a Fourier filter to remove motions on scales smaller than supergranulation ($\lambda_h < 20$ Mm) and also remove the low wavenumber modes that may be influenced by box mode ($\lambda_h \geq 98$ Mm, see §3.1.6). Since our Fourier filter requires a smooth edge to the filter to avoid ringing, we center this upper limit at $\lambda_h = 50$ Mm to remove all influence of the box mode.

The resulting correlations show small differences between the simulations that do not use the artificial energy flux: the reference (*solid* black curve), zero net (magnetic) flux (*dot* blue curve), and 10 G mean field (*dash* red curve) simulations. The full width at half maximum (FWHM), which measures the timescale for the flows to become de-correlated, is $\sim$ 11hrs for each of these simulations (see Table 5.2). While the zero net flux simulation is qualitatively shorter timescales than the reference simulations these results are within one standard deviation and, consequently, are not statistically significant. The the artificial (energy) flux 10 Mm simulation with 15 G mean field (*dot-dash* green curve) is qualitatively different for timescales greater than $\pm$6hrs from the simulations with no artificial energy flux, but the FWHM is not statistically significantly different. The artificial flux 2.56 Mm simulation with 15 G mean field (*long-dash* orange curve), however,

Figure 5.8 The temporal autocorrelation of the photospheric horizontal divergence, Fourier filtered to only include scales from 20 Mm to 50 Mm, for the reference (*solid* black curve), zero net flux (*dotted* blue curve), 10 G mean field (*dashed* red curve), artificial flux 10 Mm, 15 G (*dash-dot* green curve) and artificial flux 2.56 Mm, 15 G (*long-dashed* yellow curve) simulations. There are no statistically significant differences between any simulation except for artificial flux 2.56 Mm, 15 G.

has much shorter timescales in the photosphere, with a FWHM less than 1 hour. The large-scale horizontal flows in the photosphere of this simulation are generated only by surface motions (since the artificial energy flux suppresses subsurface motions) and thus the lifetime of these flows is reflective of photospheric timescales.

This suggests that, similar to the amplitude of the low wavenumber flows, the lifetime of the supergranular scale horizontal flows does not increase with magnetic field strength. The timescale of these low wavenumber flows, however, is sensitive to the deep flows that imprint in the photosphere since both artificial energy flux simulations show a qualitative (and, in the artificial flux 2.56 Mm simulation, a dramatic) difference from the simulations with no artificial energy flux.

5.1.4.2   Lifetime of Supergranular Scale Magnetic Fields

While the magnetic fields in our simulations do not increase the lifetime of the supergranular scale horizontal divergence, it is possible that the lifetime of the large-scale magnetic field differs from the lifetime of the flows. Since the solar network magnetic field is the dominant length scale of the quiet Sun magnetic field and this field is organized by the supergranulation, we may expect to see the supergranular scale magnetic field in our simulations organized on similar timescales as the supergranular scale motions. Previous work linking photospheric magnetic field to the supergranular flows, however, suggested that the photospheric magnetic elements have increased lifetime compared to granulation (Crouch et al., 2007). Thus we compare the timescale of $|B| = \sqrt{B_x^2 + B_y^2 + B_z^2}$ in these simulations using the same temporal autocorrelation method as we used for the horizontal divergence (described above) and Fourier filter to include only supergranular scales.

The temporal autocorrelations of the magnetic field in each magnetized simulation Figure 5.9 are well separated with apparent differences due to both the mean field in the simulation and amplitude of the low wavenumber flows. Each simulation with mean field has a statistically significant increased lifetime of the supergranular scale magnetic field compared to supergranular scale flow lifetimes (Table 5.2). The 10 G mean field simulation (*dashed* red curve) has magnetic field life-
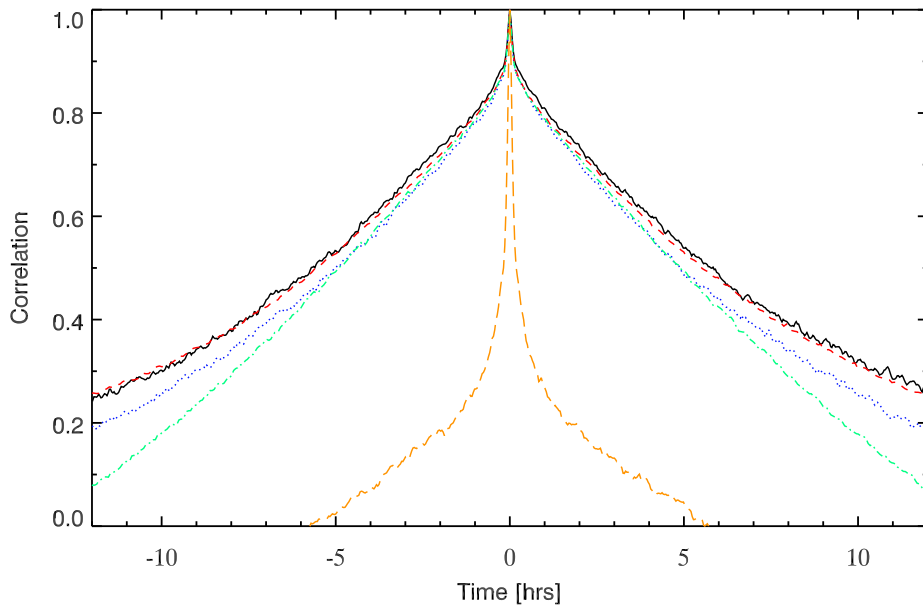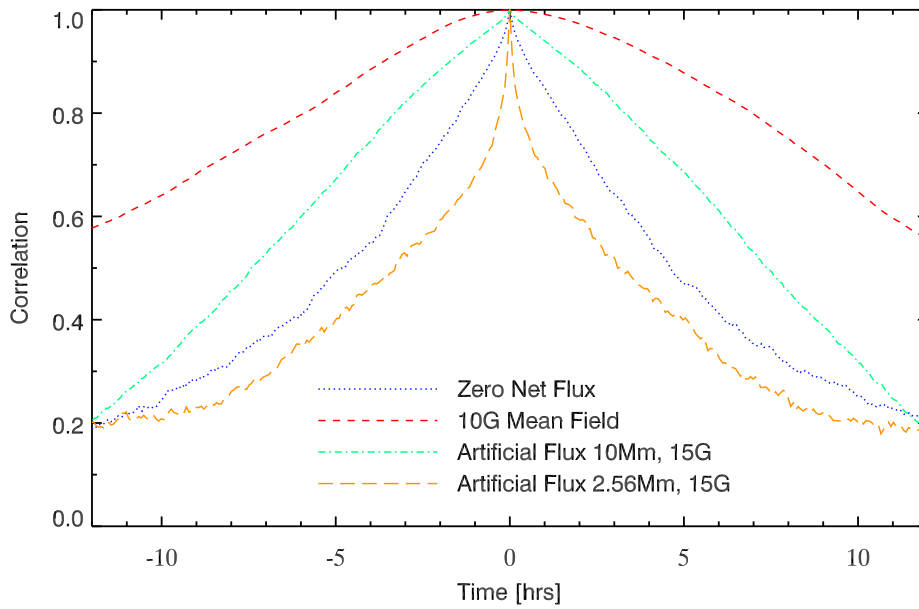
Figure 5.9 The temporal autocorrelation of the photospheric magnetic field, Fourier filtered to only include scales from 20 Mm to 50 Mm, for the zero net flux (*dotted* blue curve), 10 G mean field (*dashed* red curve), artificial flux 10 Mm, 15 G (*dash-dot* green curve) and artificial flux 2.56 Mm, 15 G (*long-dashed* yellow curve) simulations. The full width at half maximum for these correlations depends on the photospheric rms field strength and flow timescales (in the case of the artificial flux 2.56 Mm, 15 G simulation).

Table 5.2.   Photospheric Correlation Times

	Reference	Zero Net Flux	10 G Mean Field	Artificial Flux 10 Mm, 15 G	Artificial Flux 2.56 Mm, 15 G
μ_{fwhm,∇_h}	11.5	10.2	11.4	10.0	0.5
σ_{fwhm,∇_h}	1.1	1.0	1.3	1.0	0.1
$\mu_{fwhm,B}$	N/A	10.6	26.9	15.0	6.9
$\sigma_{fwhm,B}$	N/A	3.2	4.2	1.3	1.2

Note. — The mean and standard deviation of the full width at half maximum, in hours, for the horizontal divergence (Figure 5.8) and magnitude of the magnetic field (Figure 5.9).

time that is much larger than any other lifetime measure. This is caused by the pores in the photosphere (Figure 5.6) which are strong concentrations of magnetic field that suppress motions (similar to sunspots). The zero net flux simulation (*dotted* blue curve), on the other hand, is the only simulation with equal flow and magnetic field lifetime.

The mean field simulations have significant separation between the strongest concentrations of positive polarity magnetic field and negative polarity magnetic field, whereas the zero net flux simulation has an even mix of positive (white) and negative (black) polarity field concentrations (see Figure 5.6). Thus, if cancellation of opposite polarity elements is important to the lifetime of the magnetic field concentrations, then the mean field in these simulations may allow positive polarity field concentrations to live longer (since there is less negative polarity field). The low resolution may also influence the lifetime of these elements since our simulations are below the minimum resolution required for dynamo action in the photosphere (Rempel 2014, private communication) and, consequently, the field in the photosphere is advected from below (where there is dynamo action). If the dynamo were operating in the photosphere it may generate negative polarity magnetic faster than in these simulations. This mean field may also connect to deeper flows with longer lifetimes but preliminary evidence based on correlations between magnetic fields and deeper flows does not find any difference between the mean field and zero net flux simulations.

5.1.4.3   Timescales with Enhanced Radiative Cooling

While our initial motivation for enhancing the radiative cooling in regions of strong magnetic flux was that it may increase the timescale of the photospheric downflows, we find no change in the timescale of the flows in these simulations. We do not show the correlations of any of the simulations with the enhanced cooling because they are qualitatively identical to the magnetic simulations with normal cooling. This is true even when you include an artificial energy flux to reduce the amplitude of the large-scale photospheric flows. Thus we can conclude that artificially enhancing the radiative cooling has no noticeable effect on the lifetime or length scale of the flows.

5.1.5   Identifying Supergranules Beyond the Velocity Spectrum

Quiet Sun network magnetic field, observed at the boundaries of supergranular cells, is the other main method for identifying solar supergranules. While we have focused our comparison between simulations and observations on the horizontal velocity spectrum, we can also apply observational techniques to our simulation magnetic field to compare to observations. We make this comparison in Appendix A, but do not include the results here because we find that these methods are inconsistent.

5.2   The Role of Magnetic Fields in Subsurface Motions

While the magnetic fields have limited effect on the photospheric length scale or lifetime of photospheric flows, we know from Figure 5.1 that the small-scale dynamo field qualitatively suppresses low wavenumber power in the photosphere. Thus the magnetic fields may play a role in shaping the low wavenumber power at the surface but that the magnetic fields act to suppress this power as opposed to enhancing the surface flows, as had been previous suggested. Based on the two-component model introduced in §4, we expect the low wavenumber photospheric horizontal flows to depend on the rms velocity (which determines the total integrated power at depth) and the density scale height (which determines the local driving (integral) scale) below the surface which then

imprints on the surface. We previously showed the decreased equipartition field strength (which is caused by the decrease rms velocity) in §5.1.3.2 and continue that discussion here. We also compare the subsurface properties of the magnetic field and hydrodynamic reference simulations to determine what causes the qualitative decrease in low wavenumber power in the photosphere of the magnetized simulations.

5.2.1   Deep Flows in Magnetized Solutions

We begin by comparing the rms vertical velocity (which is equal to the total integrated power of the velocity spectrum) as a function of depth in Figure 5.10. The rms vertical velocities in both the 10 G mean field and zero net flux simulations are roughly 10% weaker than the reference (hydrodynamic) simulation. While this is a statically significant change in the rms velocities (since the standard deviation of the rms velocity is typically $\sim 1\%$), it is a much smaller reduction than the factor of 2.5 reduction due to the artificial energy flux that we found was necessary to match solar observations at the surface.

This suggests that magnetic fields in the solar convection zone, if they are the mechanism that reduces the rms velocity, must be substantially stronger than the fields that we find in our simulations (Figure 5.7). If a small-scale dynamo is able to generate much stronger magnetic fields, one competing effect is the decreasing equipartition field strength as stronger magnetic fields decrease the rms velocity. We see this in the decreased velocity in the 10 G mean field simulation compared to the zero net flux simulation, Figure 5.10, which results in reduced equipartition field strength in Figure 5.7. This suggests that based on our simulations, the magnetic energy would need to be in super-equipartition with the kinetic energy in the deep domain to reduce the rms velocity sufficient to match solar observations of the low wavenumber photospheric power.

While the reduction in rms velocity reduces the total integrated power in the spectrum, we know from §3.1.2.3 that the low wavenumber power in the photosphere depends on the amplitude of the large-scale flows below the surface. The two-component further suggests that only the power in the driving (integral) scale mode imprints on the surface. Thus, if magnetic fields preferentially

Figure 5.10 The rms vertical velocity for the reference (*solid* black curve), zero net flux (*dotted* blue curve) and 10 G mean field (*dashed* red curve) simulations. The magnetized simulations have reduced rms velocity below the photosphere. Based on the two-component model we expect the rms velocity to determine the photospheric horizontal velocity power for scales larger than granulation. The different velocity in the hydrodynamic simulation at the bottom boundary is due to the enhanced viscosity in the hydrodynamic bottom boundary which is not used in the magnetized simulations (see §2.1.4).
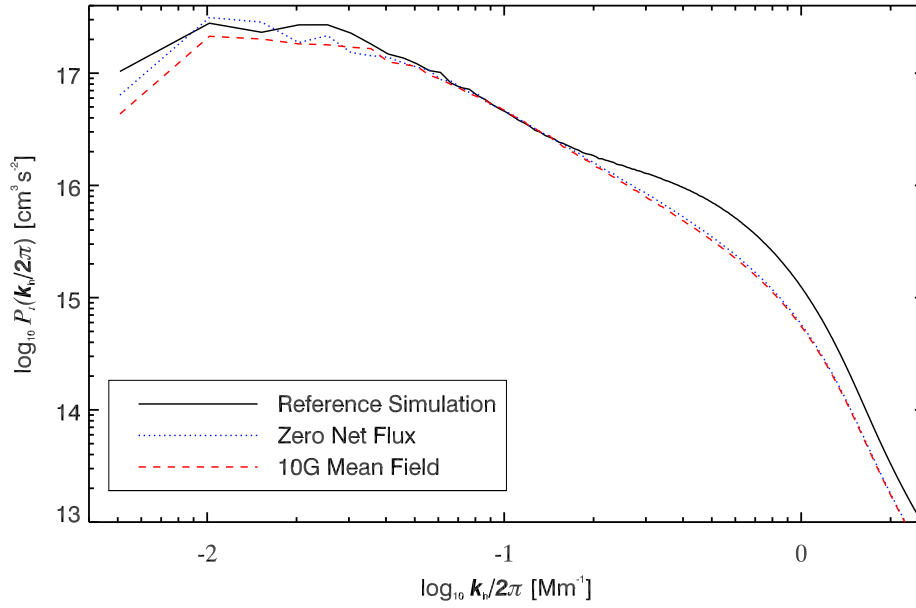
Figure 5.11 The total velocity power spectrum for the reference (*solid* black curve), zero net flux (*dotted* blue curve) and 10 G mean field (*dashed* red curve) simulations at 20 Mm depth. The low wavenumber power is qualitatively decreased but most of the reduced rms velocity in the magnetized simulations decreases the high wavenumber velocity power. Since the magnetic fields change the shape of the spectrum, this suggests that the reduced rms velocity due to the magnetic fields would result in higher photospheric velocity power than the two-component model would suggest.

decrease the amplitude of the large-scale flows, then we would expect additional reduction in low wavenumber surface flows. Examining the velocity spectrum 20 Mm below the photosphere (Figure 5.11), however, shows that the small-scale dynamo magnetic fields primarily reduce the amplitude of high wavenumber modes (with some reduction in low wavenumber modes). Thus, the $\sim 10\%$ reduction in the rms velocity may not reduce the power driving (integral) scale mode by a similar amount. If the driving (integral) scale mode is not reduced then this would cause the imprinted low wavenumber power in the photosphere to be less than our $\sim 10\%$ reduction in rms velocity would suggest. This adds to the evidence that the magnetic field must be substantially stronger to sufficiently reduce the amplitude of the large-scale flows in order to match the observed solar horizontal velocity spectrum.

5.2.2 Energy Flux with Magnetic Fields

Since the magnetic field reduces the flow speed, these simulations must maintain the solar luminosity at reduced speeds. As we can see from Figure 5.12a, the magnetic fields reduce the kinetic energy ($\frac{1}{2}\rho v^2$) carried by the downflows by a factor of ~ 1.6, which results in decreased enthalpy flux ($v_z\rho(\epsilon + P/\rho)$, Figure 5.12$b$). Thus the convective energy flux, which results from the cancellation of $\sim 10,000$ solar luminosities in upflows and $\sim -9,999$ solar luminosities downflows, can be sustained at lower velocity since the downflows carry less kinetic energy downward.

In Figure 5.13 we compare the unsigned vertical mass flux (a) and the specific enthalpy ($\epsilon + P/\rho$) difference between upflows and downflows (b). The decreased unsigned vertical mass flux, $\langle |v_z\rho| \rangle$, indicates that there is decreased convective overturning in the magnetized simulations which decreases the enthalpy flux (note that the differences below 45 Mm are due to the enhanced viscosity in the hydrodynamic bottom boundary). This is offset in the deep domain by increased difference between the specific enthalpy in upflows and downflows. These terms both decrease the enthalpy flux near the surface (~ 15 Mm depth). Thus, the magnetized simulations not only decrease the rms velocity but also increase the specific enthalpy difference in upflows and downflows (at some depths) which maintains the convective energy flux at lower speed.

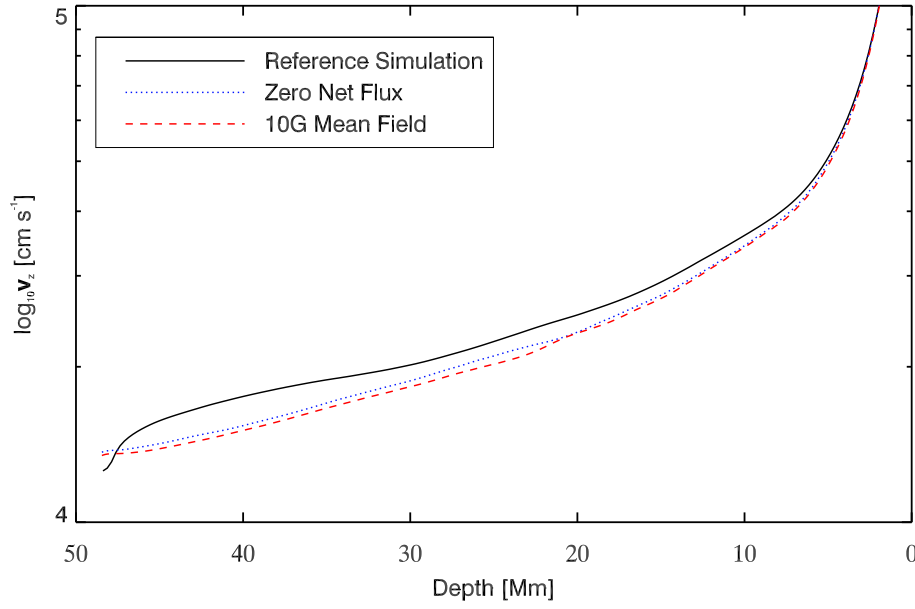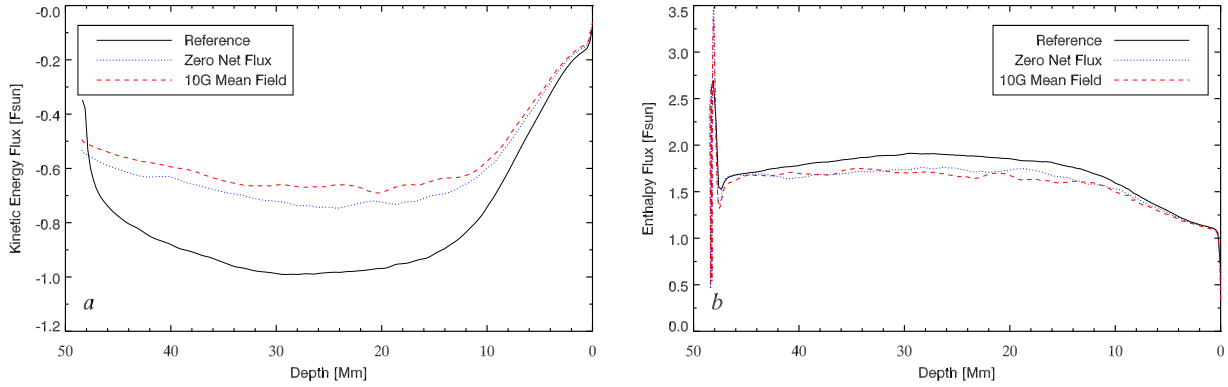Figure 5.12 The kinetic energy in downflows (*a*) and total enthalpy flux (*b*) for the reference (*solid* black curve), zero net flux (*dotted* blue curve) and 10 G mean field (*dashed* red curve) simulations. The magnetic fields reduce the kinetic energy carried deeper into the domain by the downflows by $\sim 40\%$ which reduces the enthalpy flux that is required to maintain the solar energy flux. The differences in the hydrodynamic simulation at the bottom boundary is due to the enhanced viscosity in the hydrodynamic bottom boundary which is not used in the magnetized simulations (see §2.1.4).
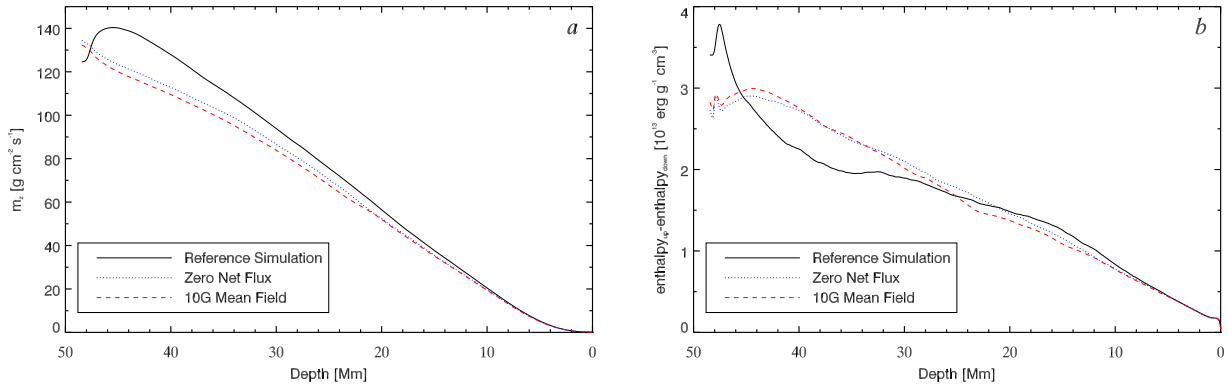
Figure 5.13 The unsigned vertical mass flux (*a*) and enthalpy (*b*) difference in upflows and downflows for the reference, zero net flux and 10 G mean field simulations. The decreased enthalpy flux $(v_z\rho(\epsilon + P/\rho))$ in the magnetized simulations is caused by a decrease in the overturning mass (which is shown by the decreased unsigned vertical mass flux) and offset by an increase in the specific enthalpy $(\epsilon + P/\rho)$ near the bottom boundary. Near the middle of the domain both of these terms reduce (~ 15 Mm) the enthalpy flux. The reduction of mass flux at the bottom of the hydrodynamic simulation are caused by the increased viscosity at the bottom boundary which is not used in the magnetized simulations (see §2.1.4).

In addition to changing the total enthalpy flux at depth, the magnetic field also changes the scales that transport the convective energy (Figure 5.14). These changes are qualitatively similar to the changes to the velocity spectrum (Figure 5.11) with reduced convective energy flux at high wavenumbers in the magnetized atmospheres. For a magnetized atmosphere to transport the energy flux with significantly reduced large-scale motions we would expect small-scale correlations between velocity and enthalpy to transport more energy. The magnetized simulation atmospheres, however, exhibit the opposite trend. This adds to the evidence that if magnetic fields are the missing physical mechanism that reduces the low wavenumber flows, then magnetic fields in the solar convection zone must be substantially stronger than in our simulations.

5.3   Conclusion

In this chapter we have examined the relationship of the quiet Sun magnetic field and supergranular (and larger) scale flows.

While previous work suggested that magnetic fields may enhance the large-scale flows in the photosphere (Rast, 2003; Crouch et al., 2007), we find that the magnetic field qualitatively decreases the amplitude of low wavenumber flows in the photosphere. The magnetic field does not enhance flows at any scale which casts doubt on this as a mechanism that organizes supergranular flows near the surface. As outlined by Table 5.3, the magnetic fields does not affect the surface flows and, instead, primarily influences the deep convective motions. In particular, we examine the enhancement of radiative cooling in strong magnetic elements in the photosphere and find that this does not significantly influence the length or time scale of the flows. The amplitude of the low wavenumber flows (controlled by using an artificial energy flux to transport the energy below the photosphere), on the other hand, plays a significant role in the length and time scale of the photospheric magnetic field. This suggests that the quiet Sun magnetic field behaves primarily as a passive tracer that is advected by the flows.

As we showed in §4, the hydrodynamic MURaM simulations (in agreement with our two-component model applied to a mixing length model atmosphere) have excess low wavenumber
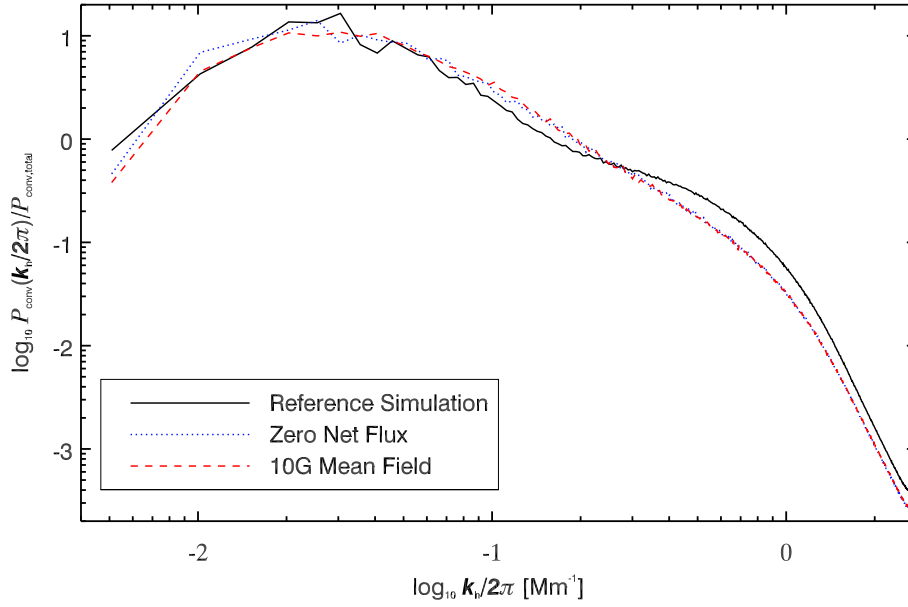
Figure 5.14 The spectrum of the convective energy flux for the reference (*solid* black curve), zero net flux (*dotted* blue curve) and 10 G mean field (*dashed* red curve) simulations at 20 Mm depth. These spectra are normalized by the total integrated power to compare the scales of convective energy transport. The hydrodynamic reference simulation transports the energy on smaller scales than the magnetized simulation, and is qualitatively similar to the velocity spectrum in Figure 5.11.

Table 5.3.   Evidence for magnetic effects on the surface flows or deep flows.

Surface Effect	Deep Effect
Temporal correlations of photospheric horizontal divergence do not depend on magnetic field strength.	The amplitude of the large-scale flows is reduced at the surface.
Temporal correlations of photospheric magnetic field primarily depend on the large-scale flows.	The rms velocity is suppressed throughout the deep domain.
Increasing the radiative cooling in strong magnetic field concentrations has no effect on the flows.	Kinetic energy flux in downflows is reduced with a corresponding reduction in upward enthalpy flux.

power compared to observations. This power comes from the deep flows which suggests that the large-scale subsurface flows in the Sun are weaker than previously thought. The magnetic fields generated by a small-scale dynamo in our simulations suppress the rms velocity (by $\sim 10\%$) in the deep domain which qualitatively decreases the low wavenumber power in the photospheric horizontal velocity spectrum. These magnetized simulations must maintain the solar luminosity and do so by reducing the kinetic energy carried by the downflows and the upward enthalpy flux. We also find that these simulations have decreased convective overturning which is compensated by increased difference between the enthalpy in upflows and downflows. This allows the simulation to maintain the solar luminosity with lower rms velocity.

The overall convective energy flux in magnetized simulations is transported primarily by large-scale motions. Furthermore, these simulations reduce the convective energy flux transported at high wavenumber. While the Lorentz force feedback on the flows also provide some suppression of low wavenumber motions, the velocity spectrum at depth shows a similar preferential suppression of high wavenumber power. Since the low wavenumber power in the photosphere is determined by the amplitude of the large-scale motions at depth, this suggests that the magnetic field may not reduce low wavenumber power sufficient to match observations without substantially stronger fields.

Since our simulations have reached $\sim 50\%$ of the equipartition field strength (with a $\sim 10\%$ reduction in rms velocity), these results suggest that if the rms velocity is reduced by a factor of 2.5 (our estimate from the artificial energy flux simulation which is required to match the observations) then the equipartition field strength would reduced below our current rms field strength. Since the amplitude of the equipartition magnetic field depends on the rms velocity, simulations with increasing field strength will have reduced equipartition field strength, which will further limit the effectiveness of the suppression of the amplitude of the convective motions.

The problem with estimating the maximum field strength at which the solar dynamo saturates is that we are in the wrong parameter regime for the solar dynamo. The solar convection zone has a magnetic Reynolds number ($Re_M = LV/\eta$ where L is a typical convective length scale, V is the rms velocity and η is the magnetic diffusivity) $\sim 10^5$ to $\sim 10^9$ and magnetic Prandtl number (the ratio between viscous and magnetic diffusion) between 10^{-3} and 10^{-7} (Martínez Pillet, 2013) whereas our small-scale dynamo simulations are in a magnetic Prandtl number one regime and diffuse magnetic energy on larger scales than the Sun (we cannot estimate the effective magnetic Reynolds number in our simulations because our diffusive scheme is highly intermittent, inhomogeneous and depends on scale).

Simulations of small-scale dynamos have found that the saturated magnetic field depends primarily on the magnetic Reynolds number and magnetic energy can reach super-equipartition with the kinetic energy (Brandenburg, 2014). Furthermore, low magnetic Prandtl number dynamos dissipate most of the energy through ohmic diffusion with less than 10% of the energy dissipated by the viscosity (Brandenburg, 2014). This leaves very little kinetic energy on scales smaller than the magnetic dissipation scale (which is larger than the viscous dissipation scale in the low magnetic Prandtl number regime) (Brandenburg, 2009, 2014). Thus, while a small-scale dynamo closer to the solar parameter regime may saturate with increased field strength, this occurs primarily on small scales and does not appear to change the Lorentz force feedback on large-scales (with little further reduction in the amplitude of low wavenumber flows) (Brandenburg, 2014). This suggests that magnetic fields generated by a small-scale dynamo in the solar convection zone may not be

limited to equipartition between magnetic and kinetic energy but this super-equipartition field may affect primarily small-scale motions.

All of this evidence suggests that magnetic fields are a mechanism that could allow convection to transport the solar luminosity with weaker flows and reconcile the simulations with observations. To match observations, however, the magnetic fields must be substantially stronger than in these simulations.

Chapter 6

Conclusion

Since the early observations of supergranulation it has been suggested that these flows originate at significant depth below the photosphere (specifically related to the depth of Helium II ionization) and imprint on the surface (Simon & Leighton, 1964; Simon & Weiss, 1968; November et al., 1981). Recent work, however, has suggested that supergranulation may be generated near the surface. In particular, theoretical calculations (using the mutual interaction of convective downflows and magnetic elements) found that large-scale flow patterns could be generated purely from granular downflows and increased lifetime of magnetic elements (Rast, 2003; Crouch et al., 2007). Time-distance helioseismic measurements of the supergranular flows also find a peak flow pattern within 3 Mm of the photosphere (Rast, 2003; Crouch et al., 2007; Duvall & Hanasoge, 2013; Duvall et al., 2014). Furthermore, the measurements of the diameter of supergranules show that it changes with the solar cycle which suggests that magnetic fields may not be a passive tracer in the photosphere and, instead, play some role in determining the supergranular length scale (McIntosh et al., 2011).

On the other hand, the length scale of convective motions increases with depth in the solar convection zone because of its increasing scale. This means that supergranular scale convection occurs at some depth independent of any physical mechanism that organizes granular flows into larger scale convection in the photosphere. Observations of the motion of supergranules in the photosphere has linked the wavelength of supergranulation with mean flows (i.e. the differential rotation and meridional circulation) at depths up to 100 Mm below the photosphere (Hathaway

et al., 2010; Hathaway, 2012a,b). While it is unclear how these flows may imprint on the photosphere, this suggests that supergranular flows originate below the surface where they are advected by the mean flows and these deep convective motions are observed as flow patterns at the surface.

This thesis has investigated these effects and this apparent contradiction via large-scale numerical simulations.

6.1   Summary

Comparing solar-like convection simulations using the MURaM code with domain depths ranging from 49 Mm to 2 Mm (in Chapter 3), we find that the low wavenumber horizontal velocity power in the photosphere depends both on the presence and amplitude of the larger scale flows deep in the domain. Furthermore, we find that each successively deeper simulation adds power on larger scales (and is consistent with the shallower simulations for all smaller scale modes). Each depth contributes power to horizontal motions in the photosphere at a specific length scale (or range of scales) with the contributed scales increasing with depth. While the horizontal velocity spectrum shows a dependence on the deep convection, the vertical motions near the surface are dominated by the processes in the radiative boundary layer. The low wavenumber vertical power (which is balanced by the density gradient, unlike the balance in the continuity equation below the surface) is stronger than any imprinted large-scale vertical motions.

The photospheric horizontal velocity spectrum motivates the two-component model presented in Chapter 4. In that model the velocity spectrum depends on the local driving (integral) scale $(4H_\rho)$, the local rms velocity and the amplitude of the large-scale convection deep in the domain which decay with height and imprint on the upper layers. Each depth contributes motions at the scale of $4H_\rho$ which suggests that the length scale and lifetime of supergranulation is determined by the properties of the convection in the depths where 20 Mm $\lesssim 4H_\rho(z) \lesssim$ 75 Mm and that supergranulation is highlighted in the photosphere by lower amplitude motions where $4H_\rho(z) \lesssim$ 20 Mm and $4H_\rho(z) \gtrsim$ 75 Mm.

The surface velocity spectra from the MURaM simulations and from applying our two-

component model to mixing length atmospheres does not match the observed power spectrum in the solar photosphere at wavenumbers lower than supergranulation. While the latent heat flux of helium ionization helps reduce the velocity at depths with driving (integral) scales at mesogranular scales (due to He I ionization) and scales larger than supergranules (due to He II ionization), this is a small effect that helps shape the spectrum but does not explain the prominence of supergranulation in the observed velocity spectrum of the solar photosphere. The only way to reconcile the simulations with observations is to use an artificial energy flux to transport the solar luminosity below 10 Mm which reduces the rms velocity deep in the simulation domain by a factor of 2.5, thus defining supergranulation by the drop in power to lower wavenumbers as in the observations.

Examining simulations with small-scale dynamo magnetic fields (in Chapter 5), we find that the magnetic fields do not enhance the lifetime of the flows or organize the surface convection into larger scale motions even with enhanced radiative cooling in strong magnetic field concentrations. The magnetic fields do, however, qualitatively reduce the low wavenumber power in the photosphere by decreasing the kinetic energy carried by downflows and allowing the solar luminosity to be transported at lower rms velocity. While this lower velocity reduces the low wavenumber power in the photosphere, the reduction is not sufficient to match the observed photospheric velocity spectrum. The small-scale dynamo simulations further suggest that even a dynamo with equipartition field strength may not reduce the rms velocity by the factor of 2.5 seen in the artificial energy flux simulation. If a small-scale dynamo were to generate magnetic field in the convection zone of sufficient strength to cause the observed low wavenumber power reduction, that magnetic field must be substantially stronger than in our simulations.

6.2   Comparing to Global Simulations

Comparing our MURaM reference simulation (*solid* black curve) to global convection simulations with rotation (*dot-dashed* orange curve, Miesch et al., 2008) and without rotation (*dashed* blue curve, Hotta et al., 2014) at $0.98R_{sun}$ (Figure 6.1), we find that the low wavenumber velocity power increases to larger scales in the all simulations. The MURaM reference simulation is also in

agreement with a local area stagger simulation (*dotted* red curve, Stein & Nordlund, 2006) which is only 20 Mm deep and, consequently, has decreased low wavenumber power compared to what we would expect from a deeper simulation. Based on our two-component model and the observed imprinting of deep convection motion on the photosphere in MURaM simulations, we would expect the motions in these global simulations to imprint on the solar photosphere with significant power at the scale of giant cells. This suggests that the low wavenumber flows must be weaker in the Sun or the solar convective motions do not imprint on the photosphere with the same amplitude as in our simulations.

6.2.1   Observational Constraints

Multiple observational constraints suggest that the large-scale subsurface convection is weaker than in simulations. Recent time-distance helioseismology observations using SDO/HMI have placed upper limits on the low wavenumber convection (*dotted* black curve in Figure 6.1) that is more than one order of magnitude weaker than in previous global simulations (Hanasoge et al., 2010, 2012). These measurements have not been reproduced and are below the estimated lower limit for the Reynolds stress to transport angular momentum to the equator and maintain the solar differential rotation (Miesch et al., 2012). If confirmed, these results suggest that solar convection transports the energy with dramatically weaker flows on large scales than theory would predict.

The differential rotation profile measured by helioseismology is one of the most consistent measurements to compare to simulations (Thompson et al., 2003). It is a long standing problem with global convection simulations that the flows that transport the solar luminosity require a mean rotation rate that is faster than the solar rotation to maintain the solar-like differential rotation (i.e. faster rotating equator and slower rotating pole; Brown, Charbonneau, Miesch, Toomre, 2014, private communication). This issue has been addressed in detail by Hotta (2014a), which examines new global convection simulations in a spherical geometry with mean solar rotation. These simulations find that the convection transports angular momentum to the poles and result in anti-solar differential rotation (with faster poles and slower equator, Hotta, 2014a; Gastine et al., 2013). The
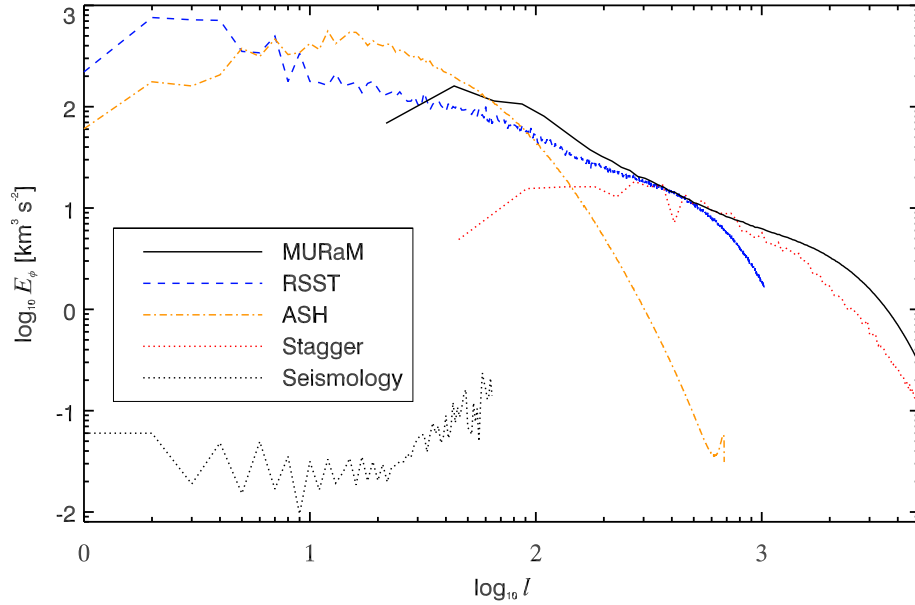
Figure 6.1 The horizontal velocity spectrum at $0.98R_{sun}$ in a global simulation without rotation (*dashed* blue curve) using the reduced speed of sound technique (RSST Hotta et al., 2014), a global simulation with rotation (*dot-dash* orange curve) using the ASH code (Miesch et al., 2008), a local area simulation using the stagger code (*dotted* red curve, Gizon & Birch, 2012; Stein & Nordlund, 2006), and the MURaM reference simulation (*solid* black curve). We also show the upper limit from time-distance helioseismic measurements of the large-scale flows (Hanasoge et al., 2010, 2012). We note that the stagger simulation appears to have decreased large-scale power but this simulation is 20 Mm deep and the power spectrum compares well to 20 Mm deep MURaM simulations. We would expect a stagger simulation with increased depth to have excess low wavenumber power as in the 49 Mm deep MURaM reference simualtion.

simulations only exhibit solar-like differential rotation by reducing the solar energy flux by a factor of 18 (which significantly reduces the rms velocity and makes the flows rotationally constrained). Decreasing the artificial diffusivity in the simulation requires a further reduction in energy flux by a factor of ~ 70 (compared to the solar luminosity) to transport angular momentum to the equator. Thus, these simulations are not converged since the Sun diffuses kinetic energy on much smaller scales than the artificial diffusivity used in these simulations. This adds to the evidence that solar convective flows are weaker than previously thought or that models can reproduce.

6.3   Influences on Solar Convective Energy Transport

These concerns raise the question of how the deep convection transports the solar luminosity with such low amplitude large-scale motions at the surface. Based on results from our simulations and the two-component model there are at least two possible explanations: either these flows do not imprint on the surface or the energy is transported with weaker subsurface flows on large scales. These in turn could result from rotation, magnetic fields or different properties of the convection in the solar parameter regime.

6.3.1   Rotation

None of our simulations included the effects of rotation or the near surface shear layer. Photospheric observations have found that supergranules are advected by the near surface shear at a depth equal to their diameter (Hathaway et al., 2010; Hathaway, 2012a,b). Our simulations suggest that supergranules imprint on the photosphere from the depth where $\lambda_h \approx 4H_\rho$ which is consistent with these observations. Thus, while the supergranules may interact with the near surface shear layer, we do not know how this shear may influence the convective flows at depth or the imprinting of these motions.

6.3.2   Magnetic Fields

The connection between the network magnetic field and solar supergranulation was discovered during the early observations of supergranulation (Simon & Leighton, 1964). While the network field is assumed to be a passive tracer, observations of increasing supergranular length scale with increasing solar magnetic activity suggests that the magnetic field may play an active role (McIntosh et al., 2011). We investigated the suggestion that magnetic fields may organize photospheric flows into supergranular scale flows (Rast, 2003; Crouch et al., 2007) by enhancing the radiative cooling through regions of strong magnetic flux and find no evidence that magnetic fields increases the low wavenumber velocity power at the surface. By computing self-consistent small-scale dynamo simulations, however, we find that the Lorentz force feedback from small-scale dynamo fields reduce the rms velocity of the deep flows which also reduces the low wavenumber power in the photosphere. The effect found is insufficient to account for the decreased power in the observed horizontal velocity spectrum at wavenumbers lower than supergranulation.

6.3.2.1   Lorentz Force Feedback from Small-Scale Dynamo Magnetic Field

Recent simulations of the deep convection have computed a small-scale dynamo down to the bottom of the convection zone (Hotta, 2014b). These simulations do not include any radiative transfer and instead include a cooling at the top boundary to generate low entropy downflows. The upper boundary of these simulations is problematic (as are all open boundaries) because the boundary conditions make unrealistic assumptions about the cooling and near-surface convection.

Comparing our small-scale dynamos to these deep convection simulations (Hotta, 2014b), we find that both types of simulations match the predicted rms magnetic field strength (Figure 6.2) and the resulting reduction in rms velocity compared to hydrodynamic simulations (Figure 6.3). The deep simulations generate 95% of the equipartition field strength near the bottom of the convection zone and this reduces the rms velocity by a factor of ~ 1.6 at these depths (Hotta, 2014b). While this is much closer to the factor of 2.5 reduction in rms velocity (compared to
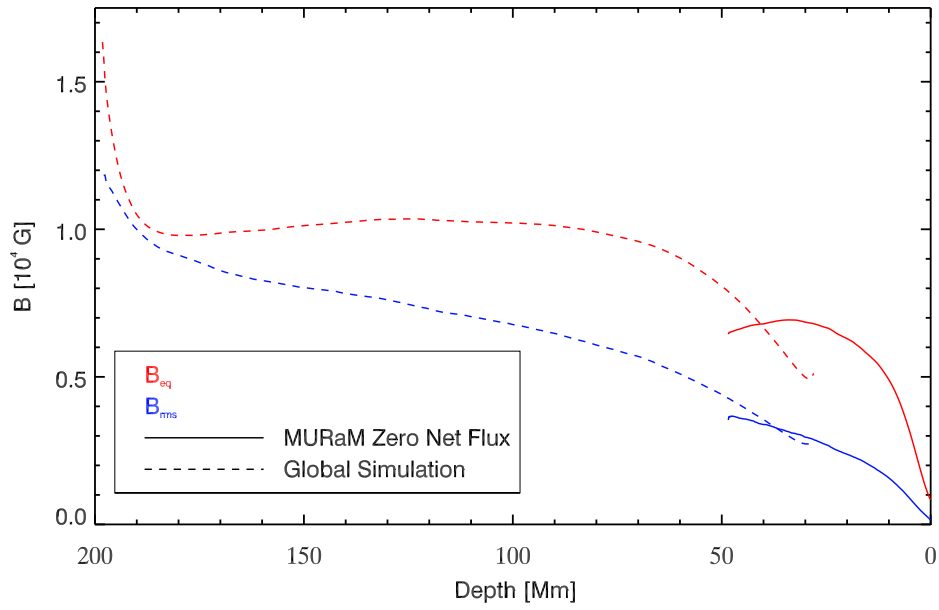
Figure 6.2 Magnetic field strength (rms and equipartition) from small-scale dynamo simulations using MURaM and a deep convection simulation (Hotta, 2014b). These are in qualitative agreement (with boundary conditions and differing magnetic diffusivity contributing to mismatched equipartition field strength where they overlap).

hydrodynamic simulations) that our artificial energy flux simulations predict is required to match solar observations, this flow speed reduction must occur in MURaM simulations for all flows below 25 Mm depth. In the Hotta (2014b) results, the most significant reduction in rms velocity only occurs over a limited range of depths below ∼ 100 Mm.
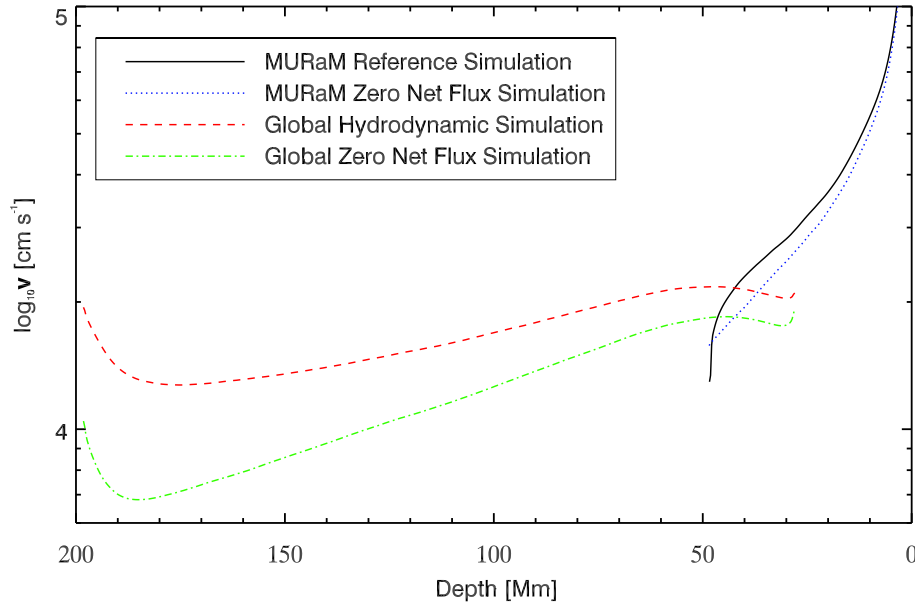

Figure 6.3 The rms velocity in hydrodynamic and small-scale dynamo simulations using MURaM and with reduced speed of sound technique to simulate deep convection (Hotta, 2014b).

While the small-scale dynamo magnetic fields in our MURaM simulations (within 50 Mm of the photosphere) suppress primarily high wavenumber convective flows, the magnetic fields deeper in the convection zone organize the enthalpy flux on smaller scales (Hotta, 2014b). In addition to the reduction in rms velocity, increasing the energy flux transported by high wavenumbers may decrease the amplitude of the driving (integral) scale mode which would reduce the imprinted low wavenumber photospheric flows. This reorganization of the enthalpy flux on smaller scales, however, is not matched in the kinetic energy spectrum (Hotta, 2014b). Both the MURaM and Hotta (2014b) small-scale dynamo simulations show that the magnetic field preferentially reduces the amplitude of high wavenumber flows with a smaller reduction in amplitude of the driving (integral) scale modes (that imprint on the photosphere). Thus, while small-scale dynamo magnetic field reduces the

amplitude of the motions required to carry the solar luminosity, these motions are still dominated by large-scale convection (just as in the hydrodynamic simulations). This suggests that if we were able to simulate a small-scale dynamo with the full extent of the solar convection zone and magnetic energy in equipartition with the kinetic energy, the deep flows would still imprint excess low wavenumber power compared to the observed photospheric horizontal velocity spectrum.

6.3.2.2 Influence of Large-Scale Dynamo

As we discussed in §6.2.1, the anti-solar differential rotation in global simulations (that transport the full solar luminosity) suggests that the Sun may require weaker flows to transport angular momentum equator-ward. Large-scale magnetic field generated in recent global dynamo simulations, however, suppresses the low wavenumber motions enough to maintain solar-like differential rotation (Fan & Fang, 2014). This can also be achieved in hydrodynamic simulations by increasing the diffusivity which suggests that the magnetic field may increase the effective viscosity in these simulations (Fan & Fang, 2014). Thus the global dynamo generated magnetic fields may play a role in maintaining the solar differential rotation by reducing the amplitude of the low wavenumber flows. This reduction may also suppress the power in the driving (integral) scale modes which imprint on the photosphere. All of these simulations, however, are far more diffusive than solar convection with maximum Reynolds number of 130 (Fan & Fang, 2014). In addition, a significant fraction of the solar luminosity (36% in the middle of the convection zone) is transported via an ad hoc thermal diffusion (i.e. conduction) term (Fan & Fang, 2014). Thus, while the large-scale dynamo magnetic fields may help reduce the photospheric horizontal velocity power for wavenumbers lower than supergranulation, this artificial conduction adds to the evidence (along with our artificial energy flux simulations) that solar convection transports energy with different flow amplitudes or at different scales than in the simulations.

6.3.3 Solar Parameters

One problem with all of these simulations is that they are not in the same parameter regime as the solar convection zone. Simulations of highly stratified convection with viscosity and Reynolds number equal to the estimates for the solar convection zone ($\nu \sim 10^{-3}$ m^2 s^{-1}, $Re \sim 10^{10} - 10^{13}$, Rieutord & Rincon, 2010) will not be available for the foreseeable future. While global convection simulations (that transport the solar luminosity without artificial conduction) have flows that exceed the upper limit required to transport angular momentum to the equator, decreasing the diffusivity in these simulations requires a further reduction in the convective energy flux required to maintain solar-like differential rotation (Hotta, 2014a). This suggests that there are aspects of convective energy transport that may behave very differently at the solar viscosity than current convection simulations (which diffuse kinetic energy on much larger scales than in the Sun).

We have also found a reduction in the rms velocity required to transport the solar luminosity in small-scale dynamo simulations. This reduction, however, is not sufficient to match the imprinted low wavenumber power in the photosphere. Results from dynamo simulations suggest that the saturation and dissipation of energy in a small-scale dynamo is closely related to the magnetic Reynolds number ($Re_M = LV/\eta$ where L is a typical convective length scale, V is the rms velocity and η is the magnetic diffusivity) and magnetic Prandtl number (i.e. the ratio of viscous and magnetic dissipation) (Brandenburg, 2009, 2014).

While it is more difficult to generate magnetic energy in a low magnetic Prandtl number small-scale dynamo (since the small-scale flows destroy magnetic energy) with magnetic Prandtl number in the Sun estimated to be between $\sim 10^{-3}$ and $\sim 10^{-7}$ (Martínez Pillet, 2013), a saturated small-scale dynamo dissipates most of the kinetic energy at the magnetic dissipation length scale, with very little energy dissipated by viscosity (Brandenburg, 2014). The saturation of the dynamo magnetic field depends primarily on the magnetic Reynolds number and dynamo simulations with large magnetic Reynolds number can reach magnetic energy in super-equipartition with kinetic energy (Brandenburg, 2014). The largest current generation DNS simulations limited to a fluid

Reynolds number of 5000 (Lee et al., 2013) which is much smaller than the magnetic Reynolds number in the solar convection zone which is estimated between $\sim 10^5$ and $\sim 10^9$ (Martínez Pillet, 2013). This suggests that the equipartition field strength in these simulations may not be the upper limit for magnetic energy in a solar small-scale dynamo and the magnetic dissipation may increase the length scale of dissipation of the flows. Thus, a saturated small-scale dynamo in the solar convection zone may cause the convection to behave very differently than in hydrodynamic simulations with much larger effective viscosity and stronger Lorentz-force feedback on the flows.

6.4   Future Work

The results of our simulations demonstrate that the deep convection imprints on the photosphere and the amplitude of the low wavenumber flows determine the power in large-scale surface motions. There are several more questions, however, that require further investigation. The most important of these questions is how the deep low wavenumber flows transport the solar luminosity. This is fundamental to the dynamics of the convection zone as the amplitude of the velocity affects the generation of mean flows such as the differential rotation and meridional circulation (Miesch et al., 2012).

While small-scale dynamo simulations show that magnetic fields reduce the rms velocity throughout the convection, this is so far insufficient to match observations of low wavenumber power or solar differential rotation (Hotta, 2014b,a). Further work is necessary to determine field strength of the saturated small-scale dynamo in the solar convection zone and if it can reach sufficient field strengths to reduce the amplitude of the flows enough to maintain the solar-like differential rotation or the observed horizontal velocity power in the photosphere. Since these small-scale dynamo magnetic fields preferentially reduce the amplitude of the high wavenumber flows (Hotta, 2014b), it is also important to determine if it is possible for the solar magnetic fields (with contributions from the small-scale and global dynamo (Fan & Fang, 2014)) to sufficiently reduce the large-scale convection to match observations.

We have also not investigated the effect of rotation or the near surface shear layer. It is

unclear if rotation can help explain how we transport the solar luminosity with low amplitude flows, but we have evidence that supergranules interact with the near surface shear (Hathaway, 2012a) and the near surface shear may play a role in how deep motions imprint on the photosphere.

While there are unanswered questions that can be addressed by future solar-like simulations, the larger question of how the solar convection transports the luminosity suggests that the next step may require a more fundamental re-examination of convective transport. While we have argued that our enhanced viscosity boundary condition that smooths inflows is more consistent with the flows in the middle of the simulation domain, the boundary without any smoothing shows that the boundary condition influences flows throughout the domain (though simulations with different boundary conditions, including global simulations, also have excess power in the low wavenumber flows). This suggests that we need to carefully examine the boundary conditions to determine the effects that they have on the convection. The dependence of the convective energy flux (and flow amplitudes) that maintain the solar-like differential rotation (Hotta, 2014a) and differences in small-scale dynamo energy dissipation and saturation field strength on magnetic Prandtl and Reynolds number (Brandenburg, 2014) suggest that flows in the solar parameter regime may behave differently than current solar-like simulations. What is the effect of increasing the length scale of flow dissipation in a low magnetic Prandtl number small-scale dynamo and does this change the effective thermal Prandtl number of the flows? How do small and large-scale magnetic fields throughout the convection zone influence the convective energy transport? The main implication of our comparison between MURaM simulations and observations is that we may not understand solar convective transport for depths greater than 10 Mm below the photosphere.

Bibliography

Aikio, J., & Mähönen, P. 1998, ApJ, 497, 534

Antia, H. M., & Chitre, S. M. 1993, Sol. Phys., 145, 227

Antia, H. M., Chitre, S. M., & Pandey, S. K. 1981, Sol. Phys., 70, 67

Berrilli, F., del Moro, D., Florio, A., & Santillo, L. 2005, Sol. Phys., 228, 81

Berrilli, F., Florio, A., & Ermolli, I. 1998, Sol. Phys., 180, 29

Berrilli, F., Scardigli, S., & Giordano, S. 2013, Sol. Phys., 282, 379

Böhm-Vitense, E. 1958, Z. Astrophys., 46, 108

Brandenburg, A. 2009, ApJ, 697, 1206

—. 2011, ApJ, 741, 92

—. 2014, ApJ, 791, 12

Brun, A. S., Miesch, M. S., & Toomre, J. 2004, ApJ, 614, 1073

Canfield, R. C., & Mehltretter, J. P. 1973, Sol. Phys., 33, 33

Christensen-Dalsgaard, J., Dappen, W., Ajukov, S. V., et al. 1996, Science, 272, 1286

Crouch, A. D., Charbonneau, P., & Thibault, K. 2007, ApJ, 662, 715

Danilovic, S., Schüssler, M., & Solanki, S. K. 2010, A&A, 513, A1

de Wijn, A. G., Stenflo, J. O., Solanki, S. K., & Tsuneta, S. 2009, Space Sci. Rev., 144, 275

Dedner, A., Kemm, F., Kröner, D., et al. 2002, Journal of Computational Physics, 175, 645

DeGrave, K., Jackiewicz, J., & Rempel, M. 2014, ApJ, 788, 127

DeRosa, M. L., & Toomre, J. 2004, ApJ, 616, 1242

Deubner, F.-L. 1971, Sol. Phys., 17, 6

Duvall, T. L., & Hanasoge, S. M. 2013, Sol. Phys., 287, 71

Duvall, T. L., Hanasoge, S. M., & Chakraborty, S. 2014, Sol. Phys., 289, 3421

Fan, Y. 2009, Living Reviews in Solar Physics, 6, 4

Fan, Y., & Fang, F. 2014, ApJ, 789, 35

Gastine, T., Wicht, J., & Aurnou, J. M. 2013, Icarus, 225, 156

Gizon, L., & Birch, A. C. 2012, PNAS, 109, 11896

Goldbaum, N., Rast, M. P., Ermolli, I., Sands, J. S., & Berrilli, F. 2009, ApJ, 707, 67

Gough, D. O. 1969, J Atmos Sci, 24, 448

Hanasoge, S. M., Duvall, T. L., & Sreenivasan, K. R. 2012, Proceedings of the National Academy of Science, 109, 11928

Hanasoge, S. M., Duvall, Jr., T. L., & DeRosa, M. L. 2010, ApJ, 712, L98

Hart, A. B. 1954, MNRAS, 114, 17

—. 1956, MNRAS, 116, 38

Hathaway, D. H. 2012a, ApJ, 749, L13

—. 2012b, ApJ, 760, 84

Hathaway, D. H., Beck, J. G., Bogart, R. S., et al. 2000, Sol. Phys., 193, 299

Hathaway, D. H., Upton, L., & Colegrove, O. 2013, Science, 342, 1217

Hathaway, D. H., Williams, P. E., Dela Rosa, K., & Cuntz, M. 2010, ApJ, 725, 1082

Hotta, H. 2014a, submitted

—. 2014b, in preparation

Hotta, H., Rempel, M., & Yokoyama, T. 2014, ApJ, 786, 24

Howe, R., Christensen-Dalsgaard, J., Hill, F., et al. 2007, Advances in Space Research, 40, 915

Kolmogorov, A. N. 1941, Proceedings of the USSR Academy of Sciences, 32, 16

Kurucz, R. 1993, ATLAS9 Stellar Atmosphere Programs and 2 km/s grid. Kurucz CD-ROM No. 13. Cambridge, Mass.: Smithsonian Astrophysical Observatory, 1993., 13

Lamb, D. A., DeForest, C. E., Hagenaar, H. J., Parnell, C. E., & Welsch, B. T. 2010, ApJ, 720, 1405

Lee, M., Malaya, N., & Moser, R. D. 2013, in Proceedings of the International Conference on High Performance Computing, Networking, Storage and Analysis, SC '13 (New York, NY, USA: ACM), 61:1–61:11

Leighton, R. B., Noyes, R. W., & Simon, G. W. 1962, ApJ, 135, 474

Lites, B. W., Kubo, M., Socas-Navarro, H., et al. 2008, ApJ, 672, 1237

Lord, J. W. 2014, in preparation

Lord, J. W., Cameron, R. H., Rast, M. P., Rempel, M., & Roudier, T. 2014, ApJ, 793, 24

Martínez Pillet, V. 2013, Space Sci. Rev., 178, 141

McIntosh, S. W., Leamon, R. J., Hock, R. A., Rast, M. P., & Ulrich, R. K. 2011, ApJL, 730, L3

Merkel, A. W., Harder, J. W., Marsh, D. R., et al. 2011, Geophys. Res. Lett., 38, 13802

Meunier, N., Tkaczuk, R., Roudier, T., & Rieutord, M. 2007, A&A, 461, 1141

Miesch, M. S. 2005, Living Reviews in Solar Physics, 2, 1

Miesch, M. S., Brun, A. S., De Rosa, M. L., & Toomre, J. 2008, ApJ, 673, 557

Miesch, M. S., Elliott, J. R., Toomre, J., et al. 2000, ApJ, 532, 593

Miesch, M. S., Featherstone, N. A., Rempel, M., & Trampedach, R. 2012, ApJ, 757, 128

Mininni, P. D., Alexakis, A., & Pouquet, A. 2006, Phys. Rev. E, 74, 016303

Nordlund, Å., Stein, R. F., & Asplund, M. 2009, Living Rev. Solar Phys., 6, lrsp

November, L. J. 1989, ApJ, 344, 494

—. 1994, Sol. Phys., 154, 1

November, L. J., & Simon, G. W. 1988, ApJ, 333, 427

November, L. J., Toomre, J., Gebbie, K. B., & Simon, G. W. 1981, ApJ, 245, L123

Orozco Suárez, D., & Bellot Rubio, L. R. 2012, ApJ, 751, 2

Pietarila Graham, J., Cameron, R., & Schüssler, M. 2010, ApJ, 714, 1606

Plaskett, H. H. 1954, MNRAS, 114, 251

Prandtl. 1925, Ztschr. angew. Math. Mech., 5, 136

Rast, M. P. 1991, LNP, 388, 179

Rast, M. P. 1995, ApJ, 443, 863

—. 2001, ApJ, 561, L191

—. 2003, ApJ, 597, 1200

Rast, M. P., Nordlund, Å., Stein, R. F., & Toomre, J. 1993, ApJ, 408, L53

Rast, M. P., & Toomre, J. 1993, ApJ, 419, 224

Rempel, M. 2014, ApJ, 789, 132

Rempel, M., Schüssler, M., & Knölker, M. 2009, ApJ, 691, 640

Richardson, R. S., & Schwarzschild, M. 1950, ApJ, 111, 351

Rieutord, M., & Rincon, F. 2010, Living Rev. Solar Phys., 7, lrsp

Rieutord, M., Roudier, T., Mlherbe, J. M., & Rincon, F. 2000, A&A, 357, 1063

Rieutord, M., Roudier, T., Rincon, F., et al. 2010, A&A, 512, A4

Rincon, F. 2007, in IAU Symposium, Vol. 239, IAU Symposium, ed. F. Kupka, I. Roxburgh, & K. L. Chan, 58–63

Rogers, F. J., & Iglesias, C. A. 1992, ApJ, 401, 361

—. 1996, ApJ, 456, 902

Rouder, T., Rieutord, M., Malherbe, J. M., & Vigneau, J. 1999, A&A, 349, 301

Roudier, T., Rieutord, M., Malherbe, J. M., et al. 2012, A&A, 540, 8

Simon, G. W., & Leighton, R. B. 1964, ApJ, 140, 1120

Simon, G. W., & Weiss, N. O. 1968, ZAp, 69, 435

Sprout, H. C., Nordlund, Å., & Title, A. M. 1990, ARA&A, 28, 263

Stein, R. F., Benson, D., Georgobiani, D., & Nordlund, Å. 2006, in ESA Special Publication, Vol. 624, Proceedings of SOHO 18/GONG 2006/HELAS I, Beyond the spherical Sun

Stein, R. F., Georgobiani, D., Schafenberger, W., Nordlund, Å., & Benson, D. 2009, in American Institute of Physics Conference Series, Vol. 1094, 15th Cambridge Workshop on Cool Stars, Stellar Systems, and the Sun, ed. E. Stempels, 764–767

Stein, R. F., & Nordlund, A. 1998, ApJ, 499, 914

—. 2006, ApJ, 642, 1246

Stuart, F. E., & Rush, J. H. 1954, ApJ, 120, 245

Thompson, M. J., Christensen-Dalsgaard, J., Miesch, M. S., & Toomre, J. 2003, ARA&A, 41, 599

Ustyugov, S. D. 2010, PhyS T, 142, 014031

van Ballegooijen, A. A. 1986, ApJ, 304, 828

Vögler, A., & Schüssler, M. 2007, A&A, 465, L43

Vögler, A., Shelyag, S., Schüssler, M., et al. 2005, A&A, 429, 335

Weiss, N. O. 1964, Royal Society of London Philosophical Transactions Series A, 256, 99

Appendix A

Supergranular Cell Identification

Quiet sun network magnetic field, observed at the boundaries of supergranular cells, is one of the primary methods for identifying solar supergranules (the other being the velocity spectrum). While we have focused our comparison between simulations and observations on the horizontal velocity spectrum, we can also apply observational techniques to our simulation magnetic field and compare the results to Hinode observations. We choose Hinode since the field of view is similar to our simulation domain width (220×120 Mm^2 for Hinode compared to 197×197 Mm^2 in the simulations) and the resolution is simulation to our simulation resolution (~ 110 km for Hinode compared to 192 km in simulations). These techniques identify the network magnetic field and use it to outline the supergranules. These observations match the power spectrum with photospheric supergranular diameter of ~ 30Mm (McIntosh et al., 2011).

A.1   Void Analysis

We apply the void analysis which is named for the "voids" between clusters of galaxies which this method was originally designed to detect (Aikio & Mähönen, 1998). This method has been adapted to observe the solar photospheric magnetic field by Berrilli et al. (2013). The method is described in detail in that work, and we focus on the details of our implementation on the MURaM simulations here.

A.1.1   Details of the Void Analysis Method

The void analysis identifies photospheric magnetic field above a certain threshold as "particles" and all regions below the threshold as voids. We apply a threshold set to 0.5% of the maximum photospheric field strength in each simulation. This makes it easier to compare with observations where the values in each pixel are a combination of field strength and filling factor. The threshold for the four simulations that we show here are: ~ 800G for the zero net flux simulation, ~ 2000G for the 10 G mean field simulation, ~ 1200G for the artificial flux 10 Mm with 15 G mean field simulation and ~ 800G for the artificial flux 2.56 Mm with 15 G mean field simulation. We give all approximate values because the actual threshold varies slightly as a function of time.

For each void grid cell we compute the minimum distance to the nearest particle, D_{min}. To determine which void a grid cell belongs to we identify all the local maxima of D_{min} and then follow a path from each void grid cell (that is not itself a local maximum) to the nearest local maximum of the D_{min} map. To determine the initial path we compute the fourth order finite difference x and y derivative of the D_{min} map. We normalize the derivatives based on their magnitude, $d_{magnitude} = \sqrt{d_x^2 + d_y^2}$, $m_x = d_x/d_{magnitude}$ and $m_y = d_y/d_{magntiude}$. Finally, we use this derivative to determine the path to the nearest local maximum in the D_{min} map.

Specifically, we find the minimum of $\sqrt{(m_x + i_x)^2 + (m_y + i_y)^2}$ for $-1 \leq i_x \leq 1$ and $-1 \leq i_y \leq 1$ and this minimum determines which adjacent grid cell will lead us towards increasing values of D_{min}. We then repeat this process at the new coordinates for five iterations. After five iterations (which is sufficient to determine the direction to the correct local maximum) we follow the adjacent cell with the largest value of D_{min} which eventually leads to a local maximum of D_{min}.

A.1.2   Periodicity

Since our data is horizontally periodic, we want the cells that are identified to include data beyond the edge of the domain (which influences the magnetic field concentrations). Thus, to deal with the periodicity, we tile the original image in a 3×3 larger image and apply the method to

this larger set of tiles. After applying the method and identifying the cells we cut back down to the original size in the center of the 3×3 network of cells. This smaller image now has matching cells across the periodic boundaries which requires accounting for cells that overlap at the edge of the periodic boundary.

A.1.3   Void Results

We use the void analysis to identify supergranular scale cells in the photospheric magnetic field ($|B|$) for all four primary magnetized simulations: 10 G mean field, zero net flux, artificial flux 10 Mm (with 15 G mean field), and artificial flux 2.56 Mm (with 15 G mean field). The magnetic energy spectrum (Figure 5.5) shows statistically significant differences between the low wavenumber power in these four simulations with the 10 G mean field simulation exhibiting much larger scale field distribution than any other simulation. Similarly, examinations by eye show that the magnetograms of these four simulations (Figure 5.6) have significant differences in the separation between the strongest magnetic flux elements. The 10 G mean field simulation and artificial flux 2.56 Mm, 15 G simulation exhibiting the largest-scale and smallest-scale magnetic flux element separations, respectively.

From Figure A.1 we can see that the artificial flux 2.56 Mm, 15 G simulation has the smallest cell diameters with the zero net flux simulation slightly increased but with smaller cells than the other simulations. This is consistent with the amplitude of the low wavenumber modes of the magnetic field spectrum (Figure 5.5). The artificial flux 10 Mm, 15 G simulation, however, has the largest cell diameters which is inconsistent with the magnetic field spectrum or by eye examination. Finally, the Hinode magnetic field is most closely fit by the 10 G mean field simulation.

A.2   Medial Axis Transform

The second method we apply is the iterative medial axis transform (Berrilli et al., 1998, 2005). This method is used to identify supergranules using Ca II K contrast images (a proxy for the photospheric magnetic field) from the Precision Solar Photometric Telescope (PSPT) at Mauna
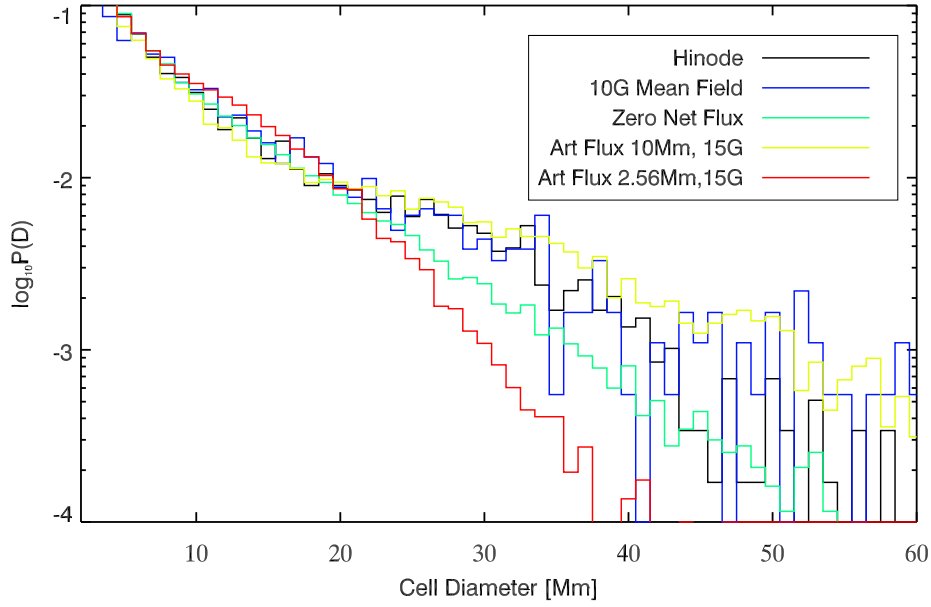
Figure A.1 The probability distribution function of cell diameters using the void analysis on the zero net flux (*solid* curve), 10 G mean field (*dashed* curve), artificial flux 10 Mm, 15 G (*dotted* curve) and artificial flux 2.56 Mm, 15 G (*long-dashed* curve) simulations and Hinode observations of photospheric magnetic fields. The artificial flux 2.56 Mm, 15 G simulation exhibits the smallest scale cells.

Loa Solar Observatory (McIntosh et al., 2011; Goldbaum et al., 2009). We give a brief description of the method and our implementation (which is nearly identical to the method applied to PSPT observations) before discussing the results.

A.2.1 Details of the Medial Axis Transform Method

The medial axis transform outlines a skeleton of complete cells in smoothed images of magnetic field. The method looks for ridges of network magnetic field and connects these ridges if they are close enough to create a complete outline. If a ridge does not connect to a cell outline then it is pruned off until only the outlines remain. We then identify the cells within the skeleton outlines.

For all parameter choices we use the same as is used on the PSPT images with good seeing (Goldbaum et al., 2009). This includes smoothing the images with a Gaussian using full width at half maximum of 4.78 Mm. We determine a threshold for magnetic flux elements that should be considered part of the network magnetic field or the background in an $L \times L$ moving window with $L = 156$ grid cells (≈ 30Mm in physical units). This threshold function is $T(x, y) = \langle |B(x, y)| \rangle_L + \zeta \sigma(x, y)_L$ where $\sigma(x, y)_L$ is the standard deviation of the magnetic field strength and $\langle |B| \rangle_L$ is the average field strength in the $L \times L$ window. ζ is a tunable parameter that we set -0.4 to match the PSPT observations.

A.2.2 Medial Axis Transform Results

We see the resulting pdf of medial axis transform cell diameters in Figure A.2. While the artificial flux 2.56 Mm, 15 G simulation has the fewest cells with diameter larger than 30Mm, the other three simulations are qualitatively indistinguishable. Furthermore, the cells from the Hinode observations are significantly smaller than the simulations. Thus the medial axis transform results are not consistent with the void analysis.
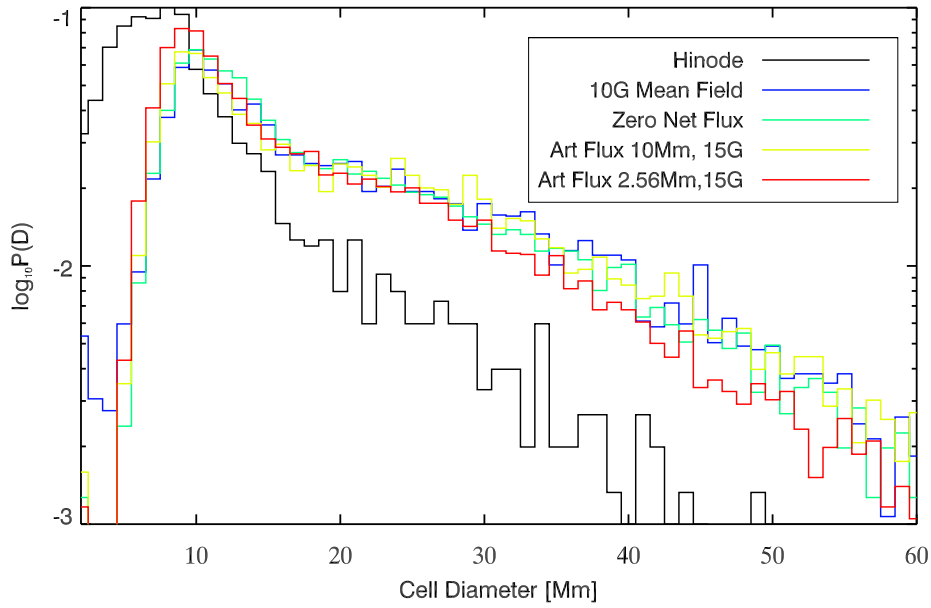
Figure A.2 The probability distribution function of cell diameters using the medial axis transform on the zero net flux (*solid* curve), 10 G mean field (*dashed* curve), artificial flux 10 Mm, 15 G (*dotted* curve) and artificial flux 2.56 Mm, 15 G (*long-dashed* curve) simulations and Hinode observations of photospheric magnetic fields. The simulations are nearly indistinguishable while the Hinode observations have much smaller cells than any simulation.

A.3   Watershed

The final detection method for the network magnetic fields is the watershed analysis used by McIntosh et al. (2011, see references within for details on the method). This method is typically applied to smoothed chromospheric white light observations and, consequently, there is no analog to the parameter choices for applying this method to the photospheric magnetic field.

A.3.1   Details of the Watershed Method

The watershed determines cells using a topographic method where the smallest magnetic field regions are considered basins where water collects. The method then determines where magnetic field boundaries would allow these basins to join into one pool or separate into different "watersheds" (a term derived from terrestrial watersheds). Without using any smoothing this method only identifies magnetic field cells on granular scales since the field is quickly advected to downflows by granular flows. To identify supergranular cells we thus apply a smoothing by convolving the magnetic field with a Gaussian. Since there is no smoothing to compare to observations we test several smoothing widths and choose a Gaussian fwhm of 6.4 Mm which maximizes the 30 Mm diameter cell sizes (the observed diameter of supergranules) in the 10 G mean field simulation.

A.3.2   Watershed Results

We see in Figure A.3 the pdf of cell diameters identified by the watershed method. Similar to the void analysis we find a clear separation of the simulations with the 10 G mean field and artificial flux 2.56 Mm, 15 G runs having the largest and smallest cells, respectively, as we expect from the magnetic field spectrum. The zero net flux and artificial flux 10 Mm, 15 G simulations are also well separated but the zero net flux simulation has larger cells even though it has lower amplitude low wavenumber power in the magnetic field spectrum. Finally, the Hinode observations have much smaller cells sizes than any simulation.
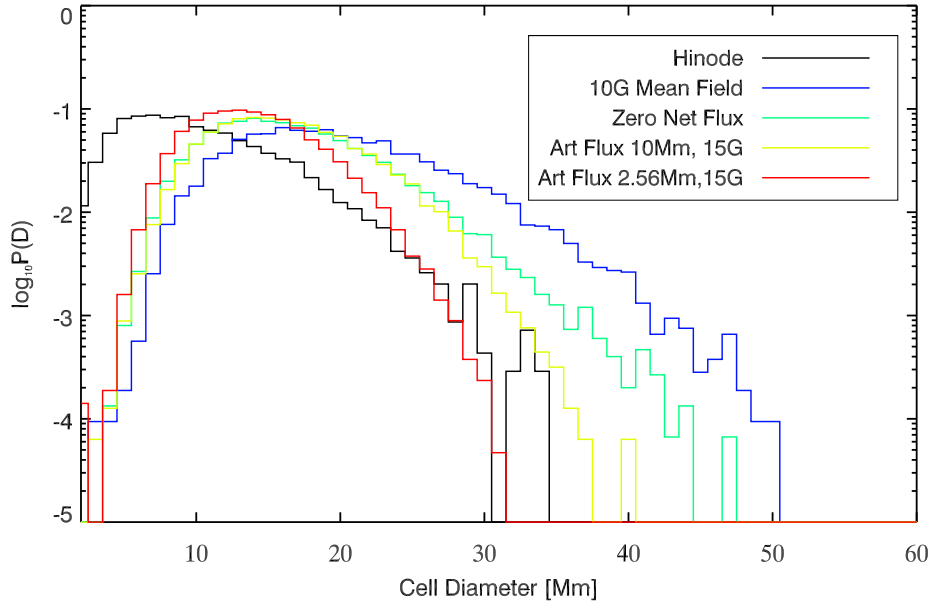
Figure A.3 The probability distribution function of cell diameters using the watershed analysis on the zero net flux (*solid* curve), 10 G mean field (*dashed* curve), artificial flux 10 Mm, 15 G (*dotted* curve) and artificial flux 2.56 Mm, 15 G (*long-dashed* curve) simulations and Hinode observations of photospheric magnetic fields. The artificial flux 2.56 Mm, 15 G and 10 G mean field simulations exhibit the smallest and largest scale cells, respectively for any simulation. The Hinode observations have smaller scale cells than any simulation.

A.4   Problems with These Methods

None of these methods are consistent between simulations or with observations (see Figure A.4), except for the small cell sizes of the artificial flux 2.56 Mm, 15 G simulation. While examining the magnetograms by eye shows obvious cell size differences (Figure 5.6) and the magnetic field spectrum finds statistically significant differences between the low wavenumber power (Figure 5.5), these differences are not reflected in any method.
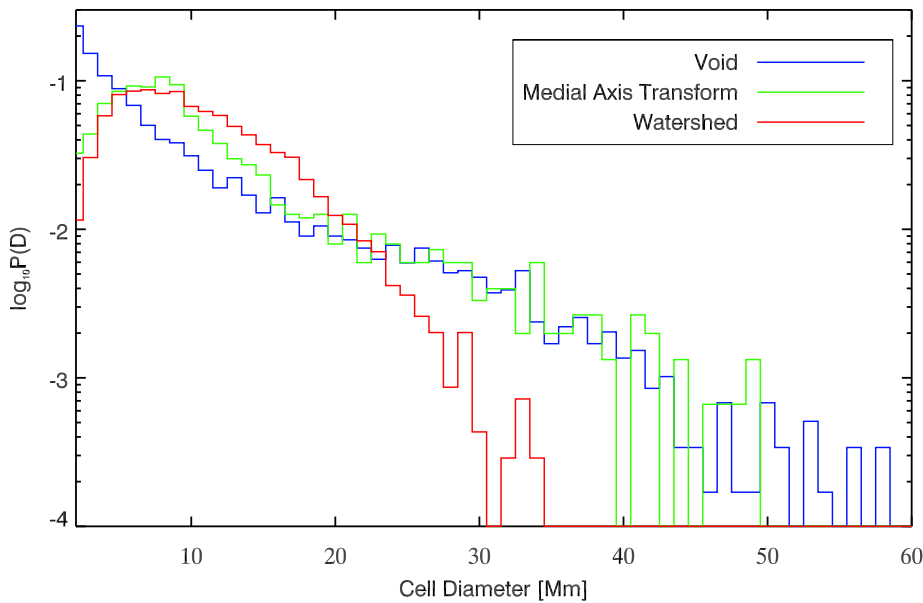

Figure A.4 The probability distribution function of cell diameters using the void, medial axis transform, and watershed analysis on Hinode observations of photospheric magnetic fields. The void and medial axis transform are consistent for cell diameters greater than 25 Mm.

Each method is dependent on parameter choices without a priori values. For all choices we use parameters that are most similar to those used in observations when applicable. We have tested several parameter choices for each method that have not been presented above, but all these tests have given similar (i.e. inconsistent) results between methods. This is shown in Figure A.5, where we compare each of the methods for the same snapshot of the vertical magnetic field of the zero net flux simulation. Each method gives very different results and it is not clear if any method is physically significant to the supergranular flows.
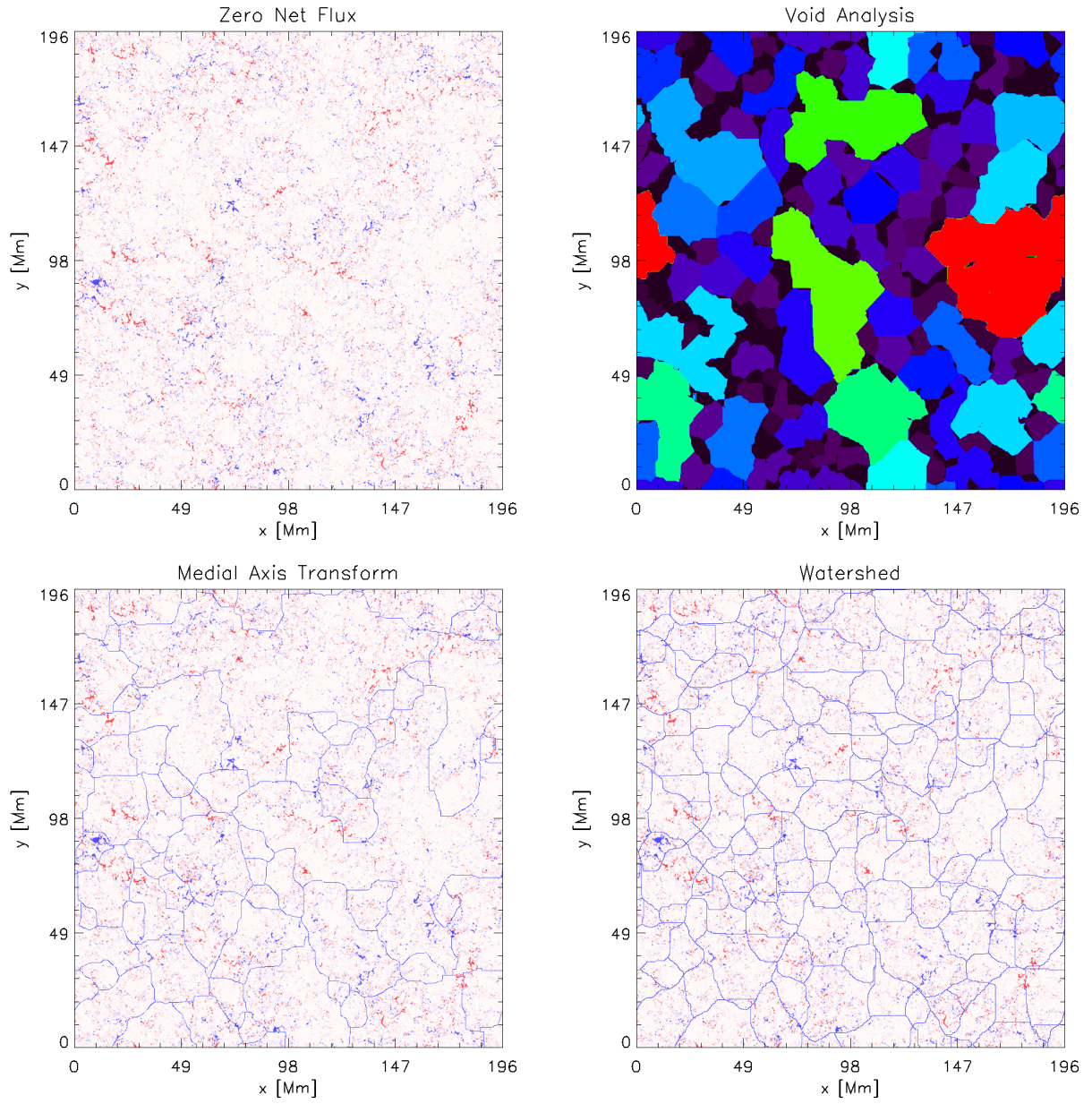
Figure A.5 Snapshot of the three magnetic field cell detection methods used in Appendix A (the void analysis, the medial axis transform and watershed method). The zero net flux simulation vertical magnetic field is shown as a comparison.